Two-dimensional emulsions and colloids formed by liquid inclusions in free-standing smectic liquid crystal films

Thesis

for the degree of

doctor rerum naturalium
(Dr. rer. nat.)

approved by the Faculty of Natural Sciences of Otto von Guericke
University Magdeburg

by M. Sc. Christoph Klopp
born on August 11th, 1990 in Gardelegen

Examiner:

Prof. Dr. rer. nat. Ralf Stannarius

Prof. Dr. rer. nat. Heinz-Siegfried Kitzerow

submitted on: April 19th, 2022
defended on: November 3rd, 2022

Foreword and publications related to this thesis

This thesis represents an excerpt of my scientific work in the “Department of Nonlinear Phenomena” in the group of Prof. Dr. Ralf Stannarius and apl. Prof. Dr. Alexey Eremin at the Otto von Guericke University in Magdeburg.
It discusses experimental investigations on the dynamics of various types of liquid inclusions in thin free-standing liquid crystal films. Due to the self-assembly of the molecules in smectic layers, smectic liquid crystal films can be seen as two-dimensional systems.
The thesis is composed as following:
The first chapter of that work introduces liquid crystal materials, freely suspended (free-standing) smectic films and its properties. As an essential part of this work, experiments under microgravity conditions and in particular a mission (OASIS) at the International Space Station are described.
In the chapter 2, the self-organization of liquid droplets in a lattice-like structure on the surface of a smectic bubble is analyzed. An investigation of the merging process of these droplets within milliseconds follows in chapter 3. Finally, in chapter 4, long-term dynamics of smectic islands and the structural change of the ensembles over time due to island coalescence or Ostwald ripening are analyzed. The results of this thesis are published in the following peer-reviewed scientific journals.

- N. A. Clark, A. Eremin, M. A. Glaser, N. Hall, K. Harth, **C. Klopp**, J. E. Maclennan, C. S. Park, R. Stannarius, P. Tin, W. N. Thurmes and T. Trittel, *Realization of hydrodynamic experiments on quasi-2D liquid crystal films in microgravity*, *Advances in Space Research*, 60: 737-751, 2017

- **C. Klopp**, T. Trittel, A. Eremin, K. Harth, R. Stannarius, C. S. Park, J. E. Maclennan and N. A. Clark, *Structure and dynamics of a two-dimensional colloid of liquid droplets*, *Soft Matter*, 15: 8156-8163, 2019

- **C. Klopp**, T. Trittel and R. Stannarius, *Self similarity of liquid droplet coalescence in a quasi-2D free-standing liquid-crystal film*, *Soft Matter*, 16: 4607-4614, 2020

- **C. Klopp** and A. Eremin, *On Droplet Coalescence in Quasi-Two-Dimensional Fluids*, *Langmuir*, 36: 10615-10621, 2020

- **C. Klopp**, T. Trittel and R. Stannarius, *Coarsening dynamics in quasi-two-dimensional emulsions*, publication in progress, 2022

In addition to the experiments presented in this thesis, I contributed to further experiments under microgravity condition concerning different scientific topics. Between 2015 and 2022, I have participated in 6 parabolic flight campaigns (organized by DLR, CNES and ESA) where I have studied, for example, the rupturing process of catenoid-shaped smectic films and shape deformations under acoustic excitation. During the last campaign in February 2022 (38th DLR parabolic flight) I was even able to write parts of this work under microgravity conditions.
Furthermore, I took part in a suborbital sounding rocket campaign at Kiruna in the northern Sweden. Here, I investigated thermally driven flow (Marangoni flow) of smectic material in a thin free-standing smectic film. My first experience of weightlessness during the first parabolic flights and the midnight sun north of the Arctic Circle during the sounding rocket experiments are among the highlights of my previous scientific work.
As part of a DAAD ("Deutscher Akademischer Austauschdienst") exchange program, I spent several weeks at our cooperation partner at the University of Colorado in Boulder (USA). With my research, I was able to significantly advance the international ISS project OASIS. The results of my work were presented at numerous national and international conferences.
All other scientific publications in which I was involved are listed below in chronological order.

Further publications

- **C. Klopp**, R. Stannarius and A. Eremin; *Brownian dynamics of elongated particles in a quasi-two-dimensional isotropic liquid*; *Physical Review Fluids*, 2(12): 124202, 2017

- M. Alaasar, S. Poppe, C. Kerzig **C. Klopp**, A. Eremin and C. Tschierske; *Cluster phases of 4-cyanoresorcinol derived hockey-stick liquid crystals*; *Journal of Materials Chemistry C*, 5(33): 8454-8468, 2017

- T. Trittel, K. Harth, **C. Klopp** and R. Stannarius; *Marangoni Flow in Freely Suspended Liquid Films*; *Physical Review Letters*, 122(23): 234501, 2019

- R. Stannarius, T. Trittel, **C. Klopp**, A. Eremin, K. Harth, N. A. Clark, C. S. Park, and J. E. Maclennan; *Freely suspended smectic films with in-plane temperature gradients*; *New Journal of Physics*, 21: 063033, 2019

- **C. Klopp**, T. Trittel, K. Harth and R. Stannarius; *Smectic free-standing films under fast lateral compression*; *Soft Matter*, 18: 146-155, 2022

- A. Missaoui, K. Harth, T. Trittel, **C. Klopp**, R. Stannarius and E. Lacaze; *Shape instabilities of islands in smectic films under lateral compression*; *Soft Matter*, Advance Article, 2022

Contents

1 Free-standing liquid crystal (LC) films

The first chapter gives the framework and motivation of the whole thesis. Liquid crystal materials are introduced and the most common application of liquid crystals, the liquid crystal display (LCD), will be explained briefly. The structure and some properties of specific liquid crystal phases are shown, whereas the focus will be on the smectic A (SmA) and smectic C (SmC) phases here. In the third part of this chapter the preparation of free-standing liquid crystal films is presented and the properties of quasi-two-dimensional free-standing films are underlined. At the end, the OASIS-ISS mission will be explained, where some experiments discussed in this thesis were performed. In addition, the advantages of these experiments under microgravitational conditions are shown.

1.1 Motivation

Liquid crystals are essential materials in today's display technology and industry, which can be found e.g. in many TVs, smartphones and computer screens and displays of wristwatches and pocket calculators.

The basic principle of all (twisted) nematic liquid crystal displays (LCDs) is that linearly polarized light passes through parallel glass plates filled with liquid crystal material and thereby can change its polarization direction. The nematic liquid crystal molecules are usually aligned parallel to the glass slides. For the configurations shown in figure 1.1, the molecules are additionally rotated from top to bottom plate by 90° in order to form a helical structure (without applied electric field). This molecular rotation rotates the polarization direction of the incident light, and depending on the orientation of the second polarizer, the light can pass the whole cell (the cell appears bright) or is extinguished by the polarizer (the cell appears dark). Applying an electric field between the electrodes at the two glass plates (twisted nematic cell: TN-cell) or between the electrodes on the side of one glass plate only (in-plane switching cell: IPS-cell) leads to an alignment of the molecules with positive dielectric anisotropy parallel to the electric field. For the shown examples, the former helical structure in the cell is broken and the linearly polarized light will not change its polarization state: the cell changes its appearance from bright to dark or vice versa [1].

The shown twisted nematic and in-plane switching cells and the arrangement of the molecules and the polarizers only represent one possible implementation of the simplest liquid crystal display cells. A rotation of the second polarizer parallel to the first one in both types of cells, for example, would lead to a swap of the bright and dark state. For the IPS-cell, it is also possible to have an untwisted molecule structure in the initial state (without E-field) and only creating the helical structure when applying the electric field. Intermediate brightness-states, i.e. changes of the emitted light intensity, can be realized by adjusting the voltage on the electrodes and thus the strength of the field. Both cell-types can be used in transmission mode with a background light or in reflection mode with an additional reflector or reflective polarizer.

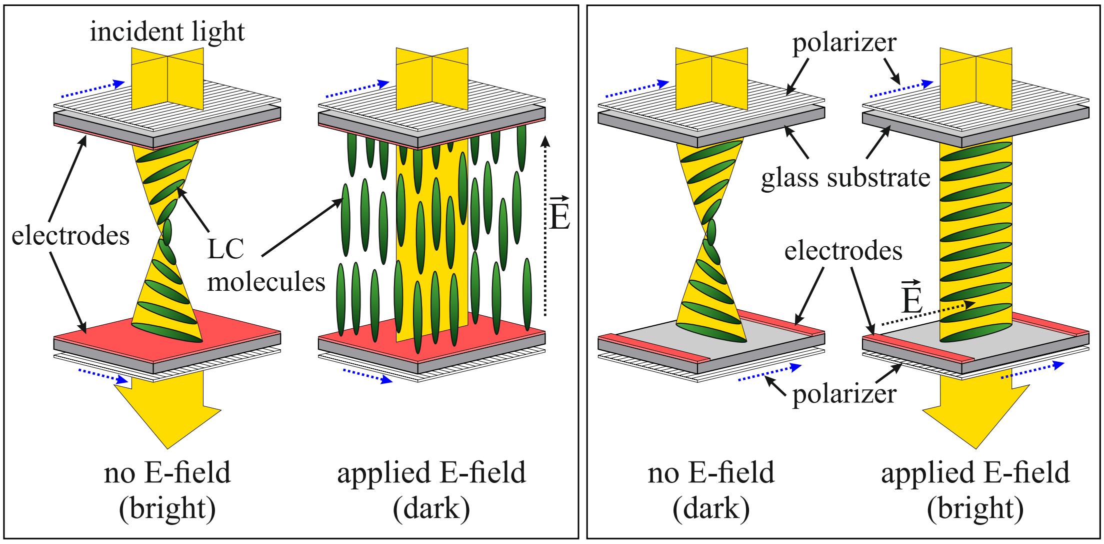

Figure 1.1: Schematic drawing of twisted nematic cells (TN) in the left-hand images and in-plane switching cells (IPS) on the right-hand side in transmission mode. In both cases, the incident light passes a polarizer, a glass substrate, the liquid crystal material, a second glass slide, and finally a second polarizer. For the shown TN cells, the two polarizers are rotated by 90° to each other and the electric field is applied between the two glass plates coated with transparent electrodes. For the IPS cells shown, the polarizers are aligned parallel to each other and the electrodes are mounted on one of the glass plates only. The electric field is applied parallel to the glass substrate (in-plane). The dashed arrows indicate the electric field direction (black) and the orientation of the polarizers (blue).

The switchable rotation of the polarization direction of light is also used to build liquid crystal spatial light modulators (LCSLM). Using spatial light modulators, it is possible to control the amount of light passing through the material independently at different positions [1, 2].

There are also applications as sensors (temperature sensors [1], DNA-biosensors or photosensors [3]) or adaptive optics and lenses [3], where the electrooptical, ferroelectrical and flexoeletrical properties of different liquid crystal materials are used.

In the context of this thesis, smectic liquid crystals are used to create unique quasi-two-dimensional (2D) systems. Due to the inner structure of smectic liquid crystals (see section 1.2), it is possible to produce thin free-standing films (in appearance comparable to thin soap films) with an aspect ratio of more than 10^6 (width of the film divided by film thickness). Within these thin freely suspended liquid crystal films (also free-standing liquid crystal films), the flow normal to the film plane can be neglected, so only flow in two dimensions is considered. Smectic liquid crystal films are ideal systems to analyze the hydrodynamics and rheology of two-dimensional liquids in order to answer fundamental questions concerning inclusion motion or flow in 2D. Whereas most hydrodynamic phenomena in common Newtonian three-dimensional liquids are investigated and well understood, the behavior in 2D systems is much more complicated or completely different and not fully understood yet. The well known Stokes equation describes the flow in 3D Newtonian fluids. Nevertheless, it diverges in 2D systems ("Stokes' paradox"). The understanding of such motion and interaction of inclusions in two-dimensional systems and their hydrodynamics is essential, as they appear in biological systems (biological membranes) or wetting-technology.

Within this thesis, the performed experiments using free-standing liquid crystal films are explained and the results are presented and discussed. The analyzed free-standing liquid crystal films with different inclusions represent a unique system and the observations help to understand fundamental problems as the merging process of liquid droplets or the long-term behavior of emulsions. Furthermore new phenomena like the self-organization of liquid droplets in a lattice structure are observed and explained.

1.2 Liquid crystals

In 1888, the Austrian botanist of the Institute for Plant Physiology of the German University of Prague, Friedrich Reinitzer, first described and explained colored phenomena during the melting process of cholesteryl acetat and cholesteryl benzoate. He noticed that cholesteryl benzoate changes its appearance from solid state to a cloudy fluid when heated above 145.5 °C. At the temperature of 178.5 °C, it turned into a clear fluid. This "double melting" behavior [4, 5] was verified by the German physicist Otto Lehmann using the new developed technique of polarizing microscopy. In August 1889, Lehmann wrote in one of his letters to Reinitzer:

> *"It is of high interest for the physicist that crystals can exist with a softness, being so considerable that one could call them nearly liquid."*
>
> Original [6]:
>
> *„Für den Physiker ist es jedenfalls von hohem Interesse, daß Kristalle existieren, deren Weichheit eine so bedeutende ist, daß man sie beinahe flüssig nennen könnte.“*

Later that year, Lehmann published his observations in his paper "Über fliessende Kristalle" [7], and since that time the term "liquid crystals" is established.

Liquid crystals are materials that have properties associated with both liquids and crystals, and there are at least two common types of molecules that form liquid crystal phases: anisotropic rod-shaped (calamtic) and anisotropic disc-like (discotic) mesogens. The molecules in a crystal are fixed according to their orientational, rotational and positional order, whereas in a liquid there is no long-range order. The molecules in a liquid are free to translate, rotate and tumble. The mesogens in liquid crystal phases are orientationally ordered, but in contrast to the crystalline phase, there is a decay of positional and translational order. By changing the temperature (thermotropic liquid crystals) or the concentration of compounds in a mixture (lyotropic liquid crystals), the degree of order will be increased or decreased and different stable liquid crystal phases arise. Depending on the liquid crystal material, different possible phases are observed at different temperatures or concentrations.

To analyze the orientational direction of the mesogenes, the average local orientation of the molecules, called the director $\hat{n}$, is defined as shown in figure 1.2. In addition, the orientational order parameter

$$S = \langle P_2(\cos\theta) \rangle = \left\langle \frac{3}{2}\cos^2\theta - \frac{1}{2} \right\rangle \tag{1.1}$$

can be defined, where P_2 represents the second Legendre polynomial and θ corresponds to the deviation of the molecule orientation from the director $\hat{n}$. For a typical transition from the crystalline state via liquid crystal phases and to the isotropic state by increasing the temperature, the order parameter S will decrease from a perfect ordered state, represented by $S = 1$, to the completely disordered state for liquids ($S = 0$).

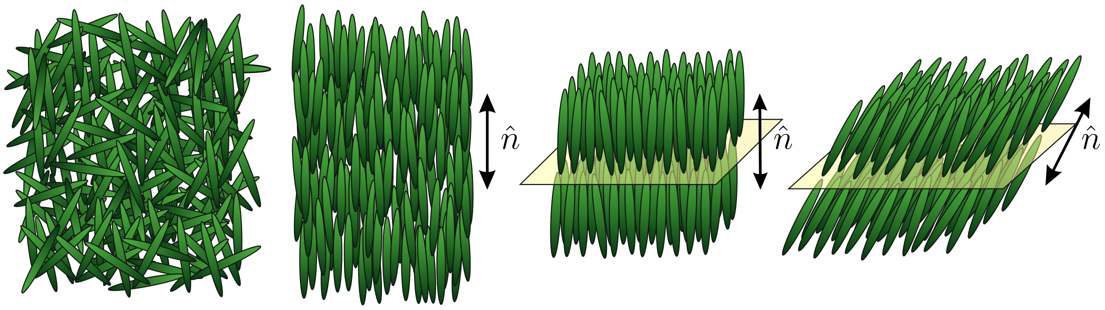

isotropic (Iso) nematic (N) smectic A (SmA) smectic C (SmC)

Figure 1.2: Molecular orientation and inner structure of the isotropic/liquid phase and three simple liquid crystal phases. In the isotropic phase (left-hand side), there is no orientational, positional or rotational order. The nematic phase (second from the left) shows orientational order but no positional order. In the smectic A phase (second from the right), the molecules are additionally ordered in a layered structure compared to the nematic phase. The smectic C phase (right-hand side) also shows a layered structure, but the molecules are on average tilted according to the layer normal.

The three liquid crystal phases visualized in figure 1.2 show orientational order and the director $\hat{n}$ represents the average direction of the long axis of the molecules. For the nematic phase, there is no further order. In the smectic A phase, the mesogenes are additionally arranged in a layered structure and the director is parallel to the layer normal. The smectic C phase shows the same layering, but the molecules are tilted in respect to the layer normal.

1.3 Freely suspended liquid crystal films

The order of the mesogenes in a lamellar structure in the smectic A and smectic C phase is essential to form free-standing liquid crystal films. Due to the layer structure, the films are extremely robust and films up to hundred square centimeters in size [8] can be drawn. The film thickness is limited by the thickness of the layers and thus by the molecular dimension itself. Film thicknesses between a few nanometers (two molecular layers) and several micrometers are possible, depending on the molecule length, the tilt of the mesogens and the number of layers. In contrast to soap films, smectic films are not subject to drainage or evaporation at ambient temperature. Different geometrical shapes of free-standing films can be realized since films form minimal surfaces due to their interfacial tension. For experimental studies, usually flat films are used [9–20], but spherical [21–24] (also see section 1.4) or catenoid shaped films [21, 25, 26] have been investigated as well. As shown in figure 1.3, free-standing smectic films are connected to the frame by the meniscus (region with increasing thickness), that additionally acts as a reservoir for the liquid crystal material. The meniscus often influences the flow of material or the motion of inclusions in the film. For the free-standing film itself, several metastable situations can be observed. In contrast to a homogeneous film of thickness N, also regions with thickness $N - k$ or $N + k$ ($k = 1, 2, 3, 4, ...$) can appear [21, 27, 28]. Domains of different thickness are separated by layer steps, where the inner layered structure of the smectic film locally is disturbed (dislocations around the regions). Domains thinner or thicker than the rest of the film are called "smectic islands" (thicker region) or "smectic holes" (thinner regions), respectively. Figure 1.3 shows a sketch of a flat homogeneous smectic A film with islands and holes which can be observed by optical microscopy.

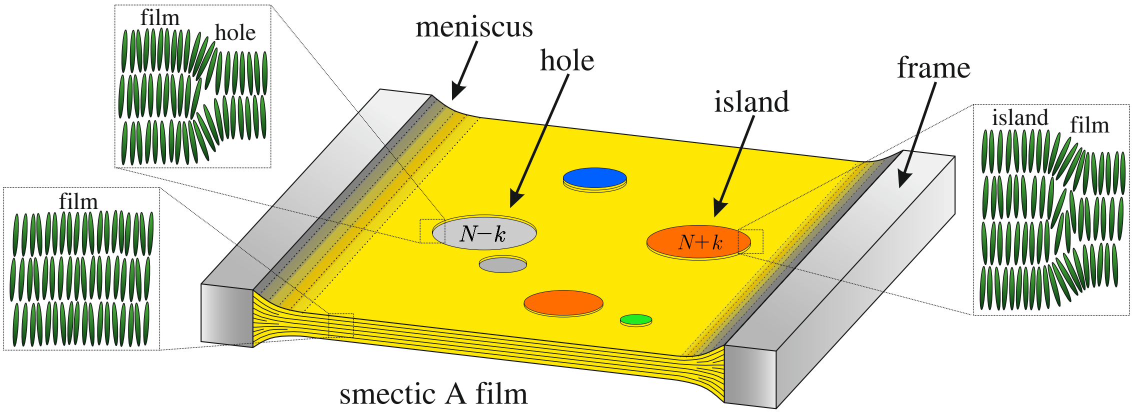

Figure 1.3: Geometry and structure of a planar freely suspended liquid crystal film in the smectic A phase. The meniscus connects the film with the film support (frame). Thinner regions with $N-k$ layers (smectic holes) and thicker domains with $N+k$ layers (smectic islands) are shown in the homogeneous background film. Different region colors correspond to different numbers of layers of these domains, which are separated by disclination lines, where the layered structure is locally disturbed (steps). The front and the rear edge of the frame has been removed for visualization. The film thickness and single layer thicknesses are highly exaggerated.

For tilted molecules forming smectic C phases, it is useful to define the “c-director” as the mean projection of the molecules long axis to the film plane. The c-director visualizes the tilt direction of the mesophase and therefore additional configurations in the film can be observed. Figure 1.4 shows several configurations of the c-director field, a 2π-wall where the director undergoes a full 2π rotation through a straight line segment, and a pair of defects in a smectic C free-standing film, where the orientation of the molecules locally changes or is not defined (center of the defect).

According to the analysis of motion of inclusions or flow phenomena in free-standing films, the situation in smectic C films becomes more complicated than in smectic A films. The c-director couples to the flow in the film and the molecules need to reorient. The configuration of the c-director field depends on film boundary anchoring conditions and on the anchoring conditions at the inclusion interfaces as well [29, 30].

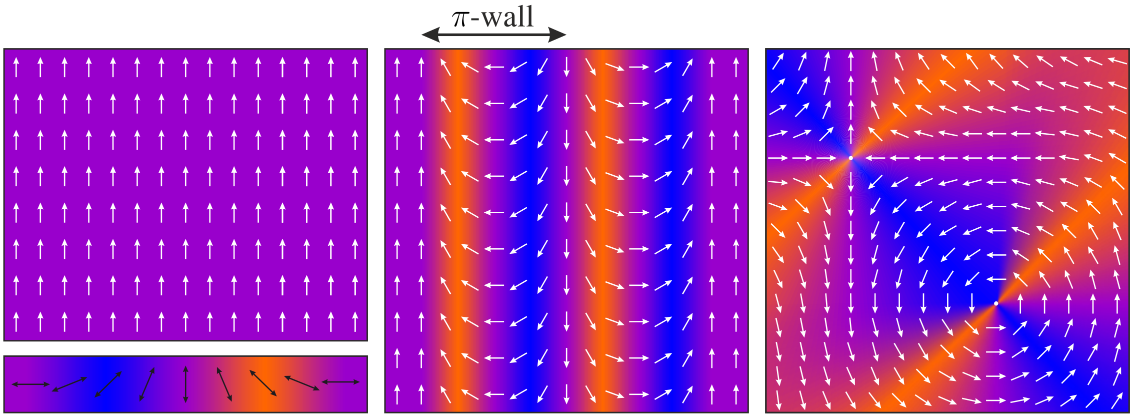

Figure 1.4: Different simulated c-director textures in the top view of a free-standing smectic C film under crossed polarizer and an additional $\lambda = 550$ nm phase plate (45° to both polarizer). On the upper left-hand side, the director is uniformly orientated, while in the middle, the c-director changes its direction by an angle of 2π (from left to right). This configuration is called a “2π-wall” (two times a π-wall). In the right-hand picture, two point defects are shown where the director in the center is not defined. The upper defect has the topological strength of “-1” and the lower the topological strength of “+1”. The left-hand bottom image visualizes the orientation of the c-director and the corresponding occurring colors in experiments with films under crossed polarizer and an additional $\lambda = 550$ nm phase plate.

1.4 Liquid crystals under microgravity conditions

In most experimental studies concerning free-standing liquid crystal films, it is important to control the material temperature and to avoid external flow in the surrounding medium (usually air). There are some experiments that additionally need microgravity conditions for a few seconds up to hours to study specific phenomena, such as Marangoni flow in thin liquid crystal films. Three different experiments on varying microgravity platforms are presented in this section: flat smectic films on sounding rockets, arbitrary shaped closed films at parabolic flights and smectic bubbles on board the International Space Station (ISS).

1.4.1 Suborbital sounding rockets

One opportunity to achieve microgravity (µg) conditions are suborbital sounding rockets like the "TEXUS" (**T**echnologische **EX**perimente **U**nter **S**chwerelosigkeit) rockets, operated by DLR, that allows scientists to use approximately 6 minutes of microgravity for biological, physical or material science experiments. The sounding rockets are often used to test experimental setups for later ISS missions, too.

Trittel et al. investigated the effect of thermal gradients on flat freely suspended liquid crystal films [24, 31, 32] during their OASIS-Tex missions. Former experiments in vacuum showed convective flow in smectic films exclusively driven by thermal gradients in the meniscus [33]. In contrast to these microgravity experiments, films surrounded by air were used since the heat conductivity of air is much bigger than that of the smectic films. Therefore, a uniform temperature gradient between hot and cold thermocontacts was achieved. In order to avoid buoyancy of the air and thus flow in the smectic film, it is essential to perform the experiments under microgravity conditions.

During their studies, Trittel et al. [31] and Stannarius et al. [24] observed laminar flow for small temperature gradients depending on the film thickness, the temperature coefficient of the material and the temperature difference. For their experiments, they used films in the smectic C phase and analyzed the occurring Schlieren textures to determine the thermally induced vortex flow velocity (figure 1.5) (Marangoni flow).

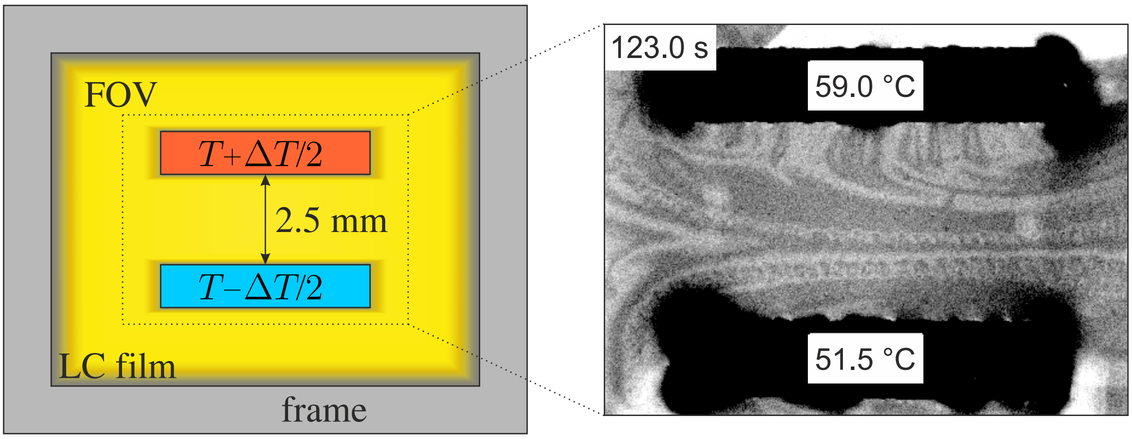

Figure 1.5: Setup and experimental image of the OASIS-Tex (TEXUS 55) mission. The picture on the left-hand side shows the film and heater geometry with cold (blue) and hot (red) thermocontacts touching the film. Between the contacts, a temperature gradient ΔT of up to 10 K/mm was set. The right-hand image shows a contrast enhanced image from the original measured data with added temperature and time labels. The Schlieren textures in the 170 nm thick film between the thermocontacts allow to measure the flow velocity of the material (material 10PP8 in the smectic C phase). The ambient temperature was $T = 50$ °C. The original photo was kindly provided by T. Trittel and coauthors [24, 31].

1.4.2 Parabolic flights

Parabolic flights are a second opportunity to perform experiments under microgravity conditions. The flights were operated by *Novespace* in Bordeaux, France, using an Airbus A300 or A310. Here, the experimental time is limited to 22 s, but there are at least 30 parabolas per flight, so the experimenters can continuously control and adjust their setups. One advantage of parabolic flights is the direct interaction of scientists with their experiments. On the other hand, the µg-quality excludes some experiments like flat free-standing film, since there is g-jitter of the airplane ranging in magnitude within several percents of g. That would influence the motion of objects and flow in the film significantly. Nevertheless, parabolic flights were used to test the experimental principles later used on the OASIS ISS mission.

While experiments with flat free-standing films would not lead to meaningful results, completely freely floating smectic bubbles are not that susceptible to the g-jitter. May et al. investigated the rupturing process of a catenoid shaped smectic A and C film and the shape deformation of these free-floating liquid crystal films. They analyzed the oscillation dynamics of smectic bubbles and observed filaments when films suddenly ruptured [21]. They also observed the creation of smectic islands on the film surface. In addition, Harth et al. later observed wrinkles occurring on the film surface and measured their wavelength. They also developed a model to explain the appearance of wrinkles and analyzed the possible influence of external acoustic excitation on the free-floating bubble and especially on the wrinkle generation process [26].

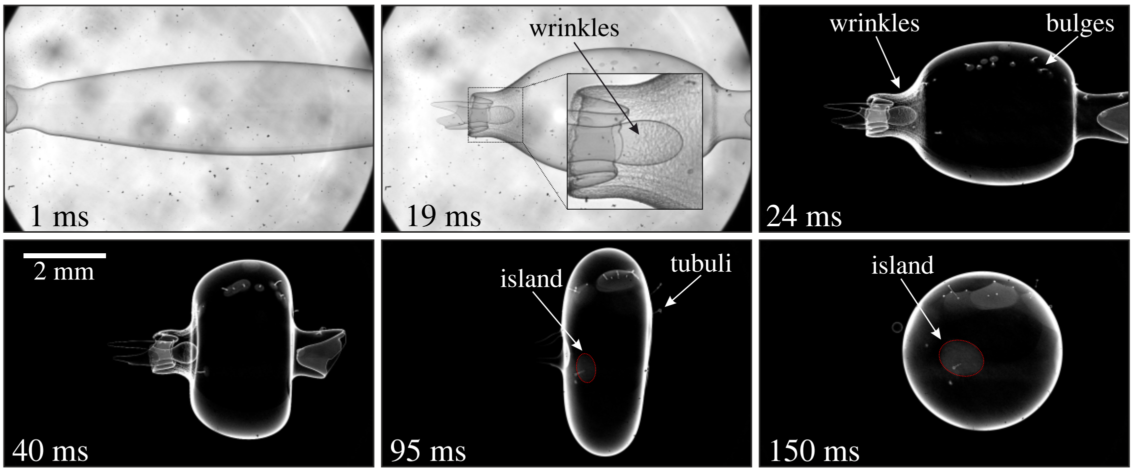

Figure 1.6: Shape evolution of a freely floating smectic bubble during the parabolic flight campaign in March 2019 (parabola 27 on March 12th). The first two pictures (top row) show the originally recorded images after 1 ms and 19 ms, regarding the pinch-off of the bubble from a collapsing catenoid. All other measured pictures were subtracted from the initial image background to better visualize important details. After 19 ms, due to an axial contraction, first wrinkles appear with a preferential orientation perpendicular to the contraction direction. Excess smectic material on the surface forms smectic islands and bulges. That bulges grow over time and sometimes form tubuli and may pinch-off as well [21,27,28].

Figure 1.6 shows an evolution of a freely floating smectic bubble after pinch-off from a collapsing catenoid under µg conditions. The shape of the film changes from a cylindrical to spherical shape by axial contraction. During that process, smectic material can form smectic islands, bulges or tubuli. Wrinkles of the smectic surface appeared already shortly after pinch-off. Further experiments during parabolic flight campaigns in 2019 showed that the wrinkle formation can be induced by acoustic excitation as well. The important parameters for the appearance of wrinkles are the initial film thickness and initial inhomogeneities on the film surface (islands). Recent experiments with the same experimental setup but a flat film in the center of the liquid crystal catenoid showed similar wrinkle formations under lateral compression [34].

1.4.3 Missions onboard the ISS

The International Space Station (ISS) is a scientific platform for a variety of long-term experiments in astrophysics, fluid physics, fundamental physics, biology, chemistry, physiology and many more. Onboard the ISS, the microgravity level is extremely good, since there is only small g-jitter and experiments ranging from a few days up to years are possible. The major disadvantages of ISS missions are extremely high costs, the lengthy planning and preparation phase and the transport of the experimental setup to the station.

1.5 The OASIS ISS mission

The OASIS (**O**bservation and **A**nalysis of **S**mectic **I**slands in **S**pace) project is a collaboration of three internationally recognized experimental groups working on free-standing liquid crystal films. The principal investigators are:

- Prof. N. A. Clark, Prof. J. E. Maclennan and Prof. M. Glaser
  from University of Colorado, Boulder (United States of America)
- Prof. A. Levchenko, Prof. V. Dolganov, Prof. P. Dolganov and Prof. E. Kats
  from Russian Academy of Science, Moscow (Russia)
- Prof. R. Stannarius
  from Otto von Guericke University Magdeburg, Magdeburg (Germany).

The setup for the OASIS mission was successfully launched at Kennedy Space Center on a SpaceX Falcon 9 Rocket on April 17, 2015. The experiments were performed between July 01, 2015 and March 18, 2016.

One of the primary goals of those free-standing liquid crystal film experiments was the investigation of hydrodynamic flow and hydrodynamic interactions in quasi-two dimensions. Interactions of emulsions of droplets and islands and their long-term dynamics were observed as well. Building on the success of the OASIS-Tex sounding rocket experiments, thermocapillary phenomena on a spherical film were also studied. Additionally, the effect of applied electric fields and inflation or deflation of the liquid crystal bubbles was investigated.

As stated in chapter 1.3, the meniscus connecting a free-standing film and the filmholder strongly influences the hydrodynamic flow and the behavior of inclusions in the film. For the OASIS experiments on ISS, a spherical shape for the free-standing film was chosen to minimize the meniscus, which only appears at the connection between the inflation needle and the bubble. As the ratio of the meniscus area to the whole bubble surface is extremely small, effects caused by the meniscus were strongly minimized. To prevent sedimentation of material and inclusions in this geometry and to avoid buoyancy driven convection in the surrounding air and in the liquid crystal film, a microgravity environment is mandatory. For long-term investigations, experiments on the ISS are required.

The OASIS setup

The setup for the OASIS mission was constructed and built by *ZIN Technologies, Inc*, financed by *NASA* and placed in the Microgravity Science Glovebox on ISS. The main elements of this setup are the concentric needle device to inflate or deflate the smectic bubble and the two high resolution CCD cameras (see figure 1.7). Four different liquid crystal materials with different properties regarding their phase sequence or their molecular structure (polar, non-polar, racemic, chiral) were used separately.

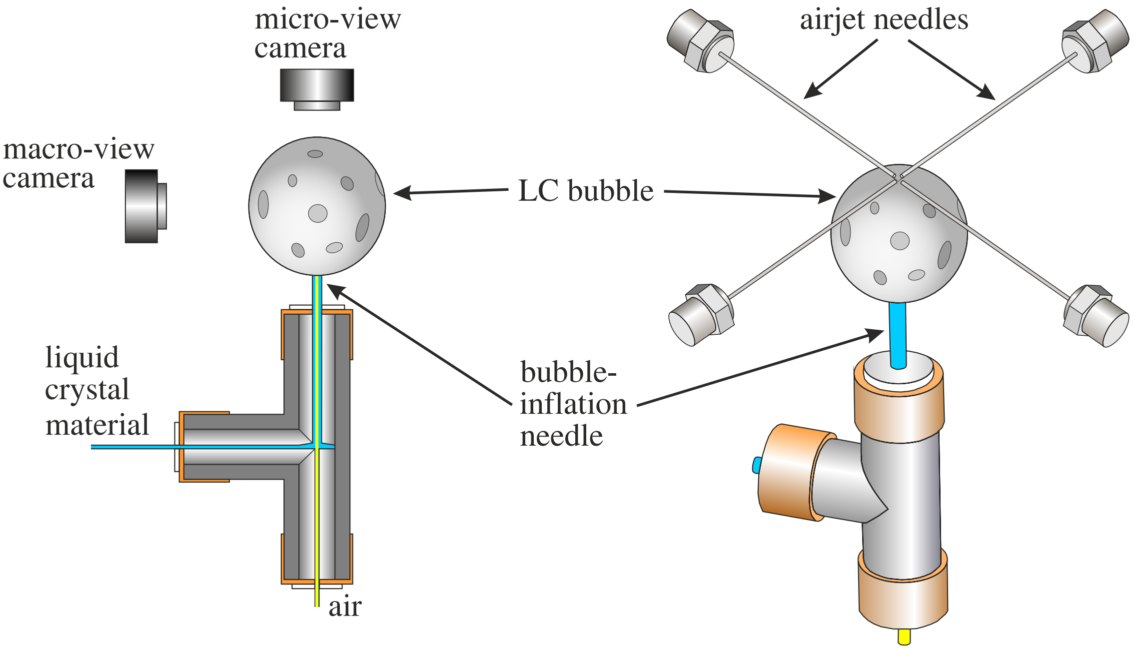

Figure 1.7: Experimental setup to generate and inflate liquid crystal bubbles during the OASIS mission onboard the ISS. The gap between inner capillary and outer capillary of the concentric needle device was filled with liquid crystal material pumped from a reservoir. Air was pumped slowly through the inner capillary to inflate the bubble. Two high resolution color CCD cameras (1024 × 1024 pixels) were used to observe the whole bubble (macro-view) and a 500 × 500 μm^2 region on the bubble (micro-view). Additionally, four airjet needles were placed above the bubble to provide controllable air flow. Two opposing needles were also used to create electric fields and one of the needles could be heated to create temperature gradients.

To create a free-standing smectic film on top of the inflation needle, liquid crystal material was pumped through the outer capillary of the concentric needle until a thin cap was formed across the opening of the inner needle. Then air was pumped gently through the inner capillary to inflate a thin smectic bubble [35]. Controlling the pumping rate of the air enables inflation or deflation of the smectic bubble. Film thicknesses between five and several thousands of nanometers were achieved using this technique. To record experimental data, a color CCD camera (*Prosilica GX 1050C, Allied Vision Technologies*) observed the whole bubble (macro-view) while a second identical camera was focused on a smaller 500 × 500 μm^2 region (micro-view). The micro-view camera was mounted on a linear actuator to change its field of view. Both cameras had a resolution of 1024 × 1024 pixels with a maximum frame rate of 112 frames per second (fps). Additionally, a spectrometer was available to measure the wavelengths of reflected light from the film to estimate its thickness. Almost uniform illumination of the bubble was achieved by using several arrays of LEDs and a parabolic diffuser. Figure 1.8 shows typical recorded pictures from the micro-view and macro-view cameras during the OASIS experiments. Due to the focal depth of the macro-view camera, the edge of the bubble often blurs with the background.

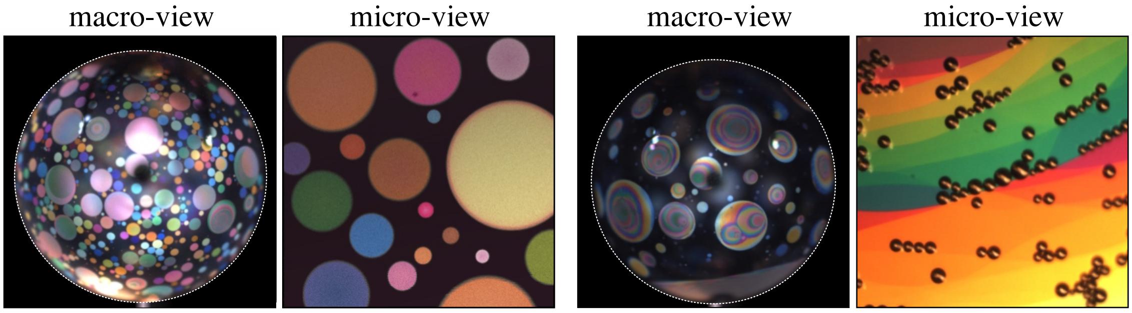

Figure 1.8: Experimental images from the OASIS experiment. The bubble diameter in the macro-view is approximately 15 mm depending on the inflating or deflating procedure. Since the depth of field of the macro-view camera was limited, the central region of the bubbles is focused while the outer region blurs with the background. The white dashed circle is added to visualize the complete bubble. The two left-hand pictures show typical situations for the coarsening experiments. The whole bubble is covered with smectic islands and they grow, shrink or merge during the experiments. Changes of the island diameter can be observed in the micro-view images as well as the coalescence of islands or droplets. The micro-view picture on the right-hand side shows isotropic droplets trapped at disclination lines (steps between regions of different thickness). These droplets can also form lattice-like structures, where they repel each other.

To create a strong airflow along the film surface and a continuous flow of material, four airjet needles, shown in figure 1.7, were used. Thereby, material from the meniscus was brought into the film and could form smectic islands of different thicknesses (left-hand picture in figure 1.8). A second mechanism to induce flow in the film was to create a thermal gradient by heating either one of the airjet needles or the inflation needle. The bubble inflating device, the airjet needles and the bubble itself were enclosed in a bubble chamber which could be heated uniformly up to 60 °C.

Controlling the temperature in the chamber, as well as of the inflation needle and the airjet needle, allowed to investigate thermally driven flow as observed earlier during the TEXUS experiments. Furthermore, temperature-dependent dynamics of coarsening of islands and interaction of islands could be observed and influenced. Heating the liquid crystal material to the phase transition temperature between smectic A and isotropic phase was a crucial method to create isotropic droplets (visible in figure 1.8 in the right-hand micro-view) and to observe their self-organization in a lattice-like structure (chapter 2).

2 Self-organization of isotropic droplets in free-standing smectic films - a real 2D colloid -

Colloids are systems in which solid, liquid or gas particles are dispersed in a continuous phase of a different material. Examples of that mixtures can be found everywhere in daily life: gas bubbles dispersed in a liquid e.g. in whipped cream (foam), liquid droplets embedded in a liquid phase for milk or mayonnaise (emulsion) or solid droplets dispersed in a liquid medium such as blood or ink (solution). The second chapter describes the restricted motion and the self-organization of flat isotropic droplets in a smectic A free-standing film. Micrometer-sized droplets form hexagonal structures since they repel each other. The nature of that repelling force is analyzed and discussed by measuring Brownian motion. The experiments are part of the OASIS mission onboard the ISS and so the first real two-dimensional colloid was created. The experimental results as well as numerical simulations are presented and compared. A model by Saffman and Delbrück to describe the motion of inclusions in two dimensions was expanded to explain the dynamics in restricted geometries as well. The results presented in that chapter are published in [23].

2.1 Introduction

2.1.1 Stokes' paradox

In December 1850, Sir George Gabriel Stokes described the motion of a viscous fluid around a solid sphere moving uniformly with a small velocity. He published his famous law for the frictional force $\boldsymbol{F}_D$ (also drag force) that opposes the motion of a sphere through the fluid.

$$\boldsymbol{F}_D = 6\pi\eta a\mathbf{u} \tag{2.1}$$

That force is derived by solving the Navier-Stokes equation for small Reynolds numbers depending on the particle velocity $\mathbf{u}$, the sphere radius a and on the viscosity η of the fluid. Stokes also tried to analyze the slow motion of an infinite cylinder in an infinite ambient viscous fluid, but at the end he failed. He then postulated that there is no solution for the steady-state flow past an infinite cylinder [36].

This problem is known as the *Stokes paradox* today. In 1888, A. N. Whitehead attempted to solve the problem by taking into account the neglected quadratic terms of Stokes' derivation. He was not able to find correction terms for the velocities $\mathbf{u}$ to solve the differential equations for the boundary conditions at the cylinder edge and at infinity [37]. Later in 1910, C. W. Oseen set up a new system of differential equations to describe flow in incompressible fluids in stationary equilibrium. His equations are very similar to the Navier-Stokes equations, but these equations are stationary (there is no time derivative) and he included a term for convection flow **b**.

$$\boldsymbol{f} = \nabla p - \eta \Delta \mathbf{u} + \rho(\mathbf{u} \cdot \nabla)\mathbf{u} + \rho \frac{\partial \mathbf{u}}{\partial t} \qquad \text{(Navier–Stokes momentum equation)} \quad (2.2)$$

$$\boldsymbol{f} = \nabla p - \eta \Delta \mathbf{u} + \rho(\mathbf{b} \cdot \nabla)\mathbf{u} \qquad \text{(Oseen momentum equation)} \quad (2.3)$$

Within these equations, **u** defines the flow velocity, ρ the density, p the pressure, η the dynamic viscosity of the fluid and $\boldsymbol{f}$ the external volume force. Oseen included the convection velocity **b** which is independent of the flow. Calculating the frictional force that retards the motion of a sphere in an incompressible fluid and neglecting second order terms in Oseen's equations leads to Stokes' drag force description [38].

2.1.2 Hydrodynamics in 2D systems

By transferring the Stokes paradox into two dimensions, the situation changes to the motion of a circular disk moving through a two-dimensional system. Whereas the hydrodynamics in 3D Newtonian fluids are well described and investigated, 2D systems have only been analyzed experimentally for the past 50 years. Saffman and Delbrück, for example, studied the Brownian motion of particles (proteins) in thin biological bilayer lipid membranes, but they also initially failed to describe the translational motion due to Stokes' paradox. Within their model (SD model) they used the Oseen equations and described two dynamic regimes in which they solved the problem [39, 40]. They derived equations for the mobility of inclusions that directly couples the particle velocity **v** and the force **F** applied to the particle with the following relation

$$\mathbf{v} = b\,\mathbf{F} \ . \quad (2.4)$$

In their first approximation, they assumed that the particle with radius a is at the center of a finite membrane or film with radius R_{film}. Taking a no-slip boundary condition on the surface of the particle into account and supposing $R_{\text{film}} \gg a$, leads to the translational mobility

$$b_T = \frac{1}{4\pi\eta h}\left(\ln\frac{R_{\text{film}}}{a} - \frac{1}{2}\right) \qquad (R_{\text{film}} \gg a) \ . \quad (2.5)$$

Here η represents the (dynamic) viscosity of the membrane of thickness h. In contrast, for their second approximation, they supposed a particle in the two-dimensional membrane surrounded by a second, less dense medium with viscosity η' ($\eta' \ll \eta$). Due to the no-slip boundary condition at the interface between the membrane and the surrounding medium, any flow in the membrane and motion of the particle itself leads to a motion and shear flow of the outer medium. Additional zero slip at the surface of the particle leads to

$$b_T = \frac{1}{4\pi\eta h}\left(\ln\frac{\eta h}{\eta' a} - \widetilde{\gamma}\right) \ , \quad (2.6)$$

where $\widetilde{\gamma} = 0.577$ is the Euler constant. Saffman and Delbrück defined the expression $\eta h/2\eta'$ as *Saffman length* L_S, a viscous length scale comparable with the radius of a hypothetical sphere around the particle. Material within this sphere is assumed to be affected by the motion of the particle and the flow in the membrane. If the size of the membrane exceeds the Saffman length $R_{\text{film}} \gg L_S$, the motion of the particle is independent with respect to the membrane size and determined only by the viscous coupling of the particle and the flow in the membrane to the flow in the surrounding medium (equations 2.6 and 2.7).

$$b_T = \frac{1}{4\pi\eta h}\left(\ln\frac{2L_S}{a} - \widetilde{\gamma}\right) \qquad (R_{\text{film}} \gg L_S) \tag{2.7}$$

For smaller membranes with $R_{\text{film}} \ll L_S$, finite size effects are more important than viscous coupling and equation 2.5 has to be used.
The model of Saffman and Delbrück was verified by analyzing the motion of submicrometer-sized lipid domains (e.g. Bacteriorhodopsin) on cell membranes and by studying Brownian motion of inclusions in flat bilayer lipid membranes [41–43]. The SD model was extended in 1981 by Hughes, Pailthorpe and White to describe the motion of inclusions of arbitrary radii in a 2D fluid (HPW model) [44]. In 2008, Petrov and Schwille derived an accurate approximation for the whole range of a/L_S [45].

As remarked in chapter 1.3, liquid crystals can form free-standing smectic films and are particularly well suited to analyzing Brownian motion in 2D. These films can be homogeneous in thickness (there is no drainage) and they are extremely robust. Furthermore, the film viscosity η can be varied using different liquid crystal materials or mixtures or by changing the temperature of the materials. Experiments with inclusions of various shapes and sizes are possible [35] as well as different film geometries (flat liquid crystal films, liquid crystal bubbles). Experiments by Eremin et al. verified the SD model by measuring the motion of micrometer-sized silica beads sliding down an inclined, freely suspended liquid crystal film [20]. Increasing the inclusion size also enables analyzing the crossover between 2D and 3D fluid dynamics described by the HPW model and experimentally shown by Nguyen et al. [19].

2.1.3 Two-dimensional colloids

Colloids are systems where submicrometer-sized particles or droplets are dispersed in another continuous medium. Since these particles are free to diffuse and due to attractive or repulsive interactions, they can form regular lattices or clusters. The self-organization of spherical particles, especially in two dimensions, offers a variety of applications in nanotechnologies, e.g. in optoelectronics, for creating photonic crystals or producing biomimetic surfaces with specific properties [46–49]. Additionally, two-dimensional colloids are used to study hydrodynamic phenomena like diffusion [50, 51], coarsening dynamics and formation of meshes [52] or to measure capillary forces between particles [53]. Williams et al. [54] for example used a suspension of water, ethanol and polystyrene colloids (with radii of 5 µm) and formed quasi-2D monolayers on a glass coverslip (figure 2.1) by sedimentation. They additionally used holographic optical tweezers to form a ring of polystyrene particles and analyzed the arrangement of freely moving particles within the confinement [54].

Within the last years, many experiments are focused on crystallization and melting phenomena as well as on properties during phase transition [55–65].

Dillmann et al. for example analyzed the 2D melting of a colloidal monolayer which consists of polystyrene spheres with diameters of 4.5 µm containing superparamagnetic nanoparticles (Fe_2O_3) confined at a water/air interface (figure 2.1). Changing a magnetic field perpendicular to the monolayer then allows to change the arrangement of the particles in the 2D system from liquid-like state up to a lattice structure [60].

Within most of the two-dimensional colloid experiments, micrometer-sized solid spherical particles are suspended in a liquid medium. The particles are then arranged in a monolayer on a solid substrate by sedimentation or at the interface between two liquids or at a liquid/gas interface (figure 2.1). Although the particles are arranged in monolayers and structurally form two-dimensional systems, their dynamics cannot be considered as two-dimensional. The motion of particles that are surrounded or partially surrounded by a liquid is determined by the flow in the 3D subphase.

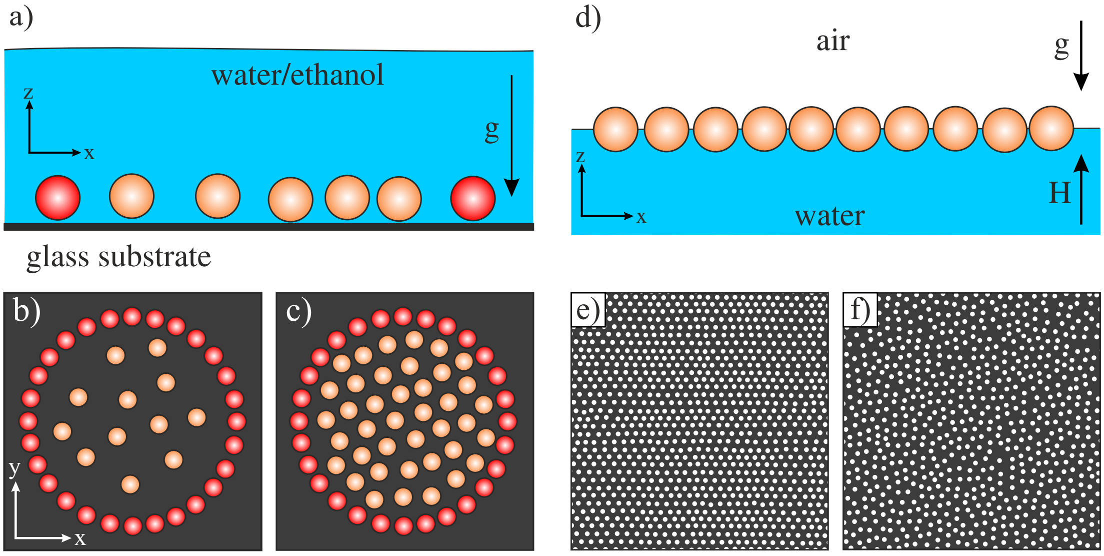

Figure 2.1: Experimental system used by Williams et al. (pictures a-c) and Dillmann et al. (pictures d-f) to create two-dimensional colloids on a glass substrate or at the air/water interface. The polystyrene spheres in picture a) form a 2D monolayer on a glass substrate due to sedimentation. The red marked particles are fixed by optical tweezers to create a confined circular region. For a small number of particles (picture b), fluid-like structure of the freely diffusing spheres within the fixed ring can be observed. With an increased number of particles (picture c), hexagonal structures appear. In picture d), polystyrene spheres with added superparamagnetic nanoparticles form a 2D colloid at a water/air interface. For high magnetic fields H perpendicular to the interface, the particles arrange in a hexagonal lattice (picture e), while at low magnetic fields the spheres form a fluid-like structure (picture f). Images are based on pictures from [54] and [60].

Other studies used solid particles trapped in thin cells to form single layers and to avoid flow in the 3D medium [55, 62]. However, cell boundaries influence the dynamics and the structure of particle arrangement as well. In 2001, Sethumadhavan et al. analyzed the stability and the stepwise thinning behavior of liquid films in the absence of any surfactant and they achieved the preparation of solid silica particles confined in these thin quasi-two-dimensional films [66]. The thin films enable the creation of structurally 2D colloidal systems with two-dimensional hydrodynamics, since the motion of these colloidal particles is confined only in the film plane. Furthermore, the dynamic viscosity of the surrounding air is about three orders of magnitude smaller than the viscosity of the fluid, so that the influence of air can be almost neglected. Nevertheless, according to the Saffman and Delbrück model, the Saffman length L_S including a small volume of the surrounding medium has to be taken into account for the description of the motion of colloidal particles.

2.1.4 Self-organization of droplets in smectic C free-standing films

In contrast to common thin liquid films such as soap films, liquid crystal films are not subject to drainage and their film thickness can be kept constant over the entire film area (see also section 1.3). Since in smectic C films the molecules are tilted with respect to the layer normal (described by the c-director), they are anisotropic in the film plane. The initially uniform c-director orientation of a smectic C film becomes distorted when inserting liquid droplets or solid particles into the film due to the specific anchoring conditions at the inclusion interfaces. The distorted c-director field then exhibits topological defects. Their strength is defined as the rotational angle of the c-director field divided by 2π when following the c-director on a circle around the defect (angle determination and rotation around the defect in the same direction).

In non-polar smectic C phases, for example, the c-director aligns tangentially at the inclusion surfaces [67] as shown schematically in figure 2.2. The insertions of such an inclusion with these boundary conditions is associated with the creation of a virtual topological defect of strength $+1$ inside the inclusion and, since the topological strength is a conserved quantity, additional defects with total strength of -1 must be created simultaneously.

In real experiments, different spatial variations of the c-director and the topological defects, e.g. topological dipoles or topological quadrupoles, can be realized [18, 67–76]. The virtual defects inside the inclusions in these experiments are compensated by isolated fully-integer defects in the smectic film or half-integer defects pinned at the inclusion boundaries. The latter configuration with two $-1/2$ defects for each droplet is shown in figure 2.2 for different droplet arrangements. Due to elastic distortion of the c-director field, defects with opposite signs attract each other while defects with the same sign repel each other.

The long-range elastic interaction and thus the defect-defect-interaction enable the pairing of the inserted inclusions and the formation of chains and lattices in the smectic C

film. Depending on the position of the peripheral $-1/2$ defects at the droplet boundaries, inclusions with quadrupolar (defects on opposite sides of the inclusion) and dipolar (angle between both $-1/2$ defects $\neq 180°$) character can be observed.
The left pictures of figure 2.2 show the sketches of the director field around circular inclusions forming chains as observed by Völtz et al. [18,67,74,75] and Cluzeau et al. [69–71]. The dipolar droplet chain in picture a) separates anti-parallel director orientations while the quadrupolar droplet chain in picture b) connects two parallel c-director configurations. The quadrupolar droplets in the second picture are aligned in an angle of approximately 30° respective to the undistorted c-director field far away from the chain [70,74].
Isotropic droplets in a smectic C film in a lattice structure as shown in the right-hand picture of figure 2.2 can be created when the density of the droplets in the film becomes very high [67,70,72].

For smectic A films that were used for the colloidal experiments during the OASIS mission, there is no molecular tilt and thus no elastic interaction between inclusions in the film plane. Nevertheless, a self-organization of inclusions in a lattice structure was observed.

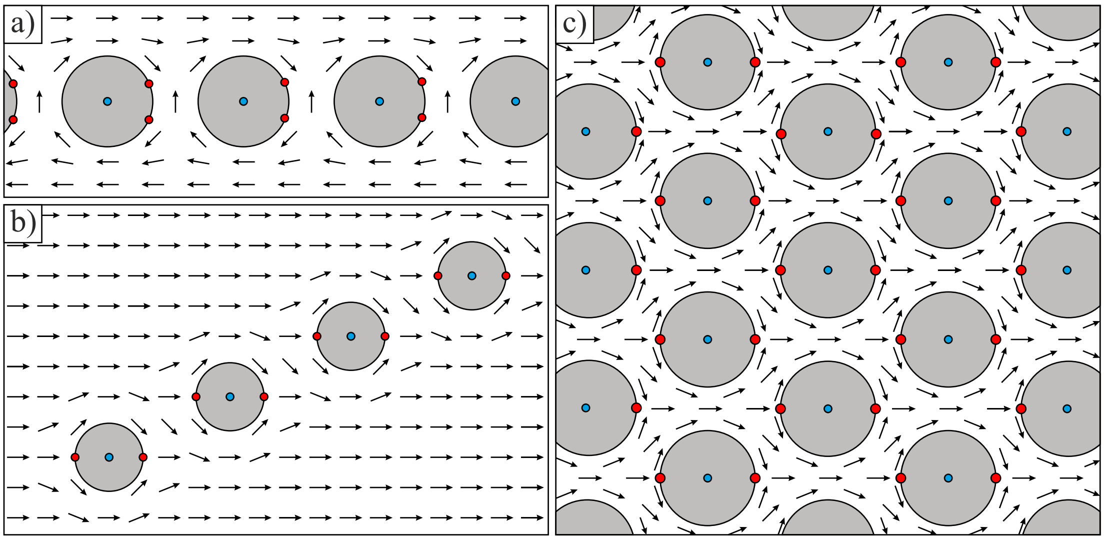

Figure 2.2: Sketch of the simulated c-director field around circular inclusions with virtual $+1$ defects (blue dots) in their centers and two $-1/2$ defects pinned at the boundary of each inclusion (red dots). The dipolar inclusions in a) form a chain separating two film regions with reversed c-director orientation. The chain is aligned with the director orientation (parallel or antiparallel). Picture b) shows a similar configuration, but with quadrupolar inclusions forming a chain and identical c-director orientations on both sides of the chain. Here, the angle between the aligned chain and the surrounding c-director field is approximately 30° [67,70,72]. With additional inclusions and thus a higher inclusion density in the film, the inclusion can arrange in a lattice structure. The inclusions have a quadrupolar character and form an almost perfect hexagonal structure (angle between inclusion $\approx 60°$). Real experimental images can be found in [67,72].

2.2 Experimental setup and materials

2.2.1 Liquid crystal mixture and isotropic droplets

During the OASIS mission onboard the ISS, smectic bubbles were prepared using the setup described in section 1.5. The observed bubbles had sizes of up to 15 mm in diameter and the film thickness could be kept constant for the whole experimental time. For the colloidal experiments, a liquid crystal mixture (Displaytech MX 12160) containing two components was used and their chemical structures can be seen in figure 2.3. The commercial Displaytech mixture is a proprietary material supplied by the *Miyota Development Center of America* (former company name: *Displaytech*). The mixture has a direct phase transition from smectic A to isotropic phase at a temperature of 51.1 °C. Inclusions on the film are created by heating the smectic A bubble slightly above the transition temperature of the mixture to the isotropic phase. Some of the inner layers of the films then melt and the isotropic material forms micrometer-sized droplets, while the film itself remains in the smectic A phase. Since the surface tension of the droplets is slightly larger than the surface tension of the smectic film, the material will not spread out, but instead forms droplets with radii in the range of a few dozen micrometers and only a few micrometers in thickness. It is assumed that the isotropic droplets are covered by at least one smectic A layer (figure 2.4 c and d).

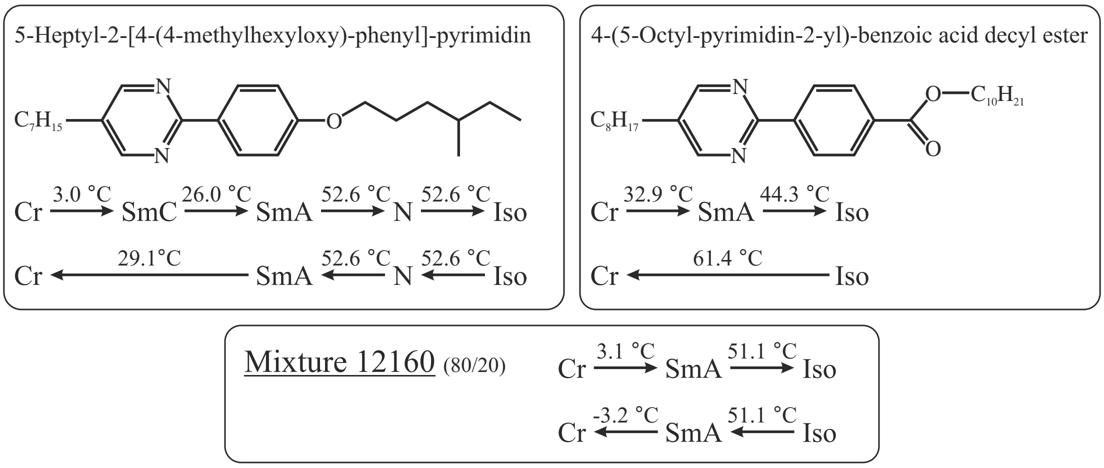

Figure 2.3: Structure and phase sequences of the two components of Mixture 12160 from Displaytech. While heating the crystalline material on the left-hand side, it will transfer into smectic C, smectic A and nematic phase until it gets isotropic. Cooling down the material from isotropic phase, it will skip the smectic C phase. The same behavior can be observed with the second material (on the right-hand side), going from crystalline state into smectic A phase and finally into isotropic phase when heated. When cooling this material, it will directly change from isotropic to crystalline state. The mixture 12160 contains 80% of the left-hand material and 20% of the right-hand component. Transition temperatures and molecule structures are taken from Displaytech (Miyota Development Center of America) [77].

Figure 2.4 b) shows a typical experimental image (500 × 500 μm^2) where the isotropic droplets spontaneously form a lattice with a short-range order. All droplets in the lattice are slowly moving together with the surrounding film and they continuously reorganize themselves in primarily hexagonal cells. Due to the motion and reorganization and since the lattice contains droplets of different size, the cells are not very regular. The macro-view image (figure 2.4 b) shows droplets on the bubble surface arranged in chains or clusters. While most droplets are trapped at layer steps between regions of different thickness (visible by different colors), there are also freely moving droplets that can spontaneously form lattice structures. Within a large, uniformly thick regions, hundreds or thousands of droplets can be arranged in lattice-like structures confined by the edge of the region. This confinement due to layer steps prevents the droplets from spreading (by repulsive interactions) over the whole bubble surface.

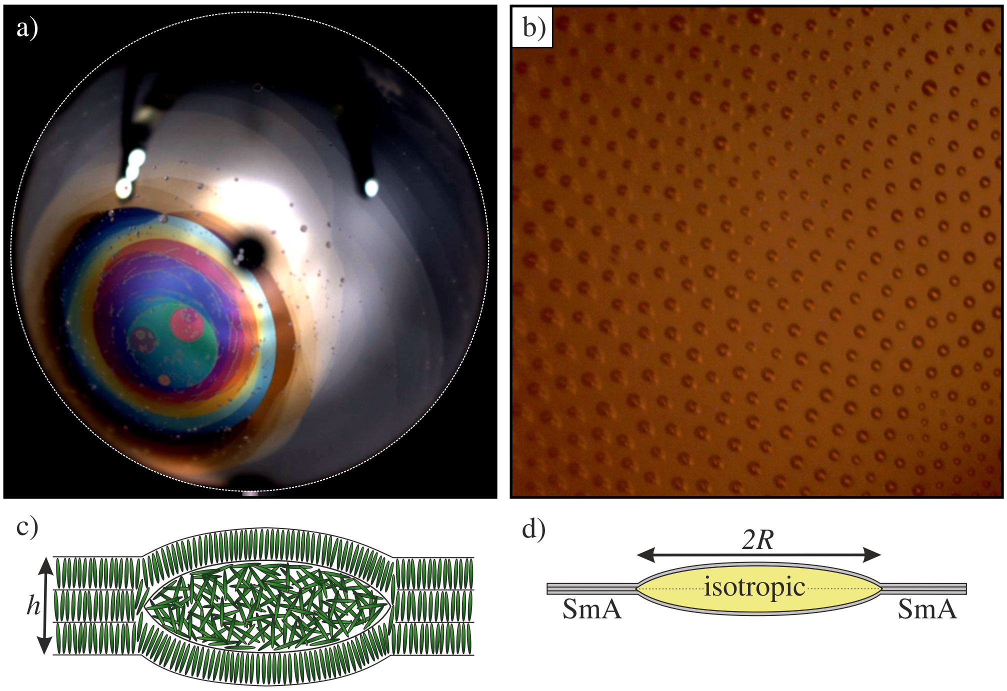

Figure 2.4: Isotropic droplets in a free-standing smectic A film. Picture a) shows the macro-view of a smectic bubble (highlighted with a white dashed circle) in reflected light. Different colors represent different film thicknesses. On the top, the shadows and reflections of the air jet needles are visible. The small objects on the bubble surface are isotropic droplets arranged in chains, clusters or lattices. Picture b) shows a typical experimental micro-view image (500×500 μm^2) of self-organization of droplets in a lattice structure during the OASIS mission. Droplets with different sizes are coexisting (see upper left and lower right regions). A scheme of the molecular arrangement of an isotropic droplet in the sectional view is presented in picture c). The droplet with radius R is covered with at least one smectic A layer. At the edge of the droplet, the layered structure is disturbed. The size of the liquid crystal molecules is greatly exaggerated. The background film with thickness h remains in the smectic A phase (picture d). The curvature of this film can be neglected due to the size of the droplets (radii of a few micrometers) compared to the bubble diameter (15 mm).

2.2.2 Surface tension and viscosity determination

The liquid crystal mixture was chosen due to its direct smectic A to isotropic phase transition. There were no other experiments with this mixture, so the main properties like surface tension γ or viscosity η had to be analyzed to interpret the observations from the ISS experiments. A setup shown in figure 2.5 (left) was build to create initially flat free-standing films above a small pressure chamber. The pressure inside the chamber could be changed in steps of 0.5 Pa and the whole setup was placed in a heating stage (Linkam THMS 600) under a polarizing microscope to verify the temperature dependence. As expected, droplets appeared at a temperature of 52 °C, but due to air convection in the heating stage chamber and due to the influence of the meniscus around the film, lattice structures could not be observed for longer than a few seconds. Reducing the pressure beneath the film and curving the film allowed to confine droplets in the center. Since there is an effective gravitational force along the curved film, the droplets finally moved towards each other and merged (see also chapter 3 - coalescence of droplets).

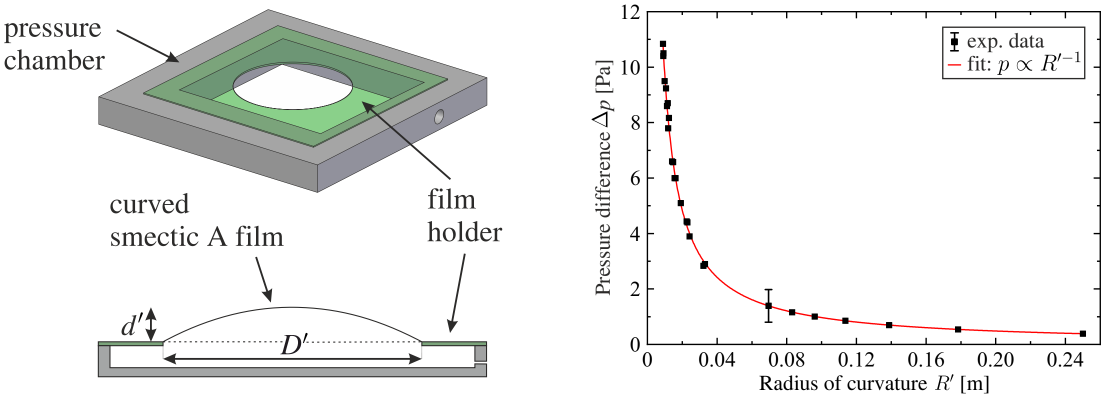

Figure 2.5: Experimental setup to measure the surface tension γ and the viscosity η of the mixture. A pressure chamber was included in a heating stage (Linkam THMS 600) to measure the curvature of the free-standing smectic A film depending on the pressure difference Δp and temperature T. The hole in the film holder has a diameter of 10 mm (left picture). The right picture shows the pressure inside the chamber depending on the radius of curvature of the film R' (calculated from the diameter of the film D' and height of the curved film d') at a temperature of 52.0 °C. The red line corresponds to a fit for the equation $\Delta p = 4\gamma/R'$. The surface tension γ was found to be 0.024 N/m at the given temperature. The error bar represents the inaccuracy of the pressure sensor.

To calculate the surface tension of the mixture, the pressure difference Δp between the pressure chamber and surrounding air was measured depending on the height of the film d' above the film holder. Assuming a spherical cap above the circular hole with diameter D' in the film holder, the radius of curvature R' of the smectic film was calculated.

$$R' = \frac{4d'^2 + D'^2}{8d'} \tag{2.8}$$

$$\Delta p = \frac{4\gamma}{R'} \tag{2.9}$$

Using the Young-Laplace equation (equation 2.9, where two surfaces, below and above the film, contribute to the pressure difference Δp), the experimental data shown in figure 2.5 could be fitted and the surface tension at a temperature of 52 °C was calculated to $\gamma = 0.024$ N/m ($\gamma = 24 \pm 0.1$ mN/m).

The second important parameter for the data analysis is the viscosity of the mixture, primarily at the temperature where droplets appear and lattices are formed. Again, the setup for the laboratory experiments (left picture of figure 2.5) was used, but in contrast to the surface tension measurements, micrometer-sized silica beads were applied to the flat film. The single silica beads with diameters ranging from 10 to 50 µm undergo Brownian motion and their trajectories were recorded with 60 frames per second.

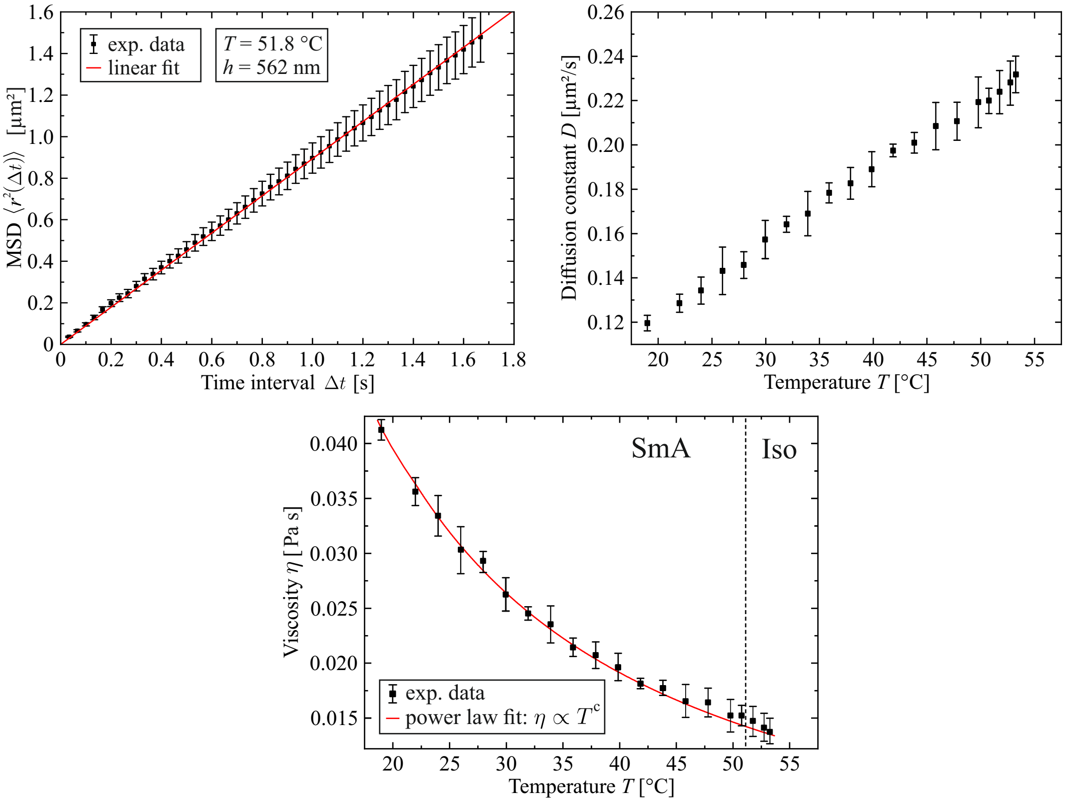

Figure 2.6: Experimental data for determining the viscosity η of the material MX12160 depending on temperature T. The top right picture shows the mean square displacement $\langle r^2(\Delta t)\rangle$ (MSD) of the particle depending on the time interval Δt at the temperature of 51.8 °C. For a freely moving particle, a linear trend is expected. The diffusion constants D at different temperatures were calculated from the slopes of the mean square displacement curves. The diffusion coefficient increases with increasing temperature (top right picture). The lower picture shows the viscosity calculated from the mobility using the Saffman Delbrück expressions (equations 2.5 and 2.7). The film thicknesses h for each experiment were determined from the reflectivity spectrum of the individual films. With increasing temperature, the viscosity of the material decreases until it reaches 14.4 mPa s at the transition temperature from smectic A to isotropic phase (dashed line). The red solid line is a power law fit ($\eta = \bar{a}T^c$, $\bar{a} = 0.69$ Pa s K^{-1}, c = -0.96) to guide the eye.

The mean square displacement $\langle r^2(\Delta t)\rangle$ (MSD), which is directly coupled to the diffusion coefficient D, was measured depending on the characteristic time interval Δt (see the top left picture in figure 2.6). For the two-dimensional system, the following equation was used to fit the mean square displacement and to calculate the diffusion coefficient for different temperatures.

$$\langle r^2(\Delta t)\rangle = 4D\Delta t \tag{2.10}$$

As visible in the top right picture of figure 2.6, the diffusion coefficient increases with increasing temperature.
Using the Einstein equation

$$D = bk_BT \tag{2.11}$$

with the Boltzmann's constant k_B and the absolute temperature T, the mobility b was calculated. With the Saffman Delbrück equation (equations 2.5 and 2.7), the dynamic viscosity η of the material at different temperatures was determined (lower picture in figure 2.6). The viscosity decreases from a value of 40 mPa s at room temperature to 14 mPa s at a temperature of 52 °C slightly above the bulk phase clearing point.

2.3 Experimental results

2.3.1 Lattice structure

The isotropic droplets observed in the experiments are arranged in a lattice structure. The background smectic A domain has a uniform thickness and is bounded by dislocations where the film thickness changes. The droplets cannot cross these boundaries, so they are confined within these regions. The confinement stabilizes the lattice structure, since the droplets would otherwise spread over the whole bubble surface due to repulsive interactions.

During all experiments, the entire lattice structure is drifting together with its background film in the film plane due to a small residual airflow from the airflow needles. This drift is shown in figure 2.7. It has a maximum velocity of 2.5 µm/s. The local lattice structure remains essentially unchanged while drifting, but the long range correlation changes.

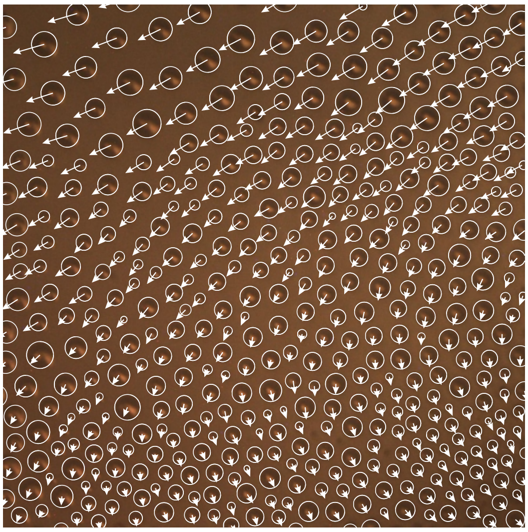

Figure 2.7: Flow field of the drift of the entire bubble surface due to the remaining airflow close to the bubble. The maximum velocity was 2.5 µm/s. The image size is 500 × 500 µm^2.

The droplet lattice primarily consists of hexagonal cells to maximize the distance between nearest neighboring droplets. Nevertheless, droplets of different size and the non-linear flow field cause, in general, a not very regular lattice. Locally, a regular hexagonal structure with droplets of the same size is assumed to simplify further interpretation of the data. To prove this assumption and to analyze the effect of droplet size, the distances between droplets of nearly the same size were measured. The probability to find a droplet at a specific distance to another droplet is shown in figure 2.8. The maxima in the upper graph (experimental data) correspond to the nearest neighbor distance as visualized in the inset. In addition, a perfect hexagonal lattice with 400 droplets of the same size ($R = 8.5$ µm) was simulated and the distances were measured. For a more realistic simulation, random noise was added to each droplet position. This led to a broadening of the Gaussian peaks in the lower probability graph (figure 2.8). It has to be mentioned that at least for distances below $4d$ (four times the distance to the nearest neighbor), the maxima of the experimental data match with the simulated peak positions. The experimentally determined maxima additionally align with the analytically calculated peak positions (inset and dashed lines in figure 2.8). That verifies the assumption, that locally the droplets form regular hexagonal cells with a distance to next neighbor of d, equivalent to the side length of the hexagon.

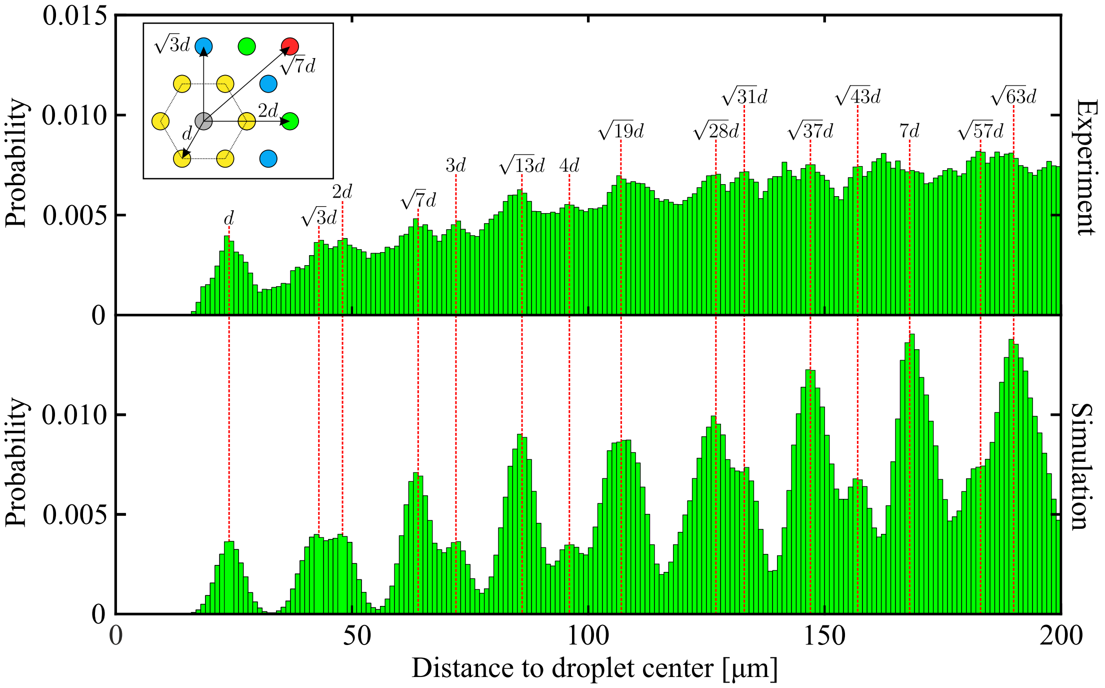

Figure 2.8: Probability to find the neighboring droplets at a specific distance. The lower picture visualizes the expected, calculated distance between a droplet and their neighbors of the same size. Random noise was added for the calculation to widen the Gaussian peaks. The distances for specific peaks are calculated concerning the distance to the nearest neighbor d, and are marked in the upper graph. For larger distances to the droplet center, the calculated peaks overlap, so not all predicted peaks are visible. The upper graph represents the measured distance between droplets of nearly the same size ($R = 8.5 \pm 0.15$ µm) in the experimental data. The peaks in the measured data match the calculated Gaussian peaks at least for distances below $4d$. The inset shows the first neighboring droplets with their predicted distance to the center droplet.

A second method to analyze the lattice structure is the construction of voronoi cells around each droplet (also Wigner-Seitz cells). Within each voronoi cell, all points are closer to the central droplet than to other droplets and so the size of voronoi cells describe the surface area, that belongs to the specific droplets. As shown in figure 2.9 a-c), voronoi cells are constructed by connecting the edges of neighboring droplets and then calculating the midpoint of these connections. The perpendicular bisectors of the edge-edge-connecting line then form the boundaries of the voronoi cells. In figure 2.9 d), the voronoi cells for a single experimental image are visualized, where approximately 64% of the cells represent hexagons and 29% are pentagons. At the end, the size of each cell was calculated and to compare it with the statistic measurements, an equivalence radius R_{equiv} was introduced. These radius defines a circle around each droplet, with the same area as the corresponding voronoi cell.

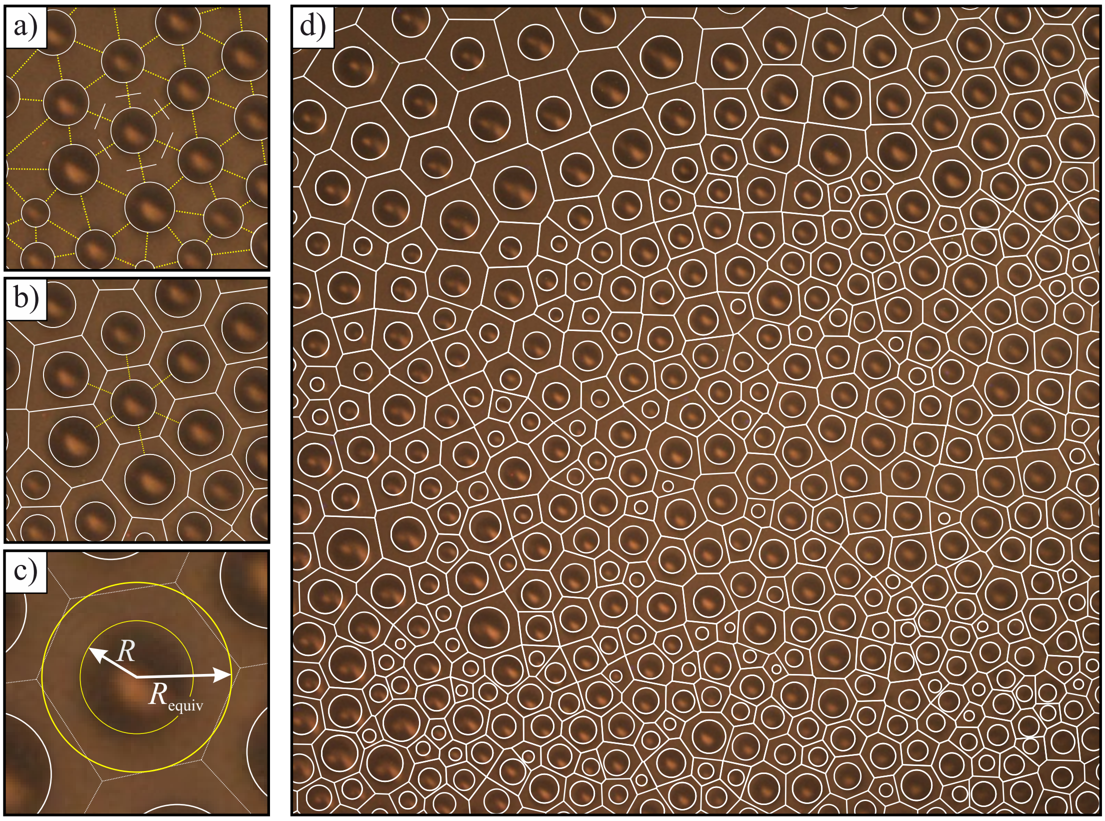

Figure 2.9: Construction of voronoi cells around the droplets in the experimental data. The yellow lines in picture a) represent the connecting lines between neighboring droplet centers. To take the size of the droplets into account, the connection starts and ends at the droplet edges (weighted voronoi cells). In the next step, the perpendicular bisectors of the edge-edge connections are constructed. The intersections of the extensions of the perpendicular bisectors form the vertices of the voronoi cell around each droplet (picture b). For each voronoi cell, a circle with the same area was calculated (radius R_{equiv}) as shown in picture c). Picture d) shows an experimental image (500×500 µm^2) with more than 400 marked droplets with radii from 3 to 13 µm. The visualized voronoi cells are constructed using the method described in a-c).

Both methods for analyzing the lattice structure (probability to find a neighboring droplet at a specific distance and the voronoi cell construction) show a dependence on the droplet size. With increasing droplet radius R, the distance to the nearest droplet is increasing as well as the size of the voronoi cells, described by the equivalence radius. For the interpretation of this behavior, the probability graphs and the voronoi cells of more that 15,000 pictures were analyzed. Data points for similar particle sizes were averaged. The results are presented in figure 2.10. A linear trend for both measurements can be observed. While the mean lattice constant $\langle d \rangle$ directly represents the mean distance to the next droplets as well as the hexagon side length, the equivalence radius for each cell is slightly larger than the mean lattice constant. Nevertheless, both measurements show the same linear behavior and the same slope of the curve.

It has to be mentioned, that the dependence of the lattice constant $\langle d \rangle$ on the droplet radius R also differs for different measurements. Since all the droplets are confined in a homogeneously thick region by layer steps, the size of that region finally defines the free space corresponding to each droplet and as a consequence the distance to the next neighbors. Nevertheless, the same linear trend was found for all other measurements, but with different slopes (e.g. $\langle d \rangle = 3.25R + 2.5$ µm). For later analysis and interpretation of the results and to compare results from different measurements, the mean aspect ratio $\langle \alpha \rangle = \langle d \rangle / R$ was introduced. This ratio weakly depends on the droplet size R, and it ranges between 2.5 and 6 for individual cells in different experiments and domains.

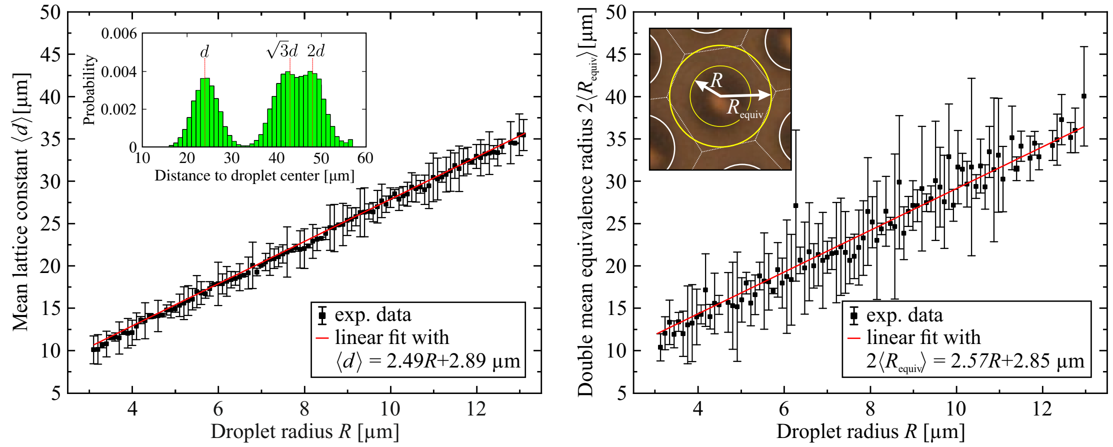

Figure 2.10: Mean lattice constant $\langle d \rangle$ and two times the mean equivalence radius $2\langle R_{\text{equiv}} \rangle$ depending on the radius of the droplets R. The data points in the left graph are extracted from the probability measurements as shown in the left-hand inset. The mean lattice constant represents the averaged distance to the nearest droplet as well as the side length of an assumed regular hexagon in the lattice, that is formed by the six neighboring droplets of the same size. The right-hand side shows the results from the voronoi cell construction. As visible in the right inset, the equivalence radius is slightly larger than half the distance to the nearest droplet. For comparison, two times the averaged equivalence radius is plotted. Both graphs show a linear tendency and by fitting the data points, a slope of approximately 2.5 was found for both measurements.

2.3.2 Repulsive interactions

The whole lattice structure is stabilized by repulsive interactions between the droplets, but the nature of these interactions is not fully understood yet. One possible explanation is the presence of elasto-capillary forces, that have been described earlier for spherical inclusions in smectic A films by Gharbi et al. [78]. In their experiments, the distortion of the uniformly thick film and the meniscus around the inclusions are essential for the observed repulsive interaction. For the isotropic droplets in the OASIS experiments, no menisci can be observed, since the droplets are extremely flat (also shown in chapter 3). Furthermore, long range capillary forces can be excluded as the film is uniformly thick. In addition, effects resulting from a molecular tilt, as known from smectic C films, are negligible since smectic A films are isotropic in the film plane.

The most convincing explanation for the repulsive force are electrostatic interactions. Experiments with the same material, forming flat films in the lab, showed that the droplets are affected by a highly charged electrode needle, placed close to the film surface. With a positive potential (approx. 150 V relative to the film holder), the droplets moved towards the needle, with a negative needle potential, they were repelled. A comparable effect with electric charges on a free-standing smectic bubble have been observed years ago by Stannarius et al. [79]. It is conceivable that charges are present on the entire bubble surface and that they are accumulated in smectic islands or droplets. It is also possible that the smectic mixture contains free ions which are expelled by the ordered smectic phase of the film and which are then trapped in the less ordered isotropic phase of the droplets.

Assuming that charges concentrated in the droplets cause the repelling interaction, the electrostatic potential $\phi(r)$ of the center droplet at a distance r from the center of a symmetrical hexagon can be described. The distance between the central droplet and one neighboring droplet can be written as $r' = \sqrt{d^2 - 2dr\cos(\beta) + r^2}$, with the lattice constant d, the distance from the center r and the angle β in respect to the outer droplet connecting line (see figure 2.11).

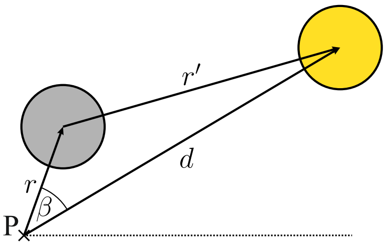

Figure 2.11: Sketch of the geometric situation where the central droplet (gray) is not in the center of the hexagon P. The hexagon is formed by 6 droplets at a distance d (lattice constant) from the center.

The potential due to a single neighboring point charge q as a function of their distance to each other results in

$$\phi(r') = \frac{q}{4\pi\varepsilon_0 r'} \ , \tag{2.12}$$

where ε_0 describes the vacuum permittivity with $8.854 \cdot 10^{-12}$ A s/V m. Expanding the potential for only one neighboring droplet ($r > r'$) to the third order in the radial distance to the center of the hexagon and averaging over the angle β (from 0 to 2π) leads to:

$$\phi(r) \approx \phi(0) + \phi'(0)r + \frac{1}{2}\phi''(0)r^2 + \frac{1}{3}\phi'''(0)r^3 + \mathcal{O}(0)r^4 \ . \tag{2.13}$$

The calculation of the terms shows that only the derivatives of even order make a contribution to the potential.

$$\begin{aligned}
\phi(0,\beta) &= \frac{q}{4\pi\varepsilon_0}\frac{1}{d} &&\Longrightarrow \frac{1}{2\pi}\int_0^{2\pi}\phi(0,\beta)\mathrm{d}\beta = \frac{q}{4\pi\varepsilon_0}\frac{1}{d}\\
\phi'(0,\beta) &= \frac{q}{4\pi\varepsilon_0}\frac{\cos(\beta)}{d^2} &&\Longrightarrow \frac{1}{2\pi}\int_0^{2\pi}\phi'(0,\beta)\mathrm{d}\beta = 0\\
\phi''(0,\beta) &= \frac{q}{4\pi\varepsilon_0}\frac{3\cos^2(\beta)-1}{d^3} &&\Longrightarrow \frac{1}{2\pi}\int_0^{2\pi}\phi''(0,\beta)\mathrm{d}\beta = \frac{q}{4\pi\varepsilon_0}\frac{1}{2d^3}\\
\phi'''(0,\beta) &= \frac{q}{4\pi\varepsilon_0}\frac{15\cos^3(\beta)d + 9\cos(\beta)}{d^4} &&\Longrightarrow \frac{1}{2\pi}\int_0^{2\pi}\phi'''(0,\beta)\mathrm{d}\beta = 0
\end{aligned}$$

Considering the six nearest neighbors and neglecting higher order terms and Debye screening by ions in the background film leads to an approximation for the potential that is only slightly underestimated (the influence of droplets outside the hexagon is ignored).

$$\phi(r) \approx \frac{q}{4\pi\varepsilon_0 d}\left[6 + \frac{3r^2}{2d^2} + \mathcal{O}\left(\frac{r^4}{d^4}\right)\right] \tag{2.14}$$

Nevertheless, the contribution from droplets outside the regular hexagon were analyzed and lead to a finite correction in the r^2 term in equation 2.14. Computing the potential close to the origin of an infinitely extended perfect triangular lattice, a correction factor of 1.836 was found. This correction term deepens the assumed potential, but taken into account the screening of long-range electrical interaction by counterions in the film and fluctuations of the position of the droplets, reduces the influence of charges that are further away than the nearest neighbors [23].

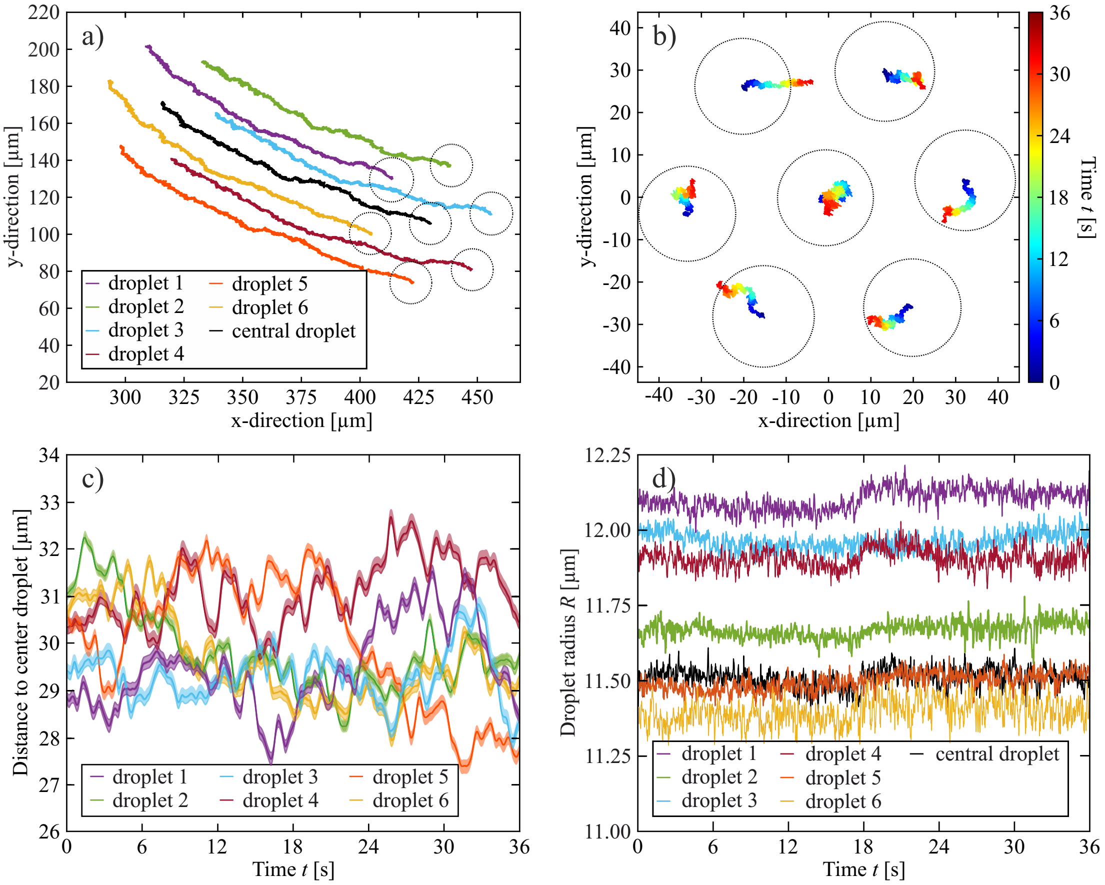

Figure 2.12: Analysis of the motion of neighboring droplets forming a hexagonal structure. At the beginning, the motion of seven neighboring droplets was recorded (picture a) and the trajectory of the whole hexagon was calculated. The trajectories of the droplets in respect to the center of the hexagon were determined as shown in picture b). Picture c) visualizes the distance from the outer droplets defining the hexagon to the central droplet. They only vary by 4 µm. The hexagonal structure is almost regular for the complete measurement. The radii of all droplets (picture d) are in the same range and hardly changed.

With the predicted potential $\phi(r)$, the radial force F_{rad} perceived by the central droplet can be calculated and written in terms of a force constant K.

$$F_{\text{rad}} = -\frac{\mathrm{d}(q\phi(r))}{\mathrm{d}r} = -Kr \approx -\frac{3q^2}{4\pi\varepsilon_0 d^3}r \tag{2.15}$$

Since the potential is slightly underestimated, also the force F_{rad} might be somewhat larger than shown in equation 2.15, but in fact it predicts the right order of magnitude. For the given system, the force constant K can be extracted from the measurements by analyzing the motion of the central droplet in respect to the center of the hexagon formed by the six nearest neighbors. Taking the specific radii of the six droplets into account, the center of the hexagon is equal to the center of mass. Figure 2.12 a) shows the motion of an arrangement of seven droplets in a hexagonal structure over a period of 36 seconds. The background motion results from the drift of the whole bubble surface and was subtracted for the analysis. The trajectories of the droplets were calculated with respect to the hexagon centers and depending on the individual droplet radii (picture 2.12 b).

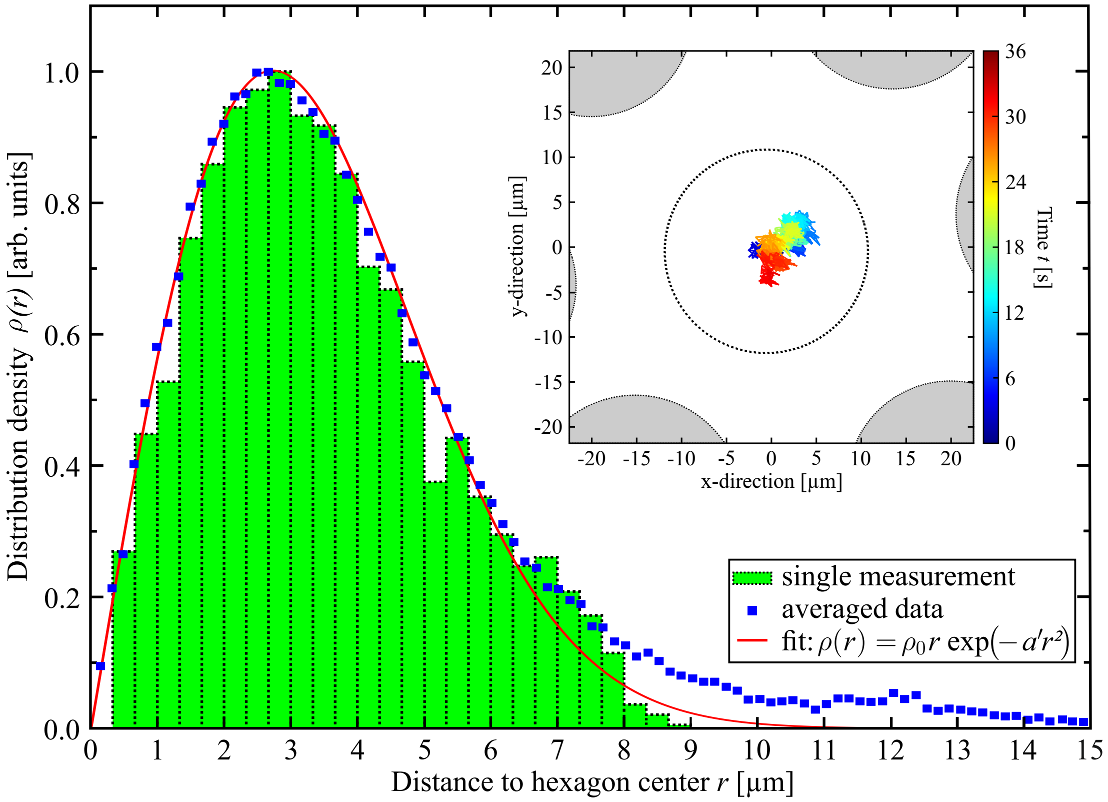

Figure 2.13: Distribution density of the position of the central droplet with a radius of 11.50 µm (green bars). Additionally, the averaged data for droplets of the same size $R = 11.50 \pm 0.25$ µm are shown as blue squares. The averaged data were fitted (red solid line) with equation 2.16 with the fitting parameter ρ_0 and a'. From the fit, the force constant is calculated to $K \approx 0.66$ nN/m. The inset shows the spatial distribution of the central droplet with respect to the hexagon center. The evolution in time is color coded.

Assuming that the spatial distribution of the central droplet describes a Boltzmann distribution in 2D with axial symmetry, the distribution density can be written as [23]:

$$\rho(r) = \rho_0 r \exp\left(-\frac{Kr^2}{2k_B T}\right) \quad \text{with} \tag{2.16}$$

$$r_{\text{max}} = \sqrt{\frac{k_B T}{K}}\,. \tag{2.17}$$

In figure 2.13, the distribution density of a single measurement (shown in figure 2.12) and the averaged data for droplets with the same radii are presented. From the fit with equation 2.16, the force constant K was calculated. For the presented example with droplets of radius $R = 11.50 \pm 0.25$ µm and an aspect ratio $\alpha = \langle d \rangle / R = 2.61 \pm 0.23$, the force constant of $K \approx 0.66$ nN/m was obtained ($r_{\text{max}} = 2.6$ µm).

For small distances to the hexagon center ($<$ 6 µm), the measured data are in very good agreement with the theoretical assumption, while for larger fluctuations, the tail deviates from the prediction. The main reason for that deviation is the structure of the lattice that is, in contrast to the above assumption, not perfectly hexagonal. In addition, also cells with five or seven nearest neighbors are observed and thus larger fluctuations can occur more frequently.

2.3.3 Mean square displacement

In order to analyze the individual droplet motion with respect to their neighboring droplets and to measure the diffusion constant, the mean square displacement (MSD) was calculated. The calculation is based on a formalism from the work of Albert Einstein [80] from 1904. For a freely moving particle (particle undergoing only Brownian motion without drift) in two dimensions, the transition probability $P(x_0, y_0, x, y, \Delta t)$ to find a particle originally at (x_0, y_0) after a time interval Δt at the new position (x, y) can be written as

$$P(x_0, y_0, x, y, \Delta t) = P(r_0, r, \Delta t) = \frac{1}{\sqrt{4\pi D \Delta t}} \exp\left(-\frac{(x - x_0)^2 + (y - y_0)^2}{4D\Delta t}\right) \tag{2.18}$$

and represents a Gaussian process with the diffusion constant D. The mean square displacement $\langle r^2(\Delta t)\rangle$ is then calculated by integrating the density function $P(r_0, r, \Delta t)$ times the square displacement $r^2(\Delta t)$ (with respect to the initial position r_0).

$$\begin{aligned}
\langle (r - r_0)^2(\Delta t)\rangle = \langle r^2(\Delta t)\rangle &= \int_{-\infty}^{\infty} \left[(r - r_0)^2\right] P(r_0, r, \Delta t)\mathrm{d}r \\
\langle r^2(\Delta t)\rangle &= \int_{-\infty}^{\infty}\int_{-\infty}^{\infty} \left[(x - x_0)^2 + (y - y_0)^2\right] P(x_0, y_0, x, y, \Delta t)\mathrm{d}x\mathrm{d}y \\
\langle r^2(\Delta t)\rangle &= 4D\Delta t
\end{aligned} \tag{2.19}$$

As expected from equation 2.19 and shown in figure 2.14 (left picture), the mean square displacement increases linearly in this simple case and the diffusion constant can be extracted from the slope of this curve.

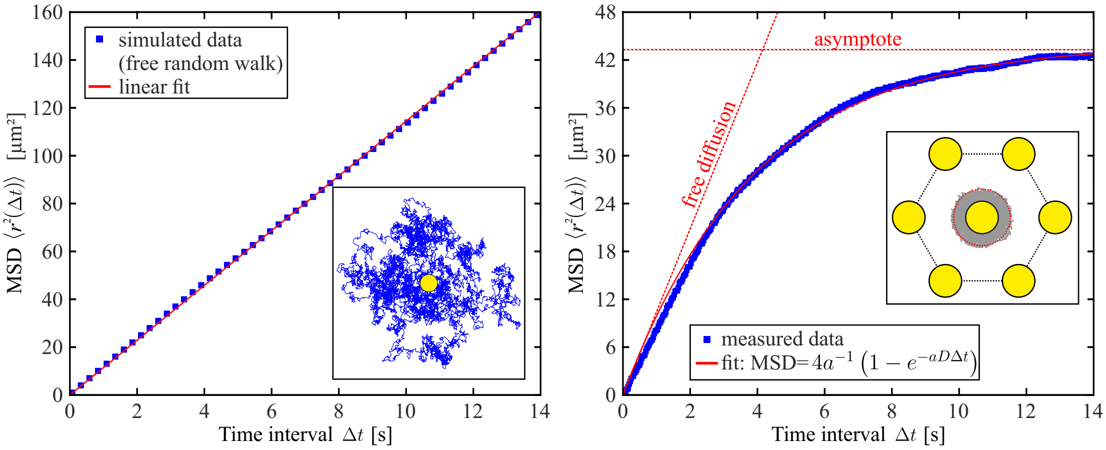

Figure 2.14: Mean square displacement (MSD) calculated for a simulated freely moving droplet and measured from the experimental data. On the left side, the diffusion constant for the unbound motion (shown in the inset) is proportional to the slope of the linear fit. The right-hand side shows the experimental data (aspect ratio $\alpha = 4.5 \pm 0.1$) fitted with equation 2.23. For small time intervals Δt, the hexagonal cage will not effect the droplet motion (free diffusion). For larger Δt, the asymptotic value of $4k_BT/K$ is reached. The right inset visualizes the motion of the central droplet within the hexagon. The dashed red circle marks the region in which the droplet position fluctuates.

For the motion of the droplets in the hexagonal structure, a diffusion in a parabolic potential with

$$V(r) = V(x,y) = \frac{K}{2}r^2 = \frac{K}{2}(x^2+y^2) \tag{2.20}$$

is assumed and the corresponding Boltzmann distribution density then is

$$\widetilde{P}(r) = \widetilde{P}(x,y) = \sqrt{\frac{K}{2\pi k_BT}}\exp\left(-\frac{K(x^2+y^2)}{2k_BT}\right) \quad . \tag{2.21}$$

Here, k_B is the Boltzmann constant, T is the temperature of the system and K describes the force constant. In contrary to the former given transition probability $P(r_0, r, \Delta t)$, the Boltzmann distribution $\widetilde{P}(r)$ describes the probability to find a particle at the position (x, y) with respect to the center of the potential and independent of time.

The following equation for diffusion in a two-dimensional harmonic potential

$$\langle r^2(\Delta t)\rangle = A(1 - e^{B\Delta t}) \tag{2.22}$$

is used and by assuming a free diffusion for small times Δt, the mean square displacement in a parabolic potential is described by the following equation:

$$\langle r^2(\Delta t)\rangle = \frac{4k_BT}{K}\left[1 - \exp\left(-\frac{DK}{k_BT}\Delta t\right)\right] . \tag{2.23}$$

For small Δt, this cage-related MSD yields a value of $4D\Delta t$ (free diffusion), while for large times the asymptotic value of $4k_BT/K$ is found (derivation in appendix A.1).
By fitting the measured data with equation 2.23, as shown in figure 2.14 (right-hand picture), the free diffusion constant D and the force constant K are determined as well.
The results for the force constant from both methods, analyzing the distribution density and measuring the cage-related mean square displacement, are comparable with each other and are summarized in figure 2.15. The data points for the same aspect ratio are averaged (bin size of $\delta\alpha = 0.1$ for the MSD measurement and $\delta\alpha = 0.25$ for the density function analysis) for better visualization. The force constant clearly decreases with increasing aspect ratios, whereas it seems that there is no obvious correlation between force constant and droplet radius R.

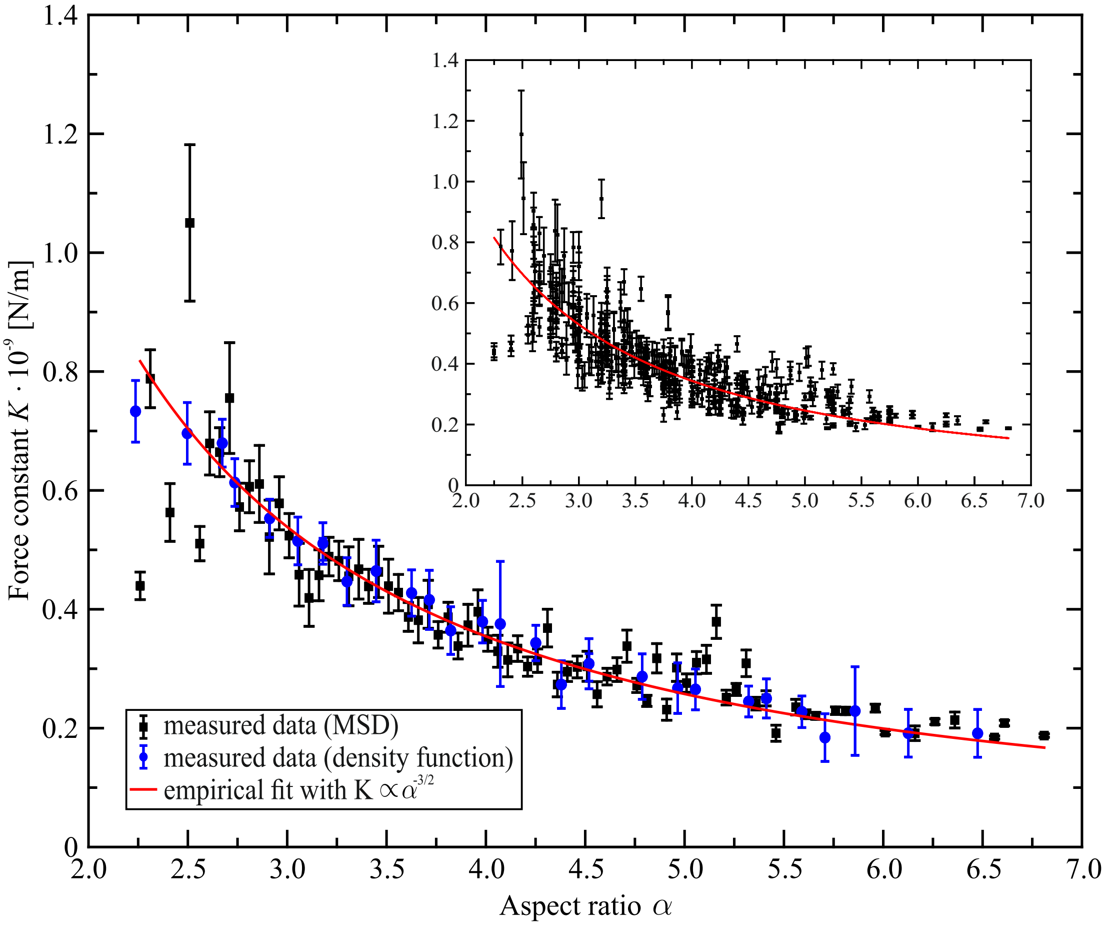

Figure 2.15: Force constant K depending on the aspect ratio α determined from the cage-related MSD measurement (black squares) and from the density functions (blue circles). Hexagonal cells with similar aspect ratios are averaged with bin widths of $\delta\alpha = 0.1$ for the MSD data points and $\delta\alpha = 0.25$ for the density distribution data points. The red solid line is an empirical fit with $K = 2.75 \cdot 10^{-9}\alpha^{-1.5}$ N/m to guide the eye. The inset shows the force constant determined from the asymptotic limit of the MSD before averaging over similar aspect ratios. The force constant decreases with increasing aspect ratio α [23].

According to equation 2.15, it is possible to estimate the net charges that are required to produce the measured force constant. This value reaches

$$q = \sqrt{\frac{4\pi\varepsilon_0 d^3 K}{3}} \approx 3 \cdot 10^{-17}\ \mathrm{C}\ \ ,$$

using $K \approx 0.6$ nN/m, $R \approx 13$ µm, $d \approx 35$ µm and $\alpha \approx 2.7$ as an example. It results in a few dozen to a few hundred negative excess elementary charges (q in the range from 0.7 ... $3 \cdot 10^{-17}$ C, elementary charge $e = 1.602 \cdot 10^{-19}$ C) [23] .

2.4 Simulation

The motion of objects in two dimensions and the interaction between different objects are essential hydrodynamic problems in biological, chemical and physical systems. The model to describe the motion of a circular object in 2D (Saffman and Delbrück model) was already introduced in chapter 2.1.2. With film thicknesses in the order of a few dozen nanometers (estimated from the color of the background film) and a material viscosity of $\eta = 14$ mPa s, the Saffman length $L_S = \eta h/(2\eta')$ yields values between 10 and 100 µm. Since the Saffman length is larger than the mean distance between the droplets, the influence of the ambient air was neglected and the Saffman and Delbrück approximation considering the film dimensions was used instead (equation 2.5). The hydrodynamics of each confined droplet are assumed to be essentially two-dimensional.

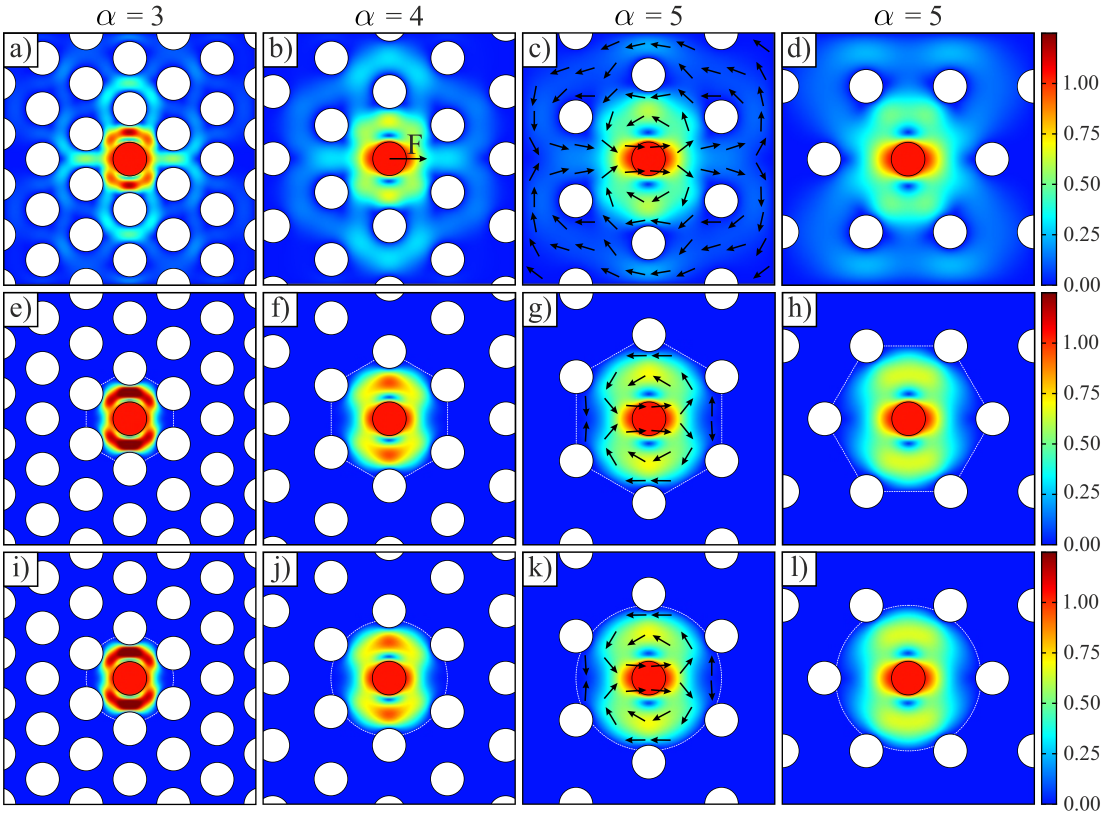

Figure 2.16: Simulated flow field around a moving droplet in a hexagonal lattice. The magnitude of the flow velocity is color-coded in units of the central droplet velocity. For the third picture of each row, the flow field was additionally visualized with arrows whose lengths have been normalized. Three different situations with different boundary conditions were simulated. Pictures a-d) show a hexagonal lattice where the flow of material is not restricted to the cell around the central droplet. In the second row (pictures e-h), the flow is confined by a perfect hexagon formed by the six neighboring droplets and in the last case (pictures i-l), the incircle of this hexagon confines the flow. From the left to the right side, the aspect ratio α increases, while the radius of all droplets is constant for all shown pictures. The last pictures on the right side correspond to a lattice rotated by 30° respective to the velocity direction of the central particle.

In order to compare the theoretical model with the experimental data and to analyze the expected curve for very small aspect ratios, the flow field around a circular object in a hexagonal lattice was simulated. The commercial Finite Elements Method (FEM) software COMSOL was used to simulate flow in a 2D environment by applying a force F on the central droplet in the cage (shown in figure 2.16 b). By extracting the resulting velocity v of the central droplet and using the experimental parameters (viscosity of the material η, viscosity of the surrounding air and the temperature of the system), the translational mobility $b_T = v/F$ can be calculated.

Three different situations with different boundary conditions were analyzed. In the first case, the flow is not restricted to some region, but is set to zero at the droplet edges. In the second case, the flow is limited to the hexagonal cell around the central droplet, thus there is no exchange of material with the neighboring cells. For the third situation, the flow was confined to a circular region by the incircle of the hexagon, formed by the six nearest neighbors. Again, the flow between neighboring cells/incircles is suppressed. For all these situations, the velocity at the edges of all other droplets was assumed to be zero. Furthermore, the last case represents the Saffman and Delbrück model (with an additional constant factor), when using the aspect ratio α instead of the radius of the inclusion a and the radius of the confinement R_{film}.

$$b_T = \frac{1}{4\pi\eta h}\left(\ln\frac{R_{\text{film}}}{a} - \frac{1}{2}\right)$$

$$b_T = \frac{1}{4\pi\eta h}\left(\ln(\alpha) - \frac{1}{2}\right) \qquad \text{(circumcircle of hexagon)} \qquad (2.24)$$

$$b_T = \frac{1}{4\pi\eta h}\left(\ln\left(\sqrt{3/4}\alpha\right) - \frac{1}{2}\right) \qquad \text{(incircle of hexagon)} \qquad (2.25)$$

Figure 2.16 shows the flow field around the central droplet for the three described situations for three aspect ratios α each. The flow velocity is color-coded with respect to the central droplet velocity v. Additionally, the flow field is visualized by normalized arrows. While the flow field in the pictures e-h) (hexagonal cage) is almost identical to the field in the circular confined situation (pictures i-l), the simulation without confinement shows additional flow around the next neighbors. This flow finally leads to a higher velocity of the central droplet compared to the confined situations.

As an additional parameter of the simulation, the orientation of the droplet lattice with respect to the direction of the applied force F was analyzed and a rotation of the lattice by 30° is shown in the right-hand pictures of figure 2.16 (pictures d, h, l). The flow field only changes marginally, but the extracted velocity v is constant, independent of the orientation between the lattice and the force direction.

The numerical results of the simulations, i.e. the calculated specific mobilities $b' = bh$ as functions of the aspect ratios α, are presented in figure 2.17. For large aspect ratios, the simulated hexagonal cage (green solid curve) as well as the simulated circular confinement (incircle of the hexagon, black solid curve) agree with the model of Saffman and Delbrück, shown as black dashed curve. For smaller values $\alpha < 6$, the calculated specific mobilities deviate from the expected curve. Apparently, the model is only valid for as-

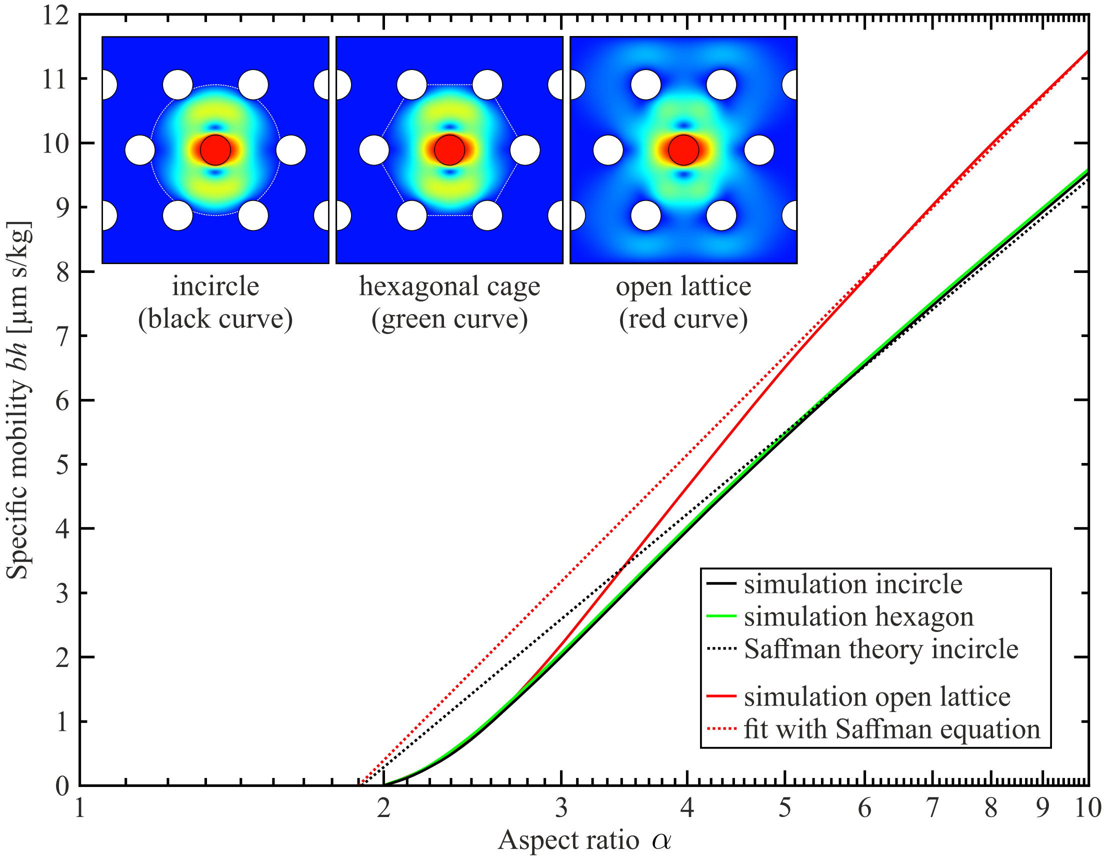

Figure 2.17: Calculated specific mobility for different boundary conditions in the flow field simulation. For small aspect ratios $\alpha < 6$, all calculated curves deviate from the prediction of Saffman and Delbrück (black dashed line). For larger aspect ratios, the flow field in the hexagonal cage (green curve) and in the incircle (black solid line) of the hexagon match with the model. In contrast to the confined situation, the open lattice simulations (red solid line) shows the same trend, but higher values for the specific mobility. The curve was fitted with the Saffman equation with additional fitting parameters: $bh = (4\pi\eta)^{-1} (\ln(A\alpha^c) - 0.5)$ where $A = 0.77$ and $c = 1.24$ (red dashed line).

pect ratios larger than 6 and for smaller values the numerical approximation has to be used to fit the experimental data. In addition, the specific mobility for the lattice without confinement was calculated (red solid curve). Due to the flow around the neighboring droplets and the resulting higher velocity v of the central droplet, the specific mobility is increased. Nevertheless, the curve shows the same trend as the curve for the hexagonal cage simulation. For completeness, the results for the open lattice were fitted with a modified Saffman Delbrück model (red dashed curve). An equation similar to the model equation with two additional fitting parameters was used: $bh = (4\pi\eta)^{-1} (\ln(A\alpha^c) - 0.5)$ with $A = 0.77$ and $c = 1.24$.

Finally, the measured diffusion constant values D were compared and fitted using the theoretical SD model as well as the simulated curves. From the simulated specific mobilities, the diffusion constants were calculated using the Einstein equation $D = bk_BT$ with the constant temperature T of 52 °C. Since the film thickness of the background film could not be measured during the experiments (malfunction of the spectrometer), the film thickness h is the only free fitting parameter for the measured data. Figure 2.18 shows the measured data and the fitted curves. Cells with similar aspect ratios ($\delta\alpha = 0.1$) are averaged for better visualization, while the inset of the figure represents the entire set of data. All fitted curves align well with the measured data. For aspect ratios smaller than 5, the theoretical model seems to deviate slightly from the measured data. Nevertheless, all curves match the measured data, but especially for small aspect ratios the simulation better represents the data. Deviations from the model and the simulated curves can be explained by variations in the hexagonal structure of the lattice. For the model and for the simulation, perfect hexagonal cells are assumed. The film thickness of the background film yields a value of 44 nm for the SD model fit, 41 nm for the hexagonal fit and 51 nm for the unbound lattice simulation curve fit. The film thickness of $h = 46 \pm 5$ nm is compatible with the expected film thickness value, that was estimated from the color of the film in the experimental images.

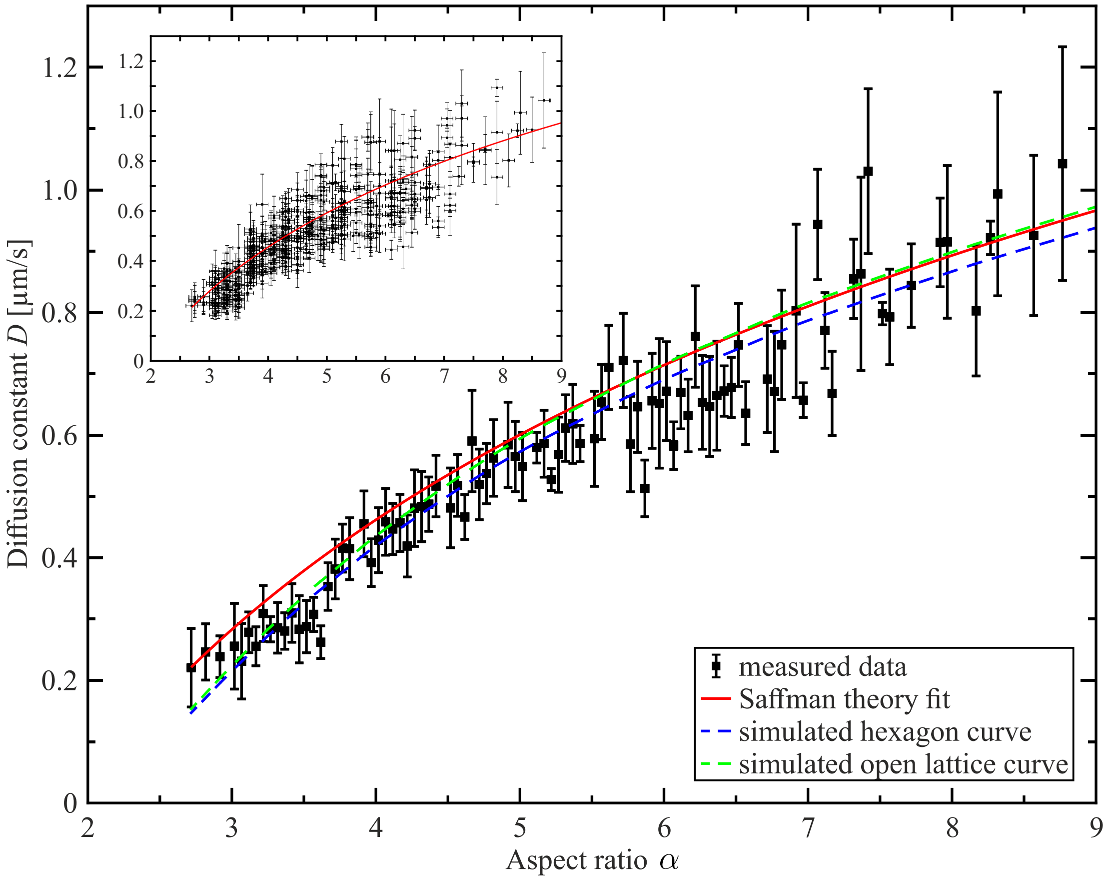

Figure 2.18: Measured diffusion constants from analyzing the MSD curves, depending on the aspect ratio α. The data points are fitted with the Saffman model (red solid curve), with the numerically computed curve for a hexagonal cell (dashed blue line) and with the simulated open lattice curve. The film thickness h of the background film is the only fitting parameter. The complete set of data points shown in the inset is averaged over cells with similar aspect ratios using bin sizes $\delta\alpha$ of 0.1.

2.5 Summary and discussion

As one part of the experiments onboard the ISS, inclusions on free-standing smectic films were created and observed. A liquid crystal mixture was heated close to the smectic to isotropic transition temperature and lens-shaped droplets were created which formed lattice-like structures. Measurements of the lattice structure and its dimensions showed a linear dependence between droplet sizes and their distance to the next neighbors. For a specific domain, the following expression $\langle d \rangle \approx 2.53\ R + 2.87$ µm (figure 2.10) was found. A similar linear dependence is assumed for all confined domains with droplets in lattice structures. The aspect ratio $\alpha = d/R$ was introduced to combine the droplet radius R and the nearest droplet distance d within one parameter.

For the first time, a real two-dimensional colloid with predominantly hexagonal cells was formed due to mutually repulsive, presumably electrostatic interactions. A point charges approach in a six-fold symmetry was made to describe the net potential experienced by each droplet in a perfect hexagonal lattice. For this approximation, only the influence of the six nearest neighbors was considered and Debye screening was neglected. Higher order terms including the more distant droplets would lead to a slightly higher potential (e.g. a factor of 1.836 in the r^2 term). These additional long-range electrical interactions are screened by counterions in the film and averaged out because of fluctuations of the whole lattice itself.

The distribution density of the position of a droplet in the hexagonal cells was calculated and fitted with a Boltzmann distribution in 2D with axial symmetry (figure 2.13). From the maximum of this curve, the force constant K was calculated. A rough estimation showed that the repulsive interaction could be caused by a few hundred negative excess charges per droplet. There is no quantitative information about screening effects. Depending on the Debye length of the lattice droplets, the assumed potential is partially screened (the Debye length lies within the order of magnitude of the distance to the nearest neighbors d) or more neighbors have to be included in the potential description (Debye length much larger than d). In both cases, the functional form of the potential around the central droplet will not change in the leading term.

The results show a dependence of the force constant K on the aspect ratio, but no physical meaning of the empirical fit $K = 2.9 \cdot 10^{-9} \alpha^{-3/2}$ N/m was found yet (figure 2.15).

In order to analyze the hydrodynamics of the droplets, the (cage-related) mean square displacement was measured and fitted with an approximation for the diffusion of a particle in a parabolic potential. The measured data showed the expected linear trend of the MSD for small time steps and an asymptotic behavior for large time steps. From the asymptotic limit of each individual curve, the force constant was calculated, while the diffusion constant D was extracted from the linear part (figure 2.14).

In addition to the experimental observations during the ISS mission, simulations of the two-dimensional flow field around a circular inclusion were performed. The model by Saffman and Delbrück was compared with the numerical simulation and deviations for small film regions with respect to the inclusion size were found. The flow field within the restricted hexagonal and circular geometry as well as in a free lattice without confinement was simulated. The simulation and the SD model are equally suitable to fit the experimental data (figure 2.18).

For the analysis and the interpretation of the isotropic droplet motion and their arrangement in a lattice structure, electrostatic forces and the resulting repulsive interactions of the droplets were assumed. Additional experiments with the liquid crystal mixture showed that a motion of the droplets can be induced if a high potential (≈ 150 V) is applied between the film holder and an electrode needle close to the film. With a positive needle potential the droplets follow the needle and with a negative needle potential the effect is reversed. Nevertheless, there is no quantitative information about screening effects and the origin of the charges. In particular, the origin of the charges is an important question that needs to be investigated in further experiments. One possible explanation is the presence of ions in the liquid crystal material due to a partial degradation of the molecules in the mixture. These ions could be expelled by the ordered smectic phase of the film and accumulated in the less ordered isotropic material of the droplets. It may also be that the ions are trapped only at the disclination lines around the droplets. Free radicals with unpaired electrons that accumulate in these regions may also be a cause of charges in the isotropic droplets or at the contact lines.
Additional experiments onboard the ISS, for example utilizing a pure liquid crystal of comparable properties and comparable transition temperatures, could help to answer at least some open questions. The experimental system under microgravity conditions allows changing the smectic bubble radius (inflating or deflating the bubble) and thus, in principle, to vary the lattice constant and the aspect ratio of the lattices. For a fixed number of droplets in an enlarged confined domain (lower droplet density), an increase of the lattice constant d, i.e. a decrease of the cell aspect ratio α, is expected. Furthermore, the force constant could be measured more accurately within optical tweezers by bringing two separated droplets close together and then measuring the repulsive behavior.

Isotropic droplets in free-standing smectic A liquid crystal films form a unique two-dimensional colloidal systems that is not affected by a solid substrate ([46, 54]) nor a liquid medium [60, 61](droplets on the liquid-gas interface). Comparable structures and a self-organization of isotropic droplets in thin films could only be observed by Völtz et al. [67] in smectic C free-standing films, but the mutual interaction are in this case caused by elastic distortions of the c-director field. Lattice-like structures and repulsive interactions due to electrostatic interactions between droplet in smectic A films have so far only been observed during the OASIS experiments.

3 Coalescence of liquid droplets in a quasi-two-dimensional liquid crystal film

Coalescence of droplets describes the merging process of liquid objects in chemical, physical and biological systems. This ubiquitous phenomenon can be observed during rain drop formation, but also in various technological processes. The dynamics of droplet coalescence has been studied experimentally and theoretically in different systems. In the previous chapter, the system of micrometer-sized isotropic droplets on a thin liquid crystal film was introduced. The third chapter deals with the coalescence of such droplets on quasi-two-dimensional films. The merging dynamics on the timescale of milliseconds is analyzed using high-speed imaging and interferometry measurements. The results are compared with a theoretical model for droplets on solid substrates and based on the thin sheet equation, a new model is developed. In addition, self-similar dynamics of the connecting region between the merging droplets during the first stage of coalescence is verified. The experimental results and the model to describe the coalescence of three-dimensional liquid droplets on a two-dimensional film are published in [81] and [82]. All necessary physical quantities are redefined in this chapter.

3.1 Introduction

The phenomenon of merging droplets is an important topic in natural science, since coalescence is a ubiquitous process in many systems. Since more than 100 years, scientists try to analyze and explain the interaction between liquid objects within other fluids. Already at the end of the 19th century, Lord Rayleigh studied the collision of liquid jets and analyzed their stability [83–89]. At almost the same time, experiments with touching soap bubbles were performed by Boys [90]. One of the first publications describing the coalescence of water droplets in experiments appeared in 1963 by Hendricks. Already then, Hendricks used a setup to record 14,000 pictures per second and analyzed the effect of humidity and surface contamination on the coalescence dynamics [91].

Due to the further development of high-speed imaging techniques during the 1980th and 1990th, processes such as raindrop formation (early experiments in 1978 by Bradley et al. [92]) or merging of heated powder to a homogeneous material (sintering [93]) could be observed in more detail. In addition, a theoretical model of the coalescence of two viscous cylinders was developed by Hopper [94–96]. With increasing importance of droplet coalescence for industrial applications, such as ink-jet printing [97], coating of surfaces [98], stabilization of emulsions [99] or oil recovering [100], a better and detailed understanding

of the merging dynamics was required. In the last decades, many experiments and simulations of three-dimensional and two-dimensional coalescence were performed to fully describe and understand this important process of merging liquid objects [101–139].
During the coalescence of liquid droplets, a connecting region between both droplets is formed. The size and the shape of that so-called “neck” or “bridge”, which changes during the merging process, and the coalescence time are important analyzing parameters in most experiments.

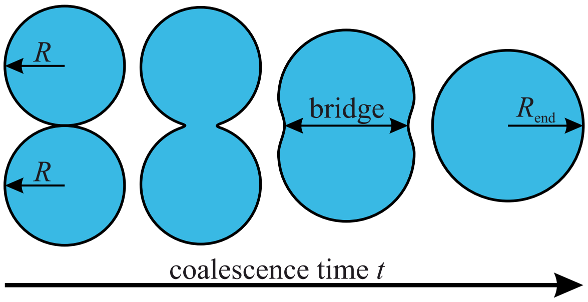

Figure 3.1: Sketch of the coalescence of two equal-sized droplets with initial radii R. During the process a bridge is formed that increases until it reaches the radius R_{end} of the final droplet.

3.1.1 Coalescence in 3D and 2D systems

The dynamics of coalescing three-dimensional droplets is basically driven by the surface tension of the droplet material. Various experiments showed that different dynamical regimes occur during the merging process: at a sufficiently early stage of the bridge formation, the surface tension is balanced by viscous forces (viscous regime), while at later times viscous effects become negligible and inertia is dominating the dynamics (inertial regime). For the very first moments of coalescence also an “inertially limited viscous” regime is described [106–109]. While the initial phases of coalescence in most experiments are comparable and agree with each other, the final stage in general depends on the experimental setup. Paulsen et al. for example used liquid hemispheres formed on top of small nozzles (left pictures in figure 3.2) to analyze droplet coalescence and especially the bridge formation. The final situation of that kind of experiments is a surface with constant mean-curvature, called *Delaunay surface*, which is connecting the supporting nozzles [103–113].
A second commonly used experimental realization of 3D coalescence of liquid droplets is that of droplets sitting on flat solid substrates (right-hand pictures in figure 3.2), called “sessile droplets”. Since there is no flow on the solid surface, the flow field of the droplets during coalescence is qualitatively different from that of free droplets. Nevertheless, the whole merging process until a final droplet is formed can be observed. The coalescence dynamics basically depends on the material viscosity, material density, and the surface tension of the droplets. For sessile droplet experiments, surface material properties and wetting conditions (e.g. contact angle between droplet and surface) also become important.
In addition to the different dynamical regimes, self-similar dynamics of the bridge formation was observed for droplets on solid substrates [119] and on liquid substrates (liquid lenses) [127]. For the latter system, the inertial regime, the viscous regimes and the crossover between them were demonstrated experimentally with materials of different

viscosity. Hack et al. also proposed a model to explain the behavior and scaling laws in the two regimes [127].

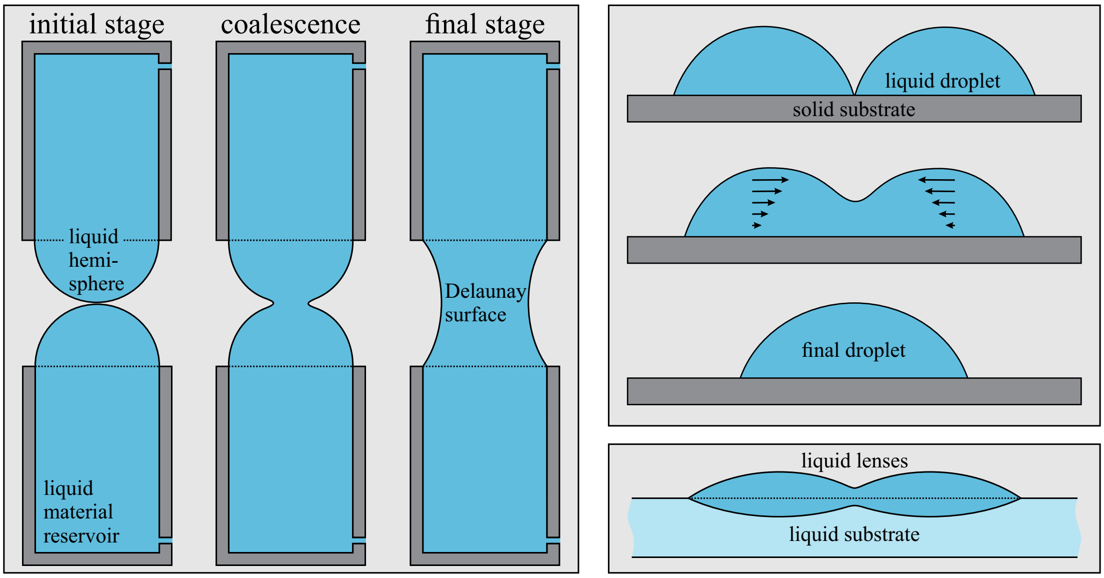

Figure 3.2: Scheme of the realization of 3D coalescence experiments. In the left-hand pictures, liquid hemispheres are formed on top of small nozzles with diameters in the range of millimeters. These kind of experiments are focused on the bridge formation and analysis of different dynamical regimes. The final stage is a surface with constant mean-curvature (Delaunay surface) connecting both supporting nozzles [103–113]. The three upper right-hand pictures show droplets on a solid substrate. Since the flow field on the substrate surface is zero, the coalescence dynamics is completely different from that on the left side [131]. The initial bridge formation as well as the complete merging process can be analyzed [115–126]. In the bottom right-hand picture, a liquid lens on the surface of a liquid substrate is shown [127].

In contrast to the 3D coalescence, the merging of liquid objects in two dimensions is driven by their line tension (2D analog of the surface tension in the 3D case). First experimental studies of 2D coalescence were done by Delabre et al. [132], where liquid crystal domains on a water surface were observed. These nematic liquid crystal islands had thicknesses of submicrometers, whereas their radii were larger than 60 µm, i.e. they can be seen as quasi-two-dimensional objects [132]. In that system, the flow of the nematic material during coalescence is coupled to the flow of the immiscible liquid substrate and regimes with surface dissipation and volume dissipation were observed. To reduce the effect of substrate coupling, later freely suspended smectic liquid crystal films were used [134–139].

As mentioned in chapter 1.3, freely suspended smectic films with thicknesses between a few nanometers and several micrometers can be created. In these quasi-two-dimensional systems, smectic islands (regions with more smectic layers with regard to the background film) or smectic holes (regions with less smectic layers) can merge. The driving force in that special case is the dislocation tension (line tension associated with dislocations) on the boundary between islands or holes and the film.

Nguyen first experimentally showed the coalescence of smectic islands in his Ph.D. thesis in 2011 [133, 139]. Later in 2019 and 2020, further experiments were performed by Shuravin et al. and Dolganov et al. [134–136] to fully understand the coalescence of smectic islands and smectic holes as well. They compared their results with a model by Hopper and confirmed a universal scaling law for the coalescence time and the bridge size.

3.1.2 The Hopper model for two coalescing circular cylinders

In the early 1980th, the material scientist Robert W. Hopper tried to describe theoretically the process of sintering, in which heated powder grains merge into a solid material. He claimed that the early stage of the particle coalescence is comparable with the plane-flow case of two coalescing cylinders. For his model, Hopper assumed two initially circular, infinitely long isothermal cylinders with diameters D consisting of a Newtonian viscous fluid of density ρ, dynamic viscosity η and surface tension γ. Additionally, all material properties are assumed to be independent of position and time and creeping viscous material flow is only considered in the x-y-plane (creeping plane flow). The whole merging process is driven by a reduction of surface energy (due to a reduction of surface area) and energy is released as heat by viscous flow dissipation.

To describe the Navier-Stokes momentum equation in a dimensionless form, the following normalization scheme was used: dimensionless spatial coordinates $\tilde{x} = x/D$ ($\tilde{y} = y/D$), dimensionless flow velocity $\tilde{\mathbf{u}} = \eta\mathbf{u}/\gamma$, dimensionless curvature $\tilde{\kappa} = \kappa D$, dimensionless pressure $\tilde{p} = Dp/\gamma$ and dimensionless time $\tilde{t} = \gamma t/\eta D$.

$$\frac{\rho\gamma D}{\eta^2}\left(\frac{\partial\tilde{\mathbf{u}}}{\partial\tilde{t}} + (\tilde{\mathbf{u}}\cdot\nabla)\tilde{\mathbf{u}}\right) = \nabla^2\tilde{\mathbf{u}} - \nabla\tilde{p} + \frac{\rho D^2\mathbf{g}}{\gamma} \tag{3.1}$$

The inertial forces shall be small compared to viscous forces (described by Laplace number La $\to 0$) and gravitational forces $\rho D^2\mathbf{g}/\gamma$ shall be negligible compared to capillary forces (small Bond number Bo $\to 0$). The Navier-Stokes equation then becomes

$$\nabla^2\tilde{\mathbf{u}} = \nabla\tilde{p} \ , \tag{3.2}$$

and the continuity equation is $\nabla\cdot\tilde{\mathbf{u}} = 0$. The curvature of the surface is defined as positive if the boundary is outwardly convex. The boundary conditions include the dimensionless surface traction being perpendicular to the boundary and, in case of the outward normal direction, being equal to the negative dimensionless curvature $-\tilde{\kappa}$ [95].

The essentially exact analytic solution for the shape of the cross-section of the cylinders as a function of dimensionless time $\tilde{t}$ can be described using equations for an inverse ellipse (Booth's curves: elliptic lemniscate and hyperbolic lemniscate). Setting the initial cylinder radii $R = D/2$ and considering a constant area $A = 2\pi R^2$, the shape during coalescence is given by

$$x(\theta) = \sqrt{2}R\frac{(1+m)\cos(\theta)(1-m^2)}{(1+m^2)^{0.5}(1+2m\cos(2\theta)+m^2)} \tag{3.3}$$

$$y(\theta) = \sqrt{2}R\frac{(1-m)\sin(\theta)(1-m^2)}{(1+m^2)^{0.5}(1+2m\cos(2\theta)+m^2)} \ . \tag{3.4}$$

The ellipse parameter m ranges within $0 \leq m < 1$ and $0 \leq \theta < 2\pi$ shall also hold true. For $m = 0$ a circle with radius $\sqrt{2}R$ is given, whereas for $m \to 1$ two circles with radii R are in tangential contact. The left-hand side of figure 3.3 shows the shape evolution for different parameters m from two circles touching each other in one point (initial state, $m = 0$) to a final circle with diameter $D_0 = \sqrt{2}D$ (final state, $m = 1$). The width of the bridge x_b connecting both cylinders can be described using equation 3.3 for $\theta = 0$:

$$x_b = 2x(\theta = 0) = D_0 \frac{1-m}{(1+m^2)^{0.5}} \quad . \tag{3.5}$$

In order to describe the time during coalescence depending on the parameter m, Hopper used

$$\tilde{t} = \frac{\gamma t}{\eta D} = \frac{\pi}{2\sqrt{2}} \int\limits_m^1 \left[\mu(1+\mu^2)^{1/2}K(\mu)\right]^{-1} d\mu \tag{3.6}$$

with the complete elliptic integral of the first kind $K(\mu)$ (normalization according to [95]).

$$K(\mu) = \int\limits_0^1 \frac{dx}{\sqrt{(1-x^2)(1-\mu^2 x^2)}} = \int\limits_0^{\pi/2} \frac{d\theta}{\sqrt{1-\mu^2 \sin^2\theta)}} \tag{3.7}$$

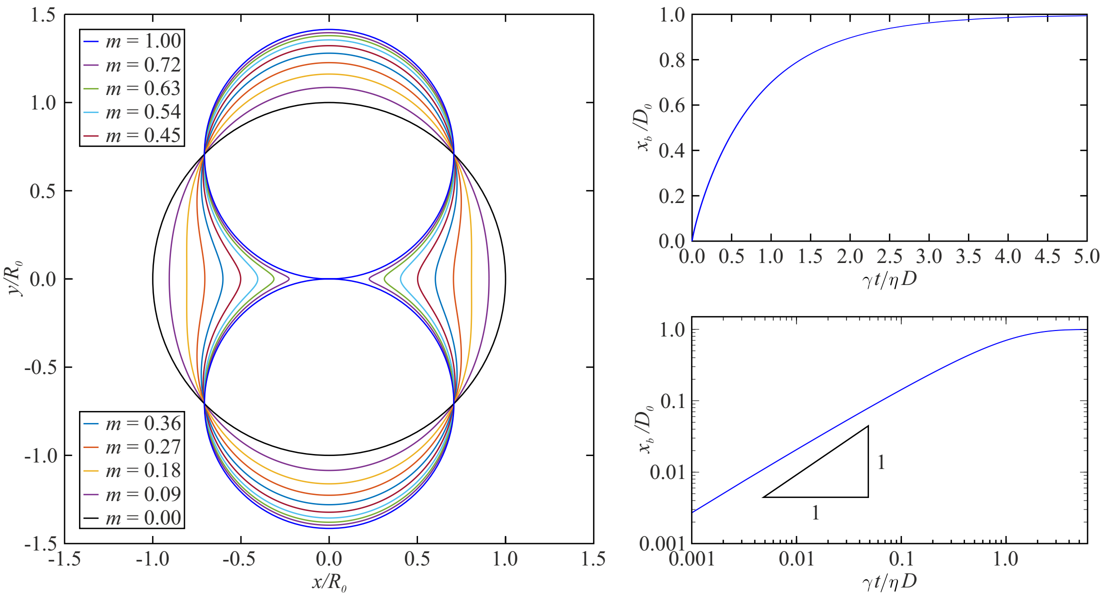

Figure 3.3: Coalescence of two circular cylinders with initial diameter D calculated with the Hopper model. The left picture visualizes the shape evolution with inverse ellipses for several ellipse parameters m. With $m = 1$ the initial stage and with $m = 0$ the final stage with the droplet of radius R_0 is described (diameter D_0). The x- and y-direction are normalized by the final radius R_0 [94]. On the top right-hand side, the bridge width x_b is shown depending on the dimensionless time $\gamma t/\eta D$. The lower right-hand picture shows the same curve with a double logarithmic scaling. The bridge size in both pictures is again normalized with the final diameter D_0 [95].

The right-hand pictures in figure 3.3 show the normalized bridge width x_b depending on the calculated dimensionless time $\tilde{t}$. The shape evolution and the bridge size growing during coalescence calculated by the Hopper model qualitatively agrees with experimental results from coalescing sessile droplets or smectic islands on free-standing films [135]. Nevertheless, there is no quantitative agreement and even Hopper himself critically discussed his assumptions especially in the early stage of coalescence [95].

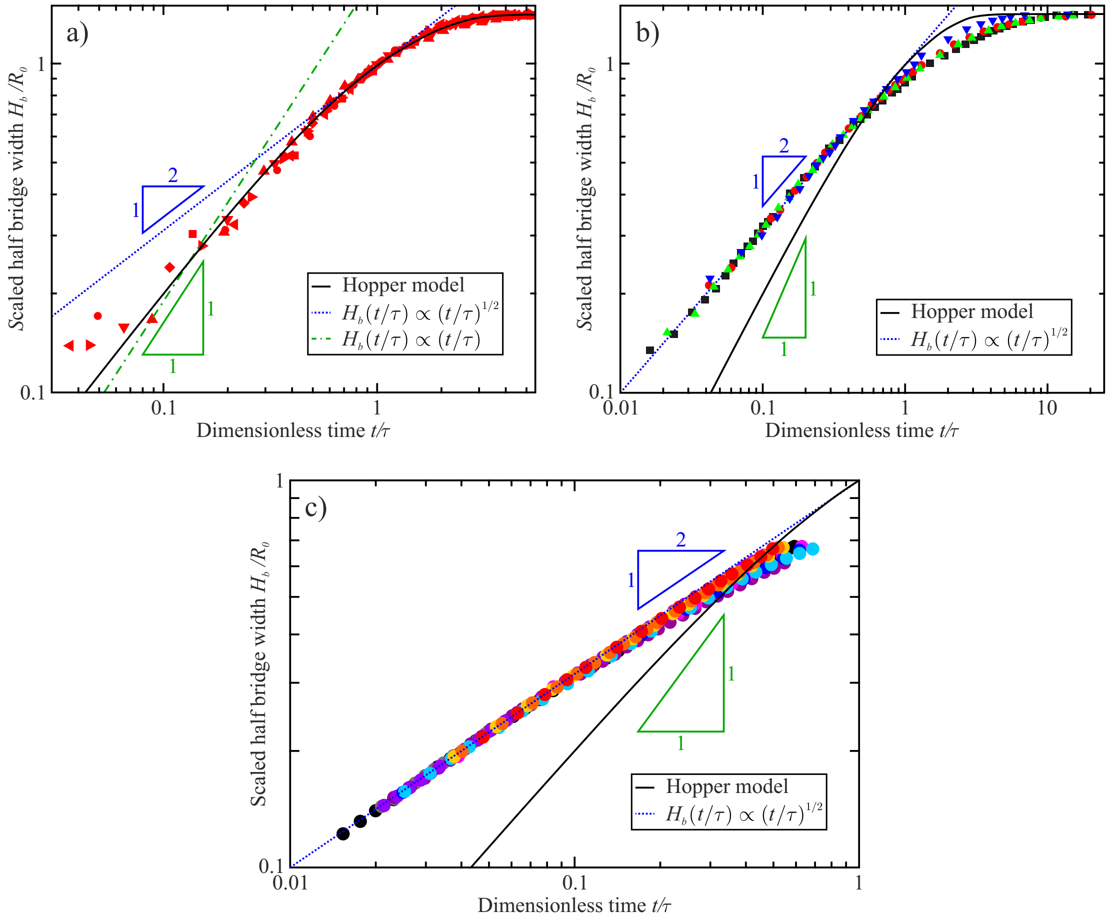

Figure 3.4: Experimental data from Shuravin et al. [135] (picture a), Dolganov et al. [136] (picture b) and Paulsen et al. [109] (picture c) compared with the Hopper model. In the experiments of Shuravin at al., the coalescence of two-dimensional smectic islands in a free-standing smectic films was observed. The experimental data are in agreement with the predictions by Hopper, although the first moments of coalescence deviate. Different symbols in picture a) correspond to different smectic island radii and thicknesses. Picture b) shows the results of the coalescence experiments of smectic holes in a free-standing smectic films (Dolganov et al.). The experimental data (different symbols for different hole radii) do not match the Hopper model. Instead, the data were fitted with a power law dependency with an exponent of $1/2$ ($H_b(t/\tau) \propto (t/\tau_R)^{1/2}$). For comparison, the coalescence of three-dimensional air bubbles in silicon oils with varied viscosity between 0.49 and 29 mPa s are shown in picture c). Again, the experimental data do not agree with the model by Hopper. A power law was used to fit the data and an exponent of $1/2$ was found. The images were reproduced from [135], [136] and [109] by permission from *APS* and *Springer Nature*.

Contrary to the described independence of the physical parameters of time and position, the pressure inside real liquid droplets, for example, significantly depends on the local curvature. For this reason, especially in the first moments of coalescence (where the curvature near the bridge is huge) or with small merging objects, the inertial effects may become important and cannot be neglected. In addition, in the limit of $m \to 1$ (initial state with two circles touching each other in one point only), the bridge velocity diverges and inertial effects become significant. In the first moments of bridge formation, the Hopper model is expected to fail.

Figure 3.4 shows the experimental results from three different systems where coalescence was observed. Shuravin et al. [135] and Dolganov et al. [136] used comparable systems for their coalescence experiments: two-dimensional free-standing smectic liquid crystal films. The merging process of smectic islands presented by Shuravin et al. (picture a) shows a very good agreement with the predicted model by Hopper and only deviates for the very first moments of the process. Comparable experiments by Nguyen et al. from 2021 [139], also with coalescing smectic islands in thin liquid crystal films, nevertheless showed different results and significant discrepancies.
Smectic holes (also see section 1.3) and their dynamics in free-standing films were investigated by Dolganov et al. [136] and although smectic holes are structural very similar to smectic islands, they show at least during coalescence a different behavior. The evolution of the bridge width follows a power law dependence $H_b(t/\tau) \propto (t/\tau_R)^{1/2}$ with an exponent of 1/2 and can not be described with the Hopper model (top right-hand picture).
For comparison and to present an example for a three-dimensional coalescence experiment, the results for the merging process of air bubbles in silicon oil are shown in the lower picture of figure 3.4. The time dependence of the bridge size again follows a power law with an exponent of 1/2.

3.2 Experimental setup and materials

The experiments of coalescing isotropic droplets in freely suspended smectic A films are based on the experiments onboard the ISS described in the previous chapter. Isotropic droplets are formed by heating a liquid crystal mixture close to the smectic A to isotropic phase transition temperature. Separated droplets are observed and their coalescence is induced by external forces.

The experimental system is comparable with that of coalescing liquid lenses presented by Hack et al. [127], but an important advantage of thin smectic films is the absence of a substrate or subphase. The isotropic droplets in the film are surrounded by air on both sides of the film only. Thus, the flow field can be assumed as two-dimensional and the vertical components of the material velocity can be neglected in the dynamic equations. With regard to the 2D flow, the presented system is comparable to the experiments by Shuravin et al. [135] and Nguyen et al. [133, 139]. In contrast to smectic islands or holes, the coalescence of isotropic droplets is driven by the reduction of surface energy. While the merging process of smectic islands and holes is driven by the line tension of the dislocations around those regions, the line tension or an effective line tension at the edge of isotropic droplets only plays a secondary role.

The coalescence of isotropic droplets in a free-standing smectic A film is a unique process that combines the assumed two-dimensional flow with the three-dimensional geometry of the observed droplets.

3.2.1 Liquid crystal mixture

The isotropic droplets used for the coalescence experiments were created with the same material that was used for the two-dimensional colloid experiment. The liquid crystalline mixture consisting of two components was heated slightly above the bulk transition temperature of 51.1 °C to create isotropic droplets.

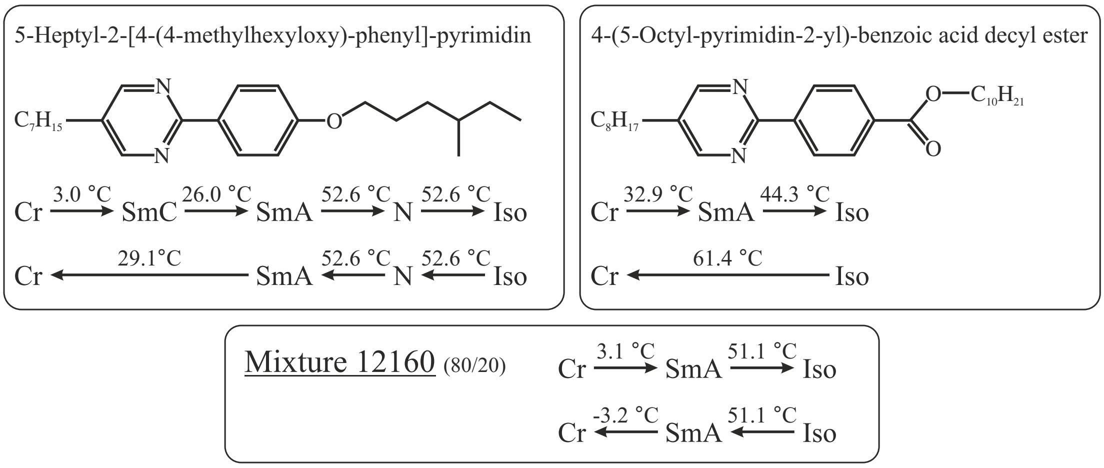

Figure 3.5: Structure and phase sequences of the two components of Mixture 12160 from Displaytech. The mixture contains 80% of the left material and 20% of the right-hand component. Transition temperatures and molecule structures are taken from Displaytech [77].

The phase sequences of the separate materials and the mixture are shown in figure 3.5. The viscosity η and the surface tension γ of the mixture were determined in previous experiments described in section 2.2.2 for a temperature of 52 °C ($\eta = 0.014$ Pa s, $\gamma = 0.024$ N m^{-1}).

3.2.2 Experimental setup

The free-standing smectic films are drawn across a glass slide with a circular hole of 10 mm diameter. The glass slide also covers the top side of a pressure chamber with a size of $15 \times 15 \times 2$ mm^3 and an initial gas volume of approximately 0.45 ml. The pressure in the chamber below the smectic film can be changed using a microsyringe to slightly bend the film upwards or downwards (pressure accuracy of ± 0.5 Pa). The pressure chamber with the film holder is placed inside a self-constructed heating stage (based on Linkam THMS 600 heating stage) to reduce external air flow. A heating element (HALJIA) with a maximum power of 48 W is used to increase the temperature in the setup and three temperature sensors (PT1000) at different positions are used to measure the temperature in steps of 0.1 K. Since the film temperature can not be measured directly, the temperature inside the pressure chamber and on the glass slide (temperature difference less than 1 K) are interpolated to calculate the film temperature. The measured pressure and calculated temperature inside the chamber are controlled and adjusted automatically with a self-written *LABVIEW* program.

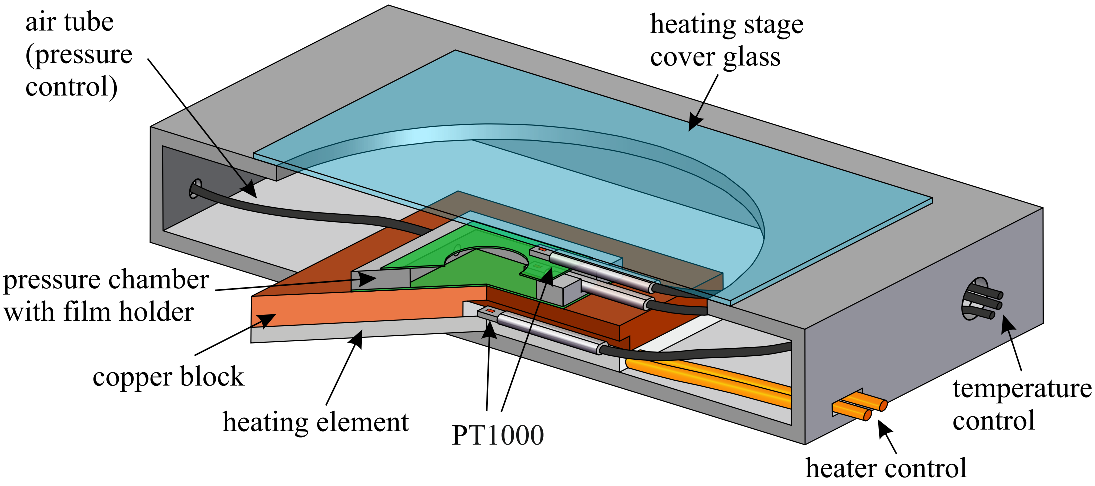

Figure 3.6: Sketch of the pressure chamber to create a free-standing smectic film inside a heating stage. The pressure can be adjusted by using a microsyringe to slightly curve the film. The temperature is controlled by a heating element below the film chamber and measured by three PT1000 temperature sensors (inside the pressure chamber close to the smectic film, directly on top of the film holder and directly above the heating element).

The setup shown in figure 3.6 is placed under a polarizing microscope (ZEISS Axiscope 40) and a mercury lamp with a 546 nm narrowband filter is used to illuminate the film with monochromatic light. Additionally, a high-speed camera (Phantom VEO 710L) is mounted to observe the coalescence with a frame rate of 24,000 fps with a typical image size of 512 × 512 pixels. The droplets are created by heating the smectic material slightly above the bulk transition temperature and then the film was slightly bent. When changing the radius of curvature of the film of several centimeters, the effective gravitational force is changed as well, and thus the motion of the droplets towards the lowest region of the film can be controlled. Without this external force, longe-range repulsion would dominate the droplet dynamics and at least for a few seconds regular lattice structures as described in section 2 could be found.

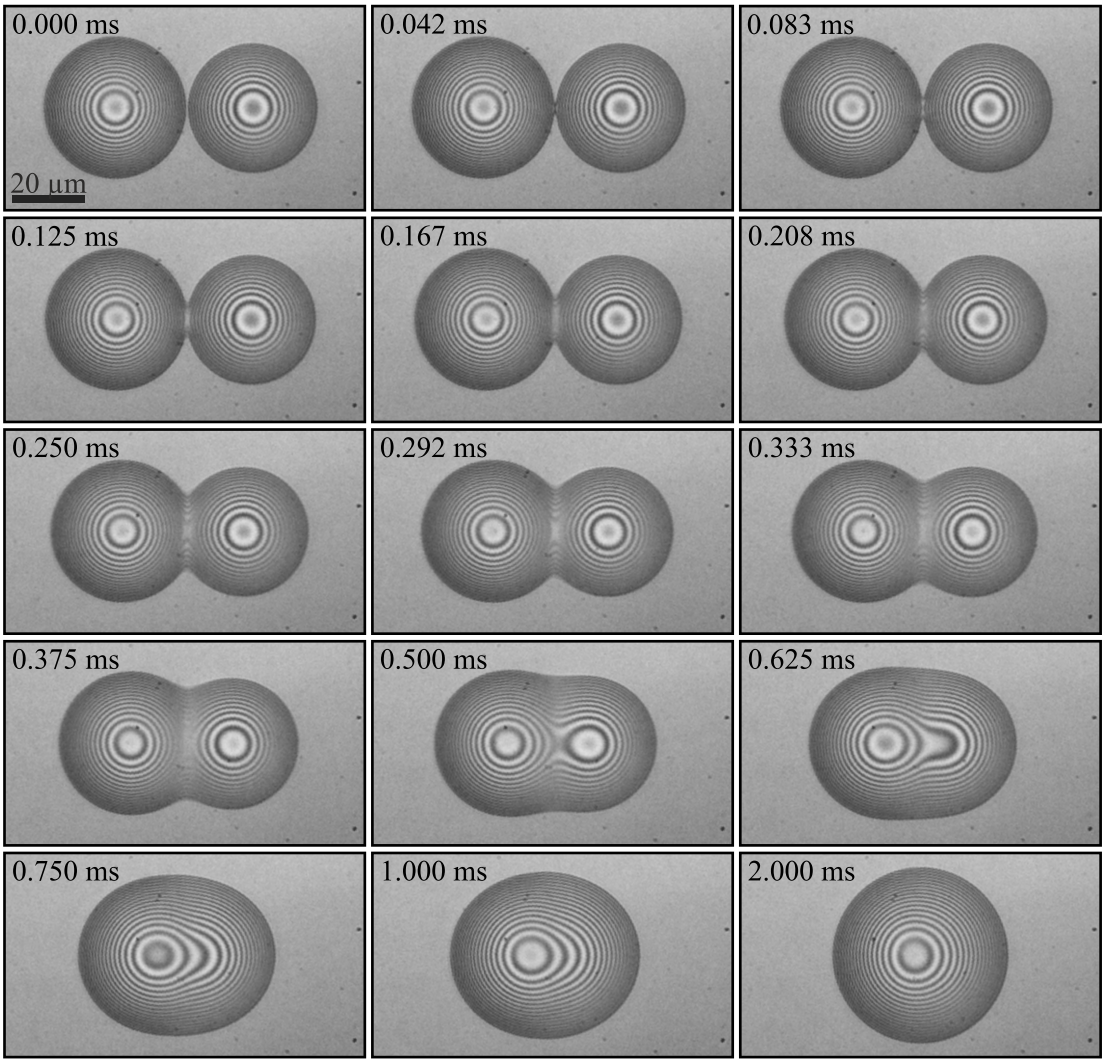

Figure 3.7: Time sequence of merging droplets with initial radii of 19.4 µm and 17.6 µm. The interference rings visualize the height profiles of the droplets with initial heights h' of 1.47 µm and 1.28 µm respectively (droplet height in their centers in respect to the film mid-plane). The final droplet has a radius of 24.5 µm and a height of 1.73 µm. The film thickness h was determined to a value of 425 nm.

Nevertheless, when droplets in the curved film meet each other, they usually remain in this intermediate state for some moments (only short range repulsion) until they overcome a

certain energetic barrier and merge. On the micrometer scale of the droplets, the curvature of the film can be neglected. Interference rings due to the monochromatic light visualize the thickness profile of the droplets.
A time sequence of merging droplets with initial radii of 19.4 µm respectively 17.6 µm is shown in figure 3.7. The entire merging process happens within two milliseconds only. The thickness of the smectic background film h (in the range from 50 nm up to 1200 nm) is determined by measuring the spectrum of the reflected light $I_{\text{ref}}(\lambda)$ and comparing it with the spectrum of the incoming light $I_0(\lambda)$ [8](measurements without a filter). The film thickness can be measured with a precision of ± 15 nm.

3.2.3 Profile determination

The droplet height h' is defined as the elevation of the droplet respective to the film mid-plane, i.e. to half the film thickness h. For the coalescence experiments, monochromatic light with a wavelength of $\lambda = 546$ nm is used and the interference between light reflected at the top surfaces of the droplets and light reflected from the bottom surface is observed. Depending on the droplet thickness $2h'(x, y)$ and the refractive index of the material $n = 1.5$, constructive (bright regions) or destructive interference (dark regions) can be observed (incidence of the light parallel to the film normal). The optical path length difference $\Delta\lambda$ has to satisfy the following conditions ($m = 1, 2, 3, ...$)(figure 3.8):

$$\begin{aligned} \Delta\lambda &= 4 \cdot n \cdot h' + \lambda/2 = m \cdot \lambda && \text{for constructive interference and} \\ \Delta\lambda &= 4 \cdot n \cdot h' + \lambda/2 = \left(m - \frac{1}{2}\right) \cdot \lambda && \text{for destructive interference.} \end{aligned}$$

The light experiences a phase shift of $\lambda/2$ if it is reflected at the upper droplet surface (transition from a medium of smaller index of refraction (air: $n \approx 1$) to an optical thicker medium).

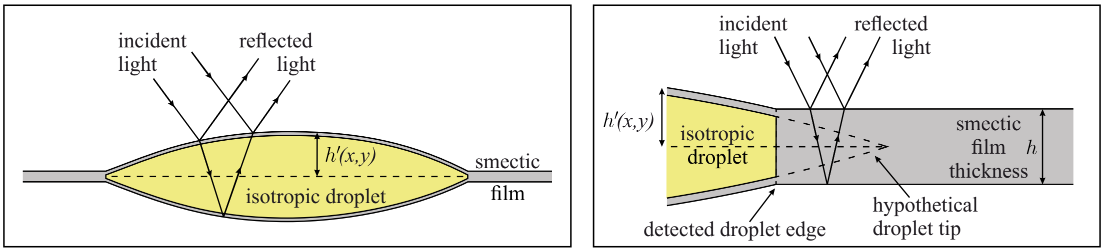

Figure 3.8: Scheme of interference of light at the isotropic droplet and the smectic film. The incident light is partially reflected at the top surface. The light passing the isotropic and smectic material is partially reflected at the bottom surface (smectic-air interface). The reflected light that emerges from the top surface then interferes with the initially reflected light. In the left picture, the light passes the covering smectic layers and the isotropic droplet and interference fringes appear. On the right-hand side, the light only passes the smectic film, since the isotropic-smectic interface at the droplet edge is assumed to be perpendicular to the film layers. Droplet sizes, curvatures and film thicknesses are greatly exaggerated. In the experiment, the incidence of light is perpendicular to the film plane.

In the experimental images shown in figure 3.9 a), the intensity along straight lines was measured and the positions of the intensity maxima and minima were detected automatically (figure 3.9 b) with an accuracy of ± 1 µm.
The droplets are embedded in the smectic film (figure 3.8), and it is assumed that they are covered by at least one smectic layer. Since the refractive indices of the smectic film and the isotropic droplet are almost equal, light just passes the smectic layers at the droplet surfaces without changing its direction. In addition, an isotropic-smectic interface perpendicular to the film layers is supposed at the droplet edge, so that interference patterns outside the detected droplet edge are created by the smectic film only (right-hand picture in figure 3.8).

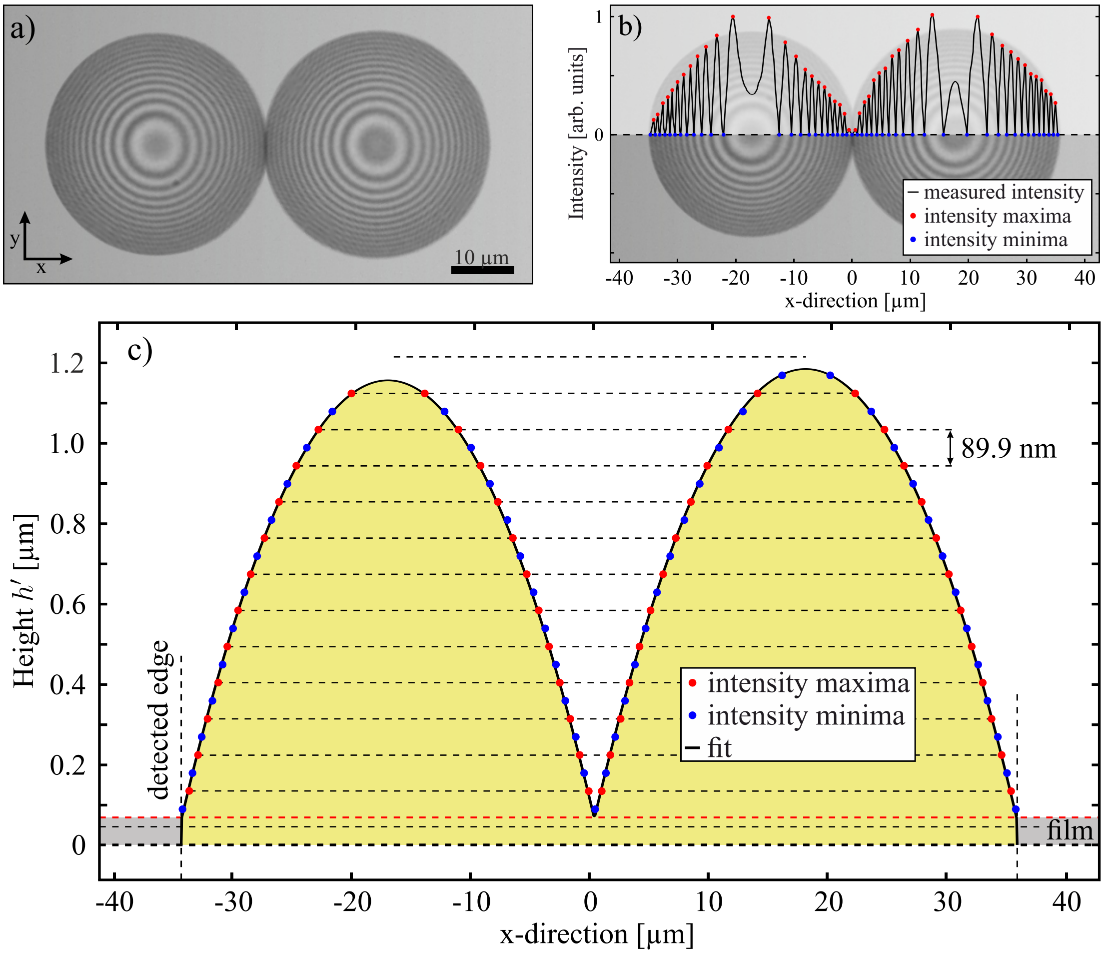

Figure 3.9: Profile determination of the droplets by measuring the position of interference rings in the experimental image. Picture a) shows the initial droplet configuration with droplet diameters of 34.7 and 35.5 µm in a 140 nm thick background film. The intensity profile along the line connecting the centers of both droplets (x-direction) is presented in picture b). For visualization only, the intensity was normalized to be zero at the position of the minima. The height profile of the droplets in picture c) was calculated from the position of the intensity maxima and minima and the constructive and destructive interference conditions (height difference between adjacent maxima: $\Delta h' = \lambda/(4n) =$ 89.9 nm). Half of the film thickness $h/2$ (gray region) is added to the calculated profile. Dotted lines connect data points of the same height.

For the profile calculation, it is assumed that the droplets in equilibrium have spherical cap shapes and that individual profile lines can therefore be plotted with a circular fit. According to the conditions for constructive and destructive interference and by measuring the exact droplet extension in the film plane (x-y-plane), the height profile of the droplets were measured and fitted. For the complete droplet height h' (droplet surface in respect to the film mid-plane), half of the film thickness h has to be added to the measured profile height as shown in picture c) of figure 3.9. Since the lateral extension of the droplet can be measured with a precision of ± 1 µm, the profile height only has an inaccuracy of 25 nm.

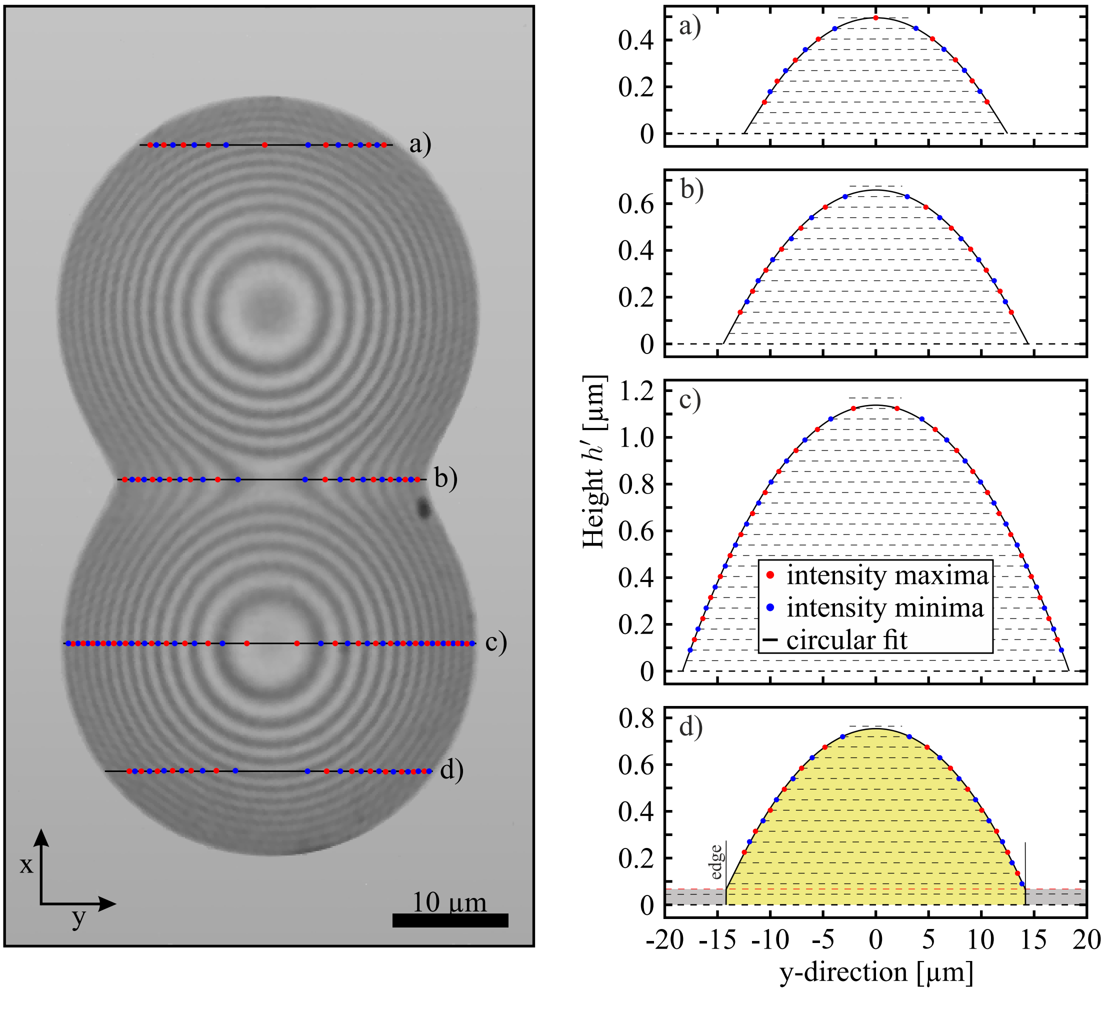

Figure 3.10: Profile determination perpendicular to the line connecting the droplet centers (x-direction). The height of each interference ring was calculated using the constructive or destructive interference condition. The positions of the intensity maxima and minima were plotted and the height profile was fitted. All data points can be fitted exactly to a segment of a circle. Picture d) additionally shows the position of the detected edge of the merging droplet. The red dashed line emphasizes the upper background film surface and their height describes the half of the film thickness $h/2$. The film thickness was previously measured to be 140 nm.

For the complete reconstruction of the droplet profile during the merging process, it is necessary to measure the height profile line perpendicular to the center-center connection line (x-direction). Figure 3.10 shows the droplet height in y-direction, and it is also shown that the data points can be plotted with a circular fit. The circular shape in y-direction verified in the right pictures of figure 3.10 allows the complete droplet height $h'(x, y)$ to be recalculated in every position by just measuring the droplet size in the film plane (droplet extension in x- and y-direction) and the height profile through the centers of the droplets. Nevertheless, more than 10 profile lines along the y-axis were measured for each experimental image to raise the accuracy of the complete profile determination.

An example of a reconstruction of a droplet pair at different times is shown in figure 3.11. It can be seen that the maximum height of the droplets is not increasing until the centers of both droplets are close to each other. On the contrary, it seems that the droplet heights are slightly decreasing in the beginning. Only at the end, where the lateral extension reaches its final configuration, the droplet height increases. The final droplet width and height are reached sequentially and not simultaneously. A detailed analysis of these phenomena will follow in the next sections.

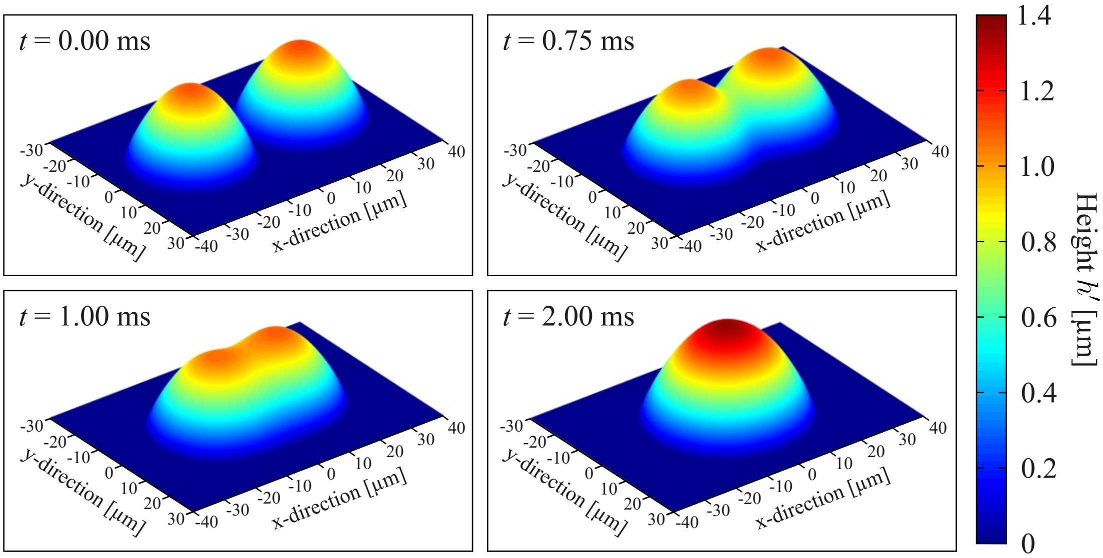

Figure 3.11: Recalculation of the complete three-dimensional profile of the droplets during coalescence. The height h' including half the film thickness is color coded. The initial droplet sizes are 34.7 and 35.5 µm in diameter and 1.16 and 1.19 µm in height. The film with a thickness of 140 nm is not shown in the images. The dark blue surface at $h' = 0$ µm in the x-y-plane corresponds to the film mid-plane.

3.3 Experimental results

3.3.1 Initial droplet shape

The complete reconstruction of the droplet profile in the initial state before merging and during coalescence showed that in equilibrium the droplets are represented by sphere caps, whereas the upper and lower parts (above and below the free-standing film) are assumed to be mirror-symmetric. The isotropic droplet surfaces are covered by smectic surface layers that are resulting from an order of the mesogens at the free isotropic-gas interface. The thickness of this smectic layers can be described by a smectic coherence length $\hat{\xi}_{\mathrm{sm}}$ of a few nanometers. The surface tension of this transition region with respect to the surrounding air or the isotropic material is assumed to be equal to the surface tension of the bulk smectic material with respect to air or the isotropic phase. Forces due to the curvature of the smectic surface layers can be neglected in comparison to surface tension effects. The shape of the droplets is determined by the surface tension of the smectic material with respect to the surrounding gas phase σ_{sm} and the tension of the interface between the smectic and the isotropic phase $\sigma_{\text{iso-sm}}$ perpendicular or parallel to the smectic layers. The surface energy of the system can be written as

$$E_{\mathrm{surf}} = \underbrace{\sigma_{\mathrm{sm}}(2A_{\mathrm{drop}})}_{\substack{\text{smectic layer}\\ \text{covering droplet}}} + \underbrace{\sigma_{\mathrm{sm}}(2A_0 - 2\pi R_0^2)}_{\text{smectic film}} + \underbrace{\sigma^{\parallel}_{\text{iso-sm}}(2A_{\mathrm{drop}})}_{\substack{\text{smectic-isotropic}\\ \text{interface at}\\ \text{droplet surface}}} + \underbrace{\sigma^{\perp}_{\text{iso-sm}}(2\pi\hat{h}R_0)}_{\substack{\text{smectic-isotropic}\\ \text{interface at}\\ \text{droplet edge}}} \tag{3.8}$$

with the film surface A_0, the surface of the droplet $A_{\mathrm{drop}} = \pi(R_0^2 + \widehat{H}_0^2)$, the initial droplet radius R_0 and the initial droplet height $\widehat{H}_0$ with respect to the film surface. The exchange of smectic material between film and meniscus for a droplet that flattens at constant volume is disregarded. The height of the droplet edge $\hat{h}$ is defined as the thickness of the smectic film h reduced by the thickness of the smectic layers covering the isotropic droplet $2\hat{\xi}_{\mathrm{sm}}$ (smectic coherence length). Note that the complete initial droplet height H_0 is the sum of the half film thickness $h/2$ and $\widehat{H}_0$ (see figure 3.12). In the center of the droplet, $h'(x,y) = H_0$ applies. The first two terms in equation 3.8 describe the interfaces of the smectic film and the covering smectic layers to the surrounding gas medium, whereas the third term represents the surface energy of the isotropic-smectic interface of the droplet surface parallel to the smectic layers ($\sigma^{\parallel}_{\text{iso-sm}}$ is used).

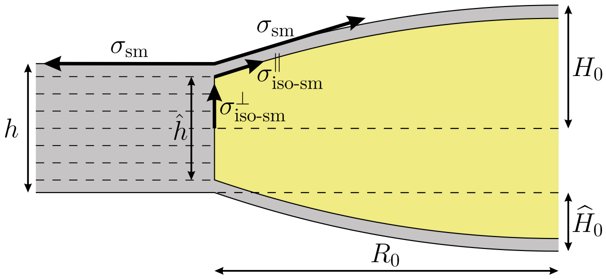

Figure 3.12: Sketch of the droplet edge embedded in the smectic film of thickness h. The droplet has an initial radius of R_0 and an initial height of H_0 respective to the film mid-plane. The surface tension of the smectic material with respect to air σ_{sm} and the isotropic-smectic interface tension perpendicular $\sigma^{\perp}_{\text{iso-sm}}$ and parallel $\sigma^{\parallel}_{\text{iso-sm}}$ to the smectic layers are marked with arrows.

Assuming a cylindrical surface around the droplet edge with height $\hat{h}$, the last term can be understood as an additional energy term from an effective line tension $\hat{h}\sigma^{\perp}_{\text{iso-sm}}$ along the droplet circumference. By minimizing the surface energy of the system E_{surf}, using Lagrange multipliers and assuming a constant droplet volume V_{droplet}, the droplet height yields the following form [17].

$$\widehat{H}_0(R_0) = -\frac{\sigma_{\text{sm}} + \sigma^{\|}_{\text{iso-sm}}}{\Pi'}\hat{h} + \sqrt{\left(\frac{\sigma_{\text{sm}} + \sigma^{\|}_{\text{iso-sm}}}{\Pi'}\hat{h}\right)^2 + \frac{\sigma^{\perp}_{\text{iso-sm}} R_0}{2\Pi'}\hat{h} + \frac{\sigma^{\|}_{\text{iso-sm}} R_0^2}{\Pi'}} \tag{3.9}$$

$$\text{with} \qquad \Pi' = \sigma^{\|}_{\text{iso-sm}} + 2\sigma_{\text{sm}} - \frac{\sigma^{\perp}_{\text{iso-sm}}}{2R_0}\hat{h}$$

Within this model, the interface between the surrounding gas phase and the isotropic droplet is considered to be composed of the isotropic-smectic interface and the surface of the smectic layers covering the droplet. Analogous to that, the surface tension of the isotropic-gas interface σ_{iso} is supposed to be composed of the smectic-gas surface tension σ_{sm} and the isotropic-smectic interface tension $\sigma^{\|}_{\text{iso-sm}}$ (parallel to the smectic layers). With the assumption that $\sigma_{\text{iso}} = \sigma^{\|}_{\text{iso-sm}} + \sigma_{\text{sm}}$, and by introducing the surface tension difference $\Delta\sigma = \sigma_{\text{iso}} - \sigma_{\text{sm}}$ that directly describes the interface tension $\sigma^{\|}_{\text{iso-sm}}$, the relation between the droplet height $\widehat{H}_0$ and the radius R_0 can be written as [17]:

$$\widehat{H}_0(R_0) = -\frac{\sigma_{\text{iso}}}{\Pi'}\hat{h} + \sqrt{\left(\frac{\sigma_{\text{iso}}}{\Pi'}\hat{h}\right)^2 + \frac{\sigma^{\perp}_{\text{iso-sm}} R_0}{2\Pi'}\hat{h} + \frac{\sigma^{\|}_{\text{iso-sm}} R_0^2}{\Pi'}} \tag{3.10}$$

$$\text{with} \qquad \Pi' = \sigma_{\text{iso}} + \sigma_{\text{sm}} - \frac{\sigma^{\perp}_{\text{iso-sm}}}{2R_0}\hat{h} \ .$$

Experimental investigations by Schüring et al. [17] showed that the isotropic to smectic interface tension perpendicular to smectic layers $\sigma^{\perp}_{\text{iso-sm}}$ is of the order of maximum 1% of σ_{iso}, so the interface at the droplet edge can be neglected in comparison with all other surface tension effects.

$$\widehat{H}_0(R_0) = -\frac{\sigma_{\text{iso}}}{\sigma_{\text{iso}} + \sigma_{\text{sm}}}\hat{h} + \sqrt{\frac{\sigma_{\text{iso}}^2}{(\sigma_{\text{iso}} + \sigma_{\text{sm}})^2}\hat{h}^2 + \frac{\sigma^{\|}_{\text{iso-sm}}}{\sigma_{\text{iso}} + \sigma_{\text{sm}}} R_0^2} \tag{3.11}$$

In the case of $\sigma_{\text{iso}} < \sigma_{\text{sm}}$, the system would gain energy by replacing smectic surface by isotropic surface: the droplet would spread over the whole film and finally the film is expected to rupture. Conversely, and experimentally proven, it means that $\sigma_{\text{iso}} > \sigma_{\text{sm}}$ and the droplet radius shrinks while the smectic-gas interface of the droplet surface is increasing. In equilibrium, the gain in surface energy is exhausted by the additional created droplet surface. At the limit of an isotropic surface tension that is equal to the smectic surface tension $\sigma_{\text{iso}} = \sigma_{\text{sm}}$, the surface tension difference $\Delta\sigma$ $(= \sigma^{\|}_{\text{iso-sm}})$ and as a result the droplet height $\widehat{H}_0$ would vanish.

Nevertheless, in first approximation, extremely flat droplets are assumed and by setting $\sigma_{\text{iso}} + \sigma_{\text{sm}} \approx 2\sigma_{\text{sm}}$, a simple equation for the droplet height depending on the droplet radius, the film thickness and the surface tensions σ_{sm} and $\sigma^{\|}_{\text{iso-sm}}$ can be found [17]:

$$\widehat{H}_0(R_0) \approx -\frac{\hat{h}}{2} + \sqrt{\frac{\hat{h}^2}{4} + \frac{\sigma^{\|}_{\text{iso-sm}}}{2\sigma_{\text{sm}}} R_0^2} \ . \tag{3.12}$$

At the beginning of the coalescence experiments, clusters of droplets were created and their sizes were measured to proof the equation above and the underlying model. For the verification of the calculated droplet heights, the droplet profiles were reconstructed and their interference patterns were calculated. Figure 3.13 shows an experimental image that has been superimposed with recalculated droplet images.

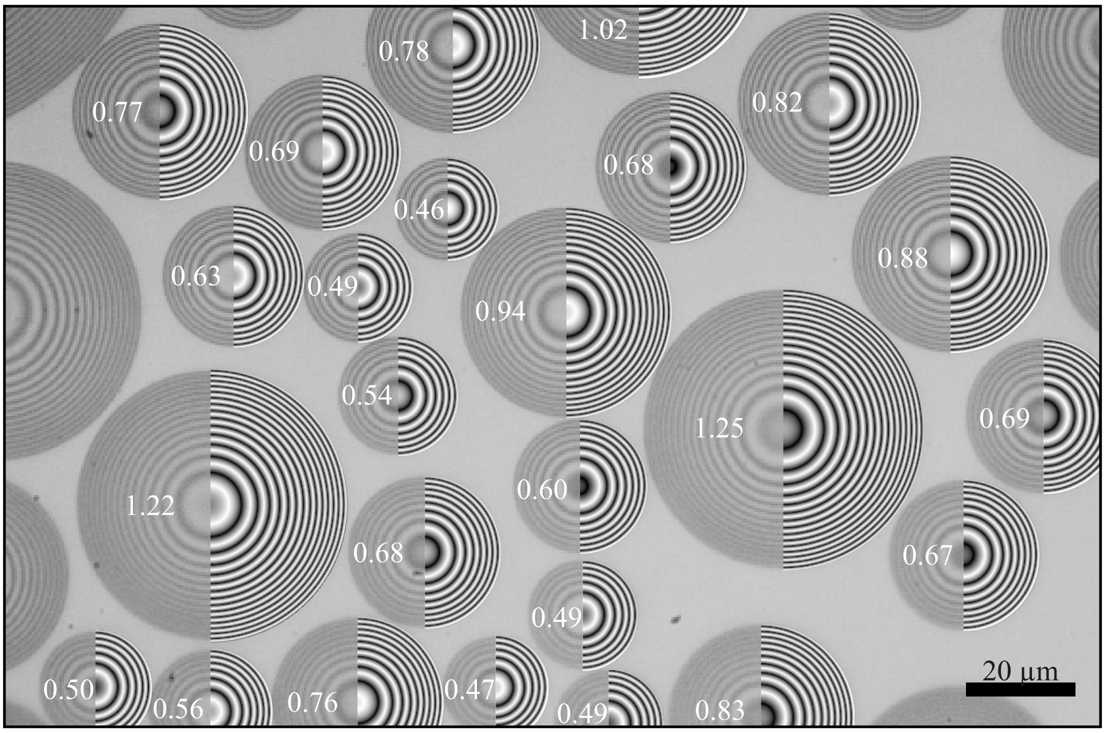

Figure 3.13: Isotropic droplets of different size in the smectic background film. The experimental image is superimposed with a recalculated interference patterns after measuring their size and profile. The white numbers represent the calculated initial droplet heights H_0 in µm.

After measuring the initial droplet lateral sizes R_0 respectively D_0 and the initial droplet height $\widehat{H}_0$ with respect to the background film surface, the contact angle θ between the film and the droplet surface could be calculated (see figure 3.14 and appendix A.2).

$$\theta = 2 \arctan\left(\frac{\widehat{H}_0}{R_0}\right) \tag{3.13}$$

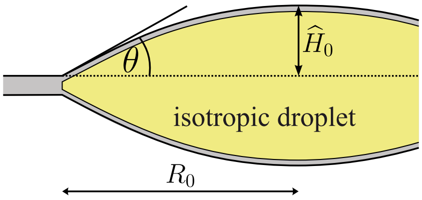

Figure 3.14: Sketch of a droplet with a contact angle θ between the droplet and the film surface. For the angle calculation, the droplet height $\widehat{H}_0$ and the droplet radius R_0 are used (see equation 3.13).

Since the surface tensions $\sigma_{\text{iso-sm}}$ and σ_{sm} weakly depend on temperature, the droplet heights can be varied by changing the film temperature according to equation 3.12. The initial droplet heights in dependence of their initial radii and contact angles are shown in figure 3.15. For constant contact angles θ and droplet sizes that are much larger than the film thickness $\hat{h} \ll R_0$, a linear behavior is predicted: $H_0(R_0) \approx (\sigma^{\|}_{\text{iso-sm}}/2\sigma_{\text{sm}})^{0.5} R_0$. This trend can be observed in the experimental data and it is in accordance with the assumed model described before [17]. For droplets with initial radii that are in the same range as the film thickness, the linear trend is expected to deviate. Within the experiments with very thin films and within the experimental accuracy of the measured droplet sizes R_0, this deviation according to equation 3.12 could not be evaluated.

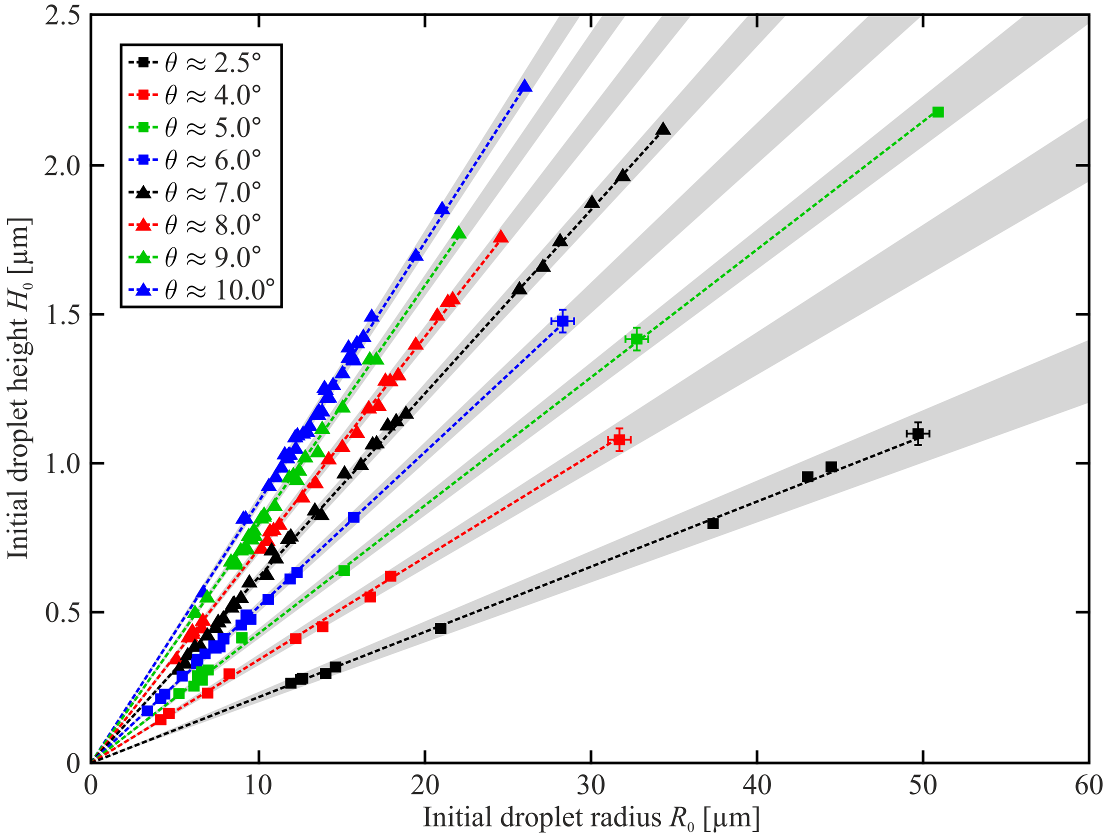

Figure 3.15: Dependence of the initial droplet height H_0 $(= \widehat{H}_0 + h/2 = \widehat{H}_0 + \hat{h}/2 + \hat{\xi}_{\text{sm}})$ in respect to the film mid-plane on the initial droplet radius R_0 for different contact angles θ. The thickness of the film is in the range between 50 nm (blue and red squares) and 260 nm (blue and green triangles). Experimental data points with similar contact angles ± 0.2° are plotted with the same symbols and colors. Gray regions visualize the angular ranges.

As seen in figure 3.15, for a given temperature and therefore at a given contact angle θ, the ratio $\varepsilon = H_0/R_0$ of the initial droplet height H_0 to the initial droplet radius R_0 remains constant for droplets of any size. In consequence, the initial droplet height and radius can be used as natural length scales to describe the changes of the droplet shape during coalescence in the film plane and perpendicular to it.

3.3.2 Coalescence dynamics

During the merging process of two droplets in a thin film, material flow with velocity $\mathbf{u}$ is assumed to be dominated by flow in the film plane only $\mathbf{u} = \mathbf{u}(x, y)$. Especially for flat droplets and regarding the thin sheet approximation, velocity gradients perpendicular to the film plane are neglected. As described earlier in section 3.1, the flow of material forms a bridge connecting the droplets and this bridge grows in time in vertical and horizontal direction. Figure 3.16 shows a sketch of a droplet profile during coalescence and additionally an experimentally measured profile where the bridge height h'_b is defined. The bridge width w_b can be measured directly from the experimental image.

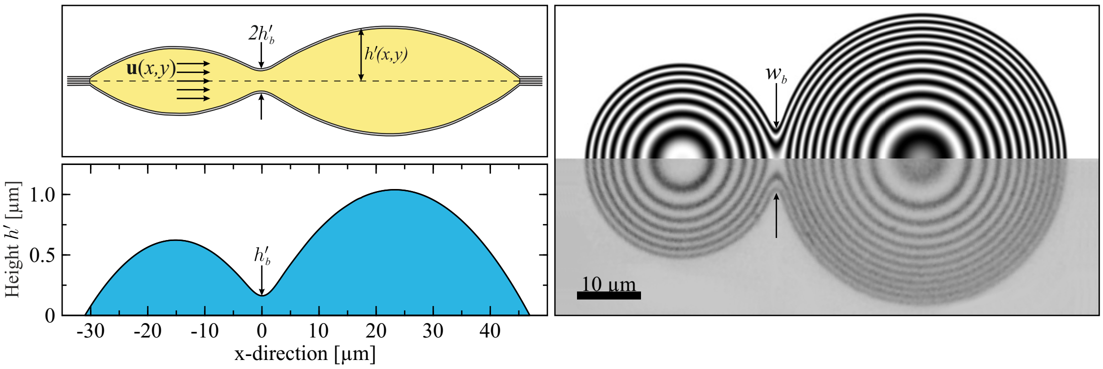

Figure 3.16: Sketch, recalculated profile and experimental image of a pair of droplets during coalescence, with the bridge height h'_b (respective to the film mid-plane) shown in the left-hand pictures and the bridge width w_b in the right-hand pictures. The top half interference pattern was recalculated using the fitted height profile. The experimental image was taken 0.5 ms after the start of coalescence. The initial droplet diameters D_0 are 30.3 µm and 45.1 µm. The corresponding initial droplet heights H_0 are 0.66 µm and 0.99 µm.

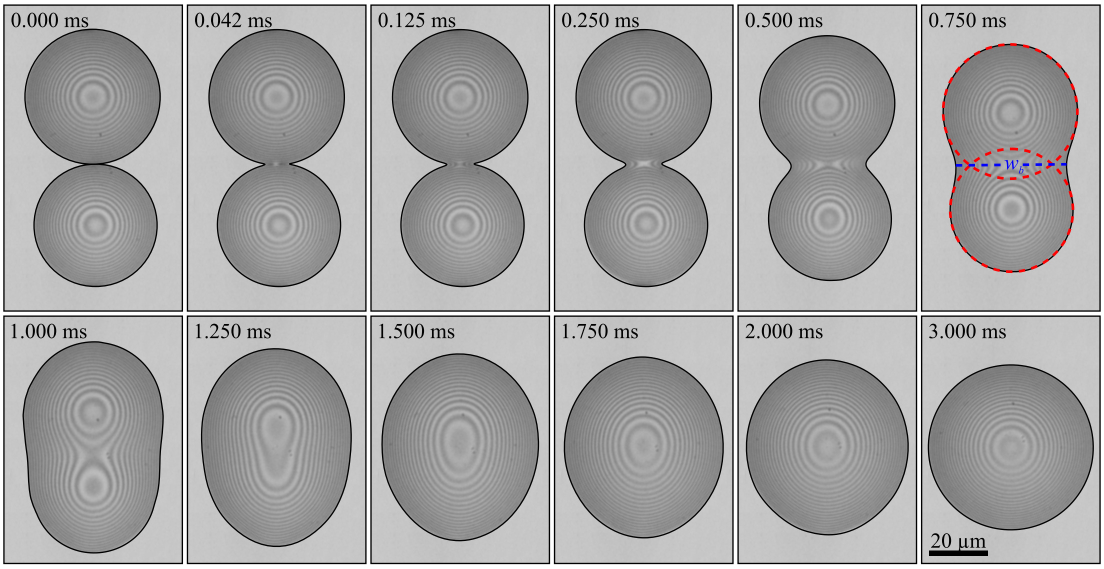

Figure 3.17: Sequence of coalescing equal-sized droplets with initial diameters D_0 of 44.6 µm and 42.8 µm and initial heights H_0 of 1.43 µm and 1.37 µm. The droplet edges are highlighted. At the time of 0.750 ms, the initial individual droplet sizes are marked with red dashed circles. Additionally, the position of the bridge is highlighted with a blue dashed line.

The sequence shown in figure 3.17 visualizes the merging process of two nearly equally sized droplets within three milliseconds. All subsequent graphs describing the evolution of the droplet sizes or the changes of the bridge size refer to this coalescence example. Since the droplets never have the exact same size, the indices (1,2) are used to distinguish the two droplets.

In addition to determining the bridge width and the bridge height, it is also possible to measure the sizes of the individual droplets, as far as their shape can be identified separately (top right picture in figure 3.17). The heights and the droplet widths during the merging process are shown in figure 3.18.

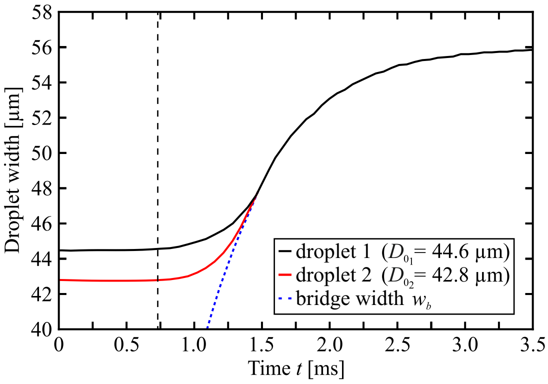

Figure 3.18: Measured individual droplet widths and heights. At the beginning, the widths and heights represent the initial droplet sizes $D_{0_{1,2}}$ and $H_{0_{1,2}}$ that remain constant for some moments (dashed lines at 0.73 ms for the droplet width and at 0.32 ms for the droplet height). After approximately 1.5 milliseconds, the bridge size exceeds the droplet widths and heights and the data points then correspond to the bridge width w_b and height h'_b.

The initial droplets widths, that are represented by the initial diameters $D_{0_{1,2}}$, first remain constant and then, after approximately 0.75 milliseconds, increase until they overlap and equal the bridge width. It was observed that while the single droplet centers move towards each other, their lateral size does not change. Only when the distance between the centers reaches about 75% of their initial distance, the lateral shape of the droplets will increase. The velocity of the droplet motion towards each other was calculated to a mean value of 15 µm/ms (0.015 m/s).

In contrast to that, the droplet heights are also constant for the first moments, but then decrease to about 97% of their initial heights (right-hand picture in 3.18). It seems, that the flow of material to form the bridge in the first moments of coalescence leads to a small shrinkage of the droplet heights, while the lateral sizes are not affected. The reason for this discrepancy may be found when analyzing the flow field inside the merging droplets in more detail. It is conceivable that due to the much smaller extension of the droplet normal to the film (up to 3 µm) than in horizontal direction (up to 50 µm), the material flow parallel to the droplet surface or through the droplet volume is higher than along the droplet film edge or in the film plane.

Figures 3.19 and 3.20 show the complete time dependence of the bridge width w_b and height h'_b for one exemplary coalescence event. The bridge exhibits a linear growth in horizontal (bridge width) and vertical (bridge height) direction during the first phase of coalescence. Here, the bridge width as well as the bridge height can be described with power law equations $w_b \propto t^{\alpha}$ and $h'_b \propto t^{\beta}$ with the exponents $\alpha \approx 1$ and $\beta \approx 1$. These results are in very good agreement with different studies [119, 127, 135, 140] in which $h'_b \propto t$ was found for the linear regimes (for high viscosities). At the end of the merging process, the bridge width and height saturate to the final droplet size.

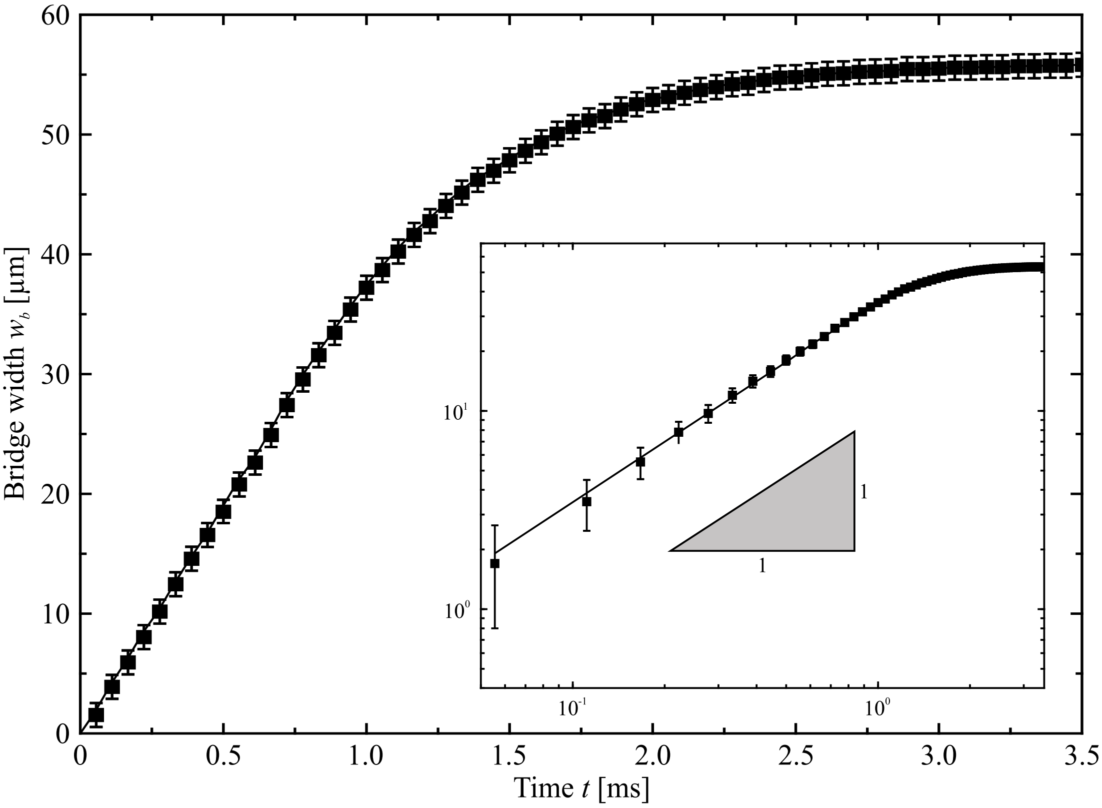

Figure 3.19: Measured bridge width w_b during coalescence of two nearly equal-sized droplets with initial diameters of $D_{0_1} = 44.6$ μm and $D_{0_2} = 42.8$ μm. The initial droplet heights are $H_{0_1} = 1.43$ μm and $H_{0_2} = 1.37$ μm. The contact angles are 7.3° for both droplets. The inset shows the same dependence with a double logarithmic scaling to confirm the linear trend $w_b \propto t$ of the initial phase.

Under the assumption that the net volume of the droplets remains constant during coalescence, the predicted final droplet width and height can be calculated. At a constant temperature, it is also assumed that the contact angle to the smectic background film and the thickness of the film are constant ($h = \text{const.}, \theta = \text{const.}$).

The droplet volume depending on the contact angle θ, the initial droplet heights H_0 and the film thickness h thus can be described in first approximation using the following equation (two spherical caps with heights $\widehat{H}_{0_1}$ and $\widehat{H}_{0_2}$ are considered, the cylindrical volume in the film of height h here is neglected for $h \ll \widehat{H}_{0_{1,2}}$).

$$V_{0_1} = \frac{2\pi}{3}\frac{(2+\cos(\theta))}{(1-\cos(\theta))}\widehat{H}^3_{0_1} \quad , \quad V_{0_2} = \frac{2\pi}{3}\frac{(2+\cos(\theta))}{(1-\cos(\theta))}\widehat{H}^3_{0_2}$$

The final volume of two equal sized droplets then yields

$$V_{\text{end}} = \frac{4\pi\cos(\theta)}{3(1-\cos(\theta))}\widehat{H}^3_{\text{end}} = \frac{4\pi\cos(\theta)}{3(1-\cos(\theta))}\left(\widehat{H}^3_{0_1} + \widehat{H}^3_{0_2}\right) \quad \text{with } h \ll \widehat{H}_{0_{1,2}} \ ,$$

and for the final radius R_{end} and height $\widehat{H}_{\text{end}}$, the following expressions can be found (a constant film thickness h is assumed, $H_{0_{1,2}} = \widehat{H}_{0_{1,2}} + h/2$, $H_{\text{end}} = \widehat{H}_{\text{end}} + h/2$).

$$\widehat{H}_{\text{end}} = \sqrt[3]{\widehat{H}^3_{0_1} + \widehat{H}^3_{0_2}} \quad \rightarrow \quad H_{\text{end}} = \sqrt[3]{H^3_{0_1} + H^3_{0_2}} \tag{3.14}$$

$$R_{\text{end}} = \sqrt[3]{R^3_{0_1} + R^3_{0_2}} \quad \rightarrow \quad D_{\text{end}} = \sqrt[3]{D^3_{0_1} + D^3_{0_2}} \tag{3.15}$$

For droplets with almost the same size ($D_{0_1} \approx D_{0_2}$ and $H_{0_1} \approx H_{0_2}$), the final droplet size can be calculated by using an factor of $\sqrt[3]{2}$ with respect to the initial droplet sizes.
Since the cylindrical droplet volume in the film ($\pi R_0^2 h$) was neglected here, a slightly bigger final droplet size depending on the film thickness has to be expected.

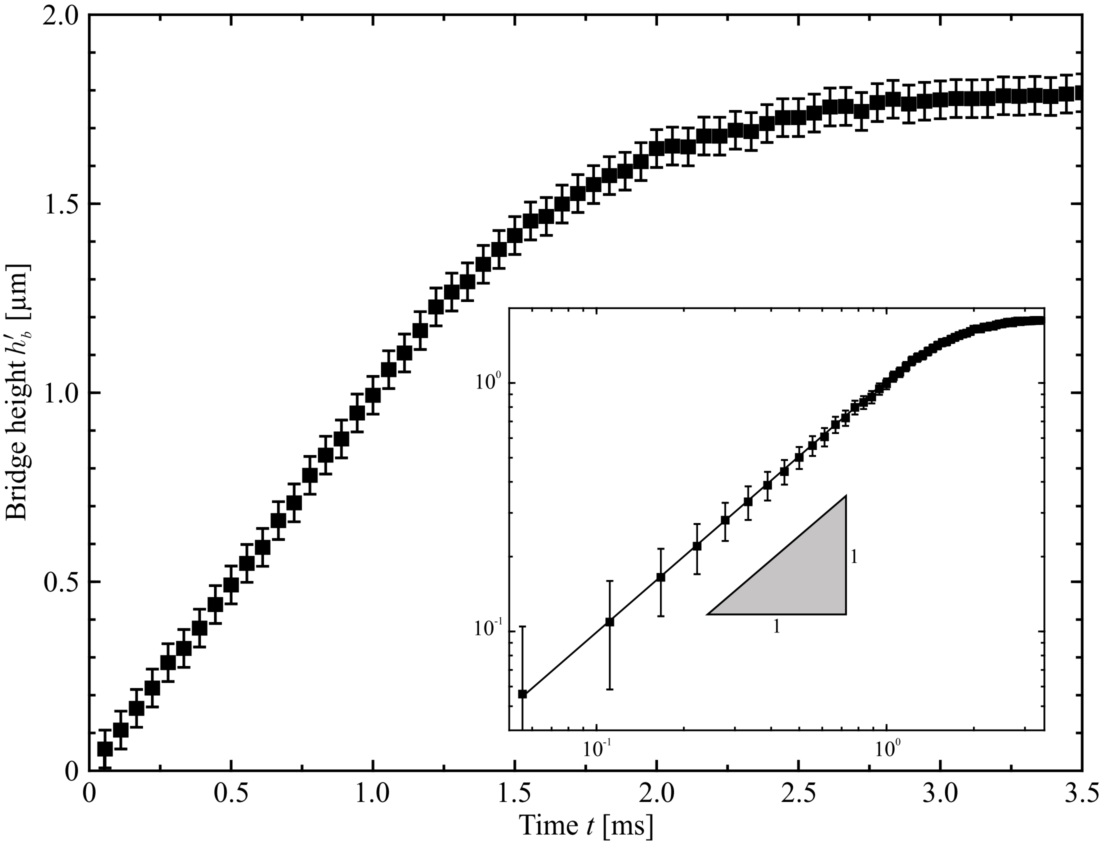

Figure 3.20: Evolution of the bridge height h'_b during the merging process of two nearly equally sized droplets. Their initial diameters are $D_{0_1} = 44.6$ µm and $D_{0_2} = 42.8$ µm. The initial droplet heights are $H_{0_1} = 1.43$ µm and $H_{0_2} = 1.37$ µm. Both droplets have a contact angles of 7.3° with the film. The inset shows the same dependence with a double logarithmic scaling to confirm the linear trend $h'_b \propto t$ of the initial phase observed in [119, 127, 135, 140].

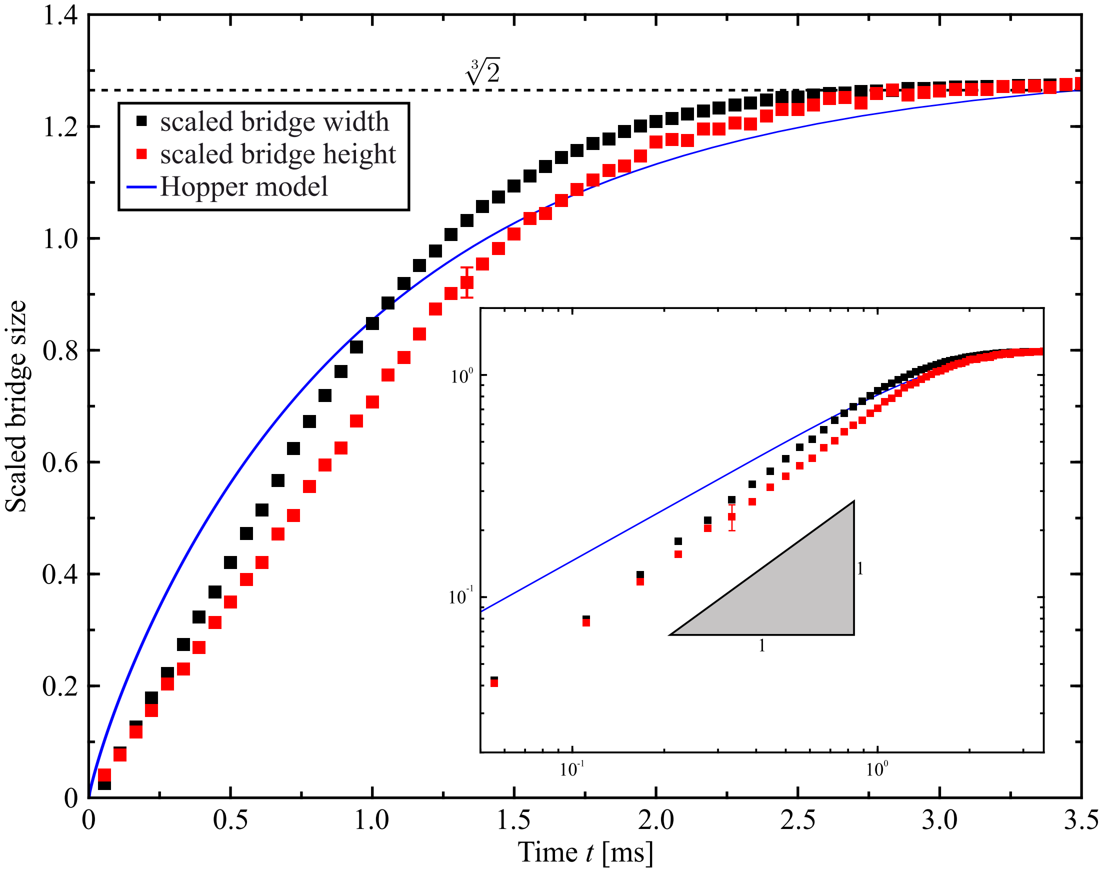

Figure 3.21: Scaled bridge width and scaled bridge height during coalescence of two nearly equal-sized droplets with initial diameters of $D_{0_1} = 44.6$ µm and $D_{0_2} = 42.8$ µm. The initial droplet heights are $H_{0_1} = 1.43$ µm and $H_{0_2} = 1.37$ µm. The contact angles are 7.3° for both droplets. Both curves have the same tendency and reach the same final value of approximately $\sqrt[3]{2}$. During coalescence, the curves slightly differ from each other. For comparison, the predicted scaled bridge size calculated from the Hopper model was added to the plot (blue curve). The error-bars for the scaled bridge width are too small to visualize.

To prove equations 3.14 and 3.15, the bridge width and height were scaled with the initial droplet sizes D_0 and H_0 as depicted in figure 3.21. Both scaled curves slightly exceed the predicted dashed line, highlighting the value of $\sqrt[3]{2}$. Additionally, the predicted scaled bridge size with regard to the Hopper model (see section 3.1.2) was added to the graph. It can be seen that the Hopper model does not fit the experimental data and deviates from them. The overall Hopper curve does not describe the data convincingly.

Nevertheless, it can be observed that the bridge width increases slightly faster and therefore also reaches its final size of $\sqrt[3]{2}$ earlier than the bridge height. This difference was found for all analyzed merging droplets, no matter which initial size or contact angle with the film they had. Especially for droplets of different size, as shown in figure 3.22, this difference in the growing rates seems to increase. Additionally, also droplets that are in contact with neighboring droplets were observed, but no influence on the coalescence dynamics was measured within the experimental accuracy.

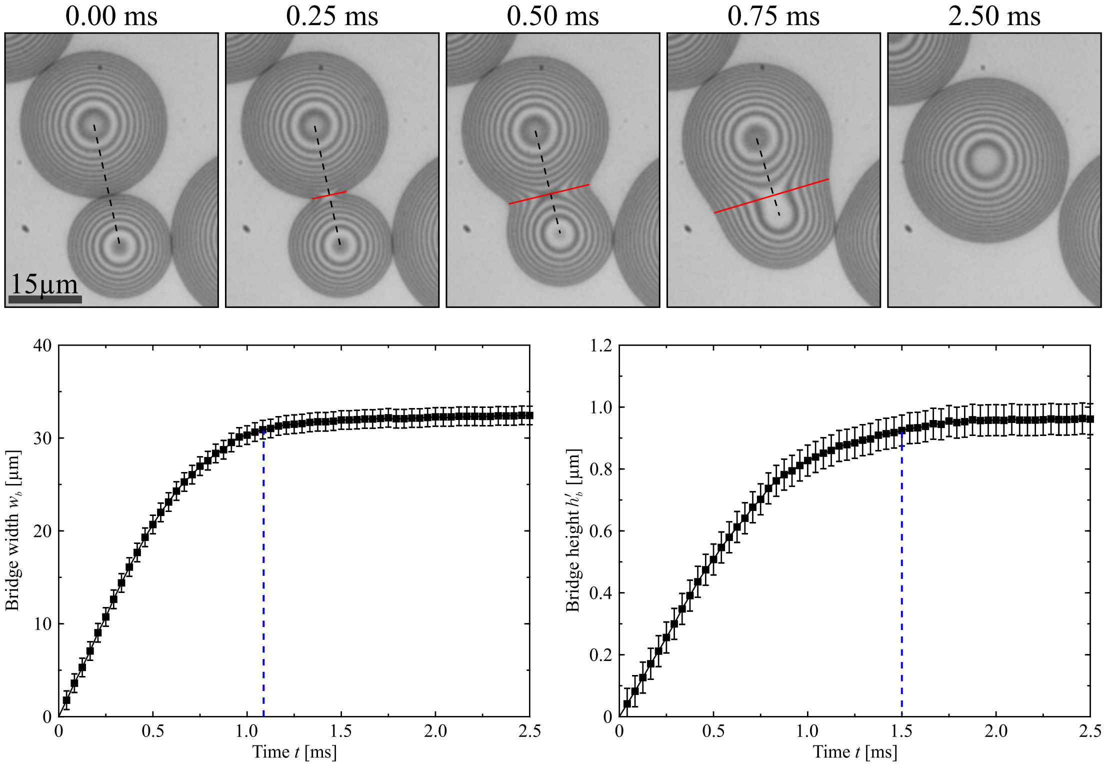

Figure 3.22: Sequence of coalescing droplets of different size and in contact with neighboring droplets. The initial diameters are $D_{0_1} = 30.3$ μm and $D_{0_2} = 21.5$ μm. The initial droplet heights are $H_{0_1} = 0.89$ μm and $H_{0_2} = 0.65$ μm, respectively. The contact angles are 6.7° for both droplets. The position of the bridge is highlighted. The lower graphs show the bridge width and bridge height growing in time. The time when 95% of the final width or the final height is reached is marked with a blue dashed line.

To determine the complete coalescence time t_{coal} for a single merging process, the time when the bridge reaches 95% of the final size was measured. As previously shown, in general, the growth rate of the bridge height perpendicular to the film plane is slightly slower than in the lateral direction. The decisive time is thus defined by the evolution of the bridge height. Depending on the initial droplet sizes and their contact angle with the film, coalescence times between 0.3 and 16 milliseconds have been measured.

In order to compare droplet pairs of nearly the same size and pairs of different size, an initial equivalence radius $\langle R_0 \rangle$ was introduced. With regard to the final droplet size, the equivalence radius was calculated as the initial radius of two identical droplets that would merge and result in the same final droplet size. In the same way also an equivalence height can be calculated.

$$\langle R_0 \rangle = \sqrt[3]{\frac{R_{0_1}^3 + R_{0_2}^3}{2}}$$

$$\langle H_0 \rangle = \sqrt[3]{\frac{H_{0_1}^3 + H_{0_2}^3}{2}}$$

The measured time for the coalescence t_{coal} of different droplet pairs as a function of their initial (equivalence) radius and their contact angle is presented in figure 3.23. The comparison of droplet pairs with the same contact angle, but different initial sizes, clearly shows a linear increase of the coalescence time with increasing initial radius. Furthermore, it can be seen that identical pairs of droplets with different contact angles would merge much slower with decreasing contact angle.

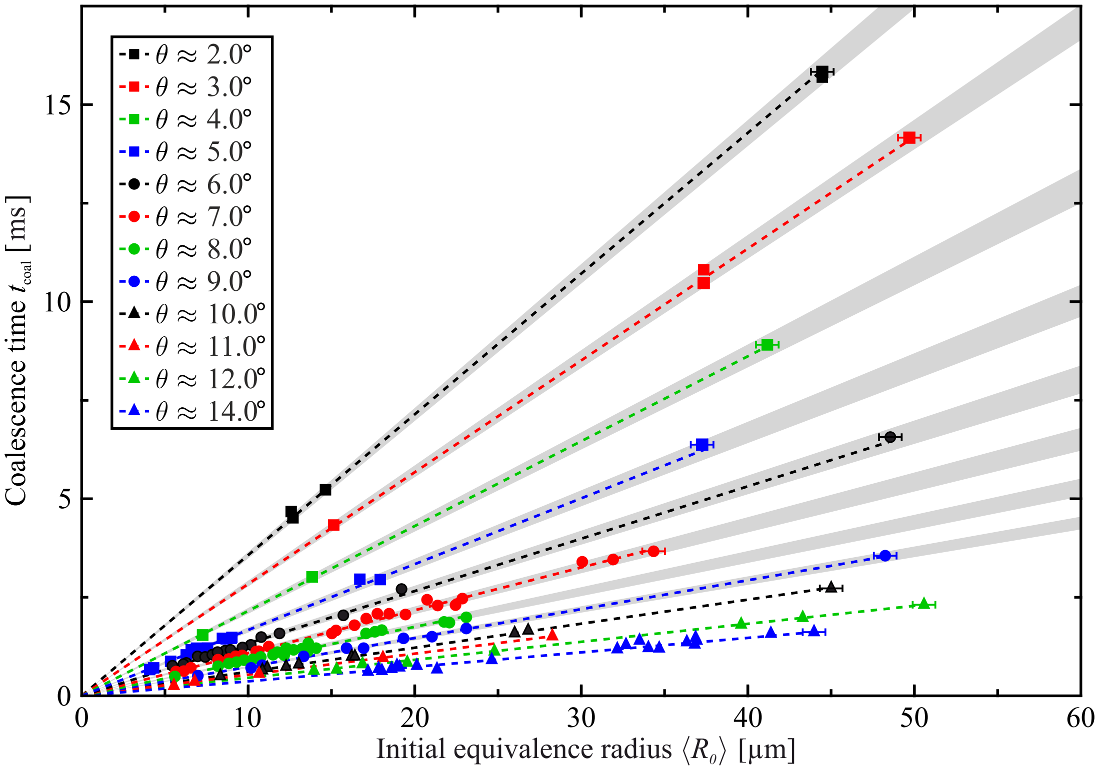

Figure 3.23: Time of coalescence t_{coal} depending on the initial equivalence radius $\langle R_0 \rangle$ of the droplet pairs and their contact angles θ. The coalescence time was determined as time when the bridge reaches 95% of their final size. Experimental data points with similar contact angles $\pm$ 0.2° are plotted with the same symbols and colors. Gray regions visualize the angular ranges.

It was experimentally proven that the coalescence dynamics and especially the bridge evolution and finally the coalescence time depend on the sizes of the observed droplets and their contact angle with the film. With regard to the contact angle, which slightly depends on the temperature, the merging dynamics also depends on the temperature. At higher temperatures (smaller contact angle) two droplets need more time to coalesce. Measurements of merging droplets in films of different thickness (h between 50 nm and 400 nm) pointed out that the film thickness, at least within the experimental accuracy, does not affect the coalescence dynamics.

The dependence of the coalescence time divided by the initial equivalence radius $t_{\text{coal}}/\langle R_0 \rangle$ on the inverse contact angle θ^{-1}, respectively $\langle R_0 \rangle / H_0$, will be analyzed in more detail in the next section.

3.3.3 Lubrication approximation and thin sheet equation

The "lubrication approximation", also known as "long-wave approximation", is a model to simplify the Navier-Stokes equation in the case that one dimension of an observed system is significantly smaller than all other dimensions. For the description of the coalescence dynamics of liquid droplets in a free-standing liquid film, this condition is fulfilled, since the smectic film thickness and the isotropic droplet heights are in the range of nanometers up to several micrometers. The film extension (with lateral size D') reaches a few hundred millimeter square and the droplet size is also in the range of several dozen up to 100 micrometers. Even small droplets with radii less than 10 µm only reach heights of maximum 1 µm depending on the contact angle.
The Navier-Stokes equation for a viscous liquid without additional forces is

$$\rho\left[\frac{\partial \mathbf{u}}{\partial t}+(\mathbf{u}\nabla)\mathbf{u}\right]=-\nabla p+\eta\nabla^2\mathbf{u} \tag{3.16}$$

with flow velocity $\mathbf{u}=(u,v,w)$ at a specific point and the pressure p. The viscosity of the material is described with η and ρ defines the density of the liquid crystal. The x-component of equation 3.16 reads as

$$\rho(u_t+uu_x+vu_y+wu_z)=-p_x+\eta(u_{xx}+u_{yy}+u_{zz}) \ , \tag{3.17}$$

where the indices here indicate spatial and temporal derivatives. All variables can then be scaled by the droplet geometrical parameters R_0 and H_0 and typical scaling values for the pressure p_0, the velocity u_0 and the time τ_0 [82, 141, 142]. The scaled parameters now have the following form:

$$\begin{gathered} x'=\frac{x}{R_0},\ y'=\frac{y}{R_0},\ z'=\frac{z}{H_0},\ u'=\frac{u}{u_0},\ v'=\frac{v}{u_0},\ w'=\frac{wR_0}{u_0H_0} \\ \tau=\frac{t}{\tau_0}\ ,\ p'=\frac{p}{p_0}\ \text{ with }\ u_0=\frac{R_0}{\tau_0}\ \text{ and }\ p_0=\frac{\gamma H_0}{R_0^2}. \end{gathered} \tag{3.18}$$

By replacing all variables with their scaled quantities, equation 3.17 now becomes

$$\begin{aligned} &\frac{u_0\rho}{\tau_0}u'_{\tau'}+\frac{u_0^2\rho}{R_0}(u'u'_{x'}+v'u'_{y'}+w'u'_{z'}) \\ &\qquad=-\frac{p_0}{R_0}p'_{x'}+\frac{\eta u_0}{H_0^2}\left(\frac{H_0^2}{R_0^2}u'_{x'x'}+\frac{H_0^2}{R_0^2}u'_{y'y'}+u'_{z'z'}\right). \end{aligned} \tag{3.19}$$

Dividing both sides by $\frac{\eta u_0}{H_0^2}$ yields

$$\begin{aligned} &\frac{H_0^2\rho}{\eta\tau_0}u'_{\tau'}+\frac{H_0u_0\rho}{\eta}\frac{H_0}{R_0}(u'u'_{x'}+v'u'_{y'}+w'u'_{z'}) \\ &\qquad=-\frac{H_0^2p_0}{\eta u_0R_0}p'_{x'}+\left(\frac{H_0^2}{R_0^2}u'_{x'x'}+\frac{H_0^2}{R_0^2}u'_{y'y'}+u'_{z'z'}\right). \end{aligned} \tag{3.20}$$

To simplify this equation, the terms in equation 3.20 are estimated with the following physical parameters: the droplet heights are in the range of a few micrometers or even less, whereas the droplet radii are at least ten times larger than their heights. The flow velocity is assumed to be in the range of a few micrometers per millisecond or even less and the characteristic pressure p_0 is in the order of magnitude of several dozen up to a few hundred pascal according to the scaling parameter in equation 3.18 (the Laplace pressure in the droplets for example is in the order of magnitude of 10^1 up to 10^2 Pa). The characteristic time τ_0 is in the range of a few milliseconds for the coalescence of isotropic droplets in free-standing smectic films. It is up to several hundred milliseconds for experiments of the coalescence of sessile droplets [116, 123, 140]. The smectic material viscosity and surface tensions were measured in previous experiments. The density of the material was estimated to be in the range of 10^3 kg/m^3, comparable with density values for commonly known liquid crystal materials with smectic and isotropic phases (8CB [143]).

$$\begin{gathered} H_0 \approx 10^{-6}\ \text{m}, \qquad R_0 \approx 10^{-5}\ \text{m}, \quad u_0 \approx 10^{-3}\ \text{m/s}, \ \ \tau_0 \approx 10^{-3}...10^{-1}\ \text{s}, \\ p_0 \approx 10^{1}...10^{2}\ \text{Pa}, \ \ \gamma \approx 10^{-2}\ \text{N/m}, \ \ \eta \approx 10^{-2}\ \text{Pa s}, \ \ \rho \approx 10^{3}\ \text{kg/m}^3 \end{gathered}$$

With these values, the pre-factors of the terms in equation 3.20 can be estimated as follows

$$\frac{H_0^2 \rho}{\eta \tau_0} \approx 10^{-6}...10^{-4}, \ \ \frac{H_0 u_0 \rho}{\eta} \approx 10^{-4}, \ \ \frac{H_0^2 p_0}{\eta u_0 R_0} \approx 10^{-1}...10^{0}, \ \ \frac{H_0^2}{R_0^2} \approx 10^{-2} \ \ .$$

It indicates that the inertia terms on the left side of equation 3.20 can be neglected in comparison with the other terms [82].

$$0 = -\frac{H_0^2 p_0}{\eta u_0 R_0} \mathrm{p}'_{x'} + \left(\frac{H_0^2}{R_0^2} u'_{x'x'} + \frac{H_0^2}{R_0^2} u'_{y'y'} + u'_{z'z'} \right) \tag{3.21}$$

Solution for sessile droplets

For sessile droplets that are in contact with a solid substrate, specific boundary conditions as no-slip at the substrate surface are assumed. Nevertheless, there is material flow in the droplets during coalescence. Thus, a velocity gradient normal to the substrate surface is assumed (see figure 3.24) [118, 123, 129, 140, 142]. Since the vertical dimension is significantly smaller than the lateral dimension $H_0 \ll R_0$ (lubrication approximation), the second derivatives of the velocity ($u'_{x'x'}$, $u'_{y'y'}$, $u'_{z'z'}$) strongly differ from each other. The second derivative with respect to the z-direction is predicted to be dominant over the x- and y-direction and in consequence, equation 3.21 finally leads to

$$0 = -\frac{H_0^2 p_0}{\eta u_0 R_0} p'_{x'} + u'_{z'z'} \ \ . \tag{3.22}$$

With the unscaled parameters and with a similar procedure for the y- and z-components, the following expressions for the pressure can be found [123, 144]

$$\frac{\partial p}{\partial x} = \eta \frac{\partial^2 u}{\partial z^2} \ , \qquad \frac{\partial p}{\partial y} = \eta \frac{\partial^2 v}{\partial z^2} \ \text{and} \ \frac{\partial p}{\partial z} = 0 \ \ . \tag{3.23}$$

To describe the change of the droplet height $h'(x,y,t)$ with respect to the substrate surface, the conservation of mass throughout the flow

$$\frac{\partial h'}{\partial t} = -\nabla \cdot Q = -\nabla \int_0^{h'} \mathbf{u} \mathrm{d}z \tag{3.24}$$

is used, where the z-component of the velocity is neglected $\mathbf{u} = (u, v, 0)$ [82, 142].
For sessile droplets on a substrate, no-slip at the surface of the substrate as well as zero tangential stress at the free surface of the droplets is assumed [82, 118, 123, 140, 142, 144].

$$\mathbf{u} = (u, v, w) = (0, 0, 0) \;\text{ at }\; z = 0 \quad \text{and} \quad \frac{\partial u}{\partial z} = \frac{\partial v}{\partial z} = 0 \;\text{ at }\; z = h' \tag{3.25}$$

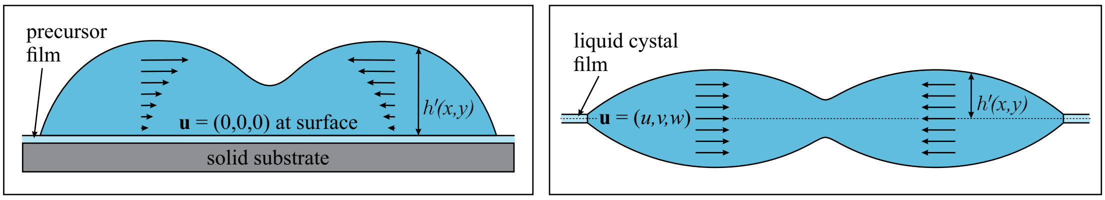

Figure 3.24: Comparison of the flow field inside the liquid droplets on a solid substrate (left) and in a free-standing smectic film (right). For sessile droplets on a substrate, a velocity gradient normal to the wetting surface is assumed, where at the substrate the velocity is zero. For liquid droplets on a thin liquid crystal film as well as for so-called “liquid lenses” (droplets on a liquid substrate), the flow field is assumed to be predominantly parallel to the film plane and velocity gradients perpendicular to it are negligible. A theoretical precursor film is sometimes introduced to overcome the contact line singularity for sessile droplets [145]. For droplets on a liquid film, the free-standing film itself represents the precursor film [82].

With the shown boundary conditions (expression 3.25) and by integrating equation 3.23 twice, the velocity profile for sessile droplets yields [142, 144]:

$$u = \frac{1}{\eta}\frac{\partial p}{\partial x}\left(\frac{z^2}{2} - h'z\right), \quad v = \frac{1}{\eta}\frac{\partial p}{\partial y}\left(\frac{z^2}{2} - h'z\right), \quad w = 0 \; . \tag{3.26}$$

By substituting these velocities into equation 3.24 and solving the integrals, an expression for the change of the droplet height $h'(x,y,t)$ can be found [82, 142, 144].

$$\frac{\partial h'}{\partial t} = \nabla\left(\frac{h'^3}{3\eta}\nabla p\right) \tag{3.27}$$

In the models for sessile droplets on a solid substrate and their coalescence, the so-called “moving contact line problem” occurs. At the contact line between the surrounding air, the solid substrate and the liquid droplet, a singularity for the stress would result in a divergence for the energy dissipation rate. As a consequence of the Navier Stokes equation coupled with no-slip boundary conditions, the contact line is not allowed to move [145, 146]. To avoid this contact line singularity, a thin precursor film of height h can be introduced, which is stabilized by a disjoining pressure $\Pi(h)$.

For the isotropic droplets on a free-standing smectic film, the precursor film is directly represented by the smectic film of height h [82]. In both cases, the thickness of the film is assumed to be significantly smaller than the droplet height $h \ll H_0$ [82, 142].
The disjoining pressure in the form of the Lennard-Jones potential is given as

$$\Pi(x,y) = \frac{(l-1)(m-1)}{h(l-m)}\gamma(1-\cos(\theta_s))\left[\left(\frac{h}{h'(x,y)}\right)^l - \left(\frac{h}{h'(x,y)}\right)^m\right] \tag{3.28}$$

with $l = 9$ and $m = 3$ and the equilibrium contact angle θ_s [82, 142]. In addition to the disjoining pressure, the Laplace pressure p_L due to the curved surface of the droplets has to taken into account. The mean curvature of the surface is given as

$$\kappa = \frac{\partial_{xx}h\left(1+(\partial_y h)^2\right) - 2\partial_x h\,\partial_y h\,\partial_{xy}h + \partial_{yy}h\left(1+(\partial_x h)^2\right)}{2\left(1+(\partial_x h)^2+(\partial_y h)^2\right)^{3/2}} \quad , \tag{3.29}$$

and under the assumption of small curvatures of the droplets, the small slope approximation ($|\partial_x h'|,\ |\partial_y h'| \ll 1$) can be used. Consequently, all terms involving gradients of h' can be neglected. The Laplace pressure thus yields:

$$p_L = -2\gamma\kappa = -\gamma\frac{\partial_{xx}h' + \partial_{yy}h'}{2} = -\gamma\nabla^2 h'(x,y) \; . \tag{3.30}$$

The net pressure then is described by the sum of Laplace pressure $p_L(x,y)$ and the disjoining pressure $\Pi(x,y)$ [82, 142]

$$p = -\gamma\nabla^2 h'(x,y) - \Pi(x,y) \; . \tag{3.31}$$

With equation 3.27 and the expression for the pressure, the coalescence dynamics of sessile droplets as well as the behavior of capillary waves in thin liquid films can be described [128, 129, 140, 142].
The characteristic time scaling parameter τ_0 now can be determined from equation 3.27 [82, 144]

$$\tau_0 = \frac{\eta R_0^4}{\gamma H_0^3} \quad \text{and with } \varepsilon = \frac{H_0}{R_0} \quad \Rightarrow \quad \tau_0 = \frac{\eta}{\gamma\varepsilon^3}R_0 \; . \tag{3.32}$$

When rearranging the scaling law $\tau = t/\tau_0$, the following expression can be found

$$t = \tau\tau_0 = \tau\frac{\eta R_0}{\gamma}\left(\frac{R_0}{H_0}\right)^3 \quad \Rightarrow \quad \frac{t}{R_0} = \tau\frac{\eta}{\gamma}\left(\frac{R_0}{H_0}\right)^3 \; . \tag{3.33}$$

The characteristic time τ_0 was calculated by using the material parameter η and γ and typical values for the droplet sizes $R_0 = 15$ µm and $H_0 = 1$ µm with a contact angle of 7.6°. The characteristic time thus yields $\tau_0 \approx 30$ ms, which is at least ten times higher than the measured times for the droplet coalescence ($\tau_0 \gg t_{\text{coal}}$).
With respect to equation 3.33, the coalescence times $t = t_{\text{coal}}$ were divided by the initial droplet radii $\langle R_0\rangle$ and their dependence on the ratio $\langle R_0\rangle/H_0$ is presented in figure 3.25. For sessile droplets, a tendency according to $t_{\text{coal}}/\langle R_0\rangle \propto (\langle R_0\rangle/H_0)^3$ is expected, but instead the data points show a linear trend.

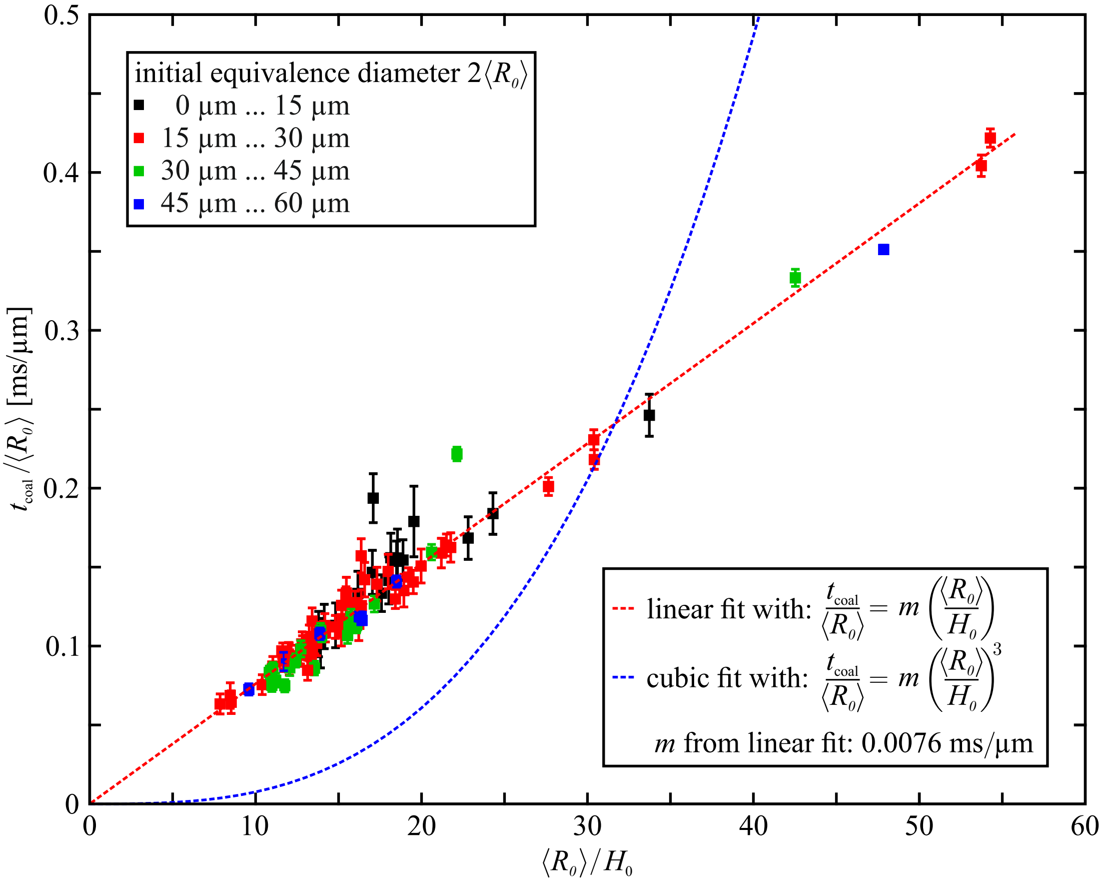

Figure 3.25: Coalescence time t_{coal} divided by the initial equivalence radius $\langle R_0 \rangle$ as a function of $\langle R_0 \rangle / H_0$. Different symbol colors correspond to different initial droplet size ranges. A cubic trend (blue dashed curve) of the data points would confirm the scaling behavior derived from the model for sessile droplets (equation 3.33). Instead, a linear behavior is observed (red dashed curve) and the slope m was calculated to a value of 0.0076 ms/µm. A dependence of the data on the initial droplet size $\langle R_0 \rangle$, visualized with different colors, was not found.

The characteristic time τ_0 is at least one order of magnitude larger than the measured coalescence time and shows a linear dependence on $\langle R_0 \rangle / H_0$. The model for sessile droplets fails for droplets on free-standing films. In fact, there are some assumptions as the no-slip boundary condition at the solid substrate surface that are not applicable for the coalescence of droplets in smectic films (right-hand image in figure 3.24).

On the contrary, the measurements suggest that the flow parallel to the film plane determines the coalescence dynamics. It is assumed that velocity gradients in vertical direction are negligible and also flow normal to the film can be neglected.

$$\frac{\partial u}{\partial z} = 0, \quad \frac{\partial v}{\partial z} = 0, \quad w = 0, \quad \mathbf{u} = (u, v, 0) \tag{3.34}$$

In addition, isotropic droplets can move freely in the smectic film. Any material exchange between the droplet and the film is expected to occur through diffusion.

Model for the coalescence of droplets on free-standing films and liquid substrates (liquid lenses)

As shown in the previous graph (figure 3.25), the model for sessile droplets does not describe the coalescence of freely floating droplets or liquid lenses on liquid substrates satisfactorily. In addition, the assumed flow profile inside the isotropic droplets in free-standing films without velocity gradients normal to the film plane does not agree with the no-slip boundary condition for sessile droplets [82].

With regard to equation 3.21,

$$0 = -\frac{H_0^2 p_0}{\eta u_0 R_0} p'_{x'} + \left(\frac{H_0^2}{R_0^2} u'_{x'x'} + \frac{H_0^2}{R_0^2} u'_{y'y'} + u'_{z'z'} \right)$$

and by neglecting all derivatives with respect to the z-direction ($u'_{z'z'} = 0$), the following expression can be derived:

$$\frac{H_0^2 p_0}{\eta u_0 R_0} p'_{x'} = \frac{H_0^2}{R_0^2} \left(u'_{x'x'} + u'_{y'y'} \right) . \tag{3.35}$$

In terms of the unscaled parameters and with a similar procedure for the y- and z-components, the pressure gradients in each direction can be described with [82]

$$\frac{\partial p}{\partial x} = \eta \frac{\partial^2 u}{\partial x^2} + \eta \frac{\partial^2 u}{\partial y^2} \tag{3.36}$$

$$\frac{\partial p}{\partial y} = \eta \frac{\partial^2 v}{\partial x^2} + \eta \frac{\partial^2 v}{\partial y^2} \tag{3.37}$$

$$\frac{\partial p}{\partial z} = 0 \ . \tag{3.38}$$

The change of the droplet height h' depending on time t is calculated by using equation 3.24 and again neglecting derivatives with respect to the z-direction (also see appendix A.3 [141]).

$$\frac{\partial h'}{\partial t} = -\nabla \int_0^{h'} \mathbf{u} \mathrm{d}z = \left(\frac{\partial h' u}{\partial x} + \frac{\partial h' v}{\partial y} \right) \tag{3.39}$$

The pressure in the system as composition of the Laplace pressure inside the droplets $-\gamma \nabla^2 h'(x,y)$ and the disjoining pressure $-\Pi(x,y)$ is identical to that described for sessile droplets. In contrast to sessile droplets, the thin free-standing smectic film represents the initially only theoretically introduced precursor film.

$$p = -\gamma \nabla^2 h'(x,y) - \Pi(x,y) \qquad \text{(identical with equation 3.31)}$$

Indicated by the experimental data shown in figure 3.25, the characteristic time scaling parameter τ_0 now becomes the following form [82]

$$\tau_0 = \frac{\eta R_0^2}{\gamma H_0} = \frac{\eta}{\gamma \varepsilon} R_0 \ . \tag{3.40}$$

With typical values for the initial droplet size, characteristic time values in the range of milliseconds ($\tau_0 = 0.13$ ms for $R_0 = \langle R_0 \rangle = 15$ µm with an angle of $\theta = 7.6°$ with the background film) can be calculated. This time underestimates the measured coalescence time t_{coal} by about a factor of ten.
However, since the time scaling is linearly dependent on the aspect ratio $\varepsilon = H_0/R_0$, the overall coalescence dynamics can be scaled. In detail, the time is divided by the characteristic scaling parameter τ_0 and the bridge width w_b is divided by twice the initial equivalence droplet radius $2\langle R_0 \rangle$. For the time scaling also the measured coalescence time t_{coal} could be used, but as presented in the inset of figure 3.26, it differs from the theoretically calculated scaling.

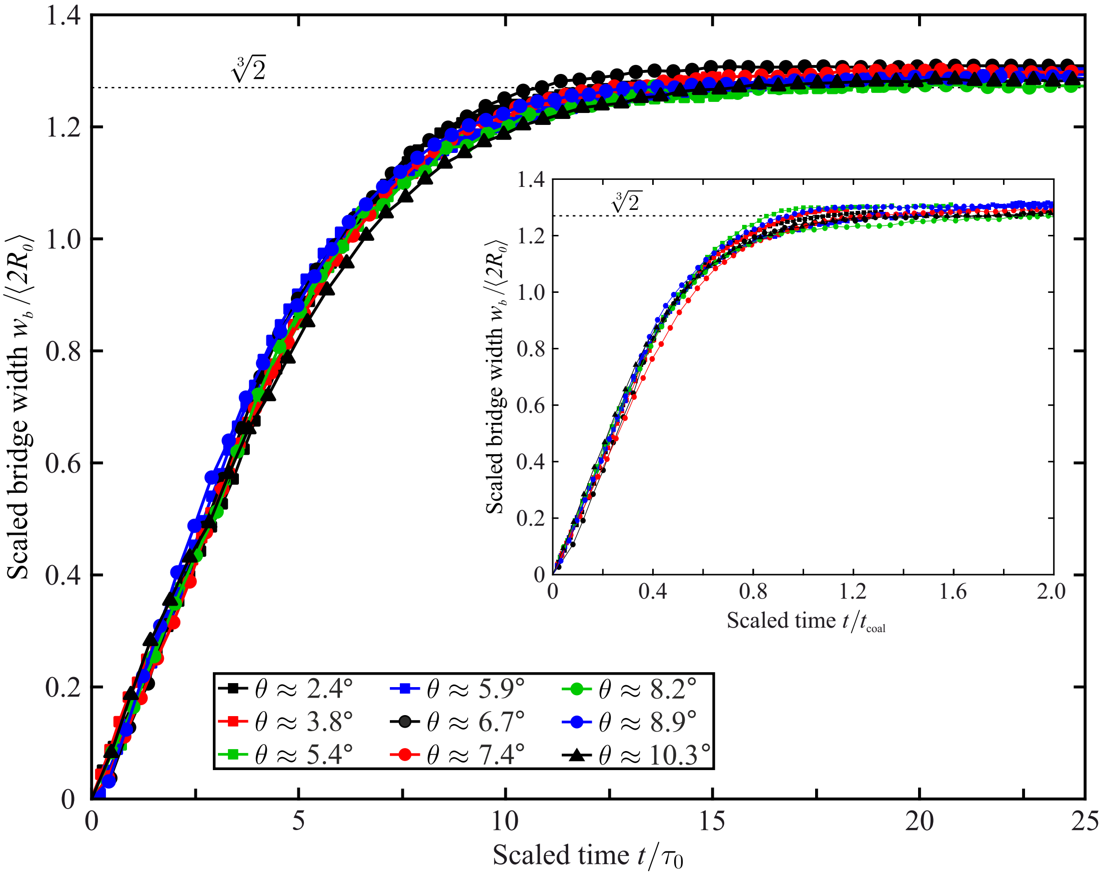

Figure 3.26: Scaled bridge width $w_b/\langle 2R_0 \rangle$ as function of the scaled time t/τ_0 for different coalescing droplets with different contact angles. All curves overlap with each other. It confirms the scaling law for the characteristic time $\tau_0 \propto R_0/\varepsilon$. The inset shows an alternative time scaling with the measured coalescence time t_{coal}. The curves overlap in the same way.

As shown in figure 3.26, all measured curves for the growth of the bridge width w_b overlap and form a kind of master curve. It can be observed that, independent of the initial droplet size and their contact angle with the film, all curves have the same tendency. In order to prove the underlying model describing the coalescence of isotropic droplets in freely suspended films in the lubrication approximation and the derived scaling parameters, the complete coalescence dynamics was simulated using a finite element method (FEM).

3.3.4 Simulation

For the simulation, the commercial software package COMSOL was used with its model for solving partial differential equations and especially in the weak form. As initial conditions, a two-dimensional surface Ω (figure 3.27) was created and the droplets with initial heights h'_0, radii R_0 and an initial distance of $2R_0$ were calculated as a function of the position. The shape of the droplets was set as the cap of a sphere with initial height H_0. To overcome the "moving contact line problem" and to stabilize the droplet shape, the disjoining pressure $\Pi(x, y)$ was calculated as described before. Additionally, the Laplace pressure inside the droplet was calculated in the beginning and within each time step of the simulation.

All necessary terms shown in the equations 3.31, 3.36, 3.37 and 3.39 are implemented in the weak form according to the following procedure (see also COMSOL documentation).

$$\frac{\partial p}{\partial x} - \eta \frac{\partial^2 u}{\partial x^2} - \eta \frac{\partial^2 u}{\partial y^2} = 0 \qquad \text{(normal form)}$$

$$\int_\Omega \left(\Psi \frac{\partial p}{\partial x} + \eta \frac{\partial \Psi}{\partial x}\frac{\partial u}{\partial x} + \eta \frac{\partial \Psi}{\partial y}\frac{\partial u}{\partial y} \right) \mathrm{d}V = 0 \qquad \text{(weak form)}$$

As shown here, the equation for the velocity in x-direction u was multiplied by a test function $\Psi(x, y)$ and integrated over the whole rectangular domain Ω. The weak formulation of partial differential equations in general is used to simplify the solving procedure of programs, in the sense that the equations are solved within the integration over the domain. The equations thus are not longer absolutely bound by the boundary conditions (e.g. smoothness or regularity conditions) and weak solutions for the equations can be found. Test functions Ψ are chosen (by the program itself) in the way that they satisfy different constraints. For the simulation of the droplet coalescence, this is the condition at the domain boundary $\Psi(x, y)|_{\partial\Omega} = 0$ (see also the COMSOL documentation).

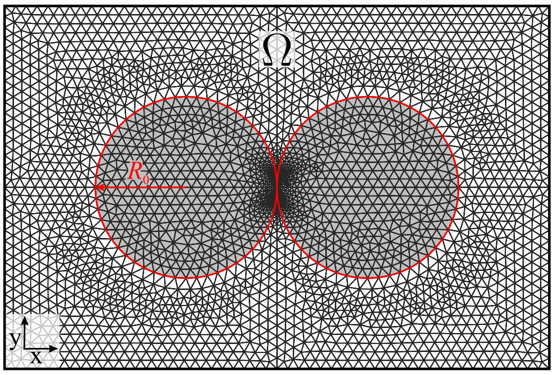

Figure 3.27: Domain Ω with a size of $6R_0 \times 4R_0$ and corresponding mesh for the FEM simulation. The initial droplet position and the radius R_0 are highlighted.

As shown in the adjacent figure, the nodes of the underlying mesh were placed at the contact line of the droplets and the background surface to realize a sufficient initial droplet height preparation. For a better lateral resolution, the red highlighted edges additionally were refined in the mesh calculation (for visualization reasons not shown in the picture). As initial values, only the droplet height $h'_0(x, y)$ and the pressure $p(x, y)$ depending on the position were calculated. The results of that simulation are shown in figure 3.28, where the complete three-dimensional profile in the top view (x-y-plane) and the side view (x-z-plane) of two equally sized droplets during coalescence are presented. The heights h' for all pictures are color-coded regarding the color bar in the central bottom image.

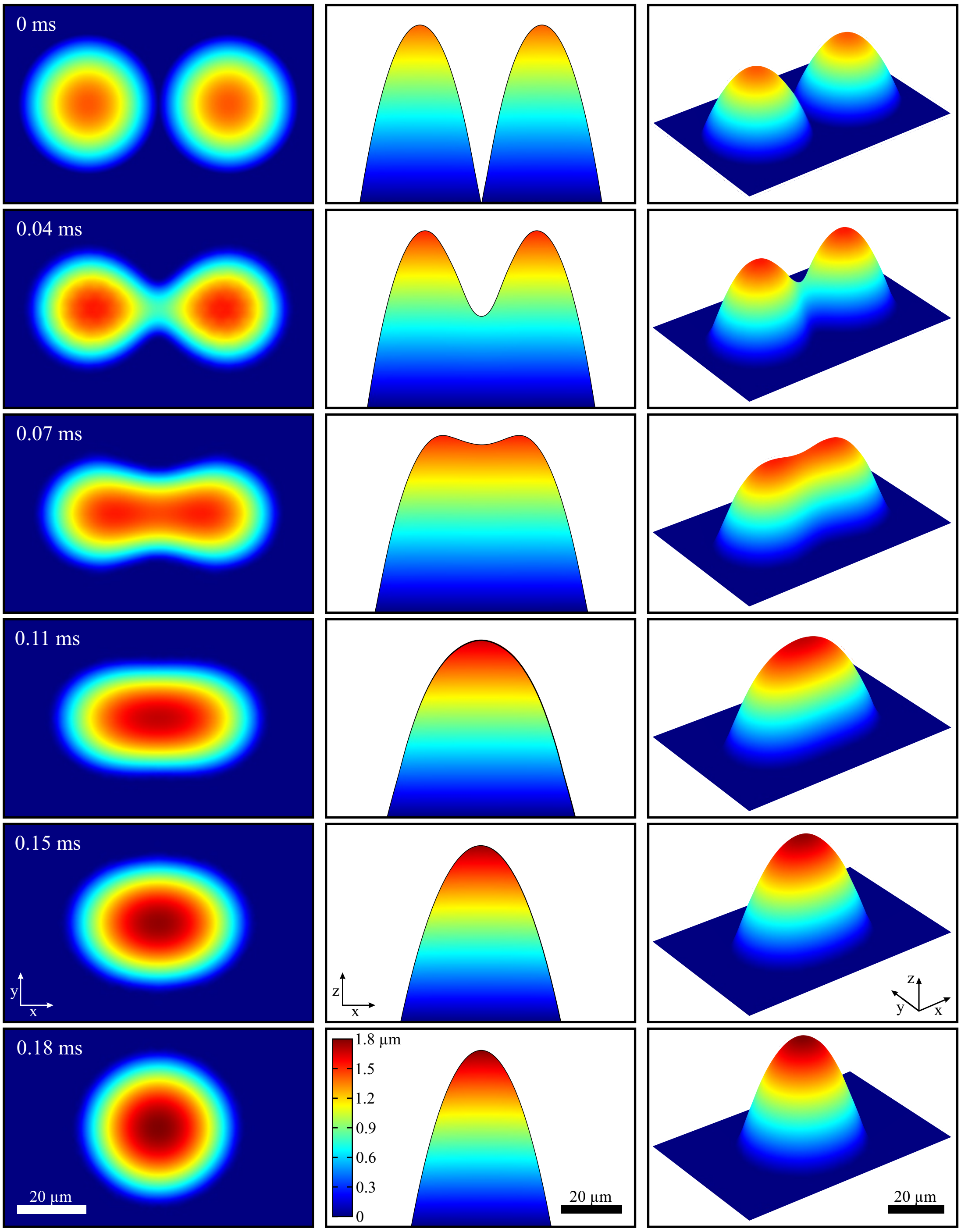

Figure 3.28: Simulated sequence of coalescing droplets on a thin film with initial radii of 20 μm and heights of 1.44 μm ($\theta = 8.2°$). At different times t, the lateral extension in the film plane (left pictures) and the profiles normal to the film plane (pictures in the center column) are shown. On the right-hand side, the complete 3D profile is visualized. The scale bars in the last picture of each column refer to the extension of the droplet in the film plane, while the height in horizontal direction is color-coded (the same color scheme for all pictures). The background film of height h is not shown here.

The sequence of the simulated coalescing droplets in figure 3.28 compared with the experimental results (see also figure 3.11) confirms the underlying model with the thin sheet equation and the lubrication approximation. The shape of real droplets during coalescence and their dynamics are well represented by the simulation. Nevertheless, it should be noted that also deviations between the experiment and simulation, especially in the first moments, can be observed. Due to the implemented precursor film and the resulting disjoining pressure including the surface tension γ, the shapes of the droplets in the simulations are predefined: a vanishing disjoining pressure would cause a spreading of the droplets. Small shape variations are observed at the beginning of each simulation to find an equilibrium situation, but obviously these small fluctuations do not affect the overall coalescence dynamics.

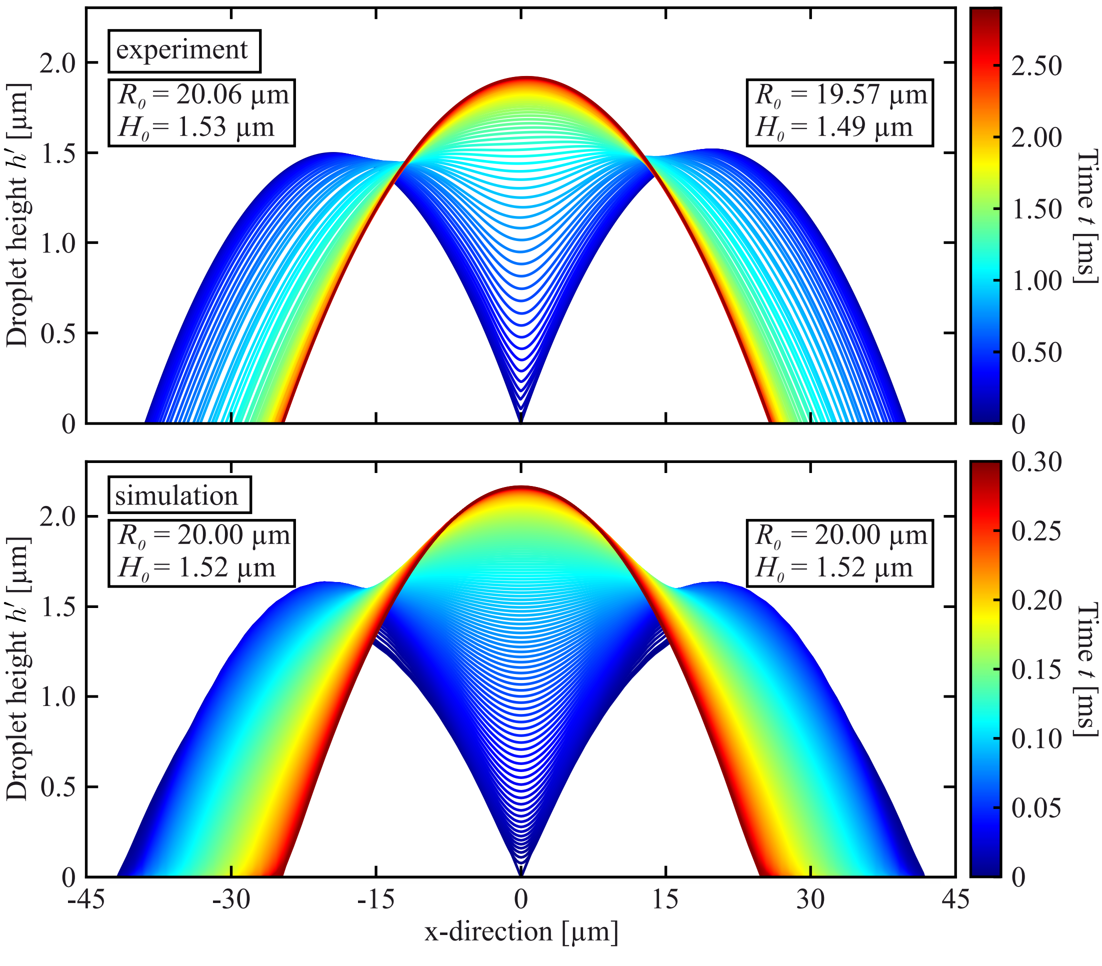

Figure 3.29: Measured and simulated cross-section profiles at the line connecting the centers of both droplets. The temporal evolution is color-coded. In the experiment, the final droplet shape is reached after approximately 3 milliseconds, whereas in the simulation the coalescence happens within 0.3 milliseconds. The initial droplet radii R_0 and heights H_0 are given in the graphs.

A second, more important and conspicuous deviation between the simulation and experiment are the measured time periods for the whole coalescence process with the specific coalescence time t_{coal}. While in the experiment coalescence times in the range of milliseconds are measured, the simulated coalescence of droplets of comparable size and with comparable contact angle is approximately ten times faster in the range of sub-milliseconds. An example for this discrepancy is shown in figure 3.29, where the evolution of the cross-section along the connecting axis of both droplets is shown for the experiment and the simulated droplets. With comparable initial droplet sizes and thus with almost the same contact angle with the film ($\theta \approx 8.7°$), the shape of the measured profiles and that of the simulation agree with each other. Nevertheless, the color-coded time axis on the right-hand side differs by at least a factor of 10.

With regard to the characteristic time scaling parameter τ_0 (see equation 3.40), the theoretical value for the shown examples yield $\tau_0 = 0.15$ ms for the experiment as well as for the simulation. This value is in the order of the coalescence time t_{coal} and only slightly underestimate this time $t_{\mathrm{coal}} = 0.16$ ms for the simulation ($\tau_0 \approx t_{\mathrm{coal}}$).

For a better comparison of the principle shape evolution of the merging process, regardless of the entire time needed in experiment and simulation, the bridge height and width were scaled by the initial droplet sizes as shown before. For the time scaling, the measured coalescence time $t_{\mathrm{coal}} = 1.66$ ms was used for the experiment and the theoretical value τ_0 was used for the simulation.

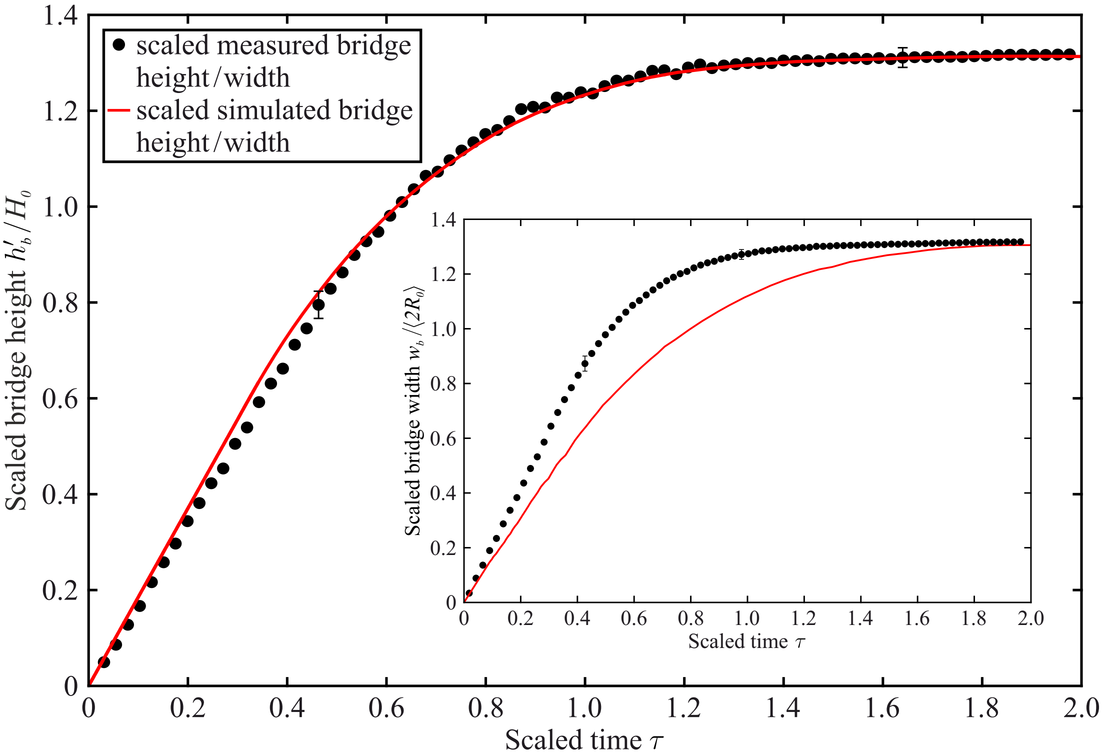

Figure 3.30: Scaled bridge height h'_b/H_0 and bridge width $w_b/\langle 2R_0\rangle$ in comparison with the simulated and scaled bridge size. The scaled time for the measured data (black circles) was calculated using the coalescence time $\tau = t/t_{\mathrm{coal}}$, while for the simulation the theoretical values $\tau = t/\tau_0$ according to 3.40 was used.

Figure 3.30 shows the scaled bridge height and in the inset the scaled bridge width from the experiment in comparison with the data from the simulation. Since two different scaling values for the time were used for the experiment and the simulation, the temporal deviations will not be considered here. While the scaled bridge height in the experiment and simulation match very well, the evolution of the scaled bridge width again shows unambiguous deviations between simulation and experiment.

Finally, also the origin for the development of the modified model for droplets in thin films, the measured linear trend of the time scaling law was verified with the simulation. For a variety of equal-sized droplet pairs with different sizes and contact angles, the coalescence time was determined. In addition, also sessile droplets with the same physical parameters were analyzed. The expected cubic trend $t_{\text{coal}}/\langle R_0\rangle \propto (\langle R_0\rangle/H_0)^3$ for droplets on a substrate and the linear behavior measured in the experiment $t_{\text{coal}}/\langle R_0\rangle \propto \langle R_0\rangle/H_0$ could be reproduced in the simulations.

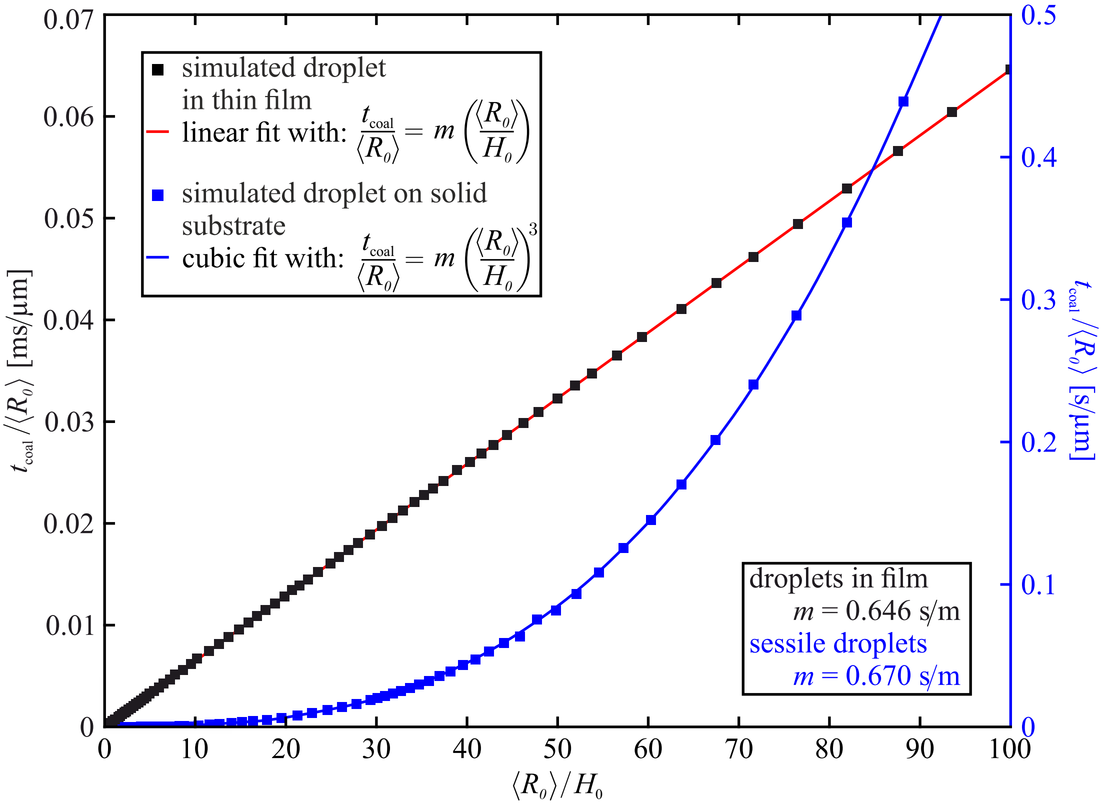

Figure 3.31: Simulated coalescence time t_{coal} divided by the initial equivalence radius $\langle R_0\rangle$ as a function of $\langle R_0\rangle/H_0$. The black symbols represent the simulation results for the coalescence in thin films, while the blue symbols correspond to a simulation for sessile droplets. Since the coalescence time t_{coal} for sessile droplets is at least four orders of magnitude longer than for droplets in thin films, the ordinate axis on the right-hand side for sessile droplets has a different scaling. According to equations 3.33 and 3.40, the data points were fitted with a linear or a cubic curve, respectively. For both cases, the pre-factor m was calculated.

The slope of the shown simulated curve in figure 3.31 was calculated and differs by more than a factor of 10 from the experiment, as expected from the previous results for the droplets in free-standing films. The inverse of the slope m^{-1} can be interpreted as the capillary velocity c. With the surface tension and the viscosity of the material, a value of

$$c \approx \frac{\gamma}{\eta} \approx m^{-1} \approx 1.7\,\frac{\mathrm{m}}{\mathrm{s}}$$

is expected. The capillary velocity describes the velocity of occurring capillary waves on the surface of the droplets during coalescence [127]. It does not refer to the flow velocity of material inside the droplets towards the bridge.

Looking more closely at the time scaling equations

$$\tau_0 = \frac{\eta}{\gamma}\frac{{R_0}^2}{H_0} \quad \text{and} \quad \frac{t}{R_0} = \tau\frac{\eta}{\gamma}\frac{R_0}{H_0} \quad \rightarrow \quad \tau = \frac{t}{\tau_0} \tag{3.41}$$

and by setting $t \rightarrow \tau_0$, the scaled time value τ would becomes “1”. Since the measured coalescence time t_{coal} was used for the analysis, the parameter τ is also expected to be slightly larger than 1. From the described theoretical model, this scaled value is predicted to be close to one, and while that is confirmed by the simulation, the experiment shows completely different values: $\tau \gg 1$.

For a better overview about the important results from the experiments and the simulation, several parameters for a specific coalescing droplet pair are collected in the following table. It again emphasizes the discrepancy of the temporal evolution of the merging droplets. A detailed discussion for that difference will follow at the end of that chapter.

Table 3.1: Measured parameters for a pair of equally sized droplets in the experiment and simulation. In the last column, m represents the slope from the linear/cubic fits of the time scaling curves (figures 3.25 and 3.31). The values in brackets in the column for the coalescence time represent the time scaling value: t_{coal}/τ_0. For the sake of completeness, also the results for the simulated sessile droplets are given.

	$\langle R_0 \rangle$ [µm]	$\langle H_0 \rangle$ [µm]	θ [°]	τ_0 [ms]	t_{coal} [ms]	m^{-1} [m/s]
Experiment droplets in film	19.81	1.51	8.72	0.15	1.66 (11.07)	0.13
Simulation droplets in film	20.00	1.52	8.70	0.15	0.16 (1.07)	1.55
Simulation sessile droplets	20.00	1.52	8.70	26.51	30.43 (1.15)	1.49

3.4 Self-similarity behavior of coalescing droplets

Geographical curves are so involved in their detail that their lengths are often infinite or, rather, undefinable. However, many are statistically "self-similar", meaning that each portion can be considered a reduced-scale image of the whole.
(B. B. Mandelbrot, 1967 [147])

As described by Mandelbrot in 1967, there exist structures or phenomena in nature where self-similarity can be observed. A famous mathematically constructed object, first published in 1904, is the so-called "Koch snowflake" shown in the left picture of figure 3.32 [148]. This fractal curve can be created iteratively on the basis of an equilateral triangle and successively dividing the edges into 3 identical parts and replacing the middle part by another smaller equilateral triangle. At different scales, always the same snowflake-like structure can be found.
An example of these self-similar structures can also be observed in nature by taking a closer look at Romanesco and its buds (right picture in figure 3.32). Here, the pyramid-like small buds with their typical twist can be found again and again in different sizes.

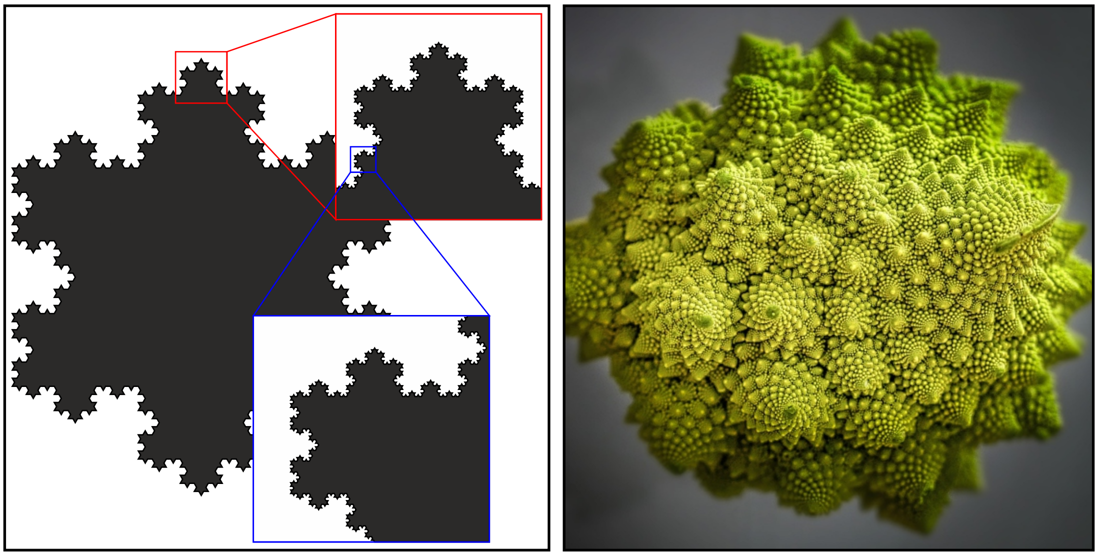

Figure 3.32: Self-similarity structures created mathematically or found in nature. The "Koch snowflakes" on the left side are constructed on the basis of equilateral triangles and the same snowflake-like curve can be observed at different length scales [148]. The Romanesco on the right side shows a comparable three-dimensional structure, where the small pyramid-like twisted buds can be found in different sizes.[1]

In the context of coalescing objects, self-similar behavior has been observed for fully three-dimensional droplets fixed at frames [108, 112, 120] as well as for sessile droplets [119, 140] and recently also for liquid lenses [127]. In all cases, the shape of the bridge

---

[1] URL: https://pixabay.com/de/photos/romanesco-blumenkohl-gemüse-gesund-3920106/
The image is released for commercial and non-commercial use without photo credits.

connecting the droplets evolves self-similar dynamics. Thoroddsen et al. additionally analyzed propagating Marangoni waves on water droplet surfaces [112].

In order to compare the experimental results for the isotropic droplets in a smectic film with liquid droplets on a liquid-air interface [127], the equation to describe the change of the droplet height shown in chapter 3.3.3 (equation 3.39) was used.
For simplification, only the dynamics in one dimension is considered ($h' = h'(x,t)$ and $u = u(x,t)$). Thus, the height evolution yields

$$\frac{\partial h'}{\partial t} = \frac{\partial (h'u)}{\partial x} \ , \tag{3.42}$$

which represents the conservation of mass. A second equation can be found regarding the Navier-Stokes equations and using the viscous stress tensor. By additionally describing the continuity equation and the boundary conditions at the fluid surfaces in terms of the aspect ratio $\varepsilon = H_0/R_0$ and by taking into account higher orders of this terms, one can find the following equation. The detailed derivation of that equation for the conservation of momentum is attached in the appendix A.3 (gravitational effects and inertia are neglected).

$$0 = \gamma \frac{\partial^3 h'}{\partial x^3} + \frac{4\eta}{h'} \frac{\partial (u_x h')}{\partial x} \tag{3.43}$$

Based on the observations of Hack et al. [127] and the experimental results in thin liquid crystal films, self-similarity solutions of the form

$$h'(x,t) = kt^{\alpha}\mathcal{H}(\xi), \quad u(x,t) = \frac{k\alpha}{\theta} t^{\beta} \mathcal{U}(\xi) \quad \text{and} \quad \xi = \frac{\theta x}{kt^{\alpha}} \tag{3.44}$$

with the self-similarity functions $\mathcal{H}$ and $\mathcal{U}$ were introduced [119,127,149]. The parameter ξ was defined in the way that $h'(x,t) \approx \theta x$ reaches the static solution with a contact angle θ far away from the bridge. The additional variable k describes the bridge growth velocity $\mathrm{d}h'_b/\mathrm{d}t$. For the viscous regime, where h'_b is proportional to t during the first stage of coalescence, Hack et al. found $\alpha = 1$ and $\beta = 0$. With neglected inertia, the terms in equation 3.44 then reduce to

$$h'(x,t) = kt\mathcal{H}(\xi), \quad u(x,t) = \frac{k}{\theta}\mathcal{U}(\xi), \quad \xi = \frac{\theta x}{kt} \ . \tag{3.45}$$

By replacing the height $h'(x,t)$ and the velocity $u(x,t)$ in equations 3.42 and 3.43 by the reduced self-similarity equations 3.45, the following expressions can be found

$$\mathcal{H} - \xi\mathcal{H} - (\mathcal{H}\mathcal{U})' = 0 \tag{3.46}$$

$$\mathcal{H}\mathcal{H}'' + K_v(\mathcal{U}'\mathcal{H})' = 0 \ . \tag{3.47}$$

K_v represents the dimensionless bridge velocity that is defined as

$$K_v = \frac{4\eta k}{\gamma\theta^2} \rightarrow K_v = \frac{\mathrm{d}h'_b}{\mathrm{d}t}\frac{4\eta}{\gamma\theta^2} \ . \tag{3.48}$$

To solve the above equations, five boundary conditions are required and normalizing the bridge height at $\xi = 0$ yields

$$\mathcal{H}(\xi = 0) = 1, \quad \mathcal{H}'(\xi = 0) = 0, \quad \mathcal{U}(\xi = 0) = 0\,. \tag{3.49}$$

In addition, for large values of $\xi \to \infty$, i.e. for infinitesimally small times t or infinitely far away from the bridge $x \to \infty$, the symmetric solutions should match with an initial droplet situation. Thus, the equations 3.45 for the height and the velocity become time-independent for large ξ-values.

$$\mathcal{H}'(\xi \to \infty) = 1 \quad \text{and} \quad \mathcal{U}(\xi \to \infty) \propto C\log(\xi) \tag{3.50}$$

Here the matching condition for the contact angle at large distances from the bridge or for the initial droplet situation was used and for $t = 0$ the parameter C yields zero and a static droplet situation can be observed ($C = 0$).
Hack et al. solved the boundary condition problem numerically with a shooting method and found a value of $K_v = 2.21$ for the dimensionless bridge velocity [127].

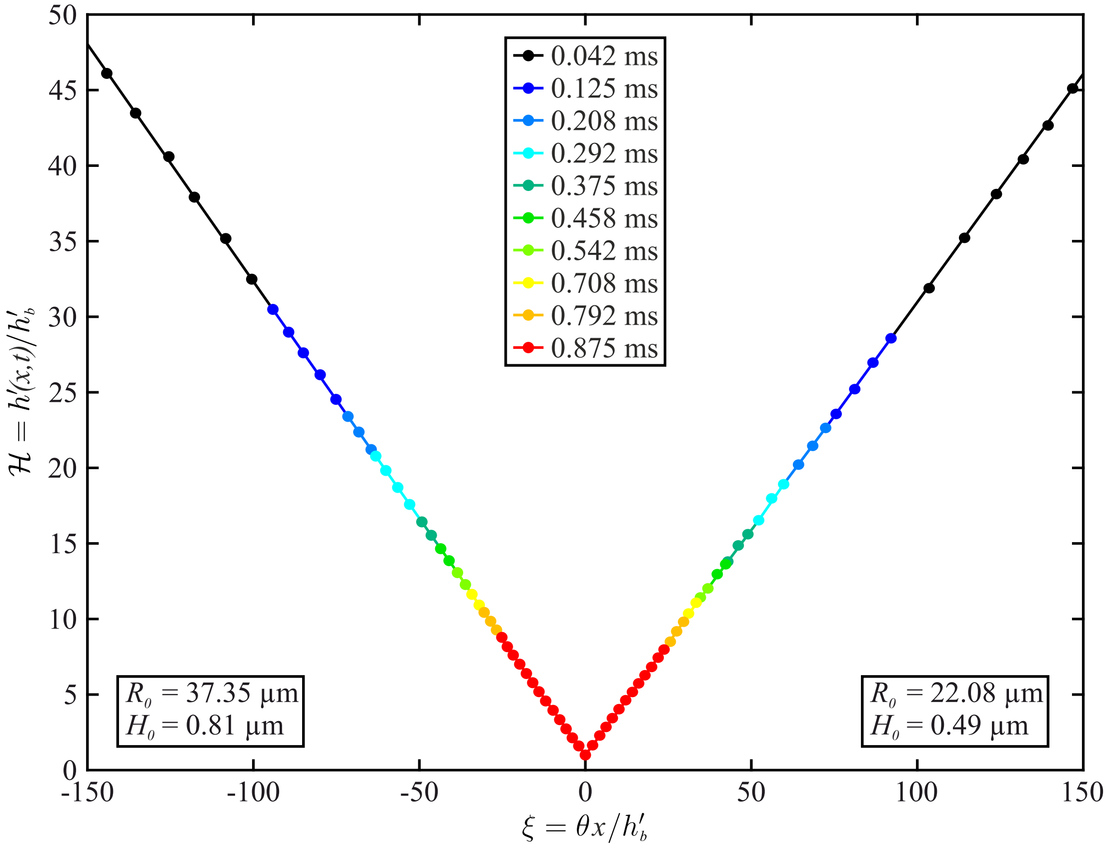

Figure 3.33: Scaled droplet height at different times t at the position of the connecting bridge ($x = 0$) in the experiment. The heights were measured along the axis connecting both droplet centers (cross-section). All curves collapse into a single curve, verifying the self-similarity of the height profile. The initial droplet heights and radii are given in the boxes on the individual side of the bridge. Different colors correspond to different moments of the coalescence process.

Figure 3.33 shows the scaled droplet height profile at the bridge position according to equation 3.45. It confirms the self-similarity behavior of the bridge profile for the initial stage of isotropic droplet coalescence.

Following the same procedure for the simulation, the scaled bridge height $\mathcal{H}$ was calculated and is presented in the left graph of figure 3.34. Within the simulation, equally sized droplets with initial radii of 50 µm and contact angles of 2.5°, comparable with the experimental results shown in figure 3.33, were used. Due to a significantly higher positional and temporal resolution in the simulation compared with the experiment, the curved bridge profile in the bridge center can be observed. For the experiment, the same steady curve is predicted.

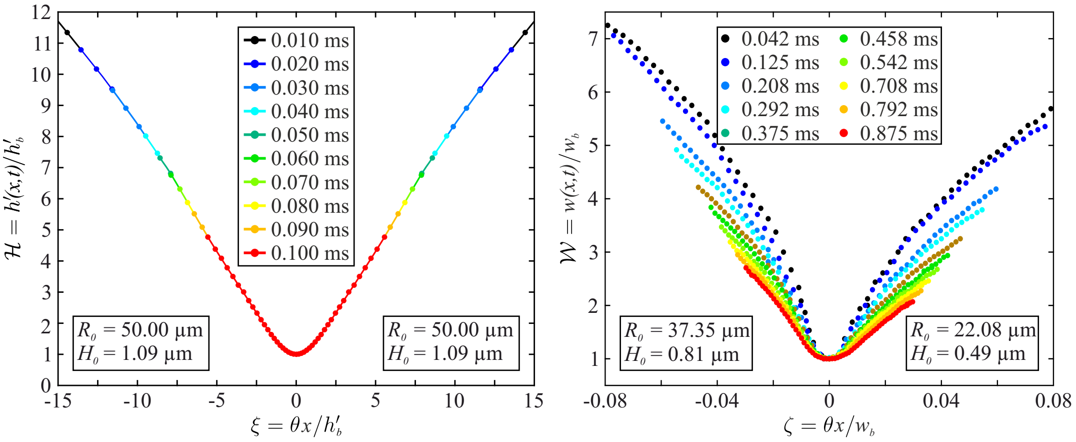

Figure 3.34: Scaled droplet height and width at different times t at the position of the connecting bridge ($x = 0$) in the simulation (left-hand graph) and the experiment (right-hand picture). The heights were measured along the axis connecting both droplet centers (cross-section). The droplet widths, representing the contact line between film and droplets, were determined in the film plane at $h' = 0$. The simulation again verifies the self-similarity behavior of the height profile. The right-hand picture shows the scaled width of the experimental data (calculated with the comparable scaling laws) and these curves do not overlap.

Since the bridge height h'_b as well as the bridge width w_b were measured in the experiment, a self-similarity behavior parallel to the film plane is also conceivable (right-hand graph in figure 3.34). Here, the scaling along the connecting axis of both droplets is the same as for the scaling of the bridge height. Therefore, the self-similarity function $\mathcal{W} = \mathcal{W}(\xi) = w(x,t)/w_b$ was introduced for the width profile. As visualized, the scaled bridge width at different times t do not overlap convincingly and thus no self-similarity behavior can be observed.

During the derivation of the self-similarity functions for the bridge height $\mathcal{H}(\xi)$, the dimensionless bridge velocity K_v was introduced (equation 3.48). Hack et al. solved the self-similarity functions numerically and found the shooting parameter to be $K_v = 2.21$ [127]. Since in the experiment droplets with different sizes and different contact angles θ were observed, it is possible to analyze the growth rate of the bridge depending on the contact angle. The growth rates of the bridge height and width were calculated from the

first moments of the bridge formations, which shows a linear increase (see figure 3.30). Figure 3.35 shows the growth rate of the bridge height depending on the contact angle, and a quadratic trend can be observed verifying the self-similarity functions. A dependence on the individual droplet sizes, visualized with different colors, was not found. For the experiment, the parameter K_v was calculated from the quadratic fit and yields a value of 0.162, which is at least one order of magnitude smaller than the predicted value from Hack et al. [127]. Once again, it verifies the discrepancy between the theoretical predictions / simulations and the experimental observations of a factor of ten or even more.
The inset of figure 3.35 represents the bridge growth rate from the FEM simulation with the same quadratic trend. Indeed, by fitting this curve, the dimensionless bridge velocity of $K_v = 2.21$ was found. It confirms the value found as shooting parameter [127].

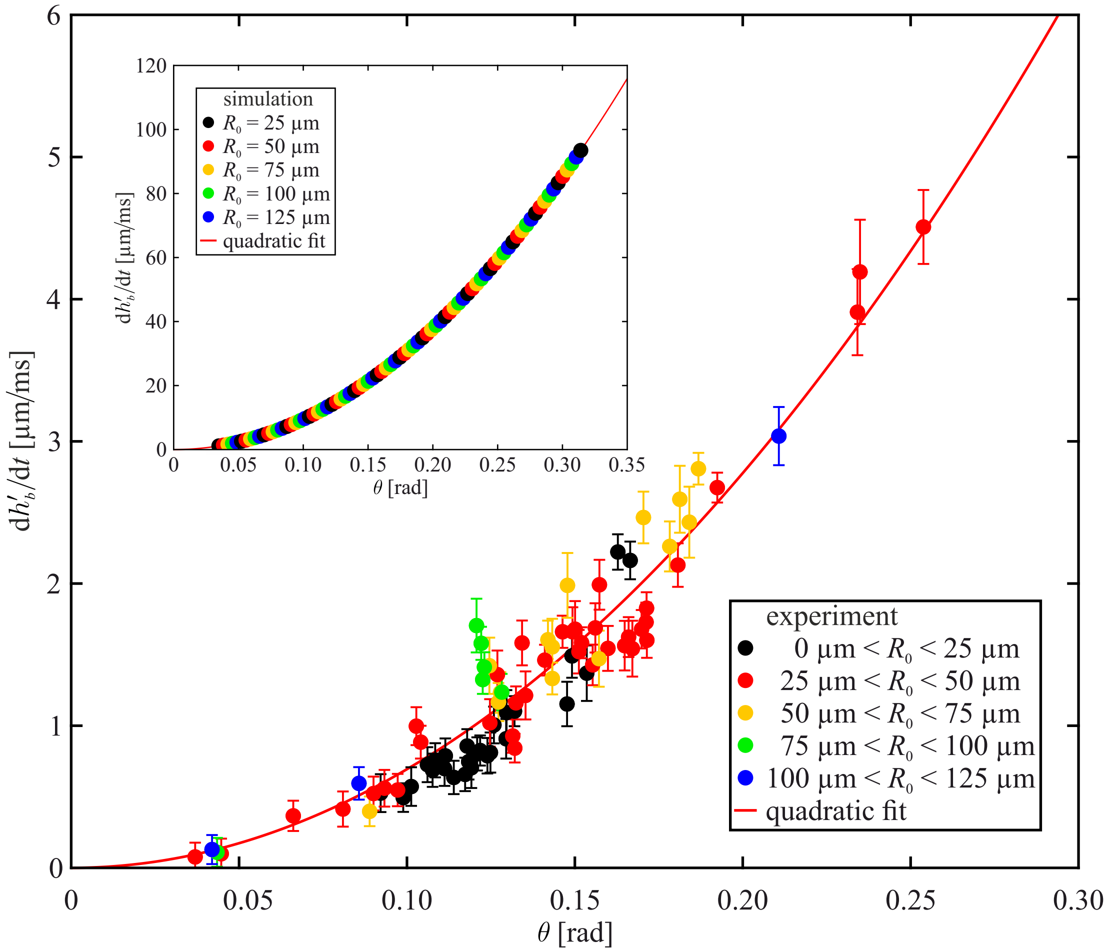

Figure 3.35: Growth rate of the bridge height h'_b depending on the contact angle θ. The bridge growth rate increases with increasing contact angle and follows a quadratic trend. From the red fitting curve, the parameter $K_v = 0.162$ was extracted. Droplets of different initial sizes were divided into individual groups (highlighted with different colors) to prove an additional size dependence. The inset shows the same physical feature determined from the simulation. Again, a quadratic behavior can be found and there is no dependency on the initial droplet sizes represented by the initial radii R_0. For the simulation the parameter K_v yields 2.21.

Analogously, the growth rate of the bridge width was measured and the results depending on the contact angle θ are shown in figure 3.36. Again, a quadratic trend is observed that is at first glance inconsistent with the theoretical predictions. The growth rate of the bridge height is defined as

$$\frac{\mathrm{d}h_b'}{\mathrm{d}t} = \frac{K_v\gamma}{4\eta}\theta^2 \tag{3.51}$$

and under the assumption of a constant contact angle θ and the equation for the bridge height $2h_b' = w_b\tan(2\theta)$, the growth rate of the bridge width yields

$$\frac{\tan(2\theta)}{2}\frac{\mathrm{d}w_b}{\mathrm{d}t} = \frac{K_v\gamma}{4\eta}\theta^2 \; . \tag{3.52}$$

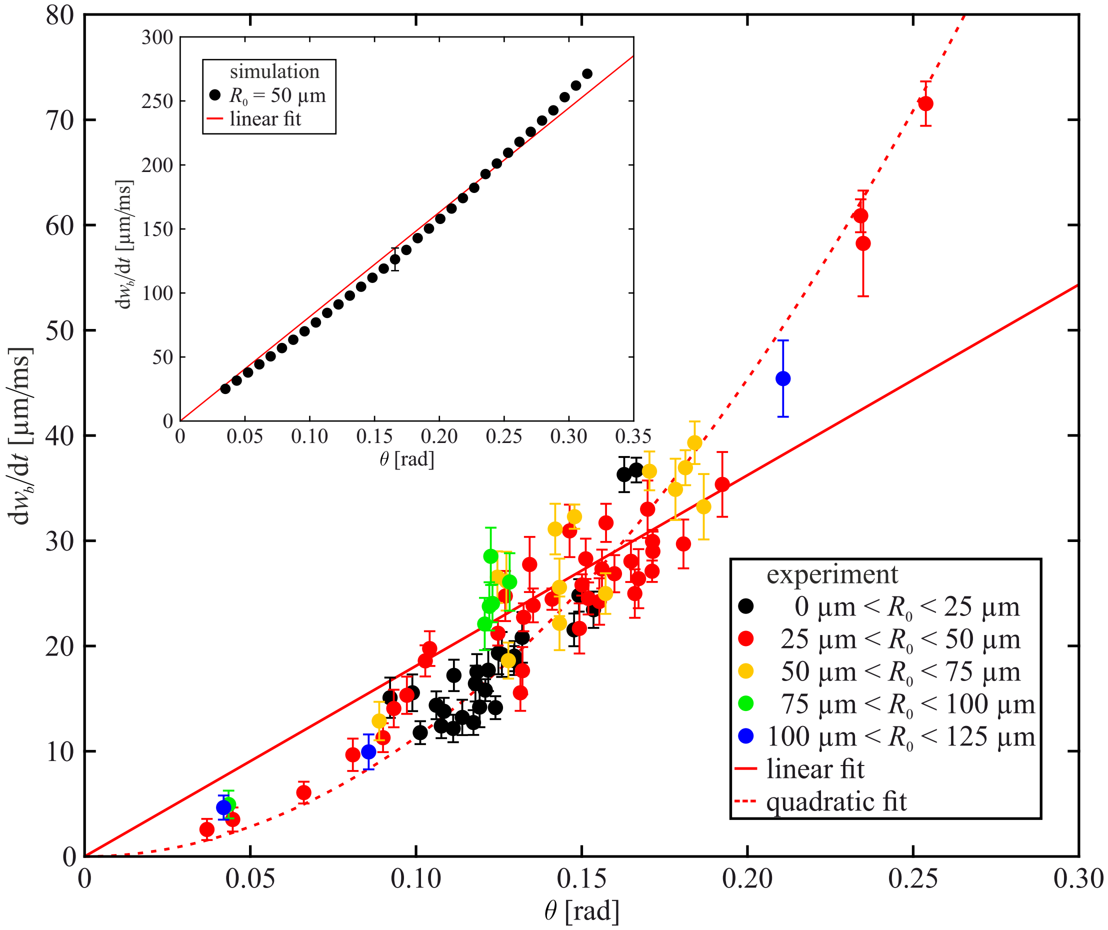

Figure 3.36: Growth rate of the bridge width w_b depending on the contact angle θ. The bridge growth rate increases with increasing contact angle and seems to follow a quadratic trend (red dashed line $\mathrm{d}w_b/\mathrm{d}t = 1.13$ m/s rad^{-2} θ^2). For comparison with the simulation and with regard to equation 3.53, the data points were additionally fitted with a linear curve (red solid line). The curve with a slope of 0.18 m/s rad^{-1} does not convincingly represent all the data. Again, no dependency on the initial droplet radii R_0, visualized with different colors, was observed. The simulation does not follow the quadratic trend. Instead, the bridge width growth rate increases almost linearly. The slope for the simulated curve was calculated to 0.82 m/s rad^{-1}.

For small contact angles θ, $\tan(2\theta) \approx 2\theta$ can be assumed and the bridge width growth rate then depends only linearly on the contact angle.

$$\frac{\mathrm{d}w_b}{\mathrm{d}t} \approx \frac{K_v \gamma}{4\eta}\theta \tag{3.53}$$

This predicted linear trend, in first approximation, is represented by the results from the simulation (inset of figure 3.36) and with the slope of this curve the dimensionless velocity parameter could be calculated to a value of $K_v \approx 1.91$. For the experiment, the linear dependence of the width growth rate on the contact angle could not be verified. On the contrary, the data seem to follow a quadratic trend.

Apparently, the assumption of a constant contact angle during the whole merging process is not valid for the experiment. For this reason, the contact angle during coalescence in dependence of the position was analyzed in more detail. Since the droplet surfaces are curved and thus also the contact line with the film is curved, the height profile normal to the droplet edge was used to calculate the correct contact angle. At the position of the bridge, the width and the height, respectively, were used to determine the contact angle for each time step.

The upper graph of figure 3.37 shows such a temporal evolution of the contact angle at the bridge position. Within the experimental resolution, the contact angle in the first moments decreases and the droplet profile seems to be approximately 30% flatter ($\approx 1.5°$) than in the initial stage with the initial and static contact angle θ. After approximately 1.5-1.6 ms, the contact angle then finally reaches the static angle similar to the initial contact angle. The trend of the contact angle curve is comparable to that of the bridge evolution, where a slight decrease of the bridge height was observed during the first moments of coalescence (see figure 3.18 in section 3.3.2). When the contact angle reaches its final value, the coalescence process is almost completed.

For the given droplet sizes in figure 3.37 and an initial angle of 8.1°, the coalescence time t_{coal} is calculated as 1.6 ms.

For the moment of the highest deviation of the measured contact angle from the static contact angle (highlighted in the upper graph of figure 3.37 at $t \approx$ 0.54 ms), the contact angle was measured depending on the position along the whole droplet edge. The lower image of figure 3.37 shows the droplet edge $w(x)/2$ and the initially circular shape (red dotted) of the droplets before forming a bridge (left-hand ordinate axis). The blue data points refer to the right-hand ordinate axis and represent the contact angle at the respective position. The region around the bridge, where the droplet edge deviates from the circular shape, also marks the region of decreased contact angle. Outside this region, the contact angle matches the static contact angle, while at the bridge position it decreases to about 70% compared to the contact angle far away from the bridge.

The discussion of this observation and a possible explanation will follow in the next section.

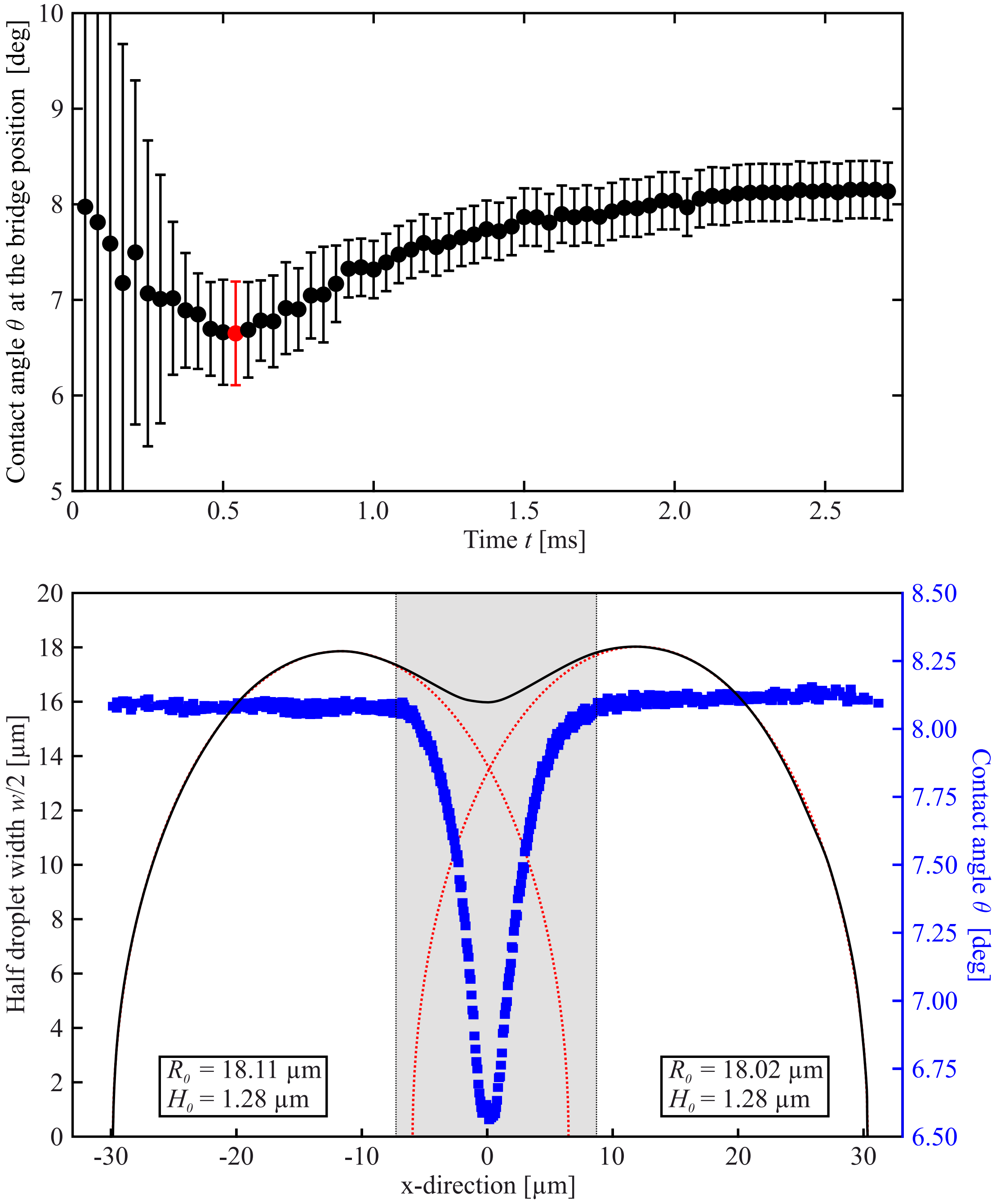

Figure 3.37: Change of the contact angle during coalescence. The upper graph shows the contact angle at the position of the bridge determined from the bridge width w_b and bridge height h_b' for the entire merging process. It first decreases by approximately 1.5° before finally reaching a static contact angle. For the time with the highest deviation from the static contact angle (highlighted in red, $t \approx 0.54$ ms), the contact angle along the droplet-film contact line is presented in the lower graph. The edge of the droplet (black curve) as well as the contact angle normal to the edge (blue data points) depending on the position along the connecting axis $w(x)/2$ and $\theta(x)$ are shown. The region of the bridge, where the measured droplet edge deviates from their initial circular shape (red dotted lines), is highlighted. Especially in this region, the contact angle strongly drops off the static contact angle observed far away from the bridge.

3.5 Summary and discussion

The shape evolution of merging isotropic droplets in free-standing smectic liquid crystal films can be excellently described with a model on the basis of the lubrication approximation and the thin sheet equation. It was shown that in contrast to sessile droplets, there should be no flow velocity gradient normal to the film plane and therefore the scaling characteristics changed between these systems. A linear dependence of the coalescence time on the aspect ratio $t_{\mathrm{coal}}/R_0 \propto R_0/H_0$ was found. Numerical simulations for sessile droplets and droplets in thin films confirmed the new scaling law.
The experimental system with isotropic droplets appearing near the clearing point of the smectic material allows the contact angle θ of the droplets to be varied by slightly changing the temperature of the system in the vicinity of the phase transition temperature (51.1 °C). In this way, very flat droplets with contact angles around 2° were created, but also comparatively thick droplets with contact angles of more than 14° were possible. The experiments with different initial droplet sizes showed a dependence of the coalescence dynamics on the contact angle. A scaling of the bridge width $w_b/\langle 2R_0\rangle$ and the scaled time t/τ_0 (see figure 3.26) showed an overlap of all experimental curves. The graph presented again confirms the new scaling law derived from the lubrication approximation.
The evolution of the bridge width $w_b \propto t$ and height $h'_b \propto t$ both show a linear increase in the early stage before saturating and reaching the final droplet size. It is in perfect agreement with the model by considering material flow only parallel to the film plane. The linear increase additionally agrees with experiments by Hack et al., who found the linear regime for highly viscous materials [127].
The self-similarity behavior of the bridge profile was verified by different experiments [108, 119, 127, 140], and the present investigations confirmed this phenomenon also for droplets in thin liquid crystal films. Due to a very high temporal (24,000 pictures/second) and lateral resolution regarding the interferometry technique, the self-similarity solution could be found over a long time range and with an excellent agreement. Additionally, the bridge growth rate $\mathrm{d}h'_b/\mathrm{d}t$ was determined and showed the predicted quadratic dependence on the contact angle θ. The FEM simulation verified the self-similarity behavior itself and the predicted shooting parameter $K \approx 2.21$.

The scaling behavior of the experimental data is in very good agreement with the theoretical predictions of the thin sheet approximation. In comparison with the simulations, it turns out that there is a strong discrepancy between the model and the experiment regarding the coalescence time. The merging process of isotropic droplets in a free-standing smectic film is at least one order of magnitude slower than expected. For a droplet pair with initial radii R_0 of 20 µm and initial heights H_0 of 1.5 µm, the theoretical characteristic coalescence time τ_0, for example, yields 0.15 ms, but 1.66 ms was measured experimentally. This tendency was measured for all droplet sizes and contact angles and by fitting the measured and scaled coalescence time t_{coal}/R_0 in dependence of the droplet aspect ratio with a linear curve (figure 3.25), the slope of the curve was calculated. From the slope of that curve, the capillary velocity of the material can be estimated and again a factor of 10 between the model expectations and the experiment was found. Finally, this trend of the measured coalescence dynamics deviating from the predictions was also observed with regard to the self-similarity behavior. In particular, the growth rate of the bridge (figure 3.35) indicates a discrepancy between liquid lenses and isotropic droplets in free-standing smectic films, but also a deviation from the theoretical model.

It is assumed that the surface tension γ and the shear viscosity η of the material mainly determine the coalescence dynamics and thus the coalescence speed. Due to the high temporal and spatial resolution in the experiment, it is unlikely that this discrepancy arises from uncertainties during the measurements. The physical parameters ($\gamma = 0.024$ N/m, $\eta = 0.014$ Pa s) were measured and confirmed in various experiments (see section 2.2.2). A comparison with other liquid crystal materials forming a smectic phase at room temperature verifies the measured parameters (for 8CB: $\gamma = 0.025$ N/m at 35 °C, $\eta = 0.035$ Pa s at 33.5 °C [143]).

Nevertheless, there are several possible approaches to explain the experimental observations. First, the ambient air, that could influence the merging dynamics, was neglected in the model. According to the model of Saffman and Delbrück (section 2.1.2), the flow of isotropic material during coalescence could cause a flow of the surrounding air as well. Within a simple approximation of a circular object with a height comparable with the bridge height in the first moments, the Saffman length would roughly yield $L_S \approx 50...5000$ µm. For the coalescing droplets and the surrounding flow, the situation becomes more difficult and a quantitative estimation of the influence of the air cannot be made. Anyhow, the experiments of Hack et al. [127] with water as subphase, with a much higher viscosity than air, showed no influence by the outer medium. For coalescing spherical droplets, Paulsen et al. analyzed the early stages of the merging dynamics and found only a little influence even for outer fluids with considerably higher viscosity than that of the droplets [109]. Overall, the surrounding air in the coalescence experiments in free-standing smectic films and their effect on the dynamics seems to be of less importance only.

A second and perhaps more plausible approach might be to take into account the smectic layers covering the isotropic droplets. These thin smectic layers are unique for the analyzed system, and the influence of that covering material is not considered in any model. In freely suspended liquid crystal films, different structures as smectic holes or islands can be found, and it is known that these objects can be created by an external change of the film surface area. During the expansion or compression of smectic films, the initially and perfectly ordered layered structure undergoes a quick reorganization of the molecules and layers. On the one hand, holes can be torn into the upper layers when the film is stretched and the film area is increased. Thus, the layers have to rearrange and dislocations have to be created or relocated [27]. On the other hand, additional smectic layers and thus dislocations can be created when the film is compressed and the surface area is decreased [21, 28, 34]. In both cases, additional energy is required to dislocate, create or remove dislocations and rearrange the smectic layers. That energy has to be provided by the surface energy reduction, mainly. For very fast processes like the collapse of catenoid-shaped smectic films and the subsequent formation of smectic bubbles and their lateral compression, also the formation of bulges, extrusions and wrinkles was observed. In that cases, the film area remains constant, and the effective surface tension is strongly reduced or almost zero [21, 26, 28, 34].

During the coalescence of isotropic droplets with their covering smectic layer, the smectic surface has to be reduced and indeed a decrease of the surface tension can be expected. Nevertheless, the effect of such a surface reduction should depend on the sizes of the coalescing droplets: it should be more relevant for larger droplets than for smaller ones. In particular, the discrepancy between the model and the experiment in terms of the coalescence dynamics, the bridge growth rate and the coalescence time should increase with increasing droplet size. Such a tendency could not be observed in the experiments.
The images in figure 3.38 sketches two possible scenarios to rearrange the mesogens of the liquid crystal material: the molecules can form an additional smectic layer (left image) or lose their positional and orientational order and move into the isotropic phase of the droplet (right-hand image).

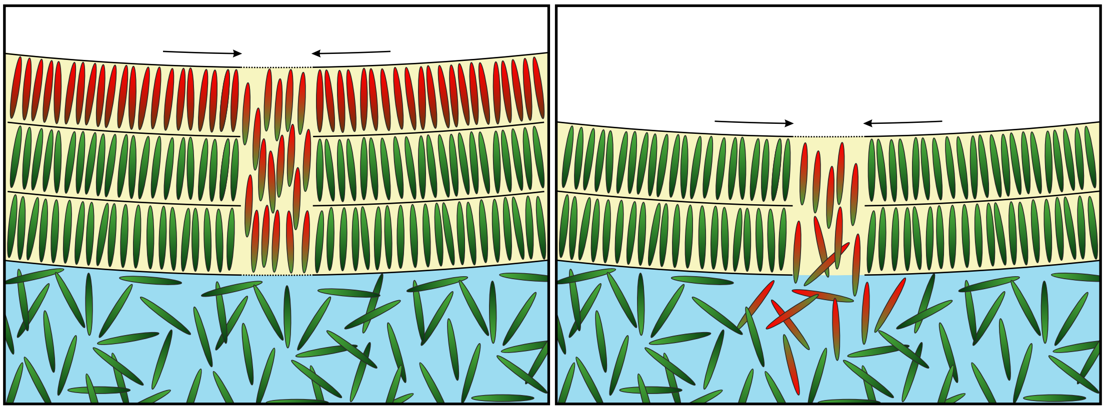

Figure 3.38: Sketch of the assumed smectic layers that cover the isotropic droplet (light blue background) at the position of the bridge. A reduction of the surface cannot be compensated by a simple displacement of the smectic material, but by creating additional smectic layers (red molecules in the left image). On the right-hand side, parts of the compressed smectic layers melt, i.e. the red marked molecules lose their positional and orientational order and move into the isotropic phase.

For both cases of molecule reorganization shown in figure 3.38 it is not straightforward to calculate the required energy, but for the melting of smectic layers into the isotropic phase, the melting enthalpy can be used. Within a rough approximation given in appendix A.4, the properties of the well known liquid crystal material 8CB (4-cyano-4’-octylbiphenyl) are used to calculate the melting energy per surface area. For a single smectic layer thus an energy per surface area of approximately 0.0091 N/m and for two layers covering the droplets 0.0182 N/m is required.
Although it is only a rough approximation and not the exact physical parameters of the liquid crystal mixture are used, the energy per surface area is in the order of magnitude of the static surface tension $\gamma = 0.024$ N/m. From this estimation, it seems conceivable that an effective and reduced dynamic surface tension causes the discrepancy of the coalescence dynamics. A reduced dynamic surface tension could also explain the change of the contact angle at the position of the bridge during coalescence, depicted in figure 3.37. However, the decrease of the contact angle in the vicinity of the bridge could also be

explained by the flow of material through respectively within the bridge. Since the flow velocity cannot be measured in the experiment, it was determined from the simulation to have a maximum value of 0.14 m/s during the first stage of the merging process. With a density of the mixture of about 1000 kg/m^3 taken from 8CB [143], the Bernoulli pressure can be calculated and yields $p_{\mathrm{Bernoulli}} \approx 10$ Pa. This additional pressure component would cause a slight flattening of the bridge height, resulting in a maximum contact angle reduction of 0.2°. The flow of the isotropic material in the bridge and the resulting Bernoulli pressure can not sufficiently explain the drop in the contact angle observed in the experiments.

An additional FEM simulation and the resulting bridge height as a function of time are shown in figure 3.39 for the static surface tension γ_{stat} and with a decreased dynamic surface tensions γ_{dyn}. From the comparison of the experimental data with the simulated curves, an effective dynamic surface tension was found, that would reproduce the observed coalescence dynamics quite well. As shown in the figure 3.39, a surface tension of $\gamma_{\mathrm{dyn}} = 0.0021$ N/m was used. This is in very good agreement with the energy reduction caused by the layer melting (static surface tension reduced by the melting energy per surface area).
However, no direct measurement of the effective surface tension has been reported so far, so it is not possible to fully prove this explanation.

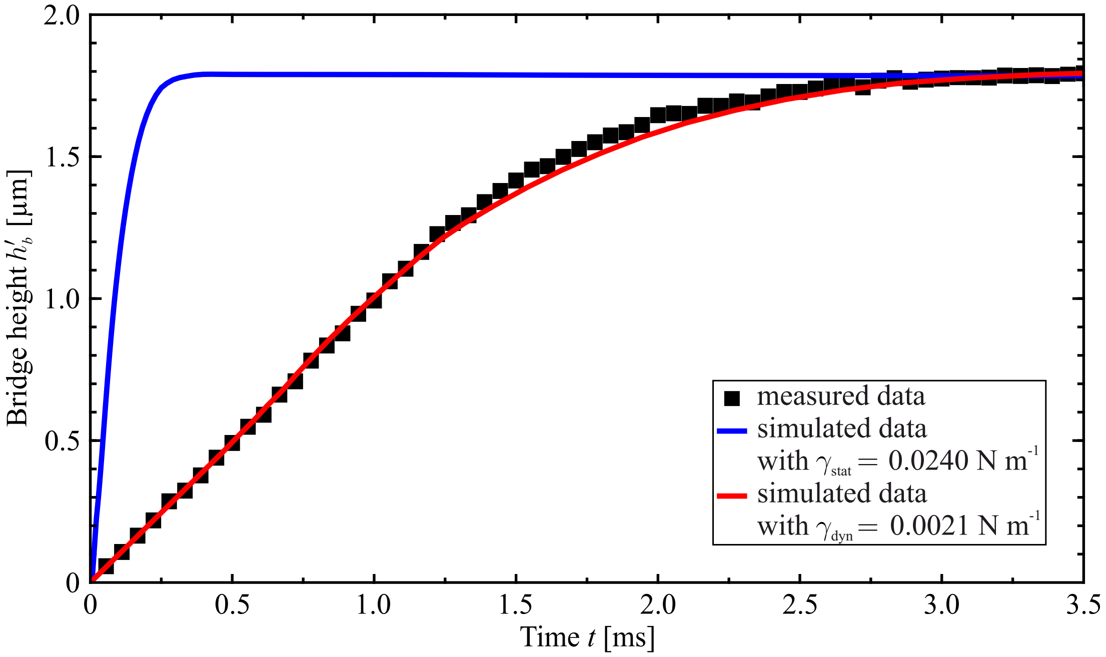

Figure 3.39: Measured bridge height depending on time in comparison with the numerical simulation. The simulation with the static surface tension γ_{stat} measured in previous experiments $\gamma_{\mathrm{stat}} = 0.024$ N m^{-1} (blue curve) does not agree with the determined bridge height. The same simulation, but with a much smaller dynamic surface tension γ_{dyn} (red curve), reproduces the experimental data points quit well.

The coalescence of isotropic droplets in free-standing smectic films was analyzed in detail, and the results of that unique system were compared with sessile droplets as well as with liquid lenses on a liquid surface. The model based on the lubrication approximation and the thin sheet equation qualitatively describes the observed coalescence dynamics. The FEM simulation with the derived equations confirmed the model. It is shown that merging isotropic droplets exhibit self-similarity behavior and again the simulation confirmed the experimental results.
The deviations of the coalescence dynamics between the model/simulation and the experiment of one order of magnitude seem to be explicable with regard to the smectic layers covering the droplets.

In order to prove the possible explanation, additional experiments with different materials of known viscosity, density and surface tension could be performed. Furthermore, the coalescence of nematic droplets in smectic films would encourage the understanding of coalescing objects in two dimensions itself and the influence of the smectic layer structure on top of the isotropic or nematic droplets.

4 Coarsening dynamics in quasi-two-dimensional emulsions

In general, coarsening describes the process of aging of different two- or multiphase systems and the effect on the stability or composition of such mixtures. While the overall number of immersed objects like solid particles or liquid droplets normally decreases with annealing time, their average size will increase. As a result, in most systems such as foams or emulsions, a more coarse arrangement of objects can be observed.

Coarsening dynamics are of common interest for various industrial and technological applications, therefore a detailed understanding of this process in both three and two dimensions is necessary.

In the present experiment, performed onboard the ISS during the OASIS mission, emulsions consisting of micrometer-sized smectic islands of different size were observed for several minutes and hours to verify coarsening dynamics. Crucial parameters for the characterization of the aging process are identified and analyzed in detail. The experimental results are compared with three-dimensional systems and deviations from the predictions are discussed. The results in this chapter are unpublished and preliminary results, since the analysis of the experimental data is still ongoing. A publication of the results is in progress. All necessary physical quantities are redefined in this chapter.

4.1 Introduction

As part of the OASIS mission, long-term experiments were performed to analyze for example droplet-droplet interactions and their arrangement in lattice-like structures (chapter 2). On the other hand, also ensembles consisting of smectic islands or holes, that do not form regular structures, are observed to understand their long-term behavior. Over time, the size of smectic islands and holes changes or different objects merge, thus the average object size of the emulsion will increase. As a consequence, several small islands or holes will disappear and the total number of objects is expected to decrease. This phenomenon, mainly defined by direct object coalescence or material diffusion through the background medium, is described by the coarsening dynamics of a mixture or an emulsion.

The process of coarsening or aging can often be observed in two- or multiphase mixtures, where objects of one component of different sizes are dispersed in another, usually liquid phase. Due to the tendency of the system to decrease the total interfacial area and hence the total free energy, the mixture will change its composition in the way that the size and the number of objects or embedded droplets will change. As the mixture evolves, small objects shrink while larger objects increase in size, and as a result the average particle size increases over time. At the same time, and with regard to the conservation of mass, the total number of objects can decrease over time. A consequence of this aging process is often a segregation and phase separation of the components of the mixtures.

Phase separation, but also its prevention in different emulsions and foams, is of general interest for various industrial and technological applications. It is important to know the crucial parameters for coarsening to stabilize for example milk, heavy cream, cosmetic creams as well as fire-fighting foams and shaving foams. With a detailed understanding of the overall aging dynamics and its different processes (in general coalescence of objects and Ostwald ripening), it is possible to control the size of the immersed objects through liquid-solid transitions, chemical reactions or treating droplets with surfactants [150].

A significant industrial process based on coarsening of objects is the sintering of metal powders into solid materials. Typically, ceramics, heavy metal alloys, hard metals and structural parts for automotive applications are created by liquid phase sintering. An initial melting of one of the phases and a following rearrangement and dissolution of the second phase due to alloying leads to unique material properties and significant shape accommodations of the new material [151, 152].

In 1900, the later Nobel Prize winner Friedrich Wilhelm Ostwald published his studies about the dependence of the solubility of small mercury oxide particles on their radii. He explained his observation with the higher vapor pressure in smaller droplets than in bigger ones, and so this phenomenon later was called “Ostwald ripening” [153]. A detailed theoretical description for this coarsening process was given by Lifshitz and Slyozov [154] and Wagner [155] in 1961. They supposed a steady diffusion flux from smaller droplets to larger ones also known as evaporation-condensation. They described the evolution of the average particle size and the particle size distribution and their predictions later were verified [156–158]. The transfer of material between droplets in their model (LSW-model) is based on material diffusion through the surrounding liquid [159–163]. As shown in the left picture of figure 4.1, no direct droplet-droplet contact is required and, as a result of the Ostwald ripening, the initially bigger droplet grows in size while the other one shrinks until it finally disappears.

The second mechanism, that results in an overall coarsening of mixtures, is the extensively discussed coalescence of particles or droplets. As shown in the previous chapter and in the right picture of figure 4.1, the objects are initially in direct contact and merge within seconds or even milliseconds to a single bigger particle.

It was observed that in the early stage of coarsening of mixtures, the growth of domains and objects can be described by Ostwald ripening, while the late stage often is dominated by interface-tension-driven coalescence of the particles [164, 165].

The observed coarsening dynamics with the measured particle size distribution and evolution additionally depends on the geometrical system [150, 166–168], the components of the mixture and possible side effects such as drainage, sedimentation or applied thermal gradients [169–173].

Within the following sections, the most commonly investigated systems where coarsening occurs are introduced and typical experiments and their results for three-dimensional mixtures, foams and two-dimensional emulsions are presented.

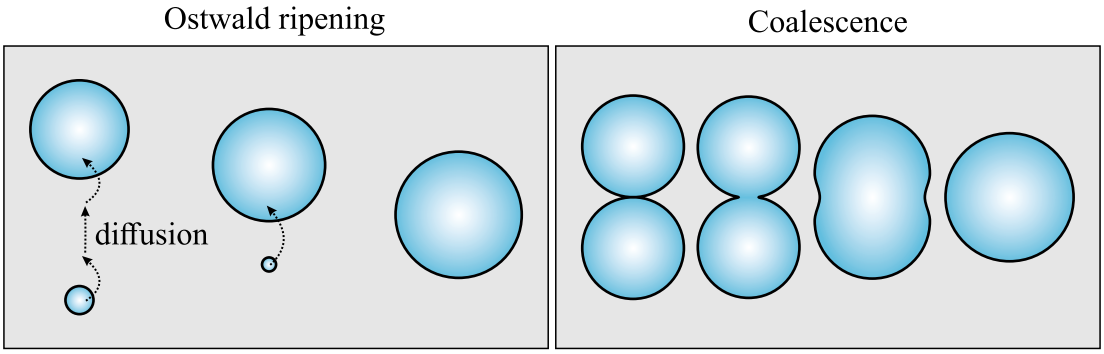

Figure 4.1: Sketch of the two main processes that are responsible for coarsening. While for Ostwald ripening on the left side there is no need of direct droplet-droplet contact and material is exchanged through the background medium, the droplets at the right-hand side are in direct contact and merge within seconds or even milliseconds. Although the droplets must first approach each other by diffusion before coalescence, Ostwald ripening is expected to occur on much longer timescales [174]. In both cases, the result is a larger droplet compared with the initial droplet sizes.

4.1.1 Coarsening of three-dimensional two-phase mixtures

Coarsening and phase separation are encountered in everyday life, but especially in the manufacturing process of new alloys and dispersions it is important to understand all aspects of the aging process depending on the initial conditions of the system.
When using different metals to create new materials, the raw materials usually have different densities and therefore often show a rapid spatial phase separation due to sedimentation. Already in the 1980th, Ratke et al. tried to solve this sedimentation problem in their zinc-lead mixture (Zn-Pb) with experiments under microgravity conditions onboard the Spacelab 1 space station. They measured particle size distributions, verified Ostwald ripening, and observed additional coarsening effects due to coagulation with increasing volume fraction [175]. Later, Ratke performed additional experiments on the EURECA satellite to confirm his observations, and he stated that coarsening, at least of alloys, is a superposition of diffusional Ostwald ripening and a coalescence of droplets (here initiated by Marangoni motion due to thermal gradients) [151, 176].

It was shown in various experiments that the volume fraction of the mixture components significantly influences the coarsening dynamics and especially the coarsening rate K and the particle size distributions. Hardy and Voorhees [157] for example analyzed tin-lead mixtures (Sn-Pb) and predicted an evolution of the average particle size $\langle R \rangle$ of the following form:

$$\langle R(t) \rangle^3 = \langle R(0) \rangle^3 + Kt \ . \tag{4.1}$$

The coarsening rate $K = K(T, D, \phi)$ here depends, among other quantities, on the temperature T, the liquid diffusion coefficient D and the volume fraction ϕ. Within their experiments, they were able to avoid direct particle-particle interaction (coalescence) often observed in liquid-liquid mixtures by using sufficiently low volume fractions of the coarsening phase. As one main result, they found that the particle distribution function broadens with increasing time, as shown in the left-hand graph of figure 4.2. Furthermore, they were able to scale these distribution functions at different times with the average particle size (here the particle intercept length L) and observed an overlap of all scaled curves. This result can be seen as a time independence of the distribution function scaled with the average particle size [157].

Hardy et al. [157] measured the coarsening rate K from a linear plot of $\langle L\rangle^3$ respectively $\langle R\rangle^3$ versus time t in the early stages of their experiments and observed increasing coarsening rates with increasing volume fraction of tin ($\langle L\rangle \propto \langle R\rangle$).

The second important results from their experiments describes the average particle size observed over more than three orders of magnitude in time. They verified the theoretical prediction of $\langle R\rangle \propto t^{1/3}$ [157]. The dependence of the average particle size on time for a volume fraction of $\phi = 0.64$ of tin is schematically shown in the right-hand graph of figure 4.2.

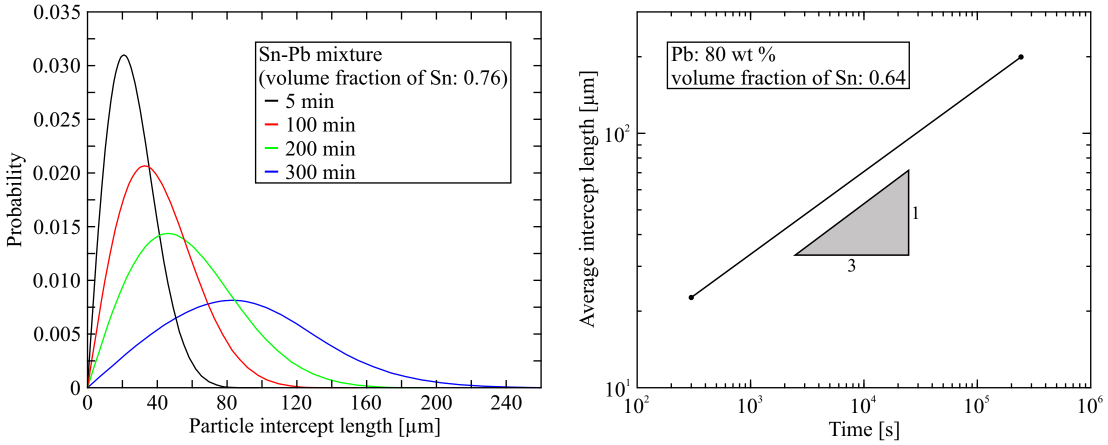

Figure 4.2: Particle intercept length distribution at different times and average particle size as a function of time for a tin-lead mixture (Sn-Pb) based on the experiments and results of Hardy and Voorhees [157]. The Weibull distribution in the left graph widens with increasing time, verifying the coarsening process in the system. For the overall time evolution of the average particle size (right picture), the predicted theoretical dependence $\langle L\rangle \propto t^{0.33}$ was observed. All curves are reproduced, approximated and interpolated from the experimental results of Hardy and Voorhees and from the theoretical predictions. The curves qualitatively represent the results from Hardy et al. [157].

While Hardy and Voorhees focused their experiments and theoretical description on Ostwald ripening and mostly neglected direct droplet-droplet interactions, Tanaka later tried to analyze this second coarsening mechanism in particular [177, 178]. He investigated binary fluid mixtures of two different oligomers and used temperature quenches to trigger the spinodal decomposition and coarsening dynamics in thin sandwich cells. Tanaka observed an “unusual droplet coarsening” [177], where the droplet collisions are not random, but triggered by other droplet collisions and the interaction between droplets through the diffusion field surrounding them. A detailed theoretical description and a comparison with different models of that temperature quenching effect on fluid mixtures was given by Otto et al. [169]. Additional theoretical works and simulations regarding the surface-tension driven coarsening and different types of the Cahn-Hillard equation followed from Kohn et al. [179] and Watson et al. [180].

With increasing interest in liquid crystal materials in the 1990th, also new systems for studying phase-separation in fluid mixtures and therefore coarsening were used. Chuang et al. and later Pargellis et al., for example, analyzed the coarsening dynamics of line defects in nematic liquid crystal phases and noted a dependence of the coarsening rate from the temperature and the pressure in the system [181, 182]. More than ten years later, Thakur et al. created a liquid crystal mixture in the isotropic phase containing of 4-octyloxy-4'-cyano-6-biphenyl (8OCB) and up to 10 wt % of an isotropic dopant. While cooling the mixture across the isotropic-nematic transition temperature, they observed the nucleation of nematic droplets and a subsequent coarsening dynamics of those droplets [183]. They investigated the self-propelled motion of the nematic droplets due to concentration gradients of the isotropic dopant (Marangoni flow) and found growth rates of the droplet sizes following $R(t) \propto t$ when cooling and quenching the system. In contrast to coarsening due to diffusive coalescence or evaporation-condensation (Ostwald ripening) with $R(t) \propto t^{1/3}$, the induced Marangoni flow appears to enhance the coarsening process and as a consequence the phase separation, at least for this mixture of ordered and disordered fluids [165].

Additional numerical simulations with regard to the effect of the Marangoni flow, interface-tension driven coalescence or Ostwald ripening have been performed by Shimizu et al. and Khedr et al. in recent years [150, 184].

4.1.2 Coarsening of foams

A second class of material mixtures where coarsening can be observed are foams, which are characterized by a dispersion of gas bubbles in a relatively small volume of liquid. In general, foams can be divided into two classes depending on the content of the liquid phase in respect to the gas phase: wet foams with relatively high proportion of liquid ($> 26\%$) and dry foams with liquid contents below that value. In dry foams, polyhedral cells separated by thin walls that meet at the Plateau borders are found, and the coarsening dynamics are dominated by a gas diffusion through these walls. In contrast to that, wet foams consist of spherical inclusions of gas immersed in a liquid medium and the exchange of material between the inclusions and the resulting coarsening is characterized by Ostwald ripening, where the gas molecules have to diffuse through the background medium between inclusions [168].

Although foams with the gas bubbles separated by Plateau borders have a completely different structure than the previously mentioned three-dimensional mixtures with their liquid droplets distributed in a liquid medium, the scientific interest of foam aging also starts in the field of metallurgy and alloys. Cyril Stanley Smith, for example, analyzed in 1952 the evolution of two- and three-dimensional soap froth to explain and model the grain growth in metals. He observed a continuous disappearance of small cells and concluded that the average area of a cell or bubble should be a linear function of time $\langle A \rangle \propto t$ [185]. Later, Aboav et al. again analyzed the evolution of 2D soap foam and even used the

data from Smith and refuted his claimed linear cell growth: they observed an increase of the cell area with the square of time $\langle A \rangle \propto t^2$ [186]. Later, Weaire et al. confirmed the initially observed linear growth of the mean cell area. Further Monte Carlo computer simulations made by Wejchert once again yield exponential dependencies with exponents between 0.82 and 0.98 ($\langle A \rangle \propto t^{0.82 \ldots 0.98}$), verifying the linear dependence [187].
These early investigations show that coarsening of foams is an important phenomenon not only for modeling grain coarsening of metals, but also to understand the stability of industrial foams (shaving foams, fire-fighting foams) and to avoid complete phase separation.

Regarding to the aging process of dry foams, Glazier et al. observed two temporal regimes depending on the initial structure of the foam. They found a crystalline order at the beginning (transient regime) and power law growth of the average bubble area with $A \propto t^{0.59}$ in the disordered state (long-term regime). They analyzed the crossover between these transient and long-term regimes and noticed deviating results for different initial conditions (initially ordered or disordered system) [188]. Glazier et al. verified the Von Neumann's law, which describes the evolution of two-dimensional soap froths as a pure diffusive process only depending on the geometrical structure of the lattice [189].
Within this simple model, Von Neumann assumed an incompressible gas in the cells of dry foams and a gas transfer that is direct proportional to the wall area and the pressure difference respectively the curvature of the walls. For all cell walls meeting in 120° angles, he claimed that the growth rate for a fixed number n of walls is constant.

$$\left\langle \frac{\mathrm{d}A_n}{\mathrm{d}t} \right\rangle = \kappa(t)(6-n) \tag{4.2}$$

Several years later, Trittel et al. used a smectic liquid crystal material (8CB) to create two-dimensional dry foams. They observed three different regimes during foam evolution, and they also confirmed Von Neumann's law describing the growth rate of the cell areas [168]. Experimental images of the smectic foams and a sodium dodecyl sulfate foam (SDS) are shown in figure 4.3. Both materials show a similar foam structure with cells separated by thin Plateau borders (dry foam), but the coarsening of the foams occurs on different time scales. Nevertheless, for 8CB and SDS foams, the linear growth of the average cell area according to $\langle A \rangle \propto t^{\beta}$ with $\beta \approx 1$ was verified [190].
Due to the two-dimensional geometry of the experiments by Trittel, but also by Marchalot et al. [191], drainage of foams, i.e. the flow of liquid material through the Plateau borders between cells, is not considered in their analysis. Notwithstanding, this effect in foams was intensively studied by Hilgenfeldt et al., who observed a kind of competition between drainage and coarsening resulting in different dynamics of foam evolution [170]. In this context, Miralles et al. for example analyzed the influence of different soluble surfactants on the drainage in a 2D microfoam driven by a thermocapillary Marangoni stress [171, 172].
To suppress drainage even in three-dimensional foams and thus to analyze coarsening as a separate process, Isert et al. designed an experiment with a levitating, diamagnetic mixture and observed the cross-over between dry and wet foams [192]. For comparable low liquid contents (dry foam), the gas bubbles of the foam are in direct contact, separated

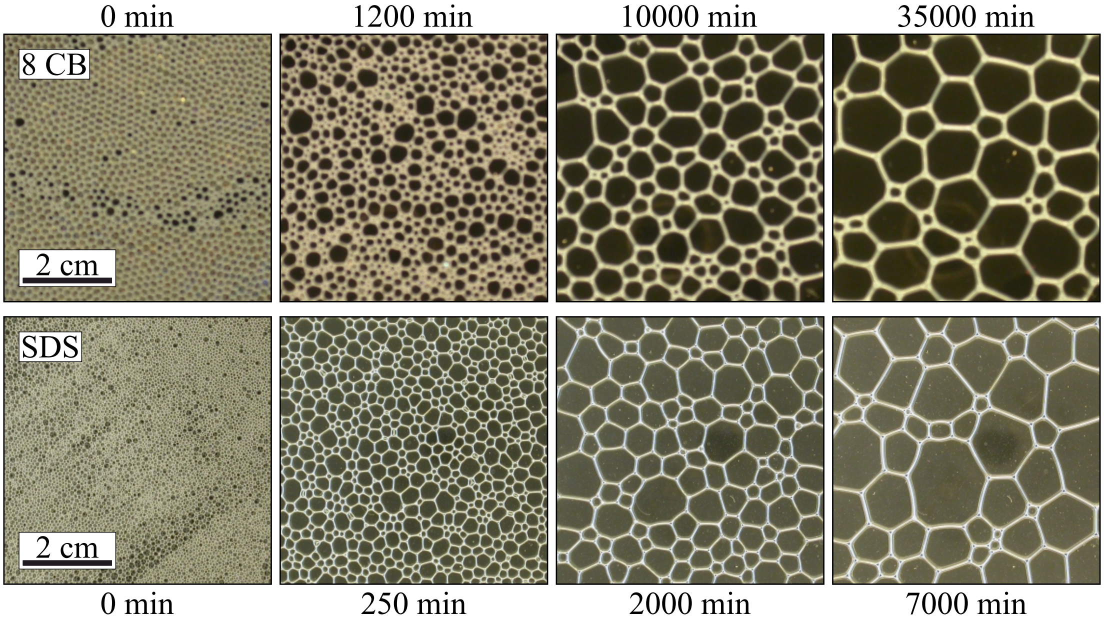

Figure 4.3: Evolution of a smectic foam (top row) and a foam made of sodium dodecyl sulfate (SDS) and water (bottom row) in comparison. The bright lines between the cells represent the thin plateau borders. With increasing time, the mixtures coarse, characterized by the increasing average bubbles size and the decreasing total number of bubbles. Experimental images are kindly provided by T. Trittel [190].

by thin boarders only, and gas exchange is driven by the Laplace pressure inside the bubbles $\Delta p = 2\sigma/R$ (liquid-gas surface tension σ, bubble radius R). Since the density of gas exchange j is proportional to the Laplace pressure, the following expression can be used [192]

$$j = \frac{\mathrm{d}V}{A\mathrm{d}t} \propto \frac{\mathrm{d}R}{\mathrm{d}t} \propto \Delta p \propto \frac{1}{R} \quad . \tag{4.3}$$

Integrating this equation leads to

$$\langle R \rangle \propto t^{1/2} \quad . \tag{4.4}$$

For wet foams as well as for three-dimensional mixtures such as alloys, the situation changes, the bubbles are no longer in direct contact and Ostwald ripening has to be considered. Here, the molecules now has to diffuse through the liquid, driven by the difference of the bubble pressure to the saturated pressure in the solvent. In fact, the density of material exchange is determined by the gradient of the pressure

$$j \propto \frac{\mathrm{d}R}{\mathrm{d}t} \propto \frac{\mathrm{d}p}{\mathrm{d}R} \tag{4.5}$$

that eventually leads to a size evolution according to [192]

$$\langle R \rangle \propto t^{1/3} \, . \tag{4.6}$$

4.1.3 Coarsening in two-dimensional films

In view of the experimental investigation of coarsening dynamics of smectic islands on the surface of smectic bubbles, it is necessary to find models that explain the observations in that unique system. At first glance, objects on a smectic liquid crystal film are comparable with droplets on a solid substrate (sessile droplets), as already discussed in the previous chapter. Especially during the dewetting process of thin liquid films on a solid substrate, small droplets can be formed, they can merge and grow in size, and holes in the film can occur.

30 years ago, Reiter analyzed thin polymer films and measured the evolution of holes in the film and the formation of small droplets [193]. He observed polygon patterns of the film material and droplets formed due to Rayleigh instabilities that finally seem to arrange in a hexagonal structure. As reason for the overall dewetting process, he described small modulations of the film surface by thermal fluctuations, which lead to a break-up of the film and a formation of small droplets. Thus, the system minimizes the contact area between the liquid material and the solid surface. Since the material is collected in the rim of holes, in fingering instabilities or in the droplets during dewetting process, there is no material flow between these structures and thus no Ostwald ripening can be observed.

A second system to analyze phase separation and late stage coarsening in two dimensions was introduced by Bassereau et al. in 1993 [194]. Thin films of symmetric diblock copolymers of polystyrene and polymethylmethacrylate (PS-b-PMMA) were prepared on Si-wafer, and micrometer-sized islands were created during heating and subsequent quenching of the film. These domains are located on top of a thin copolymer layer (thickness of a few dozen nanometers) that allows material diffusion within the film and between the islands. Bassereau et al. measured the number of islands $N_I(t)$, the number of holes $N_H(t)$, the average size of that domains $\langle R_I(t)\rangle$, $\langle R_H(t)\rangle$ and the average distance between adjacent islands and holes $\langle \xi_I(t)\rangle$, $\langle \xi_H(t)\rangle$ at different times. For all these quantities they found a power law dependence on time with the following exponents:

$$N(t) \propto t^{-2\alpha}\ , \quad \langle R(t)\rangle \propto t^{\alpha}\ , \quad \langle \xi(t)\rangle \propto t^{\alpha}$$

with $\alpha = 0.24 \pm 0.02$ for islands and $\alpha = 0.23 \pm 0.02$ for holes.

They additionally measured the island size distribution at different times and scaled their curves with the average size of the particles. They found that the scaled distributions for islands as well as for holes are invariant over time [194].

Two decades later, Limary et al. [164] used the same system of diblock copolymer films on $\mathrm{SiO_x}$/Si substrates to analyze the coarsening process of small droplets in dependence of the thickness h of the remaining film. They again measured the number of droplets and their average size and verified the power law behavior stated earlier. The exponents found in their experiments range from 0.4 for very thin films ($h = 9.5$ nm) to 0.1 for comparably thick films ($h = 19.5$ nm), indicating a strong influence of the remaining film on the coarsening dynamics.

For a more detailed and qualitative statement about the process, primarily driven by coalescence in that system, Limary et al. analyzed the normalized size distribution curves $S/\langle S\rangle$. Again, they show time invariance and structural self-similarity, where S represents the droplet area with $S \propto R^2$. Limary et al. additionally fitted the scaled curves

with theoretically predicted probability distribution functions for coarsening by Ostwald ripening and dynamic coalescence, and verified the merging process of droplets as dominant in their system.
The scaled probability function ($F(S/\langle S\rangle)$) for pure Ostwald ripening limited only by diffusion is given by

$$F(S/\langle S\rangle) = F(S') = \frac{CS'^2 \exp\left(\dfrac{-1}{1.5 - S'}\right)}{(1.5 - S')^{28/9}(3 + S')^{17/9}} \tag{4.7}$$

with the normalization constant C and with $F(S') = 0$ for $S' > 1.5$ [164, 195] (detailed derivation in [196]). For coarsening determined by diffusive coalescence, the collisions can be described with the Smoluchowski equation [197, 198] and the distribution function has the following form

$$F(S') = \frac{dW(WS')^{(d\hat{\beta}+d-1)}}{\Gamma(\hat{\beta}+1)} \exp\left\{-(WS')^d\right\} \quad . \tag{4.8}$$

Here, d describes the spatial dimension of the system, Γ the gamma function and $W = \Gamma(\hat{\beta}+1+1/d)/\Gamma(\hat{\beta}+1)$. With the fitting parameter $\hat{\beta}$, the power law exponent α, as mentioned before, is defined regarding

$$\alpha = \frac{2}{d(\hat{\beta}+1)} \quad . \tag{4.9}$$

Limary and co-workers were able to fit their data with the distribution function for the coalescence-based coarsening and explained their power law exponents depending on film thickness with a crossover from a two-dimensional to a 3D system [164, 195].

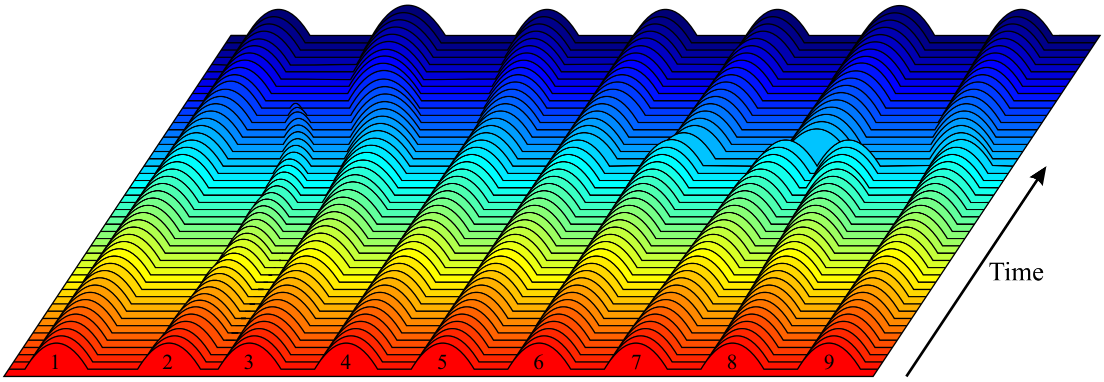

Figure 4.4: Sketch of coarsening dynamics for a dewetting thin film, reproduced from a numerical simulation based on the lubrication approximation [199, 200]. On the left, droplet 2 is shrinking while the neighboring droplet 3 growth in size (Ostwald ripening). Direct droplet-droplet interaction (droplets 7 and 8) representing coalescence is shown on the right-hand side.

A fully theoretical description of the coarsening dynamics and the dewetting process of films on solid substrates has been given by Glasner and Witelski [199, 200]. Using the one-dimensional form of the thin sheet equation (long-wave approximation) mentioned in the previous chapter, they analyzed the formation of isolated droplets and the exchange of mass that leads to the coarsening. In their model, they used the precursor film with its disjoining pressure $\Pi(h)$ to fulfill the droplet boundary conditions (contact angle of the droplets) as well as to enable mass transport through this film. The equations for the 1D lubrication approximation are used in the following form

$$\frac{\partial h}{\partial t} = \frac{\partial}{\partial x}\left(h^3 \frac{\partial p}{\partial x}\right) \ , \quad p = \Pi(h) - \frac{\partial^2 h}{\partial x^2} \ , \tag{4.10}$$

where the disjoining pressure combines all effects of intermolecular forces, van der Waals interactions and other repulsive effects [199, 200]. Glasner and Witelski on the one hand allowed the exchange of material between droplets through the thin precursor film in order to simulate droplet collapse (Ostwald ripening). On the other hand, they introduced diffusive motion of the droplets (migration) to enable direct droplet-droplet interaction and thus coalescence of droplets.

Both processes, Ostwald ripening and coalescence, are shown in figure 4.4 in a space-time plot visualizing a reproduction of the numerical results from Glasner and Witelski. With regard to the long-time dynamics in their one-dimensional system, they found a decrease of the total number of droplets according to a power law with an exponent of $-2/5$ ($N(t) \propto t^{-2/5}$). They furthermore analyzed the two different regimes and their properties, in which both processes appear dominantly.

Later, the model for the numerical simulation based on the thin sheet equation was expanded into higher dimensions [167, 173, 201–204], and for the two-dimensional case, a power law describing the total droplet number of $N(t) \propto t^{-3/4}$ was found [201, 202].

4.2 Experimental setup and materials

In the first chapter of this thesis, the OASIS mission and their experiments were briefly introduced. Due to the microgravity condition onboard the ISS and without external influences, one goal of the mission was the experimental investigation of the long-term dynamics of various inclusions on the smectic bubble surface.

For the analysis of the coarsening dynamics, smectic islands (lower images of figure 4.5) and holes were created by shearing the bubble surface with air jets. After the preparation phase, the island or hole ensembles then were observed for several minutes or hours. On the one hand, the size distributions, the average object size $\langle R(t) \rangle$ and the total number of objects $N(t)$ could be extracted from the macro-view images. On the other hand, there were also several videos from the micro-view camera that showed the behavior of individual islands in more detail (island position $x(t)$, $y(t)$ and island radius $R(t)$).

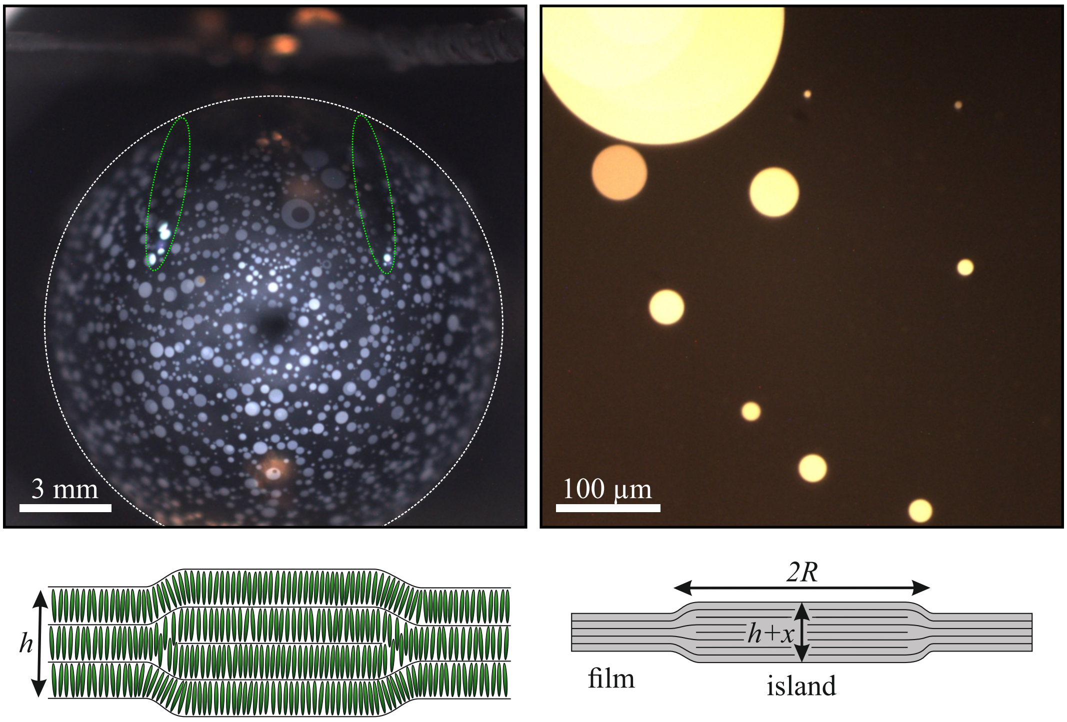

Figure 4.5: Experimental images from the macro-view camera (top left) and the micro-view camera (top right-hand) showing smectic islands in the initial stage of the coarsening process. On the left-hand side, the smectic bubble is highlighted with a white circle with a diameter of 15 mm. Almost all smectic islands are grayish and thus of similar thickness (similar number of layers). The camera is focused on the front side of the bubble and the edges are out of focus. The shadows and reflections of the airjet needles are marked in green. The right-hand image (500 × 500 µm^2) shows several islands of different size in the micro-view. The comparable colors of the islands again indicate island thicknesses of the same order of magnitude. The lower images visualize a possible arrangement of the molecules in the smectic layers in a sectional view of a smectic island with thickness $h + x$ in a film with thickness h. The size of the smectic layers and the liquid crystal molecules is greatly exaggerated.

Two images from the macro-view (17 × 17 mm^2) and the micro-view, with a significantly higher lateral resolution (500 × 500 µm^2), are shown in figure 4.5 [35].

The images were recorded with a maximum frame rate of 60 fps, i.e. every 16.67 milliseconds a picture was taken. For several experiments, this frame rate was reduced to simply save hard drive space. Since the depth of field of the macro-view was limited to approximately 4 to 5 mm, it was not possible to focus on the entire bubble and so the edges of the bubbles were often blurred. Additionally, shadows and reflection from the airjet needles, visible on the bubble surface, limited the surface of the smectic bubble that could be evaluated.

For the complete ISS mission, four different liquid crystal mixtures with smectic phases at room temperature were used. The Displaytech materials (mixtures 12160, 12805, 12864) were produced by the *Miyota Development Center of America* and the commonly used 8CB was obtained from *Sigma-Aldrich*.

In the following list, the liquid crystal mixtures with their specific phase sequences are presented.

- SN001: Displaytech mixture 12160 + 8CB (4-Cyano-4'-octylbiphenyl)
  Isotropic 56 °C Nematic 54 °C Smectic A 5 °C Crystalline
- SN002: Displaytech mixture 12864
  Isotropic 84.7-82.0 °C Nematic 81.4 °C Smectic A 66.1 °C Smectic C
- SN003: Displaytech mixture 12805
  Isotropic 84.7-82.0 °C Cholesteric 81.4 °C Smectic A* 66.1 °C Smectic C*
- SN004: Displaytech mixture 12160
  Isotropic 51.1 °C Smectic A -3.2 °C Crystalline (3.1 °C Smectic A when heating)

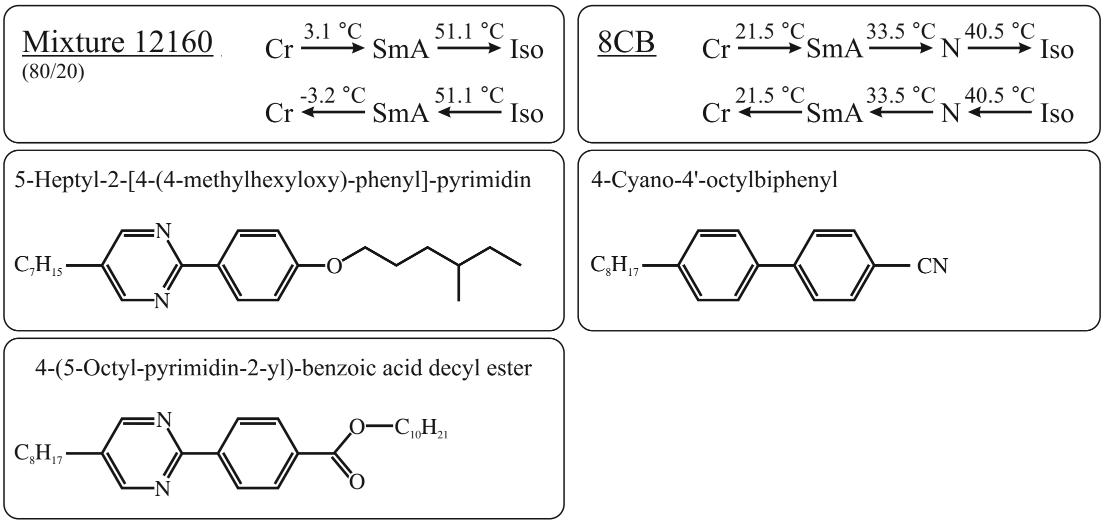

Figure 4.6: Chemical structure of mixture 12160 and the commercial used 8CB that are used for the samples 1 and 4. As already mentioned in chapter 2.2.1, the mixture 12160 consists of two different materials shown on the left side. The right-hand side shows the structure of 8CB. While the mixing ratio for material 12160 is given (80% of the branched chain mesogen and 20% of the decyl benzoate ester), the proportion of 8CB in sample 1 is not known.

For the experiments concerning the coarsening dynamics, especially sample SN001 and SN004 showed promising results and for these specific materials the chemical structure is given in figure 4.6. Both mixtures exhibit a smectic A phase at room temperature, whereas samples 2 and 3 are in the smectic C and smectic C* phase, respectively. In free-standing smectic films of the C or C* phase, an additional elastic interaction due to the molecule orientation (c-director) has to be considered for the dynamics of object motion and for the coarsening behavior. The smectic C* phase corresponds to a chiral phase in which the molecular tilt azimuth typical for smectic C phases changes between single layers, i.e. the mesogenes form a kind of helical structure perpendicular to the layer normal.
The two other compounds, SN002 and SN003, have the following chemical compositions:

	Compound	Volume fraction [%]
SN002	2-(4-Hexyloxy-phenyl)-5-nonyl-pyrimidine	28
	5-Nonyl-2-(4-octyloxy-phenyl)-pyrimidine	23
	4-(4-Methyl-pent-3-enyl)-cyclohex-3-enecarboxylic acid 4-(5-decyl-pyrimidin-2-yl)-phenyl ester	15
	4-Pentyl-cyclohexanecarboxylic acid 4-[2-(4-pentyl-cyclohexyl)-ethyl]-phenyl ester	15
	2-[4-[[-2-fluoro-2-methylheptyl]oxy]phenyl]-5-[(5,5,6,6,7,7,8,8,8-nonafluorooctyl)oxy]-pyrimidin	12
	5-[[-2,3-difluorooctyl]oxy] -2-(4-octylphenyl)pyridine	4
	Heptanoic acid 4-(5-octyl-pyrimidin-2-yl)-phenyl ester	3
SN003	2-(4-Hexyloxy-phenyl)-5-nonyl-pyrimidine	28
	5-Nonyl-2-(4-octyloxy-phenyl)-pyrimidine	23
	4-(4-Methyl-pent-3-enyl)-cyclohex-3-enecarboxylic acid 4-(5-decyl-pyrimidin-2-yl)-phenyl ester	15
	4-Pentyl-cyclohexanecarboxylic acid 4-[2-(4-pentyl-cyclohexyl)-ethyl]-phenyl ester	15
	2-[4-[[(2S)-2-fluoro-2-methylheptyl]oxy]phenyl]-5-[(5,5,6,6,7,7,8,8,8-nonafluorooctyl)oxy]-pyrimidin	12
	5-[[(2R,3R)-2,3-difluorooctyl]oxy] -2-(4-octylphenyl)pyridine	4
	Heptanoic acid 4-(5-octyl-pyrimidin-2-yl)-phenyl ester	3

The samples SN002 and SN003 are identical materials, except the blue highlighted groups for the SN003 compounds, that are responsible for the chiral character of the material.

Azimuthal projection and island recognition

For a correct island and hole detection and to measure the correct sizes of the objects on the bubble surface, it is necessary to map the curved surface onto a plane. It is important to depict all islands and holes as realistic as possible, and two types of projections are appropriate for this mapping procedure.

In both cases, the distances and the angles of all points on the surface to the center of the bubble were measured and the new distances in the mapped image were calculated. Within the so-called “Lambert azimuthal equal-area projection” all areas are represented correctly, but the angles and distances between islands are shown distorted. For the second method, namely the “azimuthal equidistant projection”, all distances and angles to the center point are represented correctly, but the surface area, especially at the bubble edge, is stretched. There is no method to map a spherical surface on a plane representing all angles, distances and areas correctly at the same time.

To compare both methods, a bubble surface with circular islands on the surface was simulated, and the different projections were calculated. As can be seen in figure 4.7, both procedures show almost identical results and only at the bubble edges small deviations with regard to the calculated islands sizes can be observed.

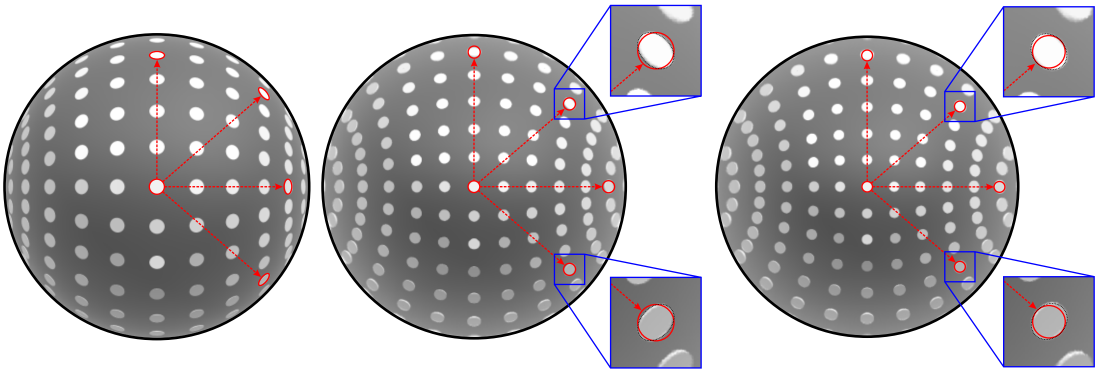

original image

Lambert azimuthal equal-area projection

azimuthal equidistant projection

Figure 4.7: Comparison of the azimuthal equal-area projection with the azimuthal equidistant projection using a simulated spherical surface covered with circular islands. Several islands are marked in the original image (left-hand picture) and the same islands are highlighted in both projections: equal area projection in the middle and equidistant projection on the right-hand side. In the mapped surface images, the red circles correspond to the size of the central island. In the enlarged section, it is shown that for the equal-area projection, the islands at the edges are more elliptical and flatter than the central island. For the azimuthal equidistant projection, the radial elongation of the edge islands is equal to the diameter of the central island, but these islands are stretched tangentially.

Although at the bubble edge, small deviations between both methods occur, the results of the procedures are almost identical. Especially in the central area of the bubble surface, differences between both projections can be neglected. Finally, the azimuthal equidistant projection was used to recalculate the bubble surface on a plane.

In the beginning of the data analysis, the complete experimental images were recalculated and projected on two-dimensional planes. As a second step and as shown in figure 4.8, a rectangular section of the experimental images was selected in which neither the mentioned shadows and reflections of the airjet needles nor the unfocused edge of the bubble were visible. All islands and holes in this region of interest (ROI) were automatically detected using a *Matlab* program. All islands and holes, that were only partially visible in the images due to the restricted region of interest or the dark region in the middle of each image, were fitted with circles.
Finally, images with a size of 400 × 400 pixel were recalculated, which correspond to an area of approximately 6.1 × 6.1 mm^2 of the bubble surface. Since the detected pixels in the images representing the islands were fitted with a circle, the detection has an inaccuracy of $\approx$15 µm only. For very small islands, however, this inaccuracy increases to at least 20 µm. The smallest detected object in the macro-view images has a size (radius) of approximately 30 µm, while the largest island radius is in the range of 600-700 µm.

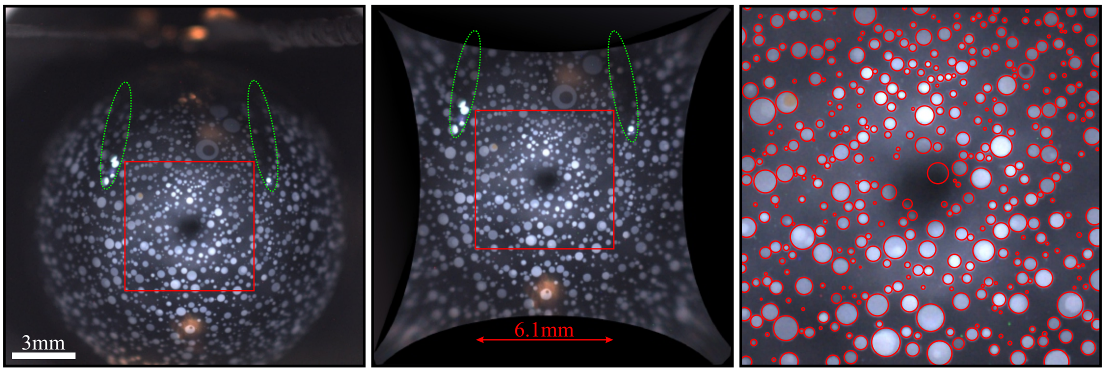

Figure 4.8: Experimental macro-view image and detected islands in the projection of the bubble surface. In the first step, the bubble surface in the original picture (left-hand image) was projected onto a flat plane and the diameter of the bubble was calculated. Then, the red highlighted region of interest (ROI) was chosen to avoid wrong detection due to the reflections and shadows (green ellipses). In the last step, all islands were detected with a *Matlab* procedure (right-hand image). The final image has a size of approximately 6.1 x 6.1 mm^2.

4.3 Preliminary experimental results

4.3.1 Overall coarsening dynamics

For a detailed analysis of the coarsening dynamics of the smectic islands covering the smectic bubble, thousands of macro-view images (showing the whole bubble) from a single video with a total length of more than 10 minutes were evaluated. As shown in figure 4.9, the composition of the two-dimensional emulsion (SN001) obviously changes with time, and the averaged island radius seems to increase during the experiments.
Since the spatial resolution of the images was limited to approximately 15 µm, it was not possible to detect very small islands or to measure small changes of individual island radii. Thus, within the macro-view images, an evaluation or verification of the expected Ostwald ripening as one of the important phenomena for coarsening was not possible.
On the other hand, the coalescence of smectic islands of different size and thickness could be observed, as highlighted in the subsequent figure. Although the detailed merging process could not be analyzed due to the comparatively low frame rate of a maximum of 60 fps (within the coalescence experiments, frame rates of 24,000 fps were used, see chapter 3), the coalescence as a single event between two or more islands could be detected by comparing consecutive images. Sometimes even intermediate stages of the coalescence could be recorded, as shown in figure 4.9 at $t = 300$ s (red highlighted).

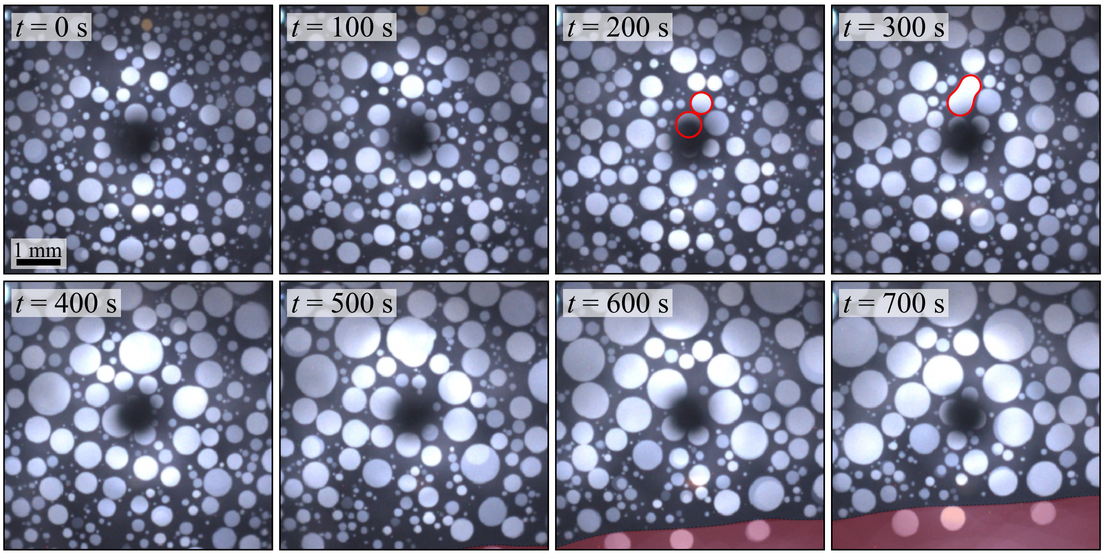

Figure 4.9: Time sequence of images showing a 6.1×6.1 mm^2 region of the bubble surface with smectic islands with almost the same thickness (most islands have the same color). With annealing time, more larger islands are formed while many small islands disappear. At $t = 200$ s, two islands are highlighted in red (partially covered by the shadow in the center of the image) that will merge and the coalescence event itself is shown at $t = 300$ s. The last two images show a large contiguous region (a thicker domain) colored in red that enters the region of interest.

As a part of the coarsening experiments, the influence of the ambient temperature was studied and for that reason the whole bubble chamber including the needles were heated or thermal gradients were applied on the bubble surface. The results of such an experiment with thermal gradient when only heating the bubble inflation needle is presented in figures 4.9 and 4.10. Here, a large and thicker contiguous region (at approximately 450 seconds) enters the central region of the bubble. This observation of a moving large region can be explained by thermally driven flow of material (Marangoni flow) described by Trittel [31] and Stannarius et al. [24].

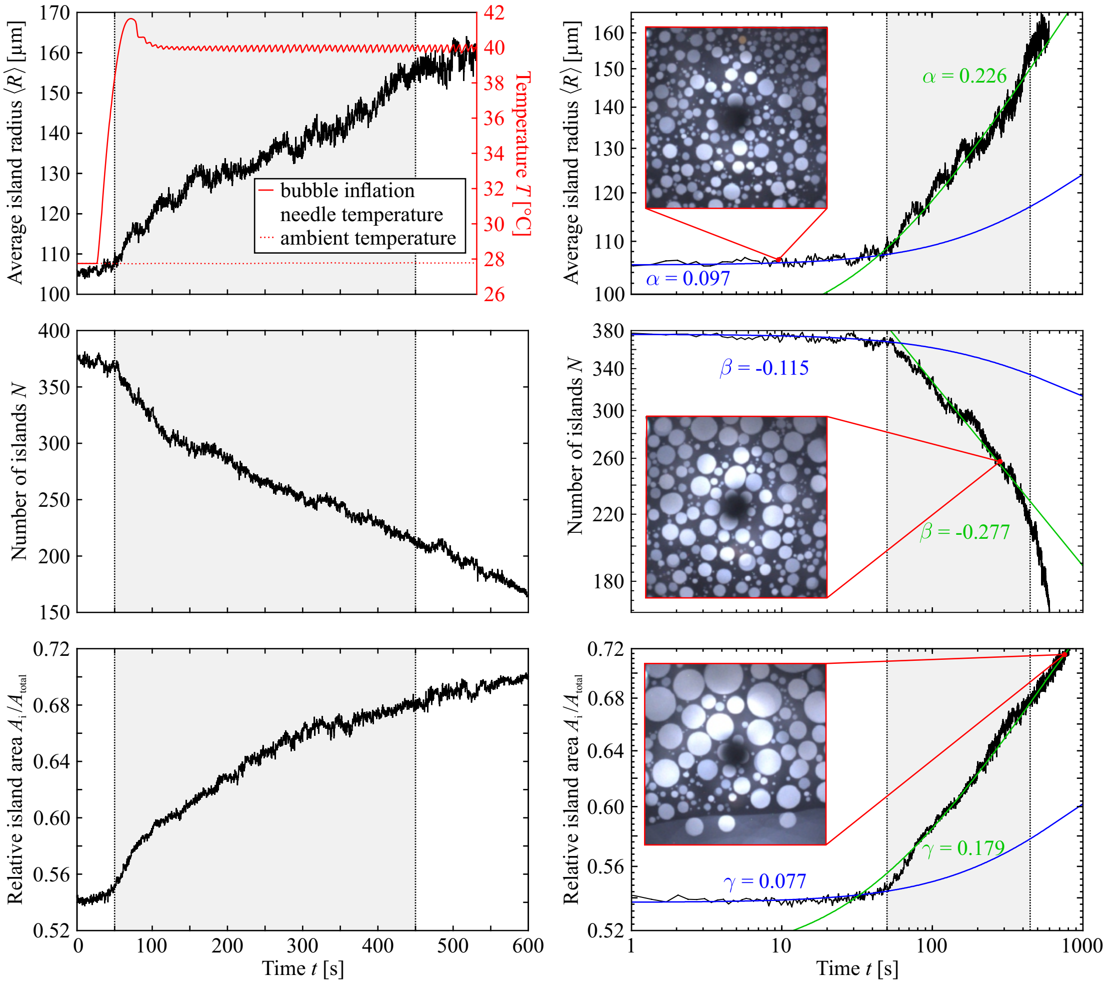

Figure 4.10: Experimental results from the macro-view images for sample SN001. The graphs show the average island radius (top), the overall number of islands (center) and the relative detected island area (islands area A_i divided by the total image area A_total) (bottom) in the observed region on the bubble surface. The top left figure additionally visualizes the temperature profile of the bubble inflation needle that was heated to 40 °C. The ambient temperature was held at 27.8 °C (red curves and scale). The phase with increased bottom needle temperature (reached at approximately 50 seconds) is marked with a gray background. After approximately 450 seconds, a thick large region enters the field of view and thus affects the measured data (visible in the bottom right-hand inset). The graphs on the right-hand side are identical to those on the left side, but with a double logarithmic scaling. The insets show the experimental image of the bubble surface for the specific time. The curves in the double logarithmic plots were fitted with a time-shifted power law function before heating (blue) and with increased temperature (green). The individual exponents are given in the graphs.

Figure 4.10 shows the average island radius, the total number of detected islands and the cumulative relative island area (detected islands area A_i divided by the total area A_total of the field of view) of one evaluated video from sample SN001. Considering the temperature profile of the bubble inflation needle compared to the ambient temperature and regarding the flow of material and the resulting large region moving into the central region, the overall coarsening dynamics for this example can be divided into two phases: an initial phase without external stimuli ($T_\mathrm{chamber} = 27.8$ °C) and a second phase in which the bubble inflation needle is heated ($T_\mathrm{needle} \approx 40$ °C).

Taking into account (time-shifted) power law dependencies based on the theoretical predictions [199–202], numerical simulations [167, 173] and other experiments [193, 194], the mean island radius $\langle R \rangle \propto (t - t_0)^\alpha$, the total number of islands $N \propto (t - t_0)^\beta$, and the total island area $A_\mathrm{i} \propto (t - t_0)^\gamma$ respectively the relative island area $A_\mathrm{i}/A_\mathrm{total} \propto (t - t_0)^\gamma$ were fitted with power law functions. Additionally, the distances between the islands were measured and the averaged center-to-center distance between adjacent islands is shown in figure 4.11. According to Bassereau et al. [194], a power law $\langle \xi \rangle \propto (t - t_0)^\delta$ should describe the experimental data. For the two phases, the following relations with their specific exponents α, β, γ and δ could be extracted from the experimental data.

Initial phase ($T_\mathrm{chamber} = 27.8$ °C, $0\ \mathrm{s} \leq t < 50\ \mathrm{s}$)	Phase with increased temperature ($T_\mathrm{needle} \approx 40$ °C, $50\ \mathrm{s} \leq t < 450\ \mathrm{s}$)
$\langle R(t) \rangle \propto (t - t_0)^\alpha \propto (t - t_0)^{0.097 \pm 0.03}$	$\langle R(t) \rangle \propto (t - t_0)^{0.226 \pm 0.05}$
$N(t) \propto (t - t_0)^\beta \propto (t - t_0)^{-0.115 \pm 0.02}$	$N(t) \propto (t - t_0)^{-0.277 \pm 0.04}$
$A_\mathrm{i}(t) \propto (t - t_0)^\gamma \propto (t - t_0)^{0.077 \pm 0.02}$	$A_\mathrm{i}(t) \propto (t - t_0)^{0.179 \pm 0.05}$
$\langle \xi(t) \rangle \propto (t - t_0)^\delta \propto (t - t_0)^{0.021 \pm 0.01}$	$\langle \xi(t) \rangle \propto (t - t_0)^{0.173 \pm 0.04}$

The parameter t_0 in that equations describes the time of the hypothetical initial situation with an infinite number of islands with infinitely small radii. For each data set, t_0 was taken from the fit of the total island number $N(t)$ (due to the highest accuracy) and used as constant to fit all curves. When assuming a conservation of the island area $A_\mathrm{i} \propto \langle R \rangle^2 N$, the following relation for the exponents can be expected (strictly speaking, only with constant radii distributions):

$$\begin{aligned} A_\mathrm{i} \propto \langle R \rangle^2 N = \text{const.} \;\; &\rightarrow \;\; (t - t_0)^{2\alpha}(t - t_0)^\beta \propto (t - t_0)^\gamma \\ &\rightarrow \;\; 2\alpha + \beta = \gamma = 0 \ . \end{aligned} \tag{4.11}$$

The determined power law exponent γ however is not vanishing for the experiments, which indicates a slight increase of the smectic island area. This increase seems to be negligible for low bubble temperatures, but especially at higher temperatures, the island area increases significantly. Nevertheless, the relation between the exponents $2\alpha + \beta = \gamma$ is still fulfilled even at higher temperatures.

With regard to the literature [164,194] and the expected conservation of island area (equation 4.11), the expression $2\alpha = -\beta$ should be applied and when recalculating these exponents for $\gamma = 0$, this relation can be confirmed. For the phase of increased needle temperature, for example, the following theoretical values α', β' could be calculated:

$$\alpha' = \alpha - \gamma/3 = 0.166 \pm 0.06 \quad \text{and} \quad \beta' = \beta - \gamma/3 = -0.336 \pm 0.05 \quad \text{for} \quad \gamma = 0 \ .$$

In that theoretical case without increasing island area, the exponents agree with each other ($2\alpha' \approx -\beta'$) and even the exponents for the mean radius and the average center-to-center distance agree $\alpha' \approx \delta$, as expected from other experiments [194].

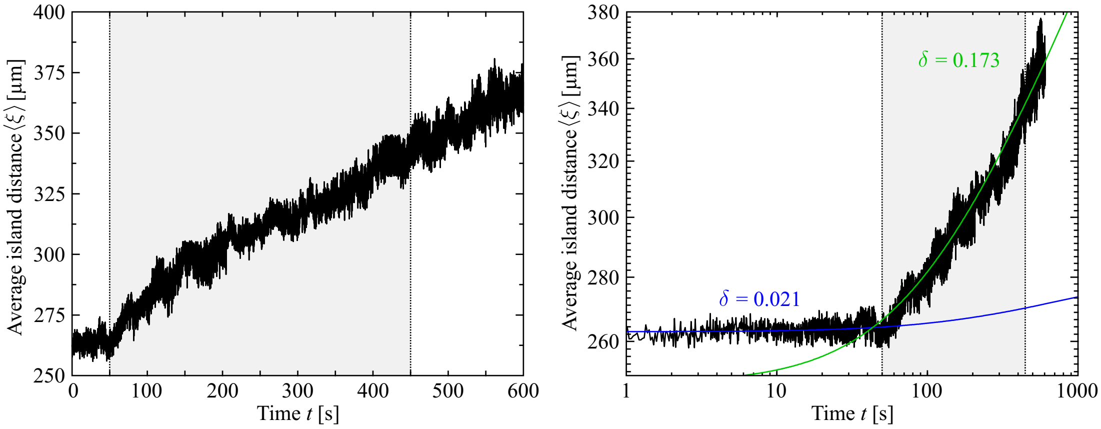

Figure 4.11: Calculated correlation length $\langle \xi(t) \rangle$ describing the average center-to-center distance between adjacent islands. The phase with increased bottom needle temperature is highlighted. Again, the two phases were fitted separately with a time-shifted power law function. The individual exponents δ are given in the right graph. With regard to the results of Bassereau et al., the exponent γ should be comparable to that of the mean island radius α.

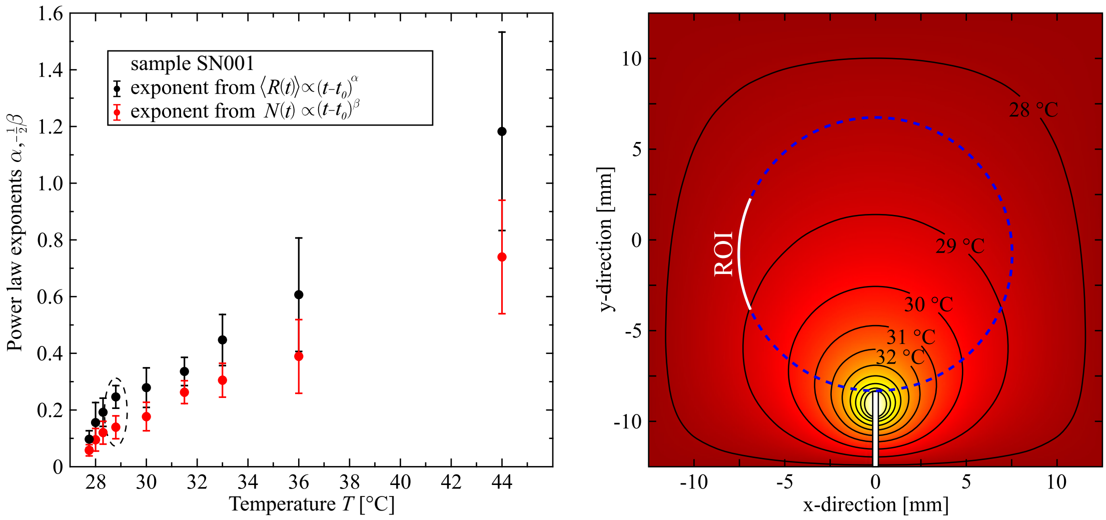

Figure 4.12: Measured power law exponents α and $-\frac{1}{2}\beta$ from the fit of the mean island radii $\langle R(t) \rangle$ and the total number of islands $N(t)$, respectively, for different coarsening experiments with sample SN001 at different temperatures T. With increasing temperature also the exponents increase. The highlighted data points in the left graph were extracted from the curves in figure 4.10 with increased inflation needle temperature. The right-hand image shows a simulation of the temperature profile for this specific experiment where only the bottom needle was heated to 40 °C. A temperature of approximately 28.8 °C can therefore be assumed in the analyzed region of interest, highlighted with a white line (ROI). The temperature is color coded from 40 °C in white to 27.8 °C in dark red. Contour lines additionally visualize the simulated temperature profile. The smectic bubble is indicated by a blue dashed circle.

As shown in the previous figures and verified by the exponents of the power law functions, the coarsening dynamics apparently depend on the temperature of the system. Higher temperatures could reinforce the merging process of islands (coalescence) and the exchange of material between them (Ostwald ripening).

The left-hand graph of figure 4.12 shows the measured power law exponents α and $-\frac{1}{2}\beta$ for different experiments at different temperatures. Since in some experiments, temperature gradients were applied and the temperature profile could not be measured except at the capillary (T_{needle}) and the outer borders of the box (T_{chamber}), the expected temperature in the observed center region (ROI, white line in the right hand graph of figure 4.12) of the bubble was simulated and calculated. An example of such a simulated temperature profile is presented in the right-hand picture of figure 4.12. For the simulation with the commercial software package COMSOL, the bubble inflation needle temperature was set to $T_{\text{needle}} = 40$ °C, whereas the walls of the box and the airjet needles had a constant temperature of $T_{\text{chamber}} = 27.8$ °C. Thus, with the stationary, axially symmetric solution of the heat diffusion equation, a temperature profile in the center of the blue dashed smectic bubble of 28.8 °C could be calculated. The white section of the blue dashed circle here represents the projection of the region of interest on the circle in the two-dimensional temperature profile.

As expected, the power law exponents show a clear dependency on the temperature. The exponents α and -0.5β increase with increasing temperature of the bubble surface. In addition, the discrepancy between these exponents also increases, verifying that the total island area A_{i} is not constant. On the contrary, it even increases stronger for higher temperatures in the experiments.

In addition to the measured island radii and the calculated mean island size, the radius and the motion of individual islands were analyzed in order to verify, for example, the thermally induced flow of material from the previous example with temperature gradients [24, 31]. As shown in the upper left-hand graph of figure 4.13, separated islands without direct interaction with other islands will only grow marginally in size (green and blue curves in the upper left-hand graph). Their radii increase with a growth rate of about 0.035 µm/s in the phase of increased temperature. Apparently, the coalescence of smectic islands here is the dominant effect that drives the coarsening dynamics.

In the upper right-hand graph, the motion of individual islands is presented, and it is shown that only when the bubble inflation temperature starts to increase (at $t \approx 30$ s), the islands start to migrate along the temperature gradient. The velocity of the thermally induced motion of the islands here seems to be independent of the island size and could be calculated to approximately 10 µm/s when the heating starts and ≈ 5 µm/s at a constant temperature gradient (after approximately 200 seconds, when an equilibrium state and a homogeneous temperature gradient between the needle and the walls of the box is reached). The discrete jumps in the experimental data for the island radii and their positions in figure 4.13 are the result of single coalescence events.

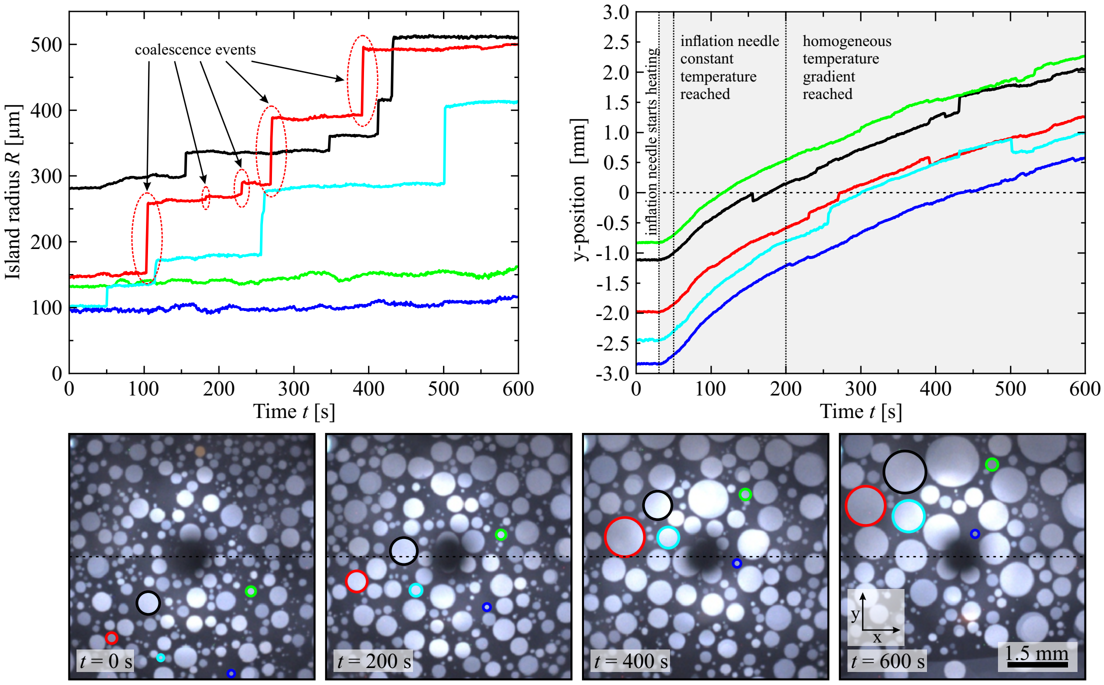

Figure 4.13: Change of the radius and the position of 5 individual islands during the coarsening experiment. The islands in the experimental images (lower images) are highlighted with the corresponding colors used for the measured radii and positional data. The radii (upper left-hand graph) of islands without direct interactions only increase marginally (blue and green curves). The dominant size changing effect can be verified as the coalescence of islands (black, red and cyan curves). Coalescence events are visible as discrete jumps of the island radii (emphasized with dashed ellipses). In the upper right-hand figure, the position of the islands between the north pole (airjet needles) and the south pole (bubble inflation needle) shows the thermally induced motion due to the increased bubble inflation needle temperature (Marangoni flow) [24,31]. The central dashed line represents the equator of the bubble. The radii and the positions could be determined with an accuracy of ±15 µm.

In order to analyze the island coalescence in more detail, all merging events were detected in the experimental images by measuring intensity changes in consecutive images. The radii of the coalescing islands were then determined manually. The coalescence probability as a function of the island radius respectively the scaled island radius could be calculated and is shown in the upper graphs of figure 4.14. Here, both radii of the merging islands have been considered. Very small islands with radii smaller than 25 µm could not be detected due to the spatial resolution of the images. It is conceivable that a significantly larger number of very small islands merges during the experiments. With increasing island radius, the probability of coalescence events decreases. This seems intuitive when assuming a larger number of small islands and a higher mobility of small islands compared with bigger ones.

Additionally, the ratio of the radii of the coalescing islands (small islands divided by the bigger islands) were calculated. Besides very small island ratios, the coalescence probability seems to be equally distributed. The coalescence of equal-sized droplets (island radius ratio ≈ 1) seems to be as probable as the merging of islands with double or triple the radius of one of the islands (island radius ratio between 0.3 and 0.5).

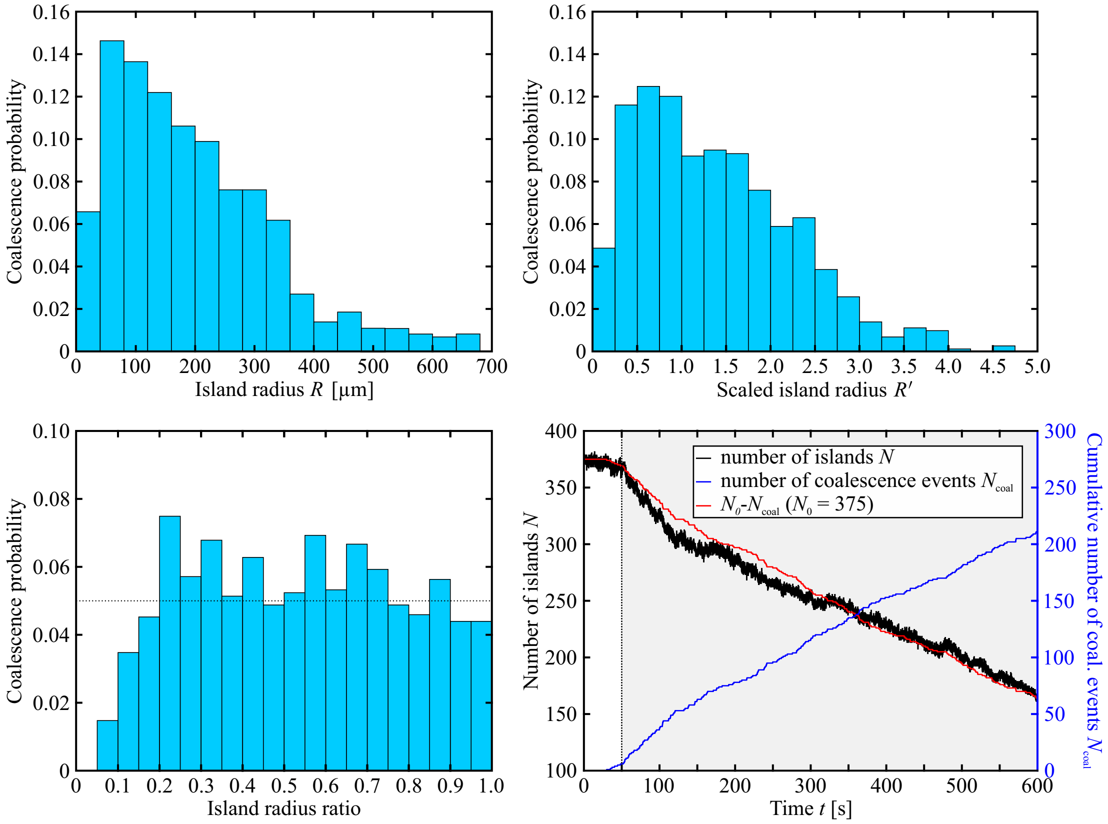

Figure 4.14: Coalescence probability as a function of the island radius R (upper left graph) and as a function of the scaled island radius R' (upper right-hand graph). Additionally, the coalescence probability in dependence of the island radius ratio (small islands divided by the bigger islands) is shown in the lower left-hand graph. The lower right-hand graph visualizes the total number of islands and the cumulative number of coalescence events depending on time. For the probability of merging events, which decreases with increasing island radius, very small islands smaller than 25 µm could not be detected due to the spatial resolution of the images. Apart from that, the coalescence events appear to be equally distributed across the radius ratios, at least above 0.1. The total number of coalescence events continuously increases over time (blue curve and scaling on the lower right-hand side), while the total number of detected islands decreases (black curve). The red curve in the graph corresponds to the difference between the initial islands number N_0 and the accumulated coalescence events. $N_0 - N_{\text{coal}}$ decreases and almost matches with the curve for the total island number. The phase of increased needle temperature is highlighted. Small deviations between the measured and the calculated number of islands can be explained with the motion of the islands on the bubble surface through the region of interest in the experimental images.

The detected coalescence events were accumulated additionally, as shown in the lower right-hand graph of figure 4.14 (blue curve and right-hand axis), to quantitatively analyze the effect on the total number of islands. Here, the black curve represents the total number of islands N (left-hand axis) with its initial value N_0 of 375 islands. To compare both curves, the cumulative number of coalescence events were subtracted from the initial number of islands $N_0 - N_{\text{coal}}$. For an ideal system without flow, where only coalescence determines the coarsening behavior, this difference should match perfectly the number of detected islands. Both curves, measured and calculated number of islands, actually agree very well and small deviations are only due to the motion of islands and the flow of material through the detected region. New islands entering the field of view and other ones leaving this region are one reason for fluctuations in the measured data and can be observed in every experiment even without thermal gradients and thermally induced motion.

Within the experiments and especially for the material SN001, the coalescence of smectic islands can be verified as the dominant and driving process for the coarsening dynamics. Based on these results and taking into account the work of Limary et al. [164] and Lo et al. [195], the size distribution of the islands can be analyzed in more detail.
The individual island radii again were scaled with the averaged radius $R' = R/\langle R\rangle$ and the probability densities $F(R')$ for these scaled radii were calculated. The probability density here describes the probability (probability density multiplied with the interval width) of measuring an island in a certain (scaled) radius interval $\mathrm{d}R'$.
As shown on the left side of figure 4.15, there is no uniform distribution of the scaled island radii, but the distributions are positively skewed. As time increases, more larger islands are formed due to coalescence and the tail of the data extends to larger values. Nevertheless, the number of very small islands does not change significantly or even slightly increases. The graphs on the right-hand side underline this tendency as the distribution of the accumulated island areas is shifted to larger radii during the experiments. The surface is more and more dominated by larger islands. The asymmetric shape of the probability density can be explained with the diffusivity of the islands, which strongly depends on their size. Regarding the Saffman equation (see section 2.1.2), larger islands are assumed to be less mobile than smaller islands. As a result, the coalescence probability, as mentioned before, decreases with increasing islands size.

In 1996, Sholl et al. [198] analyzed the coarsening dynamics of clusters on substrates, where the coarsening was limited only to the coalescence of the clusters. They determined a distribution function from the Smoluchowski equation [197, 198] to fit their cluster distribution densities.
For the probability density function, Sholl et al. [198] used the following equation containing the gamma-function Γ and the fitting parameters $\hat{\beta}$ and d.

$$\begin{aligned} F(R') &= \frac{dW(WR')^{(d\hat{\beta}+d-1)}}{\Gamma(\hat{\beta}+1)} \exp\left\{-(WR')^d\right\} \\ W &= \Gamma(\hat{\beta}+1+1/d)/\Gamma(\hat{\beta}+1) \end{aligned} \tag{4.12}$$

The calculated scaled probability densities $F(R')$ at different times t are shown on the left side of figure 4.15. In the upper left graph, the probability densities were fitted using equation 4.12 (black and blue curve) and the resulting parameters $\hat{\beta}$ and d are shown for the individual curves. Since the parameter d in the theoretical prediction should represent the spatial dimension of the system [164], this parameter was set to a fixed value of $d = 2$ for the second fit (blue curve).

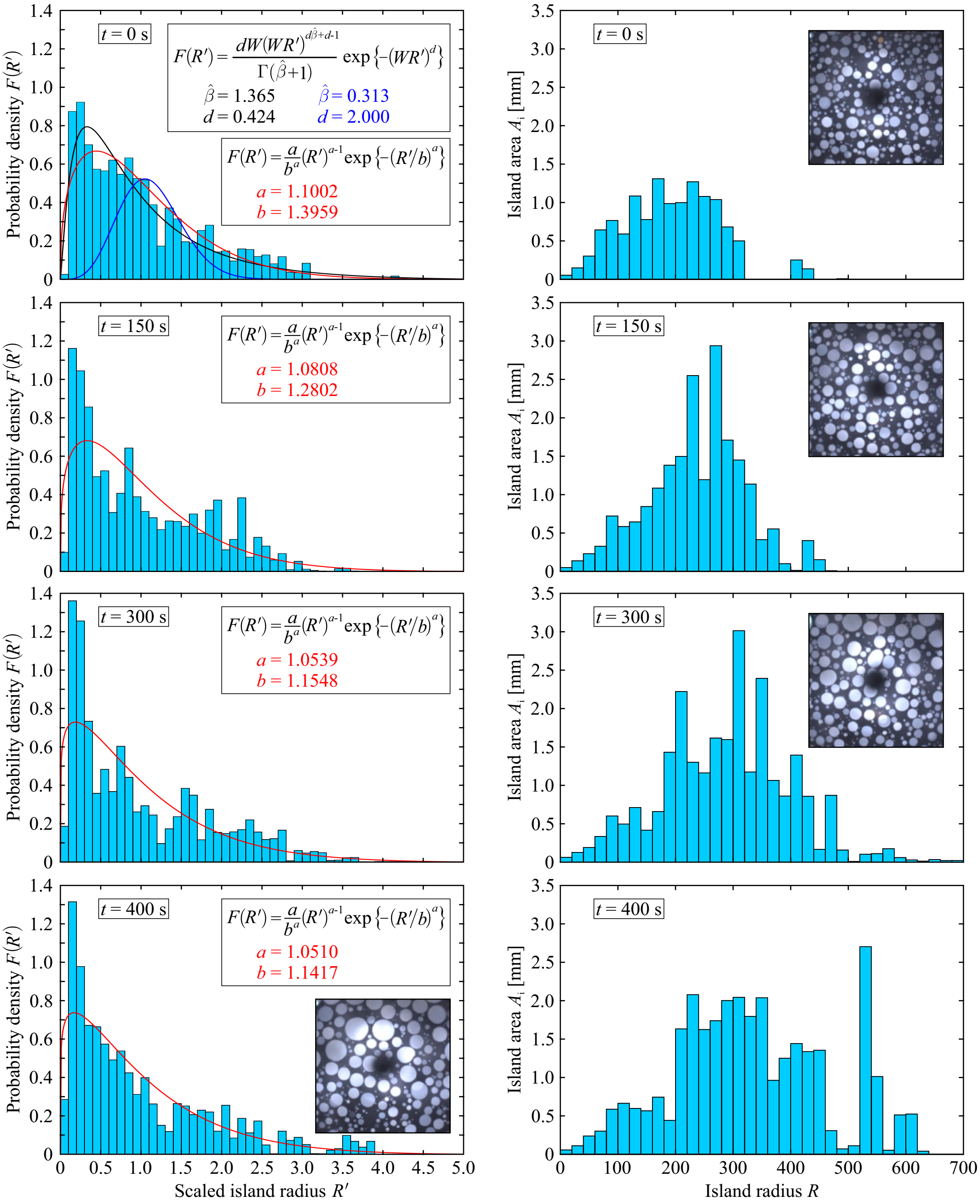

Figure 4.15: Probability density F depending on the scaled island radius $R' = R/\langle R \rangle$ at different times t of the coarsening process. The data in the upper left graph were fitted using equation 4.12 including the parameters $\hat{\beta}$ and d. With respect to Loo et al. [195] and Limary et al. [164], d describes the spatial dimension of the system and therefore was set to $d = 2$ for a second fit (blue curve). The red curves in the graphs on the left side additionally represent the fitted Weibull-function with the parameters a and b as used by Magrabi et al. [205]. The graphs on the right-hand side show the accumulated island areas as function of the corresponding island radii. The insets show typical experimental images. Due to the spatial resolution of the system, especially very small islands ($R' < 0.1$) are subject to a larger relative inaccuracy.

While the black curve in figure 4.15 convincingly reproduces the measured densities, the blue curve with the assumed dimension parameters d seems to be inappropriate to fit the data. Consequently, the fit parameters cannot be explained with the theoretical predictions and the dynamic model described by the Smoluchowski equation seems to fail here (for coalescing droplets on a substrate, parameters of $d = 2$ and $\hat{\beta}$ between 0.4 and 1 [164] were found). The subsequent graphs in figure 4.15 were not fitted using this equation. The assumption for the model of a diffusion coefficient exhibiting a power law scaling $D(R) \propto R^{-\hat{\beta}}$ is not valid, especially if the values for $\hat{\beta}$ are used and if the Saffman equation for the mobility of objects in two dimensions is considered.

Instead, for the density curves on the left-hand side a Weibull-function was used, as done previously by Magrabi et al. [205]. They analyzed the size distribution, the growth and the coarsening dynamics of bubbles in aqueous foams. Magrabi et al. extended an existing model (by Lemlich [206]), to additionally describe the effect of liquid fraction and drainage on the coarsening dynamics of the foam.

The Weibull function is defined as

$$F(R') = \frac{a}{b^a}(R')^{a-1}\exp\left\{-(R'/b)^a\right\} \tag{4.13}$$

with the two fitting parameters a and b.

As shown in figure 4.15, the Weibull distribution describes the experimental data quite well, but there is no physical meaning for the two parameters yet. It reproduces all data relatively reliable and only fails for the very small islands. The spatial resolution of the system of 15 µm should be mentioned here, i.e. very small islands in particular are subject to a larger relative inaccuracy.

When completely neglecting very small islands in the probability density functions, it is also conceivable to set the fitting parameter $a = 1$ and to use an exponential function to describe the data.

$$F(R') = \frac{1}{b}\exp\left\{-(R'/b)\right\} \tag{4.14}$$

Limary et al. analyzed the coarsening dynamics of micrometer-sized islands of symmetric diblock copolymers of polystyrene and polymethylmethacrylate (PS-b-PMMA) on a thin copolymer layer [164]. They additionally observed self-similarity of the coarsening process when their measured scaled probability density function for different times collapsed onto a single curve. Based on this observation, the island distributions for the smectic islands at different times were visualized in figure 4.16 in form of cumulative probability densities. The curves also overlap, indicating some kind of statistical self-similarity behavior [207, 208]. However, the shape of the curves slightly changes with increasing time, highlighted by arrows.

The inset of figure 4.16 shows the evolution of the fitting parameters a and b. Both decrease in time. The change of the parameter b is only marginal compared with the error of that value. With regard to the accuracy of the measurements, a constant value of $b = 1$ is also conceivable.

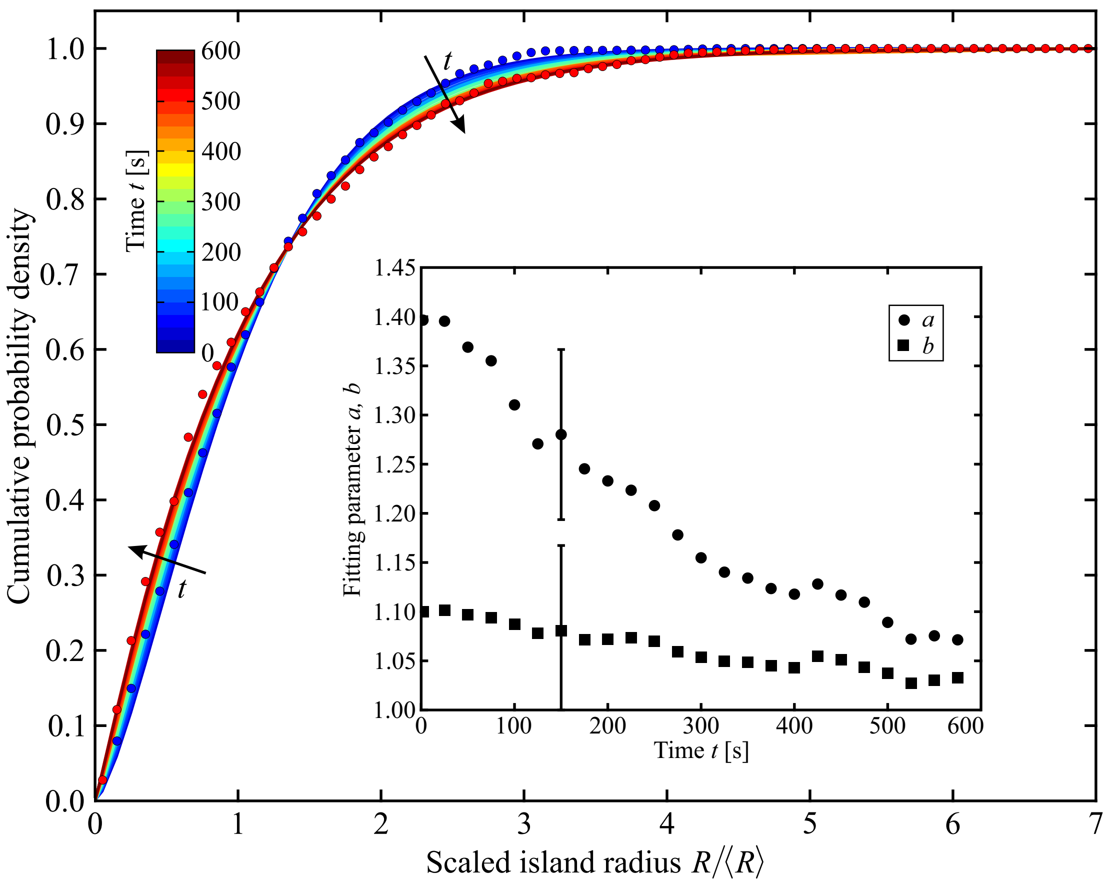

Figure 4.16: Cumulative probability density depending on the scaled island radius $R' = R/\langle R\rangle$ fitted with Weibull-type distributions at different times t. Only for $t = 50$ s (blue circles) and for $t = 500$ s (red circles) the experimental data points are shown. The curves at different moments of the coarsening dynamics are color coded. With increasing time the curves slightly change their shape, highlighted with arrows. The inset shows the fitting parameter a and b and their dependence on time. Both parameters decrease during the experiment.

4.3.2 Ostwald ripening

The second part of the long-term coarsening experiments was focused on Ostwald ripening, i.e. the direct exchange of material between islands through the background film. For the analysis, only the micro-view images (500 × 500 µm^2) with a much higher spatial resolution of 0.5 µm per pixel compared to the macro-view images could be used to measure changes in the radii of even small islands with high accuracy. Since there was no homogeneous background illumination, a background image was created by combining fragments of the backgrounds of different images from a single experiment. The resulting intensity profile was then used to recalculate the actual intensities and colors for each image.

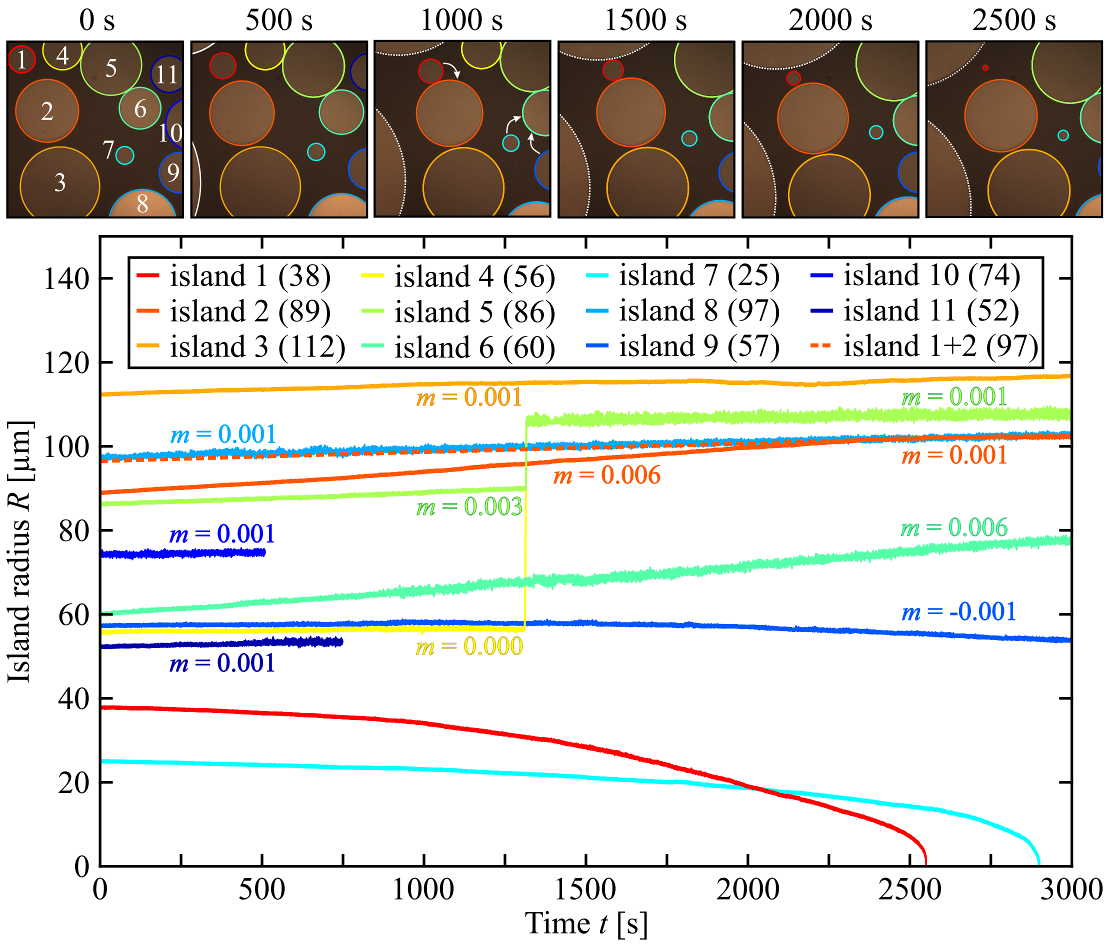

Figure 4.17: Experimental images and measured island radii from the micro-view images (500 × 500 µm^2). The top row shows original images at different times with highlighted and labeled islands, that were detected automatically. The individual colors highlighting the islands were also used for the curves that represent the radii of the islands. The numbers in brackets represent the initial radii of the islands in micrometer. During this experiment, the islands 1 and 7 continuously shrink until they finally disappear. Since the neighboring islands (number 2 and 6) at the same time slightly grow in size, this process can be identified as Ostwald ripening. The value m at each curve represents the growth rate of the island in µm/s.

Figure 4.17 shows a sequence of experimental images at a constant temperature of 24 °C, with highlighted islands and their measured radii. Over a period of 50 minutes, two islands shrink and finally disappear and two islands coalesce (number 4 and 5). To verify Ostwald ripening and the exchange of liquid crystal material through the film, the growth rate of each detected island was calculated. As shown in the graph (slopes m at each curve in µm/s), almost all individual islands seem to grow in size and their radii increase with a constant rate of 0.001 µm/s.

In figure 4.17, two different shrinking scenarios can be observed: on the one hand, island 1 is shrinking and its material is obviously accumulated in the neighboring islands 2. As a result, the radius of the receiving island increases faster and with a higher growth rate of 0.006 µm/s with respect to the other islands. When the shrinking process of the small island and thus the Ostwald ripening is completed, there is no further exchange of material and the growth rate of island 2 returns to the value observed for all other islands ($m = 0.001$ µm/s). The evidence for Ostwald ripening can be found when analyzing the sum of both island areas (1 and 2) and calculating the equivalence radius of that hypothetical object (orange dashed line in figure 4.17). Figure 4.18 additionally shows the area of both islands and the sum of them. The almost constant accumulated area verifies the Ostwald ripening (the overall growth rate was subtracted before). The smaller island is thinner (darker) than the bigger one, and thus the total island area slightly decreases.

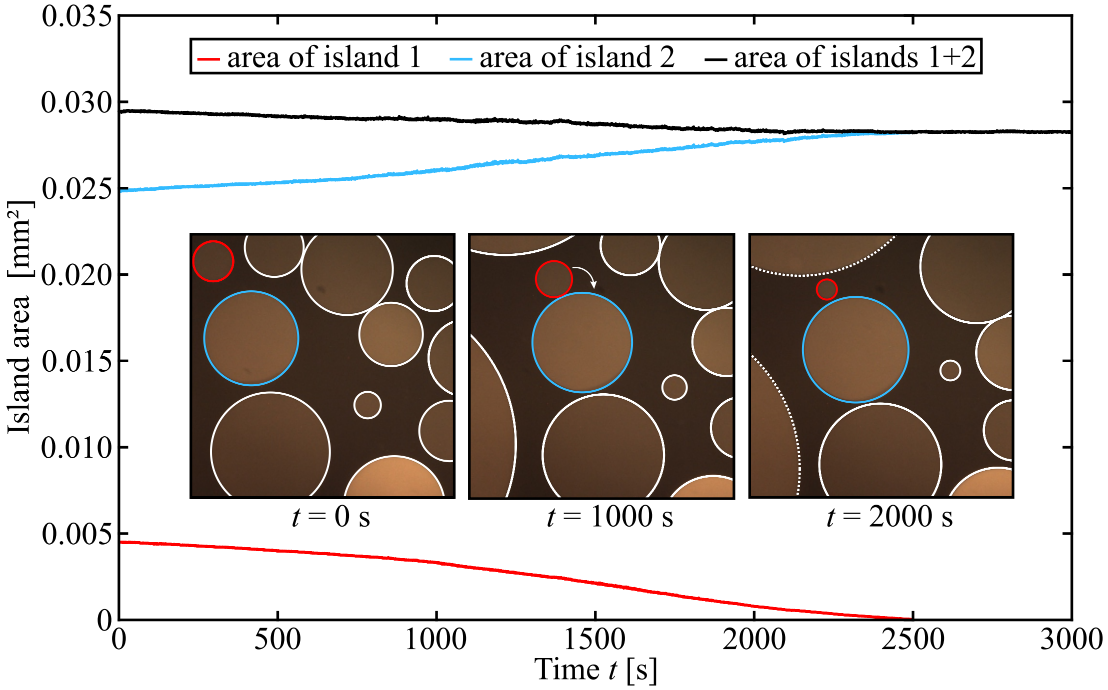

Figure 4.18: Area of the islands 1 and 2 shown in figure 4.17. The sum of both curves (black) is almost constant and verifies Ostwald ripening. The overall slight growth of the island radii (independent on Ostwald ripening) of 0.001 µm/s was subtracted from both curves. The experimental images show the islands at the specific times.

For the second example (shrinking island number 7) the same increased growth rate of the receiving island 6 could be observed, but in this case a second island (number 9) is also shrinking and island number 6 appears to receive material from both neighboring islands. The final and equilibrium state, when both small islands disappeared, is not reached in this experiment. Nevertheless, the same general growth rate of 0.001 µm/s is expected when the shrinking process of islands 7 and 9 has been finished.

In the next step of the evaluation, the individual curves of the shrinking islands were analyzed and possible dependencies of Ostwald ripening on the island radii or the island thicknesses were investigated. Figure 4.19 shows the change of the radius for 5 individual islands in the same background film in one single experiment. All curves first were fitted by a power law function $R(t) = C(t_0 - t)^{\gamma'}$, where the pre-factor C describes the strength and the quality of the material transport process. The fitting parameters of the individual curves are summarized in table 4.1. All measured curves were shifted to the annihilation point at $t = 0$, resulting in $t_0 = 0$ for all fitted curves.

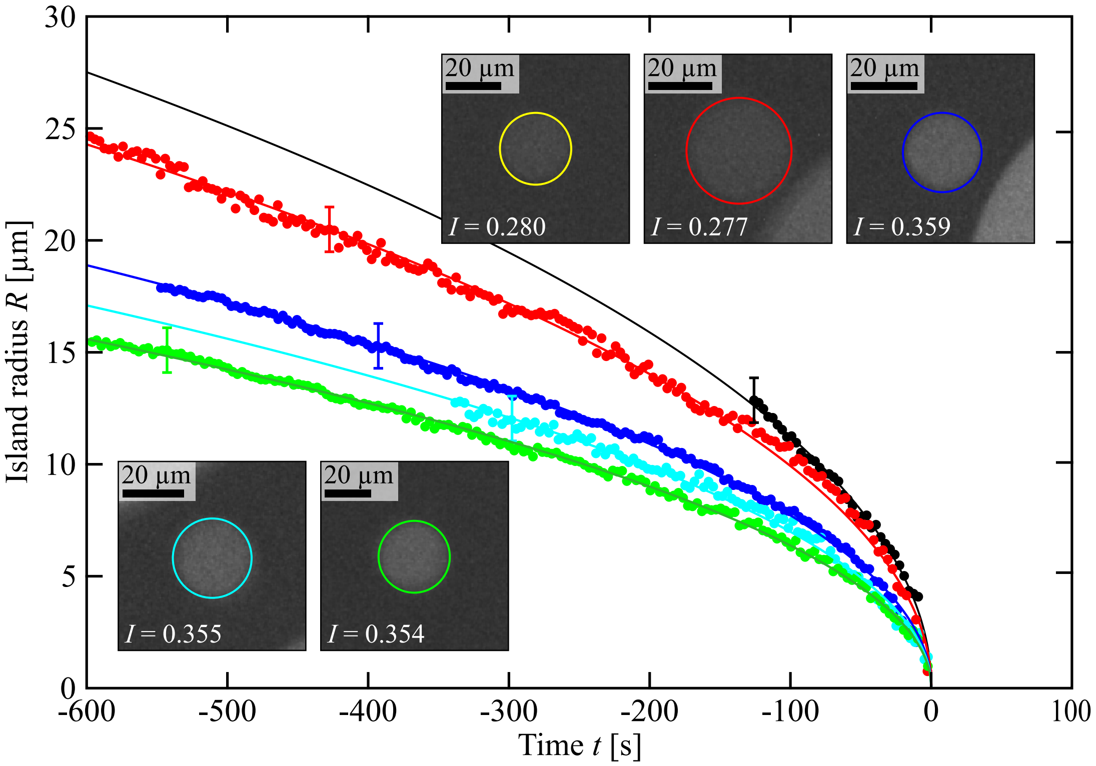

Figure 4.19: Measured island radii of 5 different islands in a single experiment. The islands shrink and finally disappear. All curves were shifted to annihilation time at $t = 0$ and they all follow a power law $R(t) = C(t_0 - t)^{\gamma'}$ with $\gamma' \approx 0.5$ and with different pre-factors C. The insets show recalculated gray-scale images of the analyzed islands highlighted with the colors used in the graph (the yellow marked island corresponds to the black curve). The intensities of the islands are given in arbitrary units. For comparison, the background has an intensity of approximately 0.2.

As presented in table 4.1, the power law exponents of the fitting curves are close to 0.5 which implies the usage of a square root law $C(t_0 - t)^{0.5}$. Small deviations from that square root law can be explained with small changes in the distance between the islands during the measurements, i.e. the material exchange rate changes slightly. In addition to the power law fit, the intensities of the islands and the background film in the recalculated images were measured. Although it is not possible to measure real film thicknesses from the intensities without a reference point, the islands can be compared among each other. The insets in figure 4.19 show the recalculated images of the analyzed islands with its intensities. It seems that only two different island thicknesses were observed.

Table 4.1: Fitting parameters from the power law function $R(t) = C(t_0 - t)^{\gamma'}$ for the curves shown in figure 4.19. The pre-factor is given in µm $s^{-1/2}$ with respect to a square root law. In addition, the intensities of the islands in the recalculated images were measured.

		C [µm $s^{-1/2}$]	γ'	Intensity I [arb. units]
$C(t-t_0)^{\gamma'}$	black curve	1.112 ± 0.081	0.502 ± 0.02	0.280 ± 0.01
	red curve	1.041 ± 0.051	0.492 ± 0.02	0.277 ± 0.01
	blue curve	0.781 ± 0.061	0.495 ± 0.01	0.359 ± 0.01
	cyan curve	0.701 ± 0.057	0.499 ± 0.02	0.355 ± 0.01
	green curve	0.672 ± 0.045	0.491 ± 0.01	0.354 ± 0.01

When analyzing the intensities of many islands and finding discrete, equidistant intensity values, it is conceivable to estimate the island thicknesses respectively the thickness difference between islands. Due to the layered structure of the smectic islands, only integer multiples of the layer thickness (≈ 3-6 nm) are possible, which allows the conclusion that the equidistant measured intensities are linked to single layer steps or at least steps of a constant number of layers. The measured intensities for various islands and the background film are presented in the right-hand graph of figure 4.20. Islands of similar intensities were averaged.

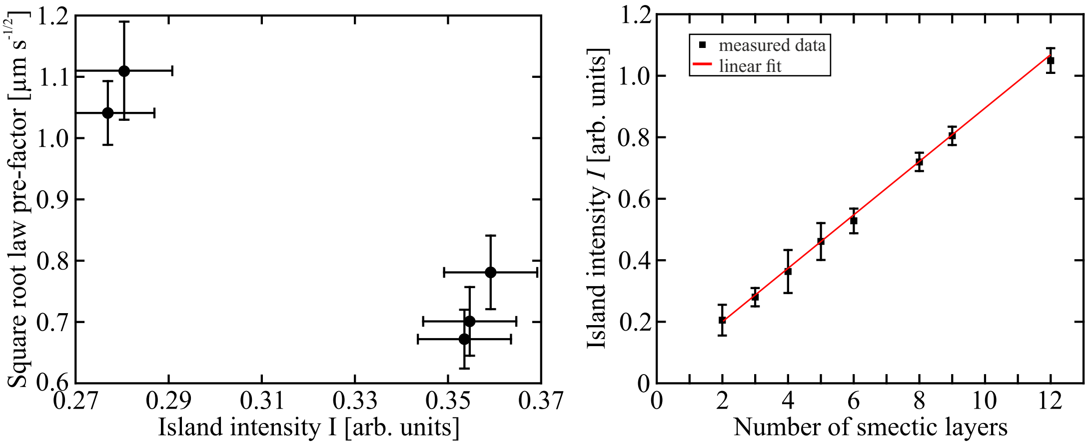

Figure 4.20: Strength of the shrinking process represented by the pre-factor C depending on the island intensity respectively the island thickness. The right-hand graph shows the island intensities of different islands and the background in one experiment. The measured intensity values are equidistant, which suggests single smectic layers as height difference between the islands. The fitted linear curve can be described with $I(N) = 0.086N + 0.025$.

First, the intensities were assigned to a consecutive number of layers. The linear trend of the intensities verifies that assignment, but also multiples of the number of smectic layers (for example double layers per intensity step) are conceivable.

From the original experimental images and with the experience from other experiments with smectic films and islands, it seems very unlikely that intensity differences caused by single layers steps only can be observed.

In the left-hand graph of figure 4.20, the pre-factor of the power law fit from figure 4.19 (summarized in table 4.1) is shown as a function of the island intensity and thus the island thickness. Since apparently only two islands thicknesses were observed (compare with the right-hand graph of figure 4.20), no functional relationship could be found from the experimental data. Nevertheless, thinner islands will shrink faster than thicker islands, which can be explained with the basic idea of the material transport through the background film. Liquid crystal molecules can only diffuse through the contact area $A_{\text{film-island}} = 2\pi R_1 h$ between the film and the shrinking island with a fixed island radius R_1 and background film thickness h. The density of material exchange then in first approximation can be written as

$$j = \frac{\mathrm{d}V}{A_{\text{film-island}}\mathrm{d}t} \tag{4.15}$$

with the volume of the island $V = \pi R_1^2(h+x)$, where $h+x$ represents the thickness of the island. When considering the Laplace pressure $\Delta p = E/R$, with the linear tension of the dislocation E inside the islands, as predominant effect driving the material exchange, the following expression can be found.

$$\frac{\mathrm{d}V}{A_{\text{film-island}}\mathrm{d}t} = \frac{\pi(h+x)}{2\pi h R_1}\frac{\mathrm{d}R_1^2}{\mathrm{d}t} \propto E\left(\frac{1}{R_1} - \frac{1}{R_2}\right) \tag{4.16}$$

Here, R_1 describes the radius of the shrinking and R_2 that of the growing island.

Assuming that the small island radius mainly defines the pressure difference $\Delta p = E/R_1$, and integrating equation 4.16 yields

$$R_1(x,t) = Ct^{\gamma'} \propto \sqrt{\frac{2hE}{(h+x)}}\sqrt{t} \ . \tag{4.17}$$

In fact, with increasing value x respectively an increasing island thickness, the pre-factor C decreases and the strength of Ostwald ripening is decreased. Furthermore, the measured power law exponent of $\gamma' \approx 0.5$, representing a square root law, can be explained with that simple model.

With equation 4.17, a relation for the island and film thickness can be found.

$$C_1 = \sqrt{\frac{2hE}{(h+x_1)}} \ , \ C_2 = \sqrt{\frac{2hE}{(h+x_2)}} \tag{4.18}$$

With the measured pre-factors from the experiment, the following ratio can be derived

$$\left(\frac{C_1}{C_2}\right)^2 = \frac{(1+x_2/h)}{(1+x_1/h)} \approx 2.23 \ . \tag{4.19}$$

4.4 Summary and discussion

Within the OASIS-ISS experiments, ensembles of smectic islands on the surface of a smectic bubble were created and observed over several minutes. In contrast to the analyzed isotropic droplets (see chapter 2), the thin islands will not arrange in lattice-like structures.

As expected, the total number of islands decreases and the averaged island size increases during the experiments. The measured curves were fitted with power law functions to describe the dependence of the averaged radius of the islands $\langle R(t)\rangle \propto (t-t_0)^{\alpha}$, the total number of islands $N(t) \propto (t-t_0)^{\beta}$, the total island area $A_{\mathrm{i}}(t) \propto (t-t_0)^{\gamma}$ and the averaged center-to-center distance between adjacent islands $\langle \xi(t)\rangle \propto (t-t_0)^{\delta}$ on the time t.

With regard to the total island area, a conservation with $\langle R\rangle^2 N(t) = A_{\mathrm{i}} =$ constant should apply and for the power law exponents the following expression should (!) be found:

$$2\alpha + \beta = \gamma = 0 \ . \tag{4.20}$$

Indeed, for all experiments a non-zero exponent $\gamma \neq 0$ for the detected island area was observed which verifies an increase of the total island area. While this effect appears to be very small and within the experimental uncertainty at low temperatures around 28 °C, it becomes important and non-negligible especially at higher temperatures.

It was shown that the smectic islands radius slightly increases during the experiments with a growth rate of 0.001 µm/s up to 0.04 µm/s even without direct contact with other islands, which finally causes the increase of the total island area.

On the one hand, it is conceivable that small islands shrink and their material is accumulated in bigger islands. Since very small islands could not be detected in the macro-view images, this possible Ostwald ripening could not be verified in the macro-view images. On the other hand, additional smectic material could directly come from the background film and thus from the meniscus around the bubble inflation needle.

Another possible explanation for the island radius increase can be found with regard to the island coalescence as analyzed by Dolganov et al. [134]. In some cases it is possible, that during the merging process of smectic islands of different thickness the thicker island collapses and the resulting object has the thickness of the initially thinner islands [134]. As a result, the total island area again increases.

Despite the growth of the island area, the relation $2\alpha + \beta = \gamma$ is still fulfilled for all experiments. When recalculating α and β for the theoretical situation of conserved island area ($\gamma = 0$), the new exponents α' and β' even agree with the exponent of the power law that describes the mean center-to-center distance δ predicted by Bassereau et al. [194].

$$\alpha' = -0.5\beta' = \delta \tag{4.21}$$

In addition to the higher growth rate of the smectic islands at higher temperatures, also the power law exponents show a temperature dependence. Figure 4.12 shows that with increasing temperature, the coarsening dynamics is accelerated, which at the first glance can be explained with a higher thermal energy and an increased diffusive motion of the islands. With an enhanced diffusivity (diffusion coefficient $D \propto k_{\mathrm{B}}T$), the probability of direct island collisions and thus the coalescence of islands is increased. The left-hand graph of figure 4.14 confirms this higher coalescence probability for smaller islands, i.e. for islands with higher mobility. For the analyzed material SN001, the following ranges for the exponents depending on temperature were measured (recalculated theoretical values for a constant island area in brackets):

$$\begin{aligned} \alpha =& 0.004 \text{ ... } 1.939 \quad (\ \ \alpha' = 0.004 \text{ ... } 1.520) \quad \text{and} \\ -\beta =& 0.007 \text{ ... } 2.622 \quad (-\beta' = 0.008 \text{ ... } 3.041) \quad \text{at} \\ T =& 27\ ^\circ\text{C ... } 44\ ^\circ\text{C} \quad . \end{aligned}$$

For a comparison of the measured exponents with the literary context, several experimental results and the found exponents are summarized in table 4.2. As presented, the values for the exponent α vary between 0.05 (calculated from Limary et al. [164]) for droplets on a substrate and $\alpha = 1$ (from Thakur et al. [165]) for nematic droplets in a flat cell. Although the values for the different systems are in the same range as for the smectic island coarsening, none of that experiments exhibits such a wide range with a single material by only changing the temperature.

Table 4.2: Comparison of the power law exponents of different experimental systems and simulations: R corresponds to a characteristic length scale (cluster size or radius of the object), N describes the number of observed objects and A the mean area of the domains.

System	Power law equations		Reference
3D two phase mixture (Pb-Sn)	$R \propto t^{0.33}$	exp.	Hardy et al. [157]
3D droplet coarsening in phase separating fluid mixture	$R \propto t^{1/3}$	exp.	Tanaka et al. [178]
3D droplet phase separation of binary liquid mixture	$R \propto t^{1/3}$, $N \propto t^{-1}$	simul.	Shimizu et al. [150]
3D aqueous wet & dry foams	$R \propto t^{0.52 \text{ ... } 0.55}$	exp.	Magrabi et al. [205]
2D smectic foam in a flat cell	$A \propto t$, $N \propto t$	exp.	Trittel et al. [168]
quasi 1D driven lattice gas	$R \propto t^{0.6}$	simul.	Mettetal et al. [166]
nematic droplets in flat cell (concentration gradient)	$R \propto t$	exp.	Thakur et al. [165]
coarsening of symmetric diblock copolymer films	$R \propto t^{0.25}$, $N \propto t^{-0.5}$	exp.	Bassereau et al. [194]
thin film coarsening on a solid surface	$N \propto t^{-0.23}$	simul.	Lo et al. [195]
coarsening of liquid droplets on a diblock copolymer substrate	$N \propto t^{-(0.1 \text{ ... } 0.4)}$	exp.	Limary et al. [164]
unstable liquid films on disordered substrate (lubrication approx.)	$N \propto t^{-1/3}$	simul.	Kumar et al. [173]

Next to the coarsening dynamics of smectic islands, the thermally induced motion of that objects could be observed during the experiments as well (Marangoni flow). The applied temperature gradients causes surface tension differences between the material at the heated needle and the rest of the bubble. The motion of the thick islands (compared with the background film) towards the colder part of the bubble and the flow of material from the meniscus at the heated needle into the bubble results in a slight increase of the film temperature. This reduces the total surface energy [24, 31].

For the analyzed example, the simulation of the temperature profile on the bubble surface (see figure 4.12) shows, that in the center of the bubble, temperatures between 28.5 and 29.1 °C can be assumed. As a consequence, temperature gradients of only 0.08 K/mm to 0.18 K/mm can be expected. Although these gradients, especially near the bubble equator, are very small, they explain the motion of the islands and the small changes of the measured drift velocity ($\approx$ 10 µm/s at the beginning in the lower hemisphere and $\approx$ 5 µm/s at the end in the upper hemisphere). Nevertheless, the island velocities seem to be independent of the individual island size and radius, respectively.

The temperature gradients and the induced flow of material and motion of smectic islands additionally could explain the increase of the total island area in these specific experiments. Due to the thermally induced motion, the island density partially increases and thus the total island area in a fixed region of interest raises. Nevertheless, also in these experiments, a growth of the radii of individual islands can be observed.

Simultaneous measurements of the total island number and the number of coalescence events verified that the coarsening dynamics in these experiments with these specific materials is predominantly driven by direct island merging processes. Furthermore, the observations and recent experiments on the smectic island coalescence showed that the merging process occurs within milliseconds [135, 139] or at most in a few seconds when islands of different thicknesses are involved [134]. In any case, the coalescence of smectic islands takes place on a much smaller timescale compared to the Ostwald ripening, where material is exchanged between islands over minutes. As a consequence, the reduction of the surface energy and thus the coarsening dynamics is dominated by direct island-island interaction and coalescence.

With regard to other coarsening experiments [150, 157, 164, 194, 195, 205], the distribution of the scaled averaged island radii $F(R/\langle R\rangle)$ were calculated and analyzed. The initial distribution shows a higher probability to find small islands than bigger ones, and this asymmetric tendency will not change or only increases over time. During the experiments, due to the island coalescence, more large islands are formed and the tail of the distributions thus is extended to larger values with increasing time. The distribution densities were fitted using a theoretical curve based on the Smoluchowski equation (equation 4.12) and a Weibull function (equation 4.14) as used by Magrabi et al. [205]. Both functions can reproduce the measured data relatively well, but while the Smoluchowski-based function underestimates the probability of larger islands, the Weibull fit seems to fail for very small islands. One parameter of the Smoluchowski based function is expected to describe the spatial dimension of the system ($d = 2$), but with this value the fit completely fails. Since the fitting parameters of the Smoluchowski-based function are not in agreement with the theoretical model, all curves were fitted using the Weibull function. The fitting parameters here show a dependence on time (see figure 4.16), but there is no physical explanation for the different parameters yet. Neglecting very small islands, which are subject to a greater inaccuracy, it is also conceivable to use an exponential function to fit the distribution densities. The overlapping cumulative probability density curves additionally suggest a self-similarity behavior of the size distribution of the coarsening dynamics.

In the second part of the experiments with the micro-view camera, it was possible to observe the shrinkage and the collapse of smectic island with a high spatial accuracy over several minutes. While some islands shrink and finally disappear, neighboring islands grow in size, which can be seen as an evidence for Ostwald ripening. In fact, when analyzing the changes of the size of different islands, it was found that all island radii grow with a constant rate of approximately 0.001 µm/s. In the observed cases of shrinking islands, the growth rate of the closest neighbors at the same time is increased due to the flow of material through the background film. Since the equivalence radius combining the radius of the shrinking islands R_{shrink} and radius of the growing island R_{grow}

$$R_{\text{equiv}} = \sqrt{R_{\text{shrink}}^2 + R_{\text{grow}}^2}$$

has the same growth rate (0.001 µm/s) as all other islands, material flow only between these two islands can be concluded. This is confirmed regarding the total island area of both islands as shown in figure 4.18. At least for small islands observed on the northern hemisphere of the smectic bubble, direct flow of material from the islands to the meniscus around the bubble inflation needle at the south pole can be neglected. This assumption of the non effecting meniscus is the basic idea of the whole OASIS mission and distinguishes the experiments on the smectic bubble surface from other ones on flat free-standing films.

With regard to the size evolution of smectic islands in smectic films, Dolganov et al. analyzed the collapse of these separated thicker domains and developed a model for the time-dependence of the island radius [209]. Their considerations are based on the work of Oswald et al. [210], in which they investigated the growth of smectic holes and finally the rupture of the film. In both experiments, the flow of material from the island and holes respectively to the meniscus at the edge of the films dominates the dynamics in the system. Actually, Dolganov et al. observed pairs of islands and verified the changes of their sizes as Ostwald ripening, but they also assumed a superimposition of material flow between islands and to the meniscus [209]. For the flow of mass of liquid crystal material j' between two islands, they assumed a Poiseuille flow

$$j' = \frac{\pi R_{\text{ch}} \rho}{8\eta} \frac{\Delta p}{L} \tag{4.22}$$

with the characteristic size of the channel R_{ch} between islands of distance L, the density of the material ρ and their viscosity η.

The pressure difference then is proportional to the inverse radii of both islands (small island with radius R_{shrink} and bigger island with radius R_{grow}) [209]

$$\Delta p \propto E\left(\frac{1}{R_{\text{shrink}}} - \frac{1}{R_{\text{grow}}}\right) \tag{4.23}$$

and in first approximation this difference is dominated by the radius of the small island $\Delta p \propto E R_{\text{shrink}}^{-1}$ (E describes the line tension of the dislocations).
Finally, using this approach from Dolganov et al., a dependence of the radius of the shrinking island on time could be found that shows a square root dependence identical to that presented for the OASIS-coarsening experiments.

$$R_{\text{shrink}}(t) \propto \sqrt{t} \tag{4.24}$$

When considering additionally the thickness of the islands (thickness of film h with additional layers of thickness x) and assuming that material only flows through the island-film-interface, equation 4.24 additionally depends on the thickness of the islands.

$$R_{\text{shrink}}(t) \propto \sqrt{\frac{2hE}{h+x}}\sqrt{t} \tag{4.25}$$

At least for the observed islands in the smectic A materials (SN001 and SN004), this square root law is in very good agreement with the measured power law exponents, as shown for two examples for each material in table 4.3. With the first material, even the dependence of the shrinking dynamics on the island thickness could be shown, whereas only two different thicknesses were measured. Since the thickness of the background film could not be determined and only estimated to a few dozen nanometers, only experiments with islands of different intensities in the same film, that also show Ostwald ripening, could be used to prove the thickness dependence of the approach. To really confirm this dependence and the whole model, further experiments with different island thicknesses showing Ostwald ripening are necessary. Ideally, the film thickness and the island thicknesses are measured directly, for example by using interferometry.
Unfortunately, for the SN002 material, no Ostwald ripening could be observed.

Table 4.3: Fitting parameters C (in µm/s$^{-1/2}$) and γ' form the power law fit for different experiments with different materials. Whereas the film generated with the samples SN001 and SN004 are in the smectic A phase, material SN003 forms a smectic C phase in the applied temperature range. With the material SN002, no Ostwald ripening could be observed.

	SN001		SN002		SN003		SN004	
	C	γ'	C	γ'	C	γ'	C	γ'
$R_{\text{shrink}} \propto C(t-t_0)^{\gamma'}$	0.222	0.499	-	-	0.468	0.420	1.249	0.493
	2.102	0.488	-	-	1.575	0.435	1.377	0.544

The smectic C material (SN003) respectively the power law exponents show small deviations from the expected value of 0.5. Presumably, the structure of the material and the resulting c-director configurations influence the transport of material between the islands. On the one hand, the director configuration in the background film has to be changed if, for example, there is a π-wall between the involved islands or at least a change in the c-director field. On the other hand, also the islands itself have a c-director configuration and additionally often exhibit a +1 or -1 defect in their centers, as the experimental images in figure 4.21 show. During the shrinking process, the mesogens in the islands need to rearrange, which leads to a loss of energy and thus possibly to a reduced material exchange rate.

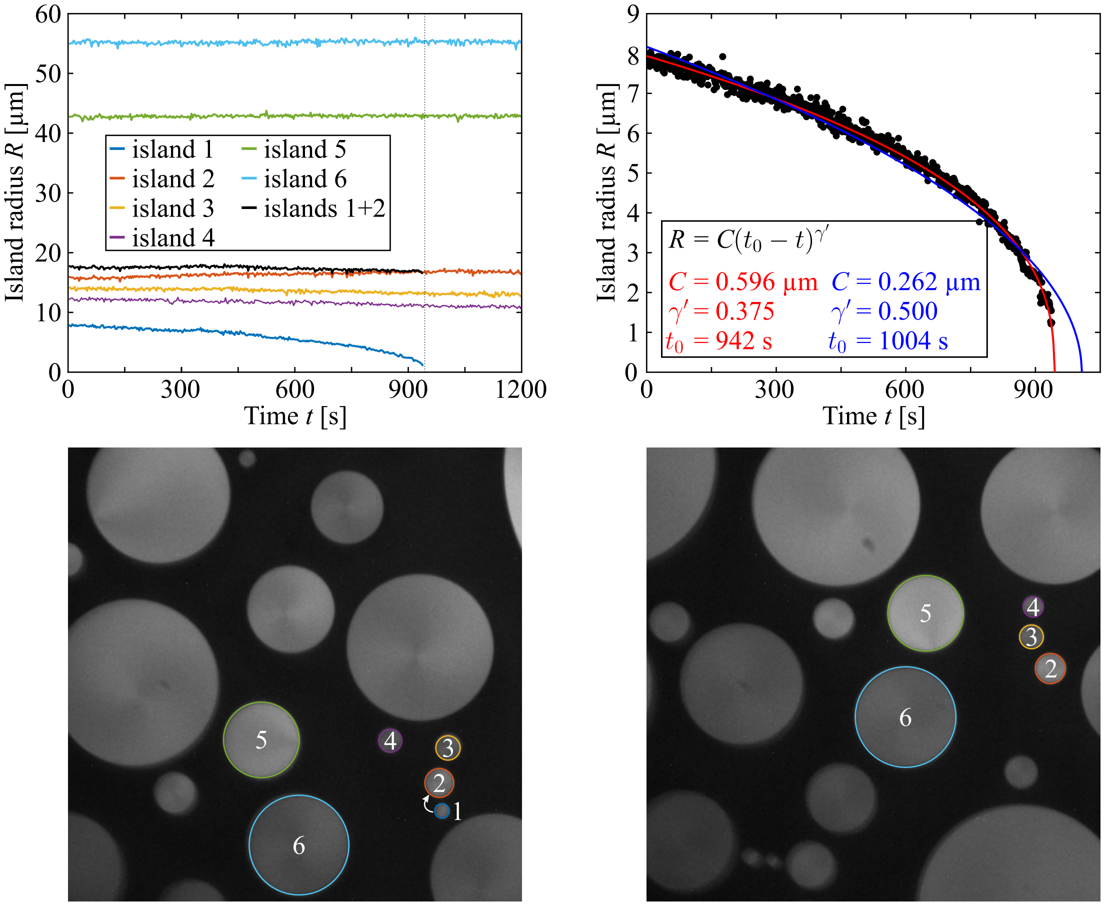

Figure 4.21: Measured island radii and power law fits for the shrinking island for an experiment with a smectic C material. The smectic C islands in the experimental images show bright and dark brushes typical for a c-director configuration with a +1 or -1 defect. The colors of the highlighted islands are also used in the upper left graph. The sum of the areas of island 1 and 2 again verifies Ostwald ripening. The dashed vertical line marks the annihilation point. The island radius of the shrinking island (top right-hand graph) was fitted with a power law according to $R(t) = C(t_0 - t)^{\gamma'}$ (red curve) and with respect to the shrinking model with a square root law $R(t) = C(t_0 - t)^{0.5}$ (blue curve). The experimental images have a size of $500 \times 500\ \mu\text{m}^2$.

As shown in the top right-hand graph of figure 4.21, especially at the end of the shrinkage, the curves deviate from the square root law, which could be explained with a homogeneous c-director field for very small islands with radii below 2 to 3 μm. It seems, that in this late stage, the c-director configuration does not retard the material exchange between the islands. Nevertheless, also for the smectic C material, Ostwald ripening could be verified.

At the end of this chapter, the uniqueness of the system with its smectic islands on a smectic film of the same material should be underlined. It is the first (quasi-two-dimensional) coarsening experiment in which flat domains can be observed on a thin film, that are only separated from the background medium by dislocation in the structure of the material. The liquid crystal material itself is the same for the islands as well as for the thin film. This peculiarity allows the consideration, that individual mesogens from the shrinking islands, not necessarily need to move through the film to the corresponding growing domain. It is also conceivable that the mesogens enter the film, rearrange themselves in the film and that a completely different molecule on the other side leaves the film and attaches itself to the growing island. Under this assumption, the distance between two material-exchanging islands becomes insignificant and also the idea of a Poiseuille flow does not seem to apply.

The verification of such an Ostwald ripening without direct flow of material between two domains seems almost impossible. First, the smectic bubble system with a comparable very small meniscus at the inflation needle only exists under microgravity conditions, when buoyancy and sedimentation effects are suppressed and the influence of the meniscus can be neglected. Furthermore, for Ostwald ripening, several minutes of microgravity are necessary that actually can only be provided by the International Space Station or satellites. With new experiments onboard the ISS, the changes of the c-director of the smectic C films could possibly be observed with a high temporal resolution to verify a transport (or absent molecule transport) through the film between islands. For the smectic A phase, the situation becomes more difficult, since there is no observable structural difference between real molecule transport or just rearrangement of the mesogens. One way to track the flow of material in that films could be the usage of fluorescent nanoparticles added to the smectic material, or the observation of photo-bleached regions in the film doped with small amounts of a fluorescent dye, as shown by Missaoui et al. [211].

5 Summary and Outlook

In the present work, the self-organization and the dynamics of different liquid inclusions in free-standing smectic films were investigated experimentally. Parts of the experiments were performed at the International Space Station under microgravity conditions, and the evaluation of that data is an important aspect of that thesis. In addition to other scientifically published phenomena, the following topics are described in this work.

- Free-standing liquid crystal films and experiments under microgravity conditions
- Self-organization of micrometer-sized isotropic droplets in a lattice-like structure on the surface of a smectic liquid crystal bubble
- Coalescence of micrometer-sized isotropic droplets in a quasi-two-dimensional free-standing smectic films
- Self-similarity behavior of the evolution of the bridge connecting two isotropic droplets during coalescence
- Coarsening dynamics of smectic islands on the surface of a smectic liquid crystal bubble based on direct island coalescence and Ostwald ripening

Within the OASIS ISS mission (Observation and Analysis of Smectic Islands in Space), smectic liquid crystal bubbles were created and inclusions on their surface were observed for several minutes up to hours. Isotropic droplets were prepared by heating the smectic material close to the smectic to isotropic phase transition temperature at approximately 51.1 °C. For the first time, a colloidal system consisting of flat isotropic droplets in a free-standing smectic A film was created and showed a self-organization in a lattice-like structure. Locally, regular hexagonal cells with a mean lattice constant, describing the side length of the hexagon, could be found. A linear dependence of the distance of neighboring droplets on their radii was observed, i.e. the mean lattice constant increases with increasing droplet sizes. The aspect ratio defined as the mean lattice constant divided by the droplet radius was introduced as an important geometrical parameter.
The dynamics of the droplets within their hexagonal lattice were analyzed by assuming electrostatic interactions and measuring the spatial distribution of the position of the central droplet inside the hexagonal cage. In addition, the mean square displacement (MSD) of the particle motion with respect to its initial position in the lattice confinement was measured. Assuming a particle motion in a parabolic potential, the Smoluchowski equation with its asymptotic behavior was used to fit the experimental data. The diffusion constant as well as the force constant could be extracted from the MSD measurements, respectively the Boltzmann distribution densities. Numerical simulations of the flow field around the inclusions in a hexagonal lattice verified the experimental data. Furthermore, the simulations showed that the Saffmann and Delbrück model for the description of the mobility of circular objects in a two-dimensional system seems to fail at very small aspect ratios. For the repulsive interactions of the droplets and the resulting arrangement

in a lattice, electrical charges due to a partial degradation of the material or free radicals accumulated in the isotropic droplets are conceivable.
In comparison with other experiments dealing with the two-dimensional self-assembly of colloids, isotropic droplets in a smectic A liquid crystal film are not effected by a solid substrate [46, 54] or a liquid subphase [60, 61]. The experiments on the smectic bubble are unique and the repulsive interaction of the liquid droplets and their arrangement in lattice structure has not been observed before in smectic A films. Indeed, Völtz et al. [67] observed a similar structure of isotropic droplets in flat smectic C free-standing films, but the mutual interactions are here caused by elastic distortions of the c-director configuration and the defects in the film.

Under the influence of external forces, such as an effective gravitational force, the discussed repulsive interactions of the isotropic droplets in the free-standing smectic A film can be compensated and the droplets can be brought into direct contact. Upon overcoming a certain energetic barrier, the droplets then start to coalesce. This process has been analyzed in detail and compared to the merging process of droplets on solid substrates.
The experiments on the droplet coalescence were performed on flat free-standing films (in contrast to the ISS experiments) using high-speed imaging and interferometry measurements. The complete three-dimensional profile of the droplets, initially represented by spherical caps, could be recalculated at any time during the merging process. The initial shape of the droplets and finally the time for the whole coalescence process of nearly equal-sized droplets is determined by the material parameters (surface tension, viscosity), but also by the initial droplet radii R_0 and the contact angles θ with the smectic film. With increasing initial radii as well as with increasing contact angle, the time for coalescence t_{coal} is extended.
A crucial parameter for the characterization of the merging process in various systems is the bridge connecting both objects and their evolution during coalescence. As expected from different other experiments [119, 127, 135, 140], the bridge width and height exhibit a linear growth at the beginning and eventually saturate to the final diameter and height of the merged droplets, respectively. Both curves show the same trend, but the bridge's lateral extension is growing slightly faster than the bridge height. The evolution of the scaled bridge sizes (width and height) can not be convincingly fitted with a theoretical model by Hopper describing the coalescence of two infinitely long cylinders with assumed creeping plane flow [94–96].
On the basis of the thin sheet equation and the lubrication approximation, the scaling law for the coalescence time, i.e. the dependence of $t_{\mathrm{coal}}/\langle R_0\rangle$ on the initial droplet size $\langle R_0\rangle/H_0$, was derived for sessile droplets on solid substrates and for liquid droplets on thin free-standing films or liquid surfaces. For sessile droplets, assuming a flow gradient within the droplets perpendicular to the substrate (no-slip at the surface of the substrate), a cubic scaling behavior is predicted. In contrast to that, for merging droplets on thin films without this flow velocity gradient, a linear dependence is expected. This could be verified within the experimental data and using numerical simulations. In addition, the FEM (finite element method) simulations show in general a very good agreement with the experiment regarding the shape deformation of the droplets and the evolution of the bridge during coalescence. Nevertheless, the theoretical model as well as the simulation

predict coalescence times that are at least one order of magnitude smaller than the measured times.
This observed discrepancy can be explained in terms of the smectic layers covering the droplets and the energy required to rearrange molecules in these smectic layers and the isotropic droplet during the coalescence. A rough calculation of the melting energy of individual smectic layers (transition from the smectic to the isotropic phase) for a comparable liquid crystal material (8CB) resulted in energies per film area in the range of the (static) surface tension. A simulation of coalescing droplets with such a dynamic surface tension (static surface tension reduced by the melting energy) showed a very good agreement with the experimental data. The simulation thus confirms the assumption of a reduced dynamic surface tension during the coalescence process that could explain the discrepancy between the model and the experiment.

With regard to the work of Hack et al. [127] describing the coalescence of droplets on a liquid surface, a self-similarity behavior of the bridge shape was expected for merging isotropic droplets on smectic A films. The experimental data as well as the numerical simulations confirmed the self-similarity of the droplets profile at the position of the bridge. In contrast, the lateral extension of the droplets does not show this behavior. Additionally, the growth rates of the bridge height and width were calculated from their linear increase during the first moments of coalescence. While the growth rate of the bridge height depends quadratically on the contact angle with the film, as expected, the growth rate of the bridge width deviates from the predicted linear dependence. An analysis of the contact angle in the vicinity of the bridge during coalescence showed a significant decrease (up to 30%) of the initial contact angle, which may account for the observed deviation of the bridge width growth rate from the linear trend. Furthermore, this change of the contact angle again verifies the assumption of a reduced dynamic surface tension during the merging process.

The experiments described up to this point with isotropic droplets on various shaped smectic A free-standing films can be summarized as the dynamic behavior of three-dimensional or ($2+\varepsilon$)-dimensional objects in two-dimensional system. With the coarsening experiments of smectic islands on the surface of the smectic A bubble onboard the ISS, two-dimensional objects have now been observed in a two-dimensional film over minutes and hours. As expected from other experiments concerning foam coarsening [168, 188, 191, 212] or the behavior of droplet on solid substrates [164, 194, 199, 200, 202, 203], the mean island radius $\langle R \rangle \propto t^{\alpha}$, the total number of islands $N \propto t^{-\beta}$ and the average distance between islands $\langle \xi \rangle \propto t^{\delta}$ all followed power law dependencies with their specific exponents. The theoretical relation between these exponents of $\alpha = -0.5\beta = \delta$ was confirmed through recalculating the measured exponents for a constant total island area. The increase in the total island area observed during all experiments could be due to an additional flow of material from the meniscus around the bubble inflation needle into the film. On the other hand, the coalescence of islands of different thicknesses could also lead to a slight increase in the total island area.
The coalescence of smectic islands was verified as dominating process for the coarsening dynamics compared to the Ostwald ripening, at least for the analyzed experiments.

In addition, the exponents for the average islands radius and the total number of islands show a significant temperature dependency. Their absolute values increase sharply with increasing temperature, presumably due to a higher mobility of the islands at higher temperatures and thus an increased probability of coalescence.
The probability distributions of the island radii are positively skewed and their tail extend to larger values as time increases. If neglecting very small islands in the distributions due to the limited lateral resolution in the experiments, the probability distributions could be fitted using an exponential function. The distribution densities of the scaled islands radii (islands radii divided by the average island radius) additionally show some kind of a statistic self-similarity [164, 207, 208].
The second process leading to an overall coarsening dynamics of the smectic island emulsion, the Ostwald ripening, was observed for only a few islands in a magnified view on the surface of the smectic bubble. Within several minutes, material is exchanged between neighboring islands without direct contact, which could be confirmed in terms of the total area of the islands and their sum during the shrinking process of one of the islands. The shrinking process of the island itself seems to follow a square root law, where the strength of the material exchange depends on the thickness of the islands. A simple model, which takes into account the Laplacian pressure inside the islands and the flow of material through the shell of the islands, verifies this square root law and a decreasing strength of the shrinkage process with increasing island thickness.

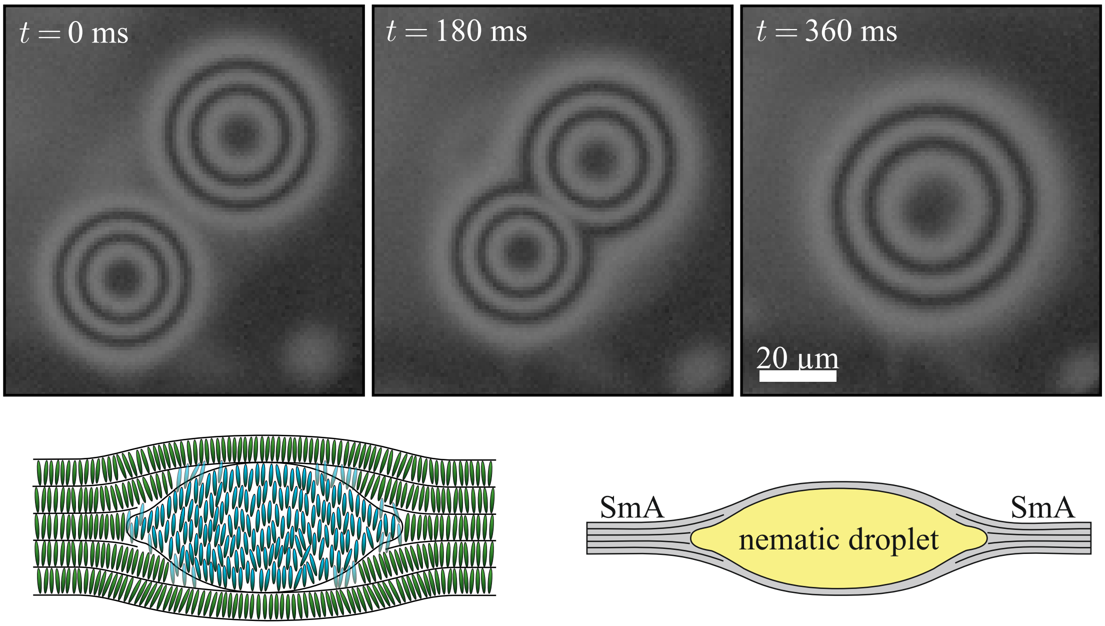

Figure 5.1: Coalescence of nematic droplets in a free-standing smectic A film. The initial droplet radii are approximately 25.7 µm and 23.1 µm. The entire merging process takes place within 360 ms, which is at least two orders of magnitude larger than for isotropic droplets. The sketches in the lower pictures represent a possible molecule arrangement in the nematic droplet (blue ellipses), covered by a smectic layer, and at the droplet edges. The real molecule configuration is not fully understood yet.

All the described experiments with their excellent results nevertheless raise some questions that need to be answered in future experiments.
The presumed electrical charges in the isotropic droplets that lead to the repulsive interactions should be verified using optical tweezers or by performing the same experiment, but with other materials, that might not show this effect of accumulated charges. A similar approach of replicate experiments, but with other materials, could also be used to analyze the effect of the smectic layers on the coalescence dynamics. It needs to be clarified whether the rearrangement of the molecules in the layered structure during coalescence really leads to a reduced dynamic surface tension and whether it could explain the discrepancy between the model and the experiment. In this context, experiments with droplets of an other liquid crystal phase, for example nematic droplets, could also help to fully understand the merging process of droplets in two-dimensional films and to verify the underlying model.
The sequence in figure 5.1 shows a preview of such an experiment of coalescing nematic droplets, where the structure and the profile of the droplets seem to differ from that of the isotropic droplets. In contrast to the isotropic droplets, the edges of the nematic droplets and the background film seem to blend into one another homogeneously.
With regard to the coarsening dynamics of smectic islands, it would be good to perform additional experiments, but with higher lateral resolution, to also identify very small islands and a larger ensemble over a long period of time. This could help to understand the overall growth of the island area and the crucial process behind the temperature dependence of the exponents of the power law. Additionally, the possible statistic self-similarity of the probability distributions of the island radii could be analyzed in more detail. As part of new experiments and with a (working) spectrometer to determine the thickness of the films and islands, the shrinking process of islands (Ostwald ripening) could also be analyzed in more detail with regard to the dependence of the strength of the material exchange on the thickness of the islands. Unfortunately, this particular type of experiments with these smectic liquid crystal emulsions and on these time scales can only be carried out on the International Space Station or satellites.

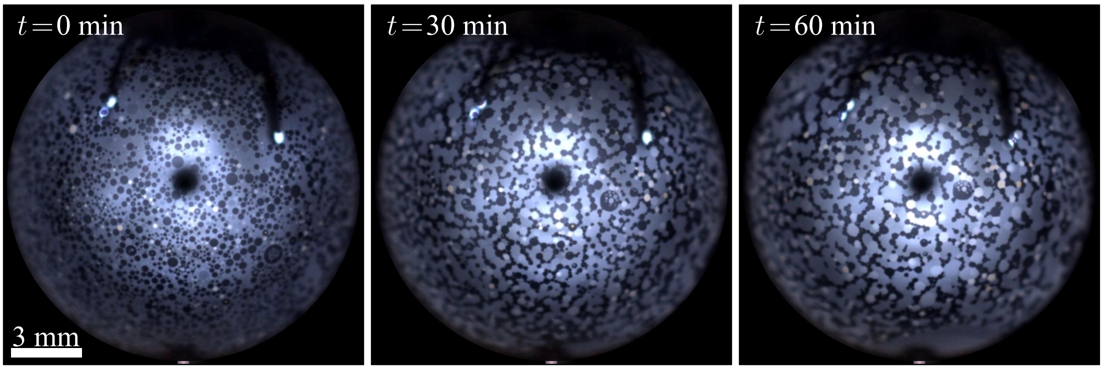

Figure 5.2: Sequence of experimental images showing the coarsening process of smectic holes on the surface of the smectic liquid crystal bubble during the OASIS ISS mission. Within 60 minutes, the smectic holes (darker regions) accumulate and form chain-like structures. Unlike the coarsening of smectic islands, the holes do not merge.

However, there are some not yet evaluated phenomena observed during the OASIS mission that need to be analyzed. One example is shown in figure 5.2. Two-dimensional smectic holes representing circular regions with less smectic layers than the background films were in that case created on the smectic bubble and observed over more than one hour. Since smectic islands and smectic holes are structural very similar (more or less smectic layers than the background film), a long-term behavior comparable to that of smectic islands could be assumed. Unexpectedly, as shown in the figure, the holes do not merge but form chain like structures. One of many tasks is therefore the evaluation and interpretation of this existing raw data to further complete the understanding of the coarsening dynamics of two-dimensional objects in two-dimensional systems.

A little off the topic of this work, but related to the current research, new and partly not yet fully understood phenomena keep emerging during the investigation and characterization of smectic films themselves. In recent years, the formation of wrinkles (until then only known from stiff solid sheets) and perturbations on freely floating smectic bubbles have been investigated and described by theoretical models. In addition, the general influence of external acoustic stimuli and the effect of specific parameters such as frequency or amplitude of the sound waves on the wrinkle formation was analyzed. In this context, the same phenomena could be observed in a flat free-standing film represented by a central equatorial film during the collapse of smectic catenoid-shaped films. Under fast lateral compression, wrinkle formations and their dependence on the local film thickness could be analyzed [34]. Further experiments, also with different materials, are necessary to validate the first observations and the underlying model.

In addition, further experiments with rupturing catenoid-shaped films and freely floating smectic bubbles will be carried out in the next few months to investigate the influence of electric fields on the smectic films. As previously shown by Stannarius et al. [79], homogeneous electric fields in the vicinity of the smectic bubbles could for example lead to an induced motion of smectic islands and new structures such as the “pearl chains” described. Furthermore, the effect of electric fields on the rupturing dynamics of smectic catenoid-shaped films should be analyzed in general.

The topics discussed and analyzed in this thesis, and various additional experiments, confirm the importance of free-standing smectic films for investigating fundamental physical questions. In this sense, quasi-two-dimensional smectic films are used to study the 2D hydrodynamics of different inclusions. In some cases, known physical principles and laws have to be adapted for the 2D system or completely new models have to be derived.

As part of this research, the described experiments on isotropic droplets in free-standing smectic A films, their arrangement in lattice structures, their coalescence in flat films, and the coarsening dynamics of smectic islands represent unique experiments and improve the understanding of the two-dimensional hydrodynamics. On the other hand, the shown results additionally enhance the general understanding for specific phenomena as the coalescence of objects or the coarsening of emulsions independent on the smectic free-standing films or the two-dimensional system.

This work therefore represents an important and unique scientific contribution to the study of the hydrodynamics of inclusions in two-dimensional systems.

Bibliography

[1] P. J. Collins and J. W. Goodby. *Introduction to Liquid Crystals: Chemistry and Physics*. CRC Press, Taylor and Fracis Group, Boca Raton (Florida, US), 1997.

[2] J. W. Goodby, P. J. Collins, T. Kato, C. Tschierske, H. Gleeson, and P. Raynes. *Handbook of Liquid Crystals, Volume 1: Fundamentals of liquid crystals*. Wiley-VCH., Weinheim, 2014.

[3] J. W. Goodby, P. J. Collins, T. Kato, C. Tschierske, H. Gleeson, and P. Raynes. *Handbook of Liquid Crystals, Volume 8: Applications of liquid crystals*. Wiley-VCH., Weinheim, 2014.

[4] F. Reinitzer. Beiträge zur Kenntniss des Cholesterins. *Monatshefte für Chemie*, 9:421–441, 1888.

[5] F. Reinitzer. Contribution to the knowledge of cholesterols. *Liq. Cryst.*, 5(1):7–18, 1989.

[6] H. Kelker and P. Knoll. Plenary lecture: Some pictures of the history of liquid crystals. *Liq. Cryst.*, 5(1):19–24, 1989.

[7] O. Lehmann. Über fliessende Kristalle. *Z. Phys. Chem.*, 4:462, 1889.

[8] P. Oswald and P. Pieranski. *Smectic and columnar liquid crystals: concepts and physical properties illustrated by experiments*. CRC Press, Taylor and Fracis Group, Boca Raton (Florida, US), 2006.

[9] C. Y. Young, R. Pindak, N. A. Clark, and R. B. Meyer. Light-Scattering Study of Two-Dimensional Molecular-Orientation Fluctuations in a Freely Suspended Ferroelectric Liquid-Crystal Film. *Phys. Rev. Lett.*, 40(12):773–776, 1978.

[10] C. Rosenblatt, R. Pindak, N. A. Clark, and R. B. Meyer. Freely Suspended Ferroelectric Liquid-Crystal Films: Absolute Measurements of Polarization, Elastic Constants, and Viscosities. *Phys. Rev. Lett.*, 42(18):1220–1223, 1979.

[11] R. A. Pelcovits and B. I. Halperin. Two-dimensional ferroelectric liquid crystals. *J. Appl. Phys.*, 50(3):1796–1798, 1979.

[12] C. Rosenblatt and N. M. Amer. Optical determination of smectic A layer spacing in freely suspended thin films. *Appl. Phys. Lett.*, 36(6):432–434, 1980.

[13] C. D. Muzny and N. A. Clark. Direct Observation of the Brwonian Motion of a Liquid-Crystal Topological Defect. *Phys. Rev. Lett.*, 68(6):804–807, 1992.

[14] J-C. Géminard, R. Holyst, and P. Oswald. Meniscus and Dislocations in Free-Standing Films of Smectic-A Liquid Crystal. *Phys. Rev. Lett.*, 78(10):1924–1927, 1997.

[15] F. Picano, R. Holyst, and P. Oswald. Coupling between meniscus and smectic-A films: Circular and catenoid profiles, induced stress, and dislocation dynamics. *Phys. Rev. E*, 62(3):3747–3757, 2000.

[16] F. Picano, P. Oswald, and E. Kats. Disjoining pressure and thinning transition in smectic-A liquid crystal films. *Phys. rev. E*, 63(021705):1–9, 2000.

[17] H. Schüring and R. Stannarius. Isotropic Droplets in Thin Free Standing Smectic Films. *Langmuir*, 18:9735–9743, 2002.

[18] C. Bohley and R. Stannarius. Inclusions in free standing smectic liquid crystal films. *Soft Matter*, 4:683–702, 2008.

[19] Z. H. Nguyen, M. Atkinson, C. S. Park, J. E. Maclennan, M. Glaser, and N. A. Clark. Crossover between 2D and 3D Fluid Dynamics in the Diffusion of Islands in Ultrathin Freely Suspended Smectic Films. *Phys. Rev. Lett.*, 105:268304, 2010.

[20] A. Eremin, S. Baumgarten, K. Harth, R. Stannarius, Z. H. Nguyen, A. Goldfain, C. S. Park, J. E. Maclennan, M. A. Glaser, and N. A. Clark. Two-Dimensional Microrheology of Freely Suspended Liquid Crystal Films. *Phys. Rev. Lett.*, 107:268301, 2011.

[21] K. May, K. Harth, T. Trittel, and R. Stannarius. Freely floating smectic films. *ChemPhysChem*, 15:1508–1518, 2014.

[22] T. Trittel, K. Harth, and R. Stannarius. Smectic C to smectic A transition induced mechanically by the rupture of freely suspended liquid crystal films. *Soft Matter*, 13:3199, 2017.

[23] C. Klopp, T. Trittel, A. Eremin, K. Harth, R. Stannarius, C. S. Park, J. E. Maclennan, and N. A. Clark. Structure and dynamics of a two-dimensional colloid of liquid droplets. *Soft Matter*, 15:8156, 2019.

[24] R. Stannarius, T. Trittel, C. Klopp, A. Eremin, K. Harth, N. A. Clark, C. S. Park, and J. E. Maclennan. Freely suspended smectic films with in-plane temperature gradients. *New J. Phys.*, 21:063033, 2019.

[25] P. Dähmlow, T. Trittel, K. May, K. Harth, and R. Stannarius. Surface reduction of freely floating smectic bubbles. *Liq. Cryst.*, 45(7):993–1003, 2018.

[26] K. Harth, T. Trittel, K. May, and R. Stannarius. Dynamic wrinkling of freely floating smectic films. *Soft Matter*, 15:6769, 2019.

[27] K. Harth and R. Stannarius. Deep Holes in Free-Standing Smectic C Films. *Ferroelectrics*, 468:92–100, 2014.

[28] K. May, K. Harth, T. Trittel, and R. Stannarius. Dynamics of freely floating smectic bubbles. *EPL*, 100:16003, 2012.

[29] A. Missaoui, K. Harth, P. Salamon, and R. Stannarius. Annihilation of point defect pairs in freely suspended liquid-crystal films. *Phys. Rev. Research*, 2:023307, 2020.

[30] K. Harth and R. Stannarius. Toplogical Point Defects of Liquid Crystals in Quasi-Two-Dimensional Geometries. *Front. Phys.*, 8:112, 2020.

[31] T. Trittel, K. Harth, C. Klopp, and R. Stannarius. Marangoni Flow in Freely Suspended Liquid Films. *Phys. Rev. Lett.*, 122:234501, 2019.

[32] T. Trittel. Statische und dynamische Eigenschaften dünner smektischer Filme. Dissertation, Otto von Guericke University, Magdeburg, 2020.

[33] M. I. Godfrey and D. H. Van Winkle. Surface-tension-gradient-induced flow in freely suspended liquid crystalline films. *Phys. Rev. E*, 54(4):3752–3764, 1996.

[34] C. Klopp, T. Trittel, K. Harth, and R. Stannarius. Smectic free-standing films under fast lateral compression. *Soft Matter*, 18:146–155, 2022.

[35] N. A. Clark, A. Eremin, M. A. Glaser, N. Hall, K. Harth, C. Klopp, J. E. Maclennan, C. S. Park, R. Stannarius, P. Tin, W. N. Thurmes, and T. Trittel. Realization of hydrodynamic experiments on quasi-2D liquid crystal films in microgravity. *ASR*, 60:737–751, 2017.

[36] G. G. Stokes. On the effect of internal friction of fluids on the motion of pendulums. *Transactions of the Cambridge Philosophical Society*, 9:8–106, 1850.

[37] A. N. Whitehead. Second Approximations to Viscous Fluid Motion: A Sphere Moving Steadily in a Straight Line. *Quart. J. Math*, 23:143–152, 1888.

[38] C. W. Oseen. Über die Stokes'sche Formel und über eine verwandte Aufgabe in der Hydrodynamik. *Arkiv för Matematik, Astronomi och Pysik*, 6:29, 1910.

[39] P. G. Saffman and M. Delbrück. Brownian motion in biological membranes. *Proc. Nat. Acad. Sci. USA*, 72:3111–3113, 1975.

[40] P. G. Saffman. Brownian motion in thin sheets of viscous fluid. *J. Fluid Mech.*, 73:593, 1976.

[41] R. Peters and R. J. Cherry. Lateral and rotational diffusion of bacteriorhodopsin in lipid bilayers: experimental test of the Saffman-Delbrück equations. *Proc. Natl. Acad. Sci. USA*, 79:4317–4321, 1982.

[42] K. Simons and E. Ikonen. Functional rafts in cell membranes. *Nature*, 387:569–572, 1997.

[43] P. Cicuta, S. L. Keller, and S. L. Veatch. Diffusion of Liquid Domains in Lipid Bilayer Membranes. *J. Phys. Chem. B*, 111:3328–3331, 2007.

[44] B. D. Hughes, B. A. Pailthorpe, and L. R. White. The translational and rotational drag on a cylinder moving in a membrane. *J. Fluid Mech.*, 110:349–372, 1981.

[45] E. P. Petrov and P. Schwille. Translational Diffusion in Lipid Membranes beyond the Saffman-Delbrück Approximation. *Biophys. J.*, 94:L41–L43, 2008.

[46] V. Lotito and T. Zambelli. Approaches to self-assembly of colloidal monolayers: A guide for nanotechnologists. *Adv. Colloid Interface Sci.*, 246:217–274, 2017.

[47] R. van Dommelen, P. Fanzio, and L. Sassa. Surface self-assembly of colloidal crystals for micro- and nano-patterning. *Adv. Colloid Interf. Sci.*, 251:97–114, 2018.

[48] G. R. Cagnani, E. R. Spada, L. D. Cagnani, B. B. M. Torres, D. T. Balogh, M. Bardosova, and R. M. Faria. Large-area flexible 2D-colloidal crystals produced directly using roll-to-roll processing. *Colloids Surf. A Physicochem. Eng. Asp.*, 588:124389, 2020.

[49] A. Corker, H. C.-H. Ng, R. J. Poole, and E. Garcia-Tunon. 3D printing with 2D colloids: designing rheology protocols to predict 'printability' of soft-materials. *Soft Matter*, 15:1444–1456, 2019.

[50] A. L. Thorneywork, D. G. A. L. Aarts, J. Horbach, and R. P. A. Dullens. Self-diffusion in two-dimensional binary colloidal hard-sphere fluids. *Phys. Rev E*, 95:012614, 2017.

[51] S. Vivek and E. R. Weeks. Decoupling of translational and rotational diffusion in quasi-2D colloidal fluids. *J. Chem. Phys.*, 147:134502, 2017.

[52] F. J. Maier and T. M. Fischer. Critical nucleation mesh-size of coarsening transient colloidal networks. *Soft Matter*, 12:614, 2016.

[53] P. A. Kralchevsky, N. D. Denkov, V. N. Paunov, O. D. Delev, I. B. Ivanov, H. Yoshimura, and K. Nagayama. Formation of two-dimensional colloid crystals in liquid films under the action of capillary forces. *Phys.: Condens. Matter*, 6:A395, 1994.

[54] I. Williams, E. C. Oguz, P. Bartlett, H. Löwen, and C. P. Royall. Direct measurement of osmotic pressure via adaptive confinement of quasi hard disc colloids. *Nat. Commun.*, 4:2555, 2013.

[55] A. H. Marcus and S. A. Rice. Phase transitions in a confined quasi-two-dimensional colloid suspension. *Phys. Rev. E: Stat. Phys., Plasmas, Fluids, Relat. Interdiscip. Top.*, 55:637, 1997.

[56] R. Bubeck, C. Bechinger, S. Neser, and P. Leiderer. Melting and Reentrant Freezing of Two-Dimensional Colloidal Crystals in Confined Geometry. *Phys. Rev. Lett.*, 82(16):3364–3367, 1999.

[57] C. Bechinger and E. Frey. Phase behaviour of colloids in confining geometry. *J. Phys.: Condens. Matter*, 13:R321–R336, 2001.

[58] C. Eisenmann, U. Gasser, P. Keim, and G. Maret. Anisotropic Defect-Mediated Melting of Two-Dimensional Colloidal Crystals. *Phys. Rev. Lett.*, 93:105702, 2004.

[59] C. Alba-Simionesco, B. Coasne, G. Dosseh, G. Dudziak, K. E. Gubbins, R. Radhakrishnan, and M. Sliwinska-Bartkowiak. Effects of confinement on freezing and melting. *J. Phys.: Condens. Matter*, 18:R15–R68, 2006.

[60] P. Dillmann, G. Maret, and P. Keim. Comparison of 2D melting criteria in a colloidal system. *J. Phys.: Condens. Matter*, 24(464118):1–11, 2012.

[61] P. Dillmann, G. Maret, and P. Keim. Two-dimensional colloidal systems in time-dependent magnetic fields -How to define crystallinity in 2D on a local scale-. *Eur. Phys. J. Special Topics*, 222:2941–2959, 2013.

[62] D. Du, M. Doxastakis, E. Hilou, and S. L. Biswal. Two-dimensional melting of colloids with long-range attractive interactions. *Soft Matter*, 13:1548–1553, 2017.

[63] A. L. Thorneywork, J. L. Abbott, D. G. A. L. Aarts, and R. P. A. Dullens. Two-Dimensional Melting of Colloidal Hard Spheres. *Phys. Rev. Lett.*, 118:158001, 2017.

[64] A. L. Thorneywork, J. L. Abbott, D. G. A. L. Aarts, P. Keim, and R. P. A. Dullens. Bond-orientational order and Frank's constant in two-dimensional colloidal hard spheres. *J. Phys.: Condens. Matter*, 30:104003, 2018.

[65] N. P. Kryuchkov, F. Smallenburg, A. V. Ivlev, S. O. Yurchenko, and H. Löwen. Phase diagram of two-dimensional colloids with Yukawa repulsion and dipolar attraction. *J. Chem. Phys.*, 150:104903, 2019.

[66] G. N. Sethumadhavan, A. D. Nikolov, and D. T. Wasan. Stability of Liquid Films Containing Monodisperse Colloidal Particles. *J. Colloid Interface Sci.*, 240:105–112, 2001.

[67] C. Völtz and R. Stannarius. Self-organization of isotropic droplets in smectic-C free-standing films. *Phys. Rev. E*, 70:061702, 2004.

[68] D. Pettey, T. C. Lubensky, and D. R. Link. Topological inclusions in 2D smectic C films. *Liq. Cryst.*, 25:579–587, 1998.

[69] P. Cluzeau, P. Poulin, G. Joly, and H.T. Nguyen. Interactions between colloidal inclusions in two-dimensional smectic-C* films. *Phys. Rev. E.*, 63(031702):1–4, 2001.

[70] P. Cluzeau, G. Joly, H.T. Nguyen, and V. K. Dolganov. Two-Dimensional Ordering of Inclusions in Smectic C Phase. *JETP Lett.*, 75(9):482–486, 2002.

[71] P. Cluzeau, V. Bonnand, G. Joly, V. Dolganov, and H.T. Nguyen. Self-organization of N* inclusions in SmC* free-standing films. *Eur. Phys. J. E.*, 10:231–240, 2003.

[72] P.V. Dolganov, E.I. Demikhov, V.K. Dolganov, B.M. Bolotin, and K. Krohn. Collective behavior of light-induced droplets in smectic membranes. *Eur. Phys. J. E.*, 12:593–597, 2003.

[73] P.V. Dolganov and V.K. Dolganov. Director configuration and self-organization of inclusions in two-dimensional smectic membranes. *Phys. Rev. E.*, 73(041706):1–10, 2006.

[74] C. Bohley and R. Stannarius. Energetics of 2D colloids in free-standing smectic-c films. *Eur. Phys. J. E.*, 20:299–308, 2006.

[75] C. Bohley and R. Stannarius. Colloidal inclusions in smectic films with spontaneous bend. *Eur. Phys. J. E.*, 23:25–30, 2007.

[76] S. P. Radzihovsky, C. Cranfill, Z. Nguyen, C. S. Park, J. E. Maclennan, M. A. Glaser, and N. A. Clark. Two-dimensional island emulsions in ultrathin, freely-suspended smectic liquid crystal films. *Soft Matter*, 13:6314, 2017.

[77] N. A. Clark and J. E. Maclennan. private communication, Sep. 2017.

[78] M. A. Gharbi, D. A. Beller, N. Sharifi-Mood, R. Gupta, R. D. Kamien, S. Yang, and K.J. Stebe. Elastocapillary Driven Assembly of Particles at Free-Standing Smectic-A films. *Langmuir*, 34:2006–2013, 2018.

[79] R. Stannarius and C. Cramer. Self-supporting bubbles of thermotropic smectic liquid crystals. *Europhys. Lett.*, 42:43–48, 1998.

[80] A. Einstein. Über die von der molekularkinetischen Theorie der Wärme geforderte Bewegung von in ruhenden Flüssigkeiten suspendierten Teilchen. *Annalen der Physik*, 17:549–560, 1905.

[81] C. Klopp, T. Trittel, and R. Stannarius. Self similarity of liquid droplet coalescence in a quasi-2D free-standing liquid-crystal film. *Soft Matter*, 16:4607, 2020.

[82] C. Klopp and A. Eremin. On Droplet Coalescence in Quasi-Two-Dimensional Fluids. *Langmuir*, 36:10615–10621, 2020.

[83] L. Rayleigh. On the Instability of Jets. *Proc. London Math. Soc.*, s1-10:4–13, 1878.

[84] L. Rayleigh. The Influence of Electricity on Colliding Water Drops. *Proc. R. Soc. London*, 28:405–409, 1879.

[85] L. Rayleigh. On the Capillary Phenomena of Jets. *Proc. R. Soc. London*, 29:71–79, 1879.

[86] L. Rayleigh. On the Stability, or Instability, of certain Fluid Motions. *Proc. London Math. Soc.*, s1-11:57–72, 1879.

[87] L. Rayleigh. Further Observations upon Liquid Jets, in Continuation of Those Recorded in the Royal Society's 'Proceedings' for March and May, 1879. *Proc. R. Soc. London*, 34:130–145, 1882.

[88] L. Rayleigh. On the Stability, or Instability, of certain Fluid Motions, (II). *Proc. London Math. Soc.*, s1-19:67–75, 1887.

[89] L. Rayleigh. On the Stability, or Instability, of certain Fluid Motions (III.). *Proc. London Math. Soc.*, s1-27:5–12, 1895.

[90] C. V. Boys. Experiments with soap-bubbles. *Philos. Mag*, 25:409–419, 1888.

[91] C.D. Hendricks. *Investigation of Water Droplet Coalescence: Final Report*. Illinois State Water Survey. Contract Report. Illinois State Wataer Survey, 1963.

[92] S. G. Bradley and C. D. Stow. Collisions between liquid drops. *Philos. Trans. R. Soc., A*, 287(1349):635–678, 1978.

[93] V. V. Skorokhod. Development of the ideas of Ya. I. Frenkel' in the contemporary rheological theory of sintering. *Powder Metall. Met. Ceram.*, 34:521–527, 1996.

[94] R. W. Hopper. Coalescence of Two Equal Cylinders: Exact Results for Creeping Viscous Plane Flow Driven by Capillarity. *J. Am. Ceram. Soc.*, 67:262–264, 1984.

[95] R. W. Hopper. Coalescence of Two Viscous Cylinders by Capillarity: Part I, Theory. *J. Am. Ceram. Soc.*, 76:2947–2952, 1993.

[96] R. W. Hopper. Coalescence of Two Viscous Cylinders by Capillarity: Part II, Shape Evolution. *J. Am. Ceram. Soc.*, 76:2953–2960, 1993.

[97] A. C. Ihnen, A. M. Petrock, T. Chou, B. E. Fuchs, and W. Y. Lee. Organic Nanocomposite Structure Tailored by Controlling Droplet Coalescence during Inkjet Printing. *ACS Appl. Mater. Interfaces*, 4:4691–4699, 2012.

[98] M. Eslamian and F. Soltani-Kordshuli. Development of multiple-droplet drop-casting method for the fabrication of coatings and thin solid films. *J. Coat. Technol. Res.*, 15:271–280, 2018.

[99] H. D. Goff. Instability and partial coalescence in whippable dairy emulsions. *J. Dairy Sci.*, 80:2620–2630, 1997.

[100] A. Perazzo, G. Tomaiuolo, V. Preziosi, and S. Guido. Emulsions in porous media: From single droplet behavior to applications for oil recovery. *Adv. Colloid Interface Sci.*, 256:305–325, 2018.

[101] L. G. Leal. Flow induced coalescence of drops in a viscous fluid. *Phys. Fluids*, 16:1833, 2004.

[102] J. C. Burton and P. Taborek. Role of Dimensionality and Axisymmetry in Fluid Pinch-Off and Coalescence. *Phys. Rev. Lett.*, 98(224502):1–4, 2007.

[103] M. Wu, T. Cubaud, and C-M. Ho. Scaling law in liquid drop coalescence driven by surface tension. *Phys. Fluids*, 16:L51, 2004.

[104] D. G. A. L. Aarts, H. N. W. Lekkerkerker, H. Guo, G. H. Wegdam, and D. Bonn. Hydrodynamics of Droplet Coalescence. *Phys. Rev. Lett.*, 95(164503):1–4, 2005.

[105] W. Yao, H. J. Maris, P. Pennington, and G. M. Seidel. Coalescence of viscous liquid drops. *Phys. Rev. E*, 71:016309, 2005.

[106] J.D. Paulsen, J. C. Burton, and S. R. Nagel. Viscous to Inertial Crossover in Liquid Drop Coalescence. *Phys. Rev. Lett.*, 106:114501, 2011.

[107] J.D. Paulsen, J. C. Burton, S. R. Nagel, S. Appathurai, M. T. Harris, and A. Basaran. The inexorable resistance of inertia determines the initial regime of drop coalescence. *Proc. Natl. Acad. Sci. USA*, 109:6857–6861, 2012.

[108] J.D. Paulsen. Approach and coalescence of liquid drops in air. *Phys. Rev. E*, 88:063010, 2013.

[109] J.D. Paulsen R. Carmigniani, A. Kannan, J. C. Burton, and S. R. Nagel. Coalescence of bubbles and drops in an outer fluid. *Nat. Commun.*, 5:3182, 2014.

[110] J. E. Sprittles and Y. D. Shikhmurzaev. Coalescence of liquid drops: Different models versus experiment. *Phys. Fluids*, 24:122105, 2012.

[111] J. E. Sprittles and Y. D. Shikhmurzaev. The coalescence of liquid drops in a viscous fluid: interface formation model. *J. Fluid Mech.*, 751:480–499, 2014.

[112] S. T. Thoroddsen and B. Qian. The initial coalescence of miscible drops. *Phys. Fluids*, 19:072110, 2019.

[113] X. Xia, C. He, and P. Zhang. Universality in the viscous-to-inertial coalescence of liquid droplets. *Proc. Natl. Acad. Sci. USA*, 116:23467–23472, 2019.

[114] J. Eggers, J. R. Lister, and H. A. Stone. Coalescence of liquid drops. *J. Fluid Mech*, 401:293–310, 1999.

[115] R. D. Narhe, D. A. Beysens, and V. S. Nikolayev. Contact Line Dynamics in Drop Coalescence and Spreading. *Langmuir*, 20:1213–1221, 2004.

[116] N. Kapur and P. H. Gaskell. Morphology and dynamics of droplet coalescence on a surface. *Phys. Rev. E*, 75:056315, 2007.

[117] R. D. Narhe, D. A. Beysens, and Y. Pomeau. Dynamic drying in the early-stage coalescence of droplets sitting on a plate. *EPL*, 81:46002–46007, 2008.

[118] M. W. Lee, D. K. Kang, S. S. Yoon, and A. L. Yarin. Coalescence of Two Drops on Partially Wettable Substrates. *Langmuir*, 28:3791–3798, 2012.

[119] J. F. Hernández-Sánchez, L. A. Lubbers, A. Eddi, and J. H. Snoeijers. Symmetric and Asymmetric Coalescence of Drops on a Substrate. *Phys. Rev. Lett.*, 109:184502, 2012.

[120] A. Eddi, K. G. Winkels, and J. H. Snoeijer. Influence of Droplet Geometry on the Coalescence of Low Viscosity Drops. *Phys. Rev. Lett.*, 111:144502, 2013.

[121] Y. Sui, M. Maglio, P. D. M. Spelt, D. Legendre, and H. Ding. Inertial coalescence of droplets on a partially wetting substrate. *Phys. Fluids*, 25:101701, 2013.

[122] S. Moghtadernejad, M. Tembely, M. Jadidi, N. Esmail, and A. Dolatabadi. Shear driven droplet shedding and coalescence on a superhydrophobic surface. *Phys. Fluids*, 27:032106, 2015.

[123] Y. Zhang, S. D. Oberdick, E. R. Swanson, S. L. Anna, and S. Garoff. Gravity driven current during the coalescence of two sessile drops. *Phys. Fluids*, 27:022101, 2015.

[124] S. Moghtadernejad, M. Jadidi, N. Esmail, and A. Dolatabadi. Shear-driven droplet coalescence and rivulet formation. *Proc. Inst. Mech. Eng. C, J. Mech. Eng. Sci.*, 230:793–803, 2016.

[125] P. M. Somwanshi, K. Muralidhar, and Sameer Khandekar. Coalescence dynamics of sessile and pendant liquid drops placed on a hydrophobic surface. *Phys. Fluids*, 30:092103, 2018.

[126] N.D Pawar, S.S.Bahga, S. R. Kale, and S. Kondaraju. Symmetric and asymmetric coalescence of droplets on a solid surface in the inertia-dominated regime. *Phys. Fluids*, 531:092106, 2019.

[127] M. A. Hack, W. Tewes, Q. Xie, C. Datt, K. Harth, J. Harting, and J. H. Snoeijer. Self-Similar Liquid Lens Coalescence. *Phys. Rev. Lett.*, 124:194502, 2020.

[128] M. Sellier and E. Trelluyer. Modeling the coalescence of sessile droplets. *Biomicrofluidics*, 3:022412, 2009.

[129] M. Sellier, Y. C. Lee, H. M. Thompson, and P. H. Gaskell. Thin film flow on surfaces containing arbitrary occlusions. *Comput. Fluids*, 38:171–182, 2009.

[130] M. Ahmadlouydarab, C. Lan, A. K. Das, and Y. Ma. Coalescence of sessile microdroplets subject to a wettability gradient on a solid surface. *Phys. Rev. E*, 94(033112):1–12, 2016.

[131] M. I. Khodabocus, M. Sellier, and V. Nock. Scaling Laws of Droplet Coalescence: Theory and Numerical Simulation. *Adv. Math. Phys.*, 2018:1–16, 2018.

[132] U. Delabre and A.-M. Cazabat. Coalescence Driven by Line Tension in Thin Nematic Films. *Phys. Rev. Lett.*, 104(227801):1–4, 2010.

[133] D. H. Nguyen. Smectic liquid crystal freely suspended films: Testing beds for the physics in thin membranes. Dissertation, University of Colorado, Boulder, 2011.

[134] P.V. Dolganov, N. S. Shuravin, E.I. Kats, and V.K. Dolganov. Coalescence of Islands of Different Thicknesses in Smectic Nanofilms. *JEPT Lett.*, 110(8):545–550, 2019.

[135] N. S. Shuravin, P. V. Dolganov, and V. K. Dolganov. Coalescence of viscous two-dimensional smectic islands. *Phys. Rev. E*, 99:062702, 2019.

[136] P.V. Dolganov, N. S. Shuravin, and V.K. Dolganov. Coalescence of holes in two-dimensional free-standing smectic films. *Phys. Rev. E.*, 101(052701):1–5, 2020.

[137] P.V. Dolganov, N. S. Shuravin, V.K. Dolganov, and E. I. Kats. Dynamics of island-meniscus coalescence in free-standing smectic films. *Soft Matter*, 16:8506–8511, 2020.

[138] E. S. Pikina and B. I. Ostrovskii andS. A. Pikin. Coalescence of isotropic droplets in overheated free standing smectic films. *Soft Matter*, 16:4591–4606, 2020.

[139] Z. H. Nguyen, K. Harth, A. M. Goldfain C. S. Park, J. E. Maclennan, M. Glaser, and N. A. Clark. Coalescence of Islands in Freely-Suspended Smectic Films. *Phys. Rev. Res*, 3:033143, 2021.

[140] S. Mitra and S. K. Mitra. Symmetric drop coalescence on an under-liquid substrate. *Phys. Rev. E*, 92:033013, 2015.

[141] P. D. Howell. Extensional thin layer flows. Dissertation, University of Oxford, Oxford, 1994.

[142] P. H. Gaskell, P. K. Jimack, M. Sellier, and H. M. Thompson. Efficient and accurate time adaptive multigrid simulations of droplet spreading. *Int. J. Numer. Meth. Fluids*, 45:1161–1186, 2004.

[143] W. Mertienssen and H. Warlimont. *Springer Handbook of Condensed Matter and Materials Data.* Springer-Verlag GmbH Berlin Heidelberg New York, 2005.

[144] S. Morris, M. Sellier, and A. R. A. Behadili. Comparison of Lubrication Approximation and Navier-Stokes Solutions for Dam-Break Flows in Thin Films. *arXiv*, arXiv:1708.00976, 2017.

[145] L. W. Schwartz and R. R. Eley. Simulation of Droplet Motion on Low-Energy and Heterogeneous Surfaces. *J. Colloid Interface Sci.*, 202:173–188, 1998.

[146] R. Weiqing and E. Weinan. Boundary conditions for the moving contact line problem. *Phys. Fluids*, 19:022101, 2007.

[147] B. Mandelbrot. How Long Is the Coast of Britain? Statistical Self-Similarity and Fractional Dimension. *Science*, 156:636–638, 1967.

[148] P. H. von Koch. Sur une courbe continue sans tangente abtenue par une construction géometrique élémentaire. *Arkiv för Matematik, Astronomi och Pysik*, 1:682, 1904.

[149] T. Erneux and S. H. Davis. Nonlinear rupture of free films. *Phys. Fluids A*, 5:1117–1122, 1993.

[150] R. Shimizu and H. Tanaka. A novel coarsening mechanism of droplets in immiscible fluid mixtures. *Nat. Commun.*, 6:7407, 2015.

[151] L. Ratke and P. W. Voorhees. *Growth and Coarsening - Ripening in Material Processing*. Springer-Verlag GmbH Berlin Heidelberg New York, 2002.

[152] J. A. Warren. Microstructural developement during the liquid-phase sintering of two-phase alloys, with special reference to the NbC/Co system. *J. Mat. Sci.*, 3:471–485, 1968.

[153] W. Ostwald. Über die vermeintliche Isomerie des roten und gelben Quecksilberoxyds und die Oberflächenspannung fester Körper. *Z. Phys. Chem.*, 34:495–503, 1900.

[154] I. M. Lifshitz and V. V. Slyozov. The kinetics of precipitation from supersaturated solid solutions. *J. Phys. Chem. Solids*, 19:35–50, 1961.

[155] C. Wagner. Theorie der Alterung von Niederschlägen durch Umlösen (Ostwald-Reifung). *Z. Elektrochemie*, 65:851–951, 1961.

[156] A. S. Kabalnov, A. V. Pertzov, and E. D. Shchukin. Ostwald ripening in emulsions: I. Direct observations of Ostwald ripening in emulsions. *J. Colloid Interface Sci.*, 118:590–597, 1987.

[157] S. C. Hardy and P. W. Voorhees. Ostwald Ripening in a System with a High Volume Fraction of Coarsening Phase. *Metall. Mater. Trans. A*, 19A:2713, 1988.

[158] A. S. Kabalnov, K. N. Makarov, A. V. Pertzov, and E. D. Shchukin. Ostwald ripening in emulsions: 2. Ostwald ripening in hydrocarbon emulsions: Experimental verification of equation for absolute rates. *J. Colloid Interface Sci.*, 138:98–104, 1990.

[159] B. Meerson. Fluctuations provide strong selection in Ostwald ripening. *Phys. Rev. E*, 60:3072–3075, 1999.

[160] B. Niethammer and R. L. Pego. Non-Self-Similar Behavior in the LSW Theory of Ostwald Ripening. *J. Stat. Phys.*, 95:867–902, 1999.

[161] B. Niethammer and F. Otto. Ostwald ripening: The screening length revisited. *Calc. Var.*, 13:33–68, 2000.

[162] B. Niethammer and R. L. Pego. On the Initial-Value Problem in the Lifshitz-Slyozov-Wagner Theory of Ostwald Ripening. *SIAM J. Math. Anal.*, 31:467–485, 2000.

[163] B. Niethammer and R. L. Pego. The LSW Model for Domain Coarsening: Asymptotic Behavior for Conserved Total Mass. *J. Stat. Phys.*, 104:1113–1144, 2001.

[164] R. Limary and P. F. Green. Dynamics of Droplets on the Surface of a Structured Fluid Film: Late-Stage Coarsening. *Langmuir*, 19:2419–2424, 2003.

[165] S. Thakur, P. A. Pullarkat, and P. B. Sunil Kumar. Coarsening through directed droplet coalescence in fluid-fluid phase separation. *Phys. Rev. E*, 80:011708, 2009.

[166] J. T. Mettetal. Coarsening dynamics of a quasi–one-dimensional driven lattice gas. *EPL*, 58:653–659, 2002.

[167] G. Kitavtsev. Coarsening rates for the dynamics of slipping droplets. *Eur. J. Appl. Math.*, 25:83–115, 2014.

[168] T. Trittel, T. John, and R. Stannarius. Smectic Foams. *Langmuir*, 26:7899–7904, 2010.

[169] F. Otto and E. Weinan. Thermodynamically driven incompressible fluid mixtures. *J. Chem. Phys.*, 107:10177, 1997.

[170] S. Hilgenfeldt, S. A. Koehler, and H. A. Stone. Dynamics of Coarsening Foams: Accelerated and Self-Limiting Drainage. *Phys. Rev. Lett.*, 86:4704–4707, 2001.

[171] V. Miralles, B. Selva, I. Cantat, and M.-C. Jullien. Foam Drainage Control Using Thermocapillary Stress in a Two-Dimensional Microchamber. *Phys. Rev. Lett.*, 112:238302, 2014.

[172] V. Miralles, E. Rio, I. Cantat, and M.-C. Jullien. Investigating the role of a poorly soluble surfactant in a thermally driven 2D microfoam. *Soft Matter*, 12:7056–7062, 2016.

[173] A. Kumar, C. Narayanam, R. Khanna, and S. Puri. Slow coarsening in unstable liquid films under gravity on a disordered substrate. *Phys. Rev. E*, 101:042801, 2020.

[174] H. Basoalto and M. Anderson. An extension of mean-field coarsening theory to include particle coalescence using nearest-neighbour functions. *Acta Mater.*, 117:122–134, 2016.

[175] L. Ratke, H. Fischmeister, and A. Kneissl. Coarsening of liquid Zn-Pb dispersions - A Spacelab Experiment. *Proc. 6th European Symp. Mat. Sci. Microgravity*, 256:161–167, 1986.

[176] L. Ratke. Coarsening of liquid Al-Pb dispersions under reduced gravity conditions. *Mat. Sci. Eng. A*, 203:399–407, 1995.

[177] H. Tanaka. New Coarsening Mechanisms for Spinodal Decomposition Having Droplet Pattern in Binary Fluid Mixture: Collision-Induced-Collisions. *Phys. Rev. Lett.*, 72:1702–1705, 1994.

[178] H. Tanaka. New mechanisms of droplet coarsening in phase-separating fluid mixtures. *J. Chem. Phys.*, 107:3734–3737, 1997.

[179] R. V. Kohn and F. Otto. Upper Bounds on Coarsening Rates. *Commun. Math. Phys.*, 229:375–395, 2002.

[180] S. J. Watson, F. Otto, B. Y. Rubinstein, and S. H. Davis. Coarsening dynamics of the convective Cahn-Hilliard equation. *Physica D*, 1178:127–148, 2003.

[181] I. Chuang, N. Turok, and B. Yurke. Late-Time Coarsening Dynamics in a Nematic Liquid Crystal. *Phys. Rev. Lett.*, 66:2472–2475, 1991.

[182] A. N. Pargellis, S. Green, and B. Yurke. Planar XY-model dynamics in a nematic liquid crystal system. *Phys. rev. E*, 49:4250–4257, 1994.

[183] S. Thakur, P. B. Sunil Kumar, N. V. Madhusudana, and P. A. Pullarkat. Self-Propulsion of Nematic Drops: Novel Phase Separation Dynamics in Impurity-Doped Nematogens. *Phys. Rev. Lett.*, 97:115701, 2006.

[184] A. Khedr and A. Striolo. Quantification of Ostwald Ripening in Emulsions via Coarse-Grained Simulations. *J. Chem. Theory Comput.*, 15:5058–5068, 2019.

[185] C. S. Smith. Grain Shapes and Other Metallurgical Applications of Topology. *Metal Interfaces*, pages 65–133, 1952.

[186] D. A. Aboav. The arrangement of cells in a net. *Metallography*, 13:43–58, 1980.

[187] J. Wejchert, D. Weaire, and J. P. Kermode. Monte Carlo simulation of the evolution of a two-dimensional soap froth. *Philos. Mag. B*, 53:15–24, 1986.

[188] J. A. Glazier, S. P. Gross, and J. Stavans. Dynamics of two-dimensional soap froths. *Phys. Rev. A*, 36:306–312, 1987.

[189] J. von Neumann. Metal interfaces. *(American Society for Metals, Cleveland*, 108, 1952.

[190] T. Trittel. Alterungsprozesse in zweidimensionalen Schäumen aus thermotropen Flüssigkristallen. Diploma thesis, Otto von Guericke University, Magdeburg, 2009.

[191] J. Marchalot, J. Lambert, I. Cantat, P. Tabeling, and M.-C. Jullien. 2D foam coarsening in a microfluidic system. *Europhys. Lett.*, 83:64006, 2008.

[192] N. Isert, G. Maret, and C. M. Aegerter. Coarsening dynamics of three-dimensional levitated foams: From wet to dry. *Eur. Phys. J. E*, 36:116, 2013.

[193] G. Reiter. Unstable Thin Polymer Films: Rupture and Dewetting Processes. *Langmuir*, 9:1344–1351, 1993.

[194] P. Bassereau, D. Brodbreck, T. P. Russell, H. R. Brwon, and K. R. Shull. Topological Coarsening of Symmetric Diblock Copolymer Films: Model 2D Systems. *Phys. Rev. Lett.*, 71:1716, 1993.

[195] A. Lo and R. T. Skodje. Kinetic and Monte Carlo models of thin film coarsening: Cross over from diffusion-coalescence to Ostwald growth modes. *J. Chem. Phys.*, 112:1966, 2000.

[196] B. K. Chakraverty. Grain size distribution in thin films - 2. Non-conservative systems. *J. Phys. Chem. Solids*, 28:2413–2421, 1967.

[197] J. Chaiken and J. Goodisman. Use of fractals and kinetic equations to model thermally induced hillock formation and growth in thin metal films. *Thin Solid Films*, 260:243–251, 1995.

[198] D. S. Sholl and R. T. Skodje. Late-stage coarsening of adlayers by dynamic cluster coalescence. *Physica A*, 231:631–647, 1996.

[199] K. B. Glasner and T. P. Witelski. Coarsening dynamics of dewetting films. *Phys. Rev. E*, 67:016302, 2003.

[200] K. B. Glasner and T. P. Witelski. Collision versus collapse of droplets in coarsening of dewetting thin films. *Physica D*, 209:80–104, 2005.

[201] F. Otto, T. Rump, and D. Slepcev. Coarsening rates for a droplet model: rigorous upper bounds. *SIAM J. Math. Anal.*, 38:503–529, 2006.

[202] K. B. Glasner. Ostwald ripening in thin film equations. *SIAM J. Appl. Math.*, 69:473–493, 2008.

[203] K. B. Glasner, F. Otto, T. Rump, and D. Slepcev. Ostwald ripening of droplets: the role of migration. *Eur. J. Appl. Math.*, 20:1–67, 2009.

[204] G. Kitavtsev and B. Wagner. Coarsening dynamics of slipping droplets. *J. Eng. Math.*, 66:271–292, 2010.

[205] S. A. Magrabi, B. Z. Dlugogorski, and G. J. Jameson. Bubble size distribution and coarsening of aqueous foams. *Chem. Eng. Sci.*, 54:4007–4022, 1999.

[206] R. Lemlich. Prediction of Changes in Bubble Size Distribution Due to Interbubble Gas Diffusion in Foam. *Ind. Eng. Chem. Fundamen.*, 12:89–93, 1978.

[207] W. W. Mullins. The statistical self-similarity hypothesis in grain growth and particle coarsening. *J. Appl. Phys.*, 59:1341–1349, 1986.

[208] J. Viñals and W. W. Mullins. Self-similarity and coarsening of three dimensional particles on a one or two dimensional matrix. *J. Appl. Phys.*, 82:621–628, 1997.

[209] P.V. Dolganov, E.I. Kats, and V.K. Dolganov. Collapse of Islands in Freely Suspended Smectic Nanofilms. *JEPT Lett.*, 106(4):229–233, 2017.

[210] P. Oswald, F. Picano, and F. Caillier. Dislocation loop dynamics in freestanding smectic films: The role of the disjoining pressure and of the finite permeability of the meniscus. *Phys. rev. E*, 68:061701, 2003.

[211] A. Missaoui, E. Lacaze, E. Eremin, and R. Stannarius. Observation of Backflow during the Anihilation of Topologocal Defects in Freely Suspended Smectic Films. *Crystals*, 11:430, 2021.

[212] D. Weaire and J. P. Kernmode. The evolution of the structure of a two-dimensional soap froth. *Philos. Mag. B*, 47:L29–L31, 1983.

Appendix

A.1 Mean square displacement in a parabolic potential

The motion of an isotropic droplet in the center of a hexagonal lattice formed by the six neighboring droplets, in first approximation, can be described by the motion in a quadratic potential ($V(x,y)$). This two-dimensional potential with the constant K has the following form

$$V(x,y) = \frac{K(x^2+y^2)}{2} = \frac{K}{2}r^2 \quad . \tag{A.1}$$

The probability $\widetilde{P}(r)$ to find the center droplet at the position (x,y) with respect to the hexagon center at $(0,0)$ can be described with the Boltzmann distribution

$$\widetilde{P}(r) = \widetilde{P}(x,y) = \frac{K}{2\pi k_B T}\text{exp}\left(-\frac{K(x^2+y^2)}{2k_B T}\right) \quad . \tag{A.2}$$

Since the distribution function is time-independent, the mean square displacement is also independent on time and will not describe the expected dynamic behavior of a droplet in a parabolic potential.

$$\int\limits_{-\infty}^{\infty}\int\limits_{-\infty}^{\infty} \widetilde{P}(r)\mathrm{d}x\mathrm{d}y = 1 \ \ \text{(normalization condition)}$$

$$\langle r^2 \rangle = \int\limits_{-\infty}^{\infty}\int\limits_{-\infty}^{\infty} \left[x^2+y^2\right]\widetilde{P}(r)\mathrm{d}x\mathrm{d}y \tag{A.3}$$

$$\langle r^2 \rangle = \frac{2k_B T}{K} \ \ \text{(time independent)} \tag{A.4}$$

Instead, the Smoluchowski equation for the diffusion in two-dimensional harmonic potential

$$\langle \widetilde{R}^2(\Delta t)\rangle = A\left(1-e^{B\Delta t}\right) \tag{A.5}$$

can be used with $\widetilde{R}^2(t) = (x(t)-x_0)^2 + (y(t)-y_0)^2$ and the parameters A and B. Here, $\widetilde{R}^2(t)$ describes the distance of the droplet in the hexagonal cage respectively in the potential at the position $(x(t), y(t))$ with respect to its initial position ($t = 0$) at (x_0, y_0). For short times Δt, it is assumed that the droplet motion is not significantly affected by the other droplets respectively the harmonic potential. Thus, a free diffusion with

$$\lim_{\Delta t\to 0}\langle \widetilde{R}^2(\Delta t)\rangle = 4D\Delta t \tag{A.6}$$

is expected. Using the first approximation of the exponential function (first terms of the power series, exp$(x) \approx 1 + x$), the Smoluchowski equation for short times gives

$$\lim_{\Delta t \to 0} \langle \widetilde{R}^2(\Delta t) \rangle \approx A(1 - 1 - B\Delta t) = -AB\Delta t = 4D\Delta t \ . \tag{A.7}$$

For long times Δt, the mean square displacement $\langle \widetilde{R}^2(\Delta t) \rangle$ can be calculated analogously to equation A.3 by averaging over $(x(t), y(t))$ and the initial positions (x_0, y_0).

$$\langle \widetilde{R}^2(\Delta t) \rangle = \int\limits_{-\infty}^{\infty} \int\limits_{-\infty}^{\infty} \int\limits_{-\infty}^{\infty} \int\limits_{-\infty}^{\infty} \left[(x - x_0)^2 + (y - y_0)^2\right] \widetilde{P}(x_0, y_0)\widetilde{P}(x, y)\mathrm{d}x_0\mathrm{d}y_0\mathrm{d}x\mathrm{d}y \tag{A.8}$$

With a substitution according to

$$a = \frac{K}{2k_BT} \tag{A.9}$$

in the Boltzmann distribution, equation A.8 becomes

$$\begin{aligned}
\langle \widetilde{R}^2(\Delta t) \rangle =& \frac{a^2}{\pi^2} \left[\int\limits_{-\infty}^{\infty} \int\limits_{-\infty}^{\infty} \int\limits_{-\infty}^{\infty} \int\limits_{-\infty}^{\infty} x^2 \quad e^{-a(x^2+y^2)} e^{-a(x_0^2+y_0^2)} \mathrm{d}x_0\mathrm{d}y_0\mathrm{d}x\mathrm{d}y \right] + \\
& \frac{a^2}{\pi^2} \left[\int\limits_{-\infty}^{\infty} \int\limits_{-\infty}^{\infty} \int\limits_{-\infty}^{\infty} \int\limits_{-\infty}^{\infty} 2xx_0 \, e^{-a(x^2+y^2)} e^{-a(x_0^2+y_0^2)} \mathrm{d}x_0\mathrm{d}y_0\mathrm{d}x\mathrm{d}y \right] + \\
& \frac{a^2}{\pi^2} \left[\int\limits_{-\infty}^{\infty} \int\limits_{-\infty}^{\infty} \int\limits_{-\infty}^{\infty} \int\limits_{-\infty}^{\infty} x_0^2 \quad e^{-a(x^2+y^2)} e^{-a(x_0^2+y_0^2)} \mathrm{d}x_0\mathrm{d}y_0\mathrm{d}x\mathrm{d}y \right] + \\
& \frac{a^2}{\pi^2} \left[\int\limits_{-\infty}^{\infty} \int\limits_{-\infty}^{\infty} \int\limits_{-\infty}^{\infty} \int\limits_{-\infty}^{\infty} y^2 \quad e^{-a(x^2+y^2)} e^{-a(x_0^2+y_0^2)} \mathrm{d}x_0\mathrm{d}y_0\mathrm{d}x\mathrm{d}y \right] + \\
& \frac{a^2}{\pi^2} \left[\int\limits_{-\infty}^{\infty} \int\limits_{-\infty}^{\infty} \int\limits_{-\infty}^{\infty} \int\limits_{-\infty}^{\infty} 2yy_0 \, e^{-a(x^2+y^2)} e^{-a(x_0^2+y_0^2)} \mathrm{d}x_0\mathrm{d}y_0\mathrm{d}x\mathrm{d}y \right] + \\
& \frac{a^2}{\pi^2} \left[\int\limits_{-\infty}^{\infty} \int\limits_{-\infty}^{\infty} \int\limits_{-\infty}^{\infty} \int\limits_{-\infty}^{\infty} y_0^2 \quad e^{-a(x^2+y^2)} e^{-a(x_0^2+y_0^2)} \mathrm{d}x_0\mathrm{d}y_0\mathrm{d}x\mathrm{d}y \right] \ .
\end{aligned} \tag{A.10}$$

The single terms of that extensive integral result in

$$\langle \widetilde{R}^2(\Delta t) \rangle = \left[\frac{1}{2a}\right] + 0 + \left[\frac{1}{2a}\right] + \left[\frac{1}{2a}\right] + 0 + \left[\frac{1}{2a}\right] = \frac{2}{a} \ . \tag{A.11}$$

For long times, the mean square displacement thus yields

$$\lim_{\Delta t \to \infty} \langle \widetilde{R}^2(\Delta t) \rangle = A = \frac{4k_BT}{K} \ . \tag{A.12}$$

With the results for the free diffusion for short times and the asymptotic behavior for long times, the parameters A and B can be calculated.

$$A = \frac{4k_BT}{K} \quad \text{and} \quad B = -\frac{DK}{k_BT}$$

Finally, the expression for the cage related mean square displacement can be found.

$$\langle r^2(\Delta t)\rangle = \frac{4k_BT}{K}\left[1 - \exp\left(-\frac{DK}{k_BT}\Delta t\right)\right] \tag{A.13}$$

A.2 Contact angle derivation

The adjacent figure shows the geometrical sketch of a circular segment with radius R_0 that is assumed for the profile (side-view) with height $\widehat{H}_0$ of the isotropic droplets.
With the green highlighted orthogonal triangle, the central angle θ can be described with the following equations:

$$\sin(\theta) = \frac{R_0}{r} \tag{A.14}$$

$$\cos(\theta) = \frac{r - \widehat{H}_0}{r} \quad . \tag{A.15}$$

The relation for the radius of the circle r then yields

$$r = \frac{\widehat{H}_0}{1 - \cos(\theta)} \quad , \tag{A.16}$$

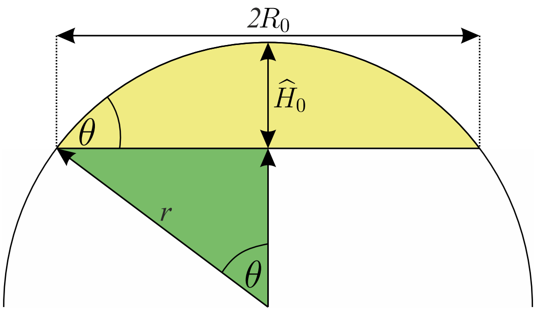

Figure A.1: Geometrical sketch of a circular segment with the chord length representing the initial diameter $D_0 = 2R_0$ of an isotropic droplet. The height of the segment is equal to the initial droplet height $\widehat{H}_0$. The circle has a radius of r. The contact angle θ can be found at the edge of the droplet as well as in the center of the circle.

and replacing r in equation A.14 and rearranging this equation results in:

$$R_0 = \widehat{H}_0 \frac{\sin(\theta)}{1 - \cos(\theta)} \quad . \tag{A.17}$$

With the half-angle formula (trigonometric identity)

$$\cot(\theta/2) = \frac{\sin(\theta)}{1 - \cos(\theta)} \quad , \tag{A.18}$$

the equation for the initial droplet radius R_0 has the following form:

$$R_0 = \widehat{H}_0 \cot(\theta/2) \quad . \tag{A.19}$$

Rearranging this formula eventually leads to an equation for the contact angle.

$$\theta = 2 \arctan\left(\frac{\widehat{H}_0}{R_0}\right) \tag{A.20}$$

A.3 Derivation of stress balance equation

The following derivation of the stress balance equation is based on the work of Howell [141]. The Stokes equation for the flow in a thin film with height h reads as

$$\begin{aligned}\nabla \cdot \mathbf{u} &= 0 \\ &\rightarrow u_x + v_y = 0 \ , &\text{(A.21)}\\ -\nabla p + \eta \nabla^2 \mathbf{u} &= 0 \\ &\rightarrow p_x = \eta(u_{xx} + u_{yy}) \ , &\text{(A.22)}\\ &\rightarrow p_y = \eta(v_{xx} + v_{yy}) \ , &\text{(A.23)}\end{aligned}$$

where gravitational effects and inertia are neglected. For simplicity, only flow in the film plane (x-direction) and perpendicular to it (y-direction) is considered. Thus, $\mathbf{u} = (u, v)$ and the normal and tangential stress conditions at the free surface are

$$\begin{aligned}\mathbf{n} \cdot \tau \cdot \mathbf{n} &= 2\kappa(\gamma + \eta \nabla_s \cdot \mathbf{u}) \ \text{and} \\ \mathbf{t}' \cdot \tau \cdot \mathbf{t}' &= \mathbf{t}' \cdot \nabla_s(\gamma + \eta \nabla_s \cdot \mathbf{u})\end{aligned}$$

with the fluid stress tensor τ, the mean surface curvature κ, and the vector normal $\mathbf{n}$ and tangential $\mathbf{t}'$ to the surface ($y = h$). The surface gradient operator ∇_s is defined as $\nabla_s = \nabla - \mathbf{nn} \cdot \nabla$.

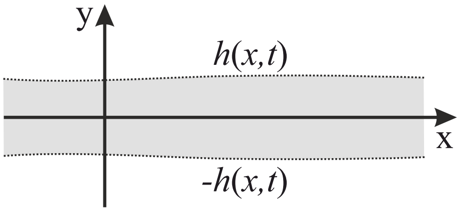

Figure A.2: Two-dimensional thin film with a thickness of $2h$ depending on time and position.

The viscous stress tensor can be calculated using the following definition:

$$\tau = \begin{bmatrix} \tau_{xx} & \tau_{xy} \\ \tau_{yx} & \tau_{yy} \end{bmatrix} = \begin{bmatrix} 2\eta u_x - p & \eta(u_y + v_x) \\ \eta(u_y + v_x) & 2\eta v_y - p \end{bmatrix} \ .$$

The kinematic boundary condition and the zero stress boundary condition at the two free surfaces at $y = \pm h$ thus are

$$\begin{aligned}\pm h_t \pm u h_x - v &= 0 &\text{on } y = \pm h \ , \quad &\text{(A.24)}\\ (-p + 2\eta u_x)(\pm h_x) &= \eta(u_y + v_x) &\text{on } y = \pm h \ , \quad &\text{(A.25)}\\ \eta(u_y + v_x) h_x &= (-p + 2\eta v_y) &\text{on } y = \pm h \ . \quad &\text{(A.26)}\end{aligned}$$

For a non-dimensional description of these equations, the following scaling is used:

$$\begin{gathered} x' = \frac{x}{R_0}, \ y' = \frac{y}{H_0}, \ u' = \frac{u}{u_0}, \ v' = \frac{v R_0}{u_0 H_0}, \\ h' = \frac{h}{H_0}, \ t' = \frac{u_0}{R_0} t, \ p' = \frac{R_0}{\eta u_0} p \ . \end{gathered}$$

Using this scaling, and only considering the positive y-direction for symmetry reasons and dropping the primes, results in

$$u_x + v_y = 0 \ , \tag{A.27}$$

$$\varepsilon^2 p_x = \varepsilon^2 u_{xx} + u_{yy} \ , \tag{A.28}$$

$$p_y = \varepsilon^2 v_{xx} + v_{yy} \ , \tag{A.29}$$

$$v = h_t + u h_x \ , \tag{A.30}$$

$$\varepsilon^2 (2u_x - p) h_x = u_y + \varepsilon^2 v_x \ , \tag{A.31}$$

$$(u_y + \varepsilon^2 v_x) h_x = 2v_y - p \ , \tag{A.32}$$

where $\varepsilon = H_0/R_0$ describes the ratio between the typical length H_0 in y-direction and R_0 in x-direction. Within the lubrication approximation and for the thin sheet equations $\varepsilon \ll 1$. An asymptotic expansion for u, v and p in powers of the small ratio ε^2 leads to

$$\begin{aligned} u &\approx u_0 + \varepsilon^2 u_1 + \varepsilon^4 u_2 + \ldots \ , \\ v &\approx v_0 + \varepsilon^2 v_1 + \varepsilon^4 v_2 + \ldots \ , \\ p &\approx p_0 + \varepsilon^2 p_1 + \varepsilon^4 p_2 + \ldots \ . \end{aligned}$$

The asymptotic expansions are now used in equations A.27-A.32 and the following terms can be found (the free surface boundary conditions at $y = h$).

$$u_{0x} + \varepsilon^2 u_{1x} + \varepsilon^4 u_{2x} + v_{0y} + \varepsilon^2 v_{1y} + \varepsilon^4 v_{2y} = 0 \tag{A.33}$$

$$\begin{aligned} &\varepsilon^2 p_{0x} + \varepsilon^4 p_{1x} + \varepsilon^6 p_{2x} \\ &\qquad = \varepsilon^2 u_{0xx} + \varepsilon^4 u_{1xx} + \varepsilon^6 u_{2xx} + u_{0yy} + \varepsilon^2 u_{1yy} + \varepsilon^4 u_{2yy} \end{aligned} \tag{A.34}$$

$$\begin{aligned} &p_{0y} + \varepsilon^2 p_{1y} + \varepsilon^4 p_{2y} \\ &\qquad = \varepsilon^2 v_{0xx} + \varepsilon^4 v_{1xx} + \varepsilon^6 v_{2xx} + v_{0yy} + \varepsilon^2 v_{1yy} + \varepsilon^4 v_{2yy} \end{aligned} \tag{A.35}$$

$$\begin{aligned} &v_0 + \varepsilon^2 v_1 + \varepsilon^4 v_2 \\ &\qquad = h_t + u_0 h_x + \varepsilon^2 u_1 h_x + \varepsilon^4 u_2 h_x \end{aligned} \tag{A.36}$$

$$\begin{aligned} &(2\varepsilon^2 u_{0x} + 2\varepsilon^4 u_{1x} + 2\varepsilon^6 u_{2x} - \varepsilon^2 p_0 - \varepsilon^4 p_1 - \varepsilon^6 p_2) h_x \\ &\qquad = u_{0y} + \varepsilon^2 u_{1y} + \varepsilon^4 u_{2y} + \varepsilon^2 v_{0x} + \varepsilon^4 v_{1x} + \varepsilon^6 v_{2x} \end{aligned} \tag{A.37}$$

$$\begin{aligned} &(u_{0y} + \varepsilon^2 u_{1y} + \varepsilon^4 u_{2y} + \varepsilon^2 v_{0x} + \varepsilon^4 v_{1x} + \varepsilon^6 v_{2x}) h_x \\ &\qquad = 2v_{0y} + 2\varepsilon^2 v_{1y} + 2\varepsilon^4 v_{2y} - p_0 + \varepsilon^2 p_1 + \varepsilon^4 p_2 \end{aligned} \tag{A.38}$$

The only leading order term in equation A.34 directly reveals

$$u_{0yy} = 0 \ , \tag{A.39}$$

and from equations A.33 and A.37

$$u_{0x} + v_{0y} = 0, \quad u_{0y} = 0 \ \text{ at } y = h \quad \rightarrow \quad u_0 = u_0(x,t) \tag{A.40}$$

can be found. The velocity in x-direction does not depend on y and hence it describes extensional flow with uniform axial velocity. Integrating the first equation in A.40 yields

$$v_0 = -y u_{0x} \ . \tag{A.41}$$

With regard to the leading order of the kinematic boundary condition (equation A.36)

$$v_0 = h_t + u_0 h_x \ , \tag{A.42}$$

the following term can be found (at $y = h$):

$$\begin{aligned} h_t + h_x u_0 + h u_{0x} &= 0 \ , \\ h_t + (h u_0)_x &= 0 \ , \end{aligned} \tag{A.43}$$

which represents the conservation of mass. Equation A.38 additionally gives the leading-order pressure term

$$p_0 = 2 v_{0y} = -2 u_{0x} \ . \tag{A.44}$$

With regard to the next order $\mathcal{O}(\varepsilon^2)$, additional relations for the pressure and the velocities can be found (equation A.34). Deriving equation A.44 and substituting yields

$$\begin{aligned} p_{0x} =& u_{0xx} + u_{1yy} \ , \\ \rightarrow u_{1yy} =& p_{0x} - u_{0xx} = -3 u_{0xx} \ . \end{aligned} \tag{A.45}$$

The boundary condition from equation A.37 is

$$(2u_{0x} - p_0) h_x = u_{1y} + v_{0x} \ , \tag{A.46}$$

and using the expression for the leading order pressure p_0 and equation A.41 leads to

$$u_{1y} = 4 u_{0x} h_x + h u_{0xx} \quad \text{at } y = h \ . \tag{A.47}$$

Finally, integrating equation A.47 from $y = 0$ to $y = h$ and applying A.45 leads to

$$\begin{aligned} -3 u_{0xx} h &= 4 u_{0x} h_x + h u_{0xx} \ , \\ 0 &= 4 u_{0x} h_x + 4 u_{0xx} h \ , \\ 0 &= (4 u_{0x} h)_x \ . \end{aligned} \tag{A.48}$$

By using again dimensional terms and with introducing the additional Laplace pressure $\nabla p = \gamma h h_{xxx}$, the stokes equation finally has the following form:

$$0 = \gamma h_{xxx} + 4\eta \frac{(u_x h)_x}{h} \ . \tag{A.49}$$

A.4 Rough calculation of the melting energy per film area

In order to classify the possible explanation for the discrepancy between the theoretical predictions and the experimental results regarding the coalescence duration, the energy required to melt smectic layers covering the isotropic droplets will be calculated.
The initial droplet surface A_0 can be determined to a value between 100 µm^2 and 15.000 µm^2, depending on their initial height H_0, diameter D_0 and contact angle θ. When assuming droplets of the same size and thus with a final droplet size defined as $D_{\text{end}} = \sqrt[3]{2}D_0$ and $H_{\text{end}} = \sqrt[3]{2}H_0$, the surface reduction ΔA yields

$$\Delta A = 2A_0 - A_{\text{end}} = \left(2 - 2^{2/3}\right) A_0 \approx 40\ \mu\text{m}^2\ ...\ 6200\ \mu\text{m}^2\ . \tag{A.50}$$

Since several physical parameters for the used liquid crystal mixture are not known yet, the properties of the well known and analyzed material 8CB that also has a smectic A phase are used for that rough approximation (parameters from [143]).

Molecular mass M:	291.44 g/mol
Phase transition enthalpy $\Delta H_{\text{SmA-N}}$ (SmA - N):	0.2 kJ/mol
Phase transition enthalpy $\Delta H_{\text{N-Iso}}$ (N - Iso):	0.7 kJ/mol
Density ρ:	$\approx$ 0.98 g/cm^3

The isotropic droplets in the experiments are assumed to be covered by at least one smectic layer with a layer thickness h_{layer} of approximately 3 nm. Thus, the volume of the excess material during coalescence and their mass can be calculated and yields

$$\begin{aligned}\Delta V &= (0.12\ ...\ 18.60)\ \mu\text{m}^3\\ \Delta m &= (1.18\ ...\ 182.28) \cdot 10^{-13}\ \text{g}\ .\end{aligned}$$

With these values, the required energy per film area can be estimated, using the sum of the given transition enthalpies $\Delta H_{\text{SmA-Iso}}$ (smectic A to nematic and nematic to isotropic) for the smectic A to isotropic phase transition enthalpy.

$$\frac{\Delta m\ \Delta H_{\text{SmA-Iso}}}{M\ \Delta A} = \frac{\rho\ h_{\text{layer}}\ \Delta H_{\text{SmA-Iso}}}{M} \approx 0.0091\ \text{N m}^{-1}\ . \tag{A.51}$$

This calculated value is of the order of the static surface tension of the material γ_{stat} and reaches almost the same value with two covering layers.

$$\frac{\Delta E}{\Delta A} \approx 0.0091\ \text{N m}^{-1} \quad \text{(for a single smectic layer covering the droplet)} \tag{A.52}$$

$$\approx 0.0182\ \text{N m}^{-1} \quad \text{(for two smectic layers covering the droplet)} \tag{A.53}$$

$$\gamma_{\text{stat}} = 0.0240\ \text{N m}^{-1} \quad \text{(static surface tension)} \tag{A.54}$$

Declaration of Honour

I hereby declare that I prepared this thesis without the impermissible help of third parties and that none other than the aids indicated have been used; all sources of information are clearly marked, including my own publications.

In particular I have not consciously:

- fabricated data or rejected undesirable results,
- misused statistical methods with the aim of drawing other conclusions than those warranted by the available data,
- plagiarized external data or publications,
- presented the results of other researchers in a distorted way.

I am aware that violations of copyright may lead to injunction and damage claims by the author and also to prosecution by the law enforcement authorities.

I hereby agree that the thesis may be electronically reviewed with the aim of identifying plagiarism.

This work has not yet been submitted as a doctoral thesis in the same or a similar form in Germany, nor in any other country. It has not yet been published as a whole.

Magdeburg, April 19th, 2022

M. Sc. Christoph Klopp